Nature and organization of the CuO_2-plane

as experimentally probed in the prototype high-temperature superconductor Bi2201

DISSERTATION

zur Erlangung des akademischen Grades
doctor rerum naturalium
(Dr. rer. nat.)
im Fach Physik

eingereicht an der
Mathematisch-Naturwissenschaftlichen
Fakultät I
Humboldt-Universität zu Berlin

von
Herr Dipl.-Phys. Lenart E. Dudy
geboren am 10.06.1975 in Neustadt/Holstein

Präsident der Humboldt-Universität zu Berlin:
Prof. Dr. Dr. h.c. Christoph Markschies

Dekan der Mathematisch-Naturwissenschaftlichen
Fakultät I:
Prof. Dr. Lutz-Helmut Schön

Gutachter:

1. Prof. Dr. R. Manzke
2. Priv.-Doz. Dr. J. Röhler
3. Dr. N. Koch

eingereicht am: 1. August 2008
Tag der mündlichen Prüfung: 16. Dezember 2008

Abstract

This thesis deals with the experimental exploration of the high-temperature superconducting Bi-cuprate system and mainly with single crystals of the one-layer Bi2201.

To begin, the structural change resulting from Pb substitution was explored by using topological scanning tunneling microscopy (STM) and low-energy electron diffraction (LEED). The resulting morphologies were explained in a pseudo-binary phase-diagram.

Using energy dispersive x-ray analysis and AC-susceptibility, it was proven that, for two variations of Bi2201 and also for LSCO, the superconducting transition temperature (T_C) always drops at the same hole-doping values - an effect that might be explained by the so-called 'magic doping fractions'.

By analyzing STM-data, it was reasonably argued that the so-called 'checkerboard order' is not preferentially due to an ordering of the carriers in the Copper-Oxygen-plane. In the interpretation presented here, it is caused by dopant-atoms or dopant-complexes. The role of the Oxygen might be of particular importance.

Measurements concerning the pseudogap-phase were then shown. Using angular resolved photoemission (ARPES), it was found that the gap in the antinodal direction is dominantly caused by the pseudogap-phase. Interestingly, while resistivity measurements detect two crossover temperatures, ARPES detects only the lower pseudogap-temperature. It can also be stated that the pseudogap also exists in the overdoped region. The most important finding about the pseudogap-temperature and the pseudogap-magnitude was that they also react on the doping values of the depressions in T_C. Due to this finding, it was proposed that superconductivity occurs when an otherwise perfect charge-ordered and spin-ordered two-dimensional electronic system has mobile defective holes.

Zusammenfassung

Diese experimentelle Arbeit beschäftigt sich mit Einkristallen der Bi Kuprate.

Mittels Rastertunnelmikroskopie und der Beugung langsamer Elektronen wurde die strukturellen Eigenschaften untersucht. Es wurde ein bestehendes pseudobinäres Blei-Temperatur Phasendiagram erweitert.

Mittels der Charakterisierungsresultate der energiedispersive Röntgenspektroskopie und der AC-Suszeptibilität wurde gezeigt, dass an bestimmten Lochdotierungen die Sprungtemperatur unterdrückt ist. Diese Tatsache wird für zwei Variationen des Bi2201 Kuprat-Systems bewiesen - durch Literaturdaten auch für LSCO.

Desweiteren wurde argumentiert, dass die sogenannte Checkerboard-Ordnung nicht eine Ordnung der elektronischen Struktur ist. Vielmehr kann davon ausgegangen werden, dass Sie durch Dotanten-Atome verursacht wird. Dabei könnte der zusätzlichen Sauerstoff eine Bedeutung haben.

Die Pseudolücken-Phase wurde mittels winkelaufgelöster Photoemission (ARPES) sowie Widerstandsmessungen untersucht. Durch ARPES konnte gezeigt werden, dass die Lücke in der antinodalen Richtung keinen grossen Anteil einer Supraleitungslücke aufweist, sondern mehr von der Pseudolückenphase bestimmt ist. Es wurde festgestellt, dass in der winkelaufgelösten Photoemission nur eine Übergangstemperatur sichtbar war, während bei den Widerstandsmessungen zwei Übergangstemperaturen sichtbar waren. Zudem wurde gezeigt, dass die Pseudolückenphase auch auf der überdotierten Seite existiert. Ein ganz und gar neues Ergebniss ist der dotierungsabhängige Verlauf der Pseudolücken-Temperatur und der in ARPES gemessenen Pseudolücke. Es zeigte sich dort zweifelsfrei, dass die Pseudolücken-Eigenschaften an genau denselben Dotierungen starke Änderungen aufweisen, an denen auch die Sprungtemperatur unterdrückt ist. Deshalb wurde propagiert, dass die Supraleitung durch Paarung von Defektlöchern in einem ansonsten magnetisch- und ladungs-hochgeordnetem Elektronensystem entsteht.

Eine Hauptursache der Armut in den Wissenschaften ist meist eingebildeter Reichtum.
Es ist nicht ihr Ziel, der unendlichen Weisheit eine Tür zu öffnen, sondern eine Grenze zu setzen dem unendlichen Irrtum.
[1]

A main cause of the poverty of sciences is usually its conceited wealth. It is not its goal to open a door for the infinite wisdom but to set a limit to the infinite mistake.

Contents

I

Motivation

The discovery of superconductivity at T≈ 30 K in the cuprate $La_{2-x}Ba_xCuO_4$ by Bednorz and Müller in 1986 [2] ignited enormous interest and was the catalyst for many investigations of these new types of superconductors called 'high-temperature superconductors' (HTSC). Through an intense worldwide research effort, an increasing number of compounds of these new materials was been discovered. Connected with that effort was the discovery of higher transition temperatures T_C. The highest transition temperature until now was found in $HgBa_2Ca_2Cu_3O_{8+\delta}$ which is approximately 164 K under pressure of approximately 30 GPa [3].

Superconductivity of the conventional low-temperature superconductors is explained well by Bardeen, Cooper and Schrieffer (BCS-theory) [4]. This theory is valid within the weak coupling limit and the attractive interaction for the Cooper-pairs due to electron-phonon coupling. For the high-temperature superconductors, it was already clear after initial investigations that the BCS theory, at least in its present form, would not be able to explain many of the unexpected and uncommon properties. Although the mechanism leading to high-temperature superconductivity has not yet been discovered, the enormous research effort has led to interesting results: All HTSC's have a layered crystal structure composed of CuO_2-planes. The CuO_2-planes are separated from each other by planes of various other oxides and alkaline earth metals which act as charge reservoirs - basically stabilizing the crystal structure and introduce holes into the CuO_2-planes, a mechanism called 'doping'. Because of the structure and the kind of carriers, these HTSC's are also called 'hole-doped cuprates'.

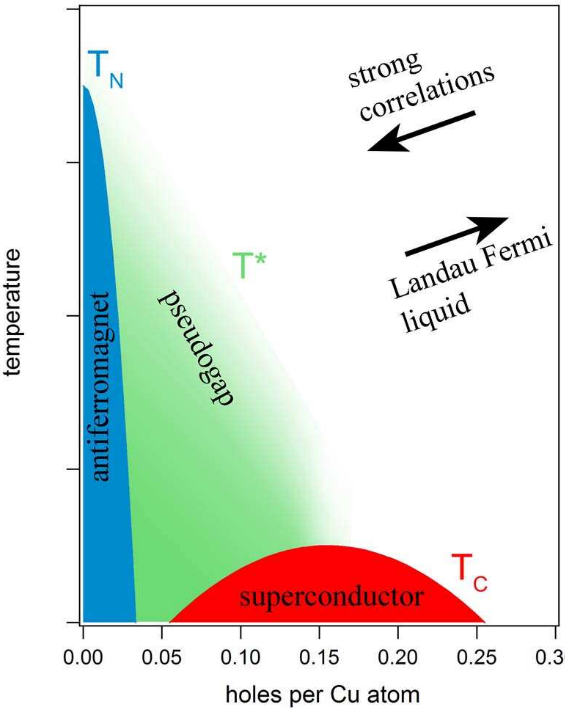

Figure 1.0: Generic electronic phase diagram of the HTSC's. T_N, T^* and T_C mark respectively the Néel-temperature, Pseudogap-temperature, and superconducting-transition-temperature.

With different numbers of holes per Cu atom, the doping process produces large variations in the electronic and magnetic properties of the compound, which are antiferromagnetic and charge transfer insulating, superconducting and metallic. It is common to visualize these properties in a so-called 'generic phase diagram' which is depicted in Fig. 1.0. At low doping, the system is an antiferromagnetic insulator, which is a consequence of the presence of strong correlations. At low temperatures and hole-doping between 5% and 25%, the system becomes superconductive. This 'superconducting dome' is ordinarily illustrated as a parabola which exhibits a maximum at an optimal doping of 16%. The region lower than this optimally doping is called 'underdoped', whereas the region higher than this doping is called 'overdoped'. An absolutely new phase of this system is the 'pseudogap phase' (see, e.g., [5]). The pseudogap phase is a partially-gapped state of the electronic structure which sets in below the characteristic temperature T*: In the so-called 'antinodal' direction a gap is present, whereas in the 'nodal' direction it is not. This $d_{x^2-y^2}$-like symmetry is similar to the symmetry of the superconducting order-parameter. The origin of the pseudogap as well as its exact shape within the phase diagram is still under heavy debate. In one line of thinking, it can be suggested that the origin of the pseudogap is connected with the origin of pairing.

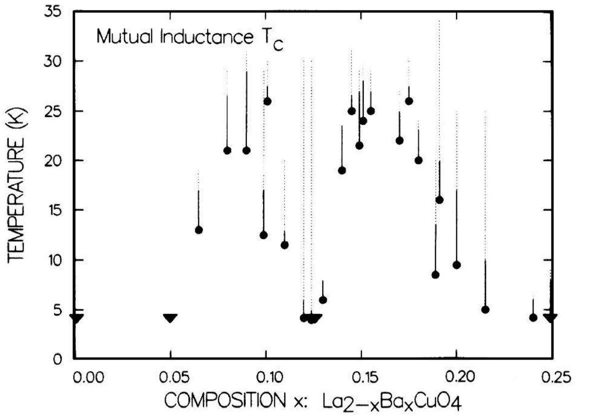

Figure 1.1: From Moodenbaugh et al. [6]: T_C vs Ba substitution x for $La_{2-x}Ba_xCuO_4$. The Ba substitution is proportional to the hole doping. The triangles indicate T_C<4.2 K. The depression of T_C around 1/8 is clearly visible.

The superconducting dome is typically described by a parabola and is called the 'universal curve' [7]. By scaling the maximum transition temperature, the curve is meant to fit every hole-doped high-temperature superconductor. However, there are often suggestions that the 'universal curve' is only a zeroth-order estimate of the true T_C vs doping curve. It is widely known that the 1/8 anomaly breaks the concept of the parabola-like T_C curve: For the high-temperature superconductor $La_{2-x}Ba_xCuO_4$ (LBCO) it was found by Moodenbaugh et al. [6] in 1988 that at a hole filling of 1/8 a depression in T_C occurs. Fig. 1.1 shows a graph from this publication. Recently, Komiya et al. [8] showed for $La_{2-x}Sr_xCuO_4$(LSCO) indications that, at fractional fillings other than 1/8, depressions of T_C may additionally exist. These fractional fillings can also be called 'magic doping fractions'. It can be suggested that the depression in T_C at these fillings is a manifestation of distinct ground states within the electronic structure. For LBCO and LSCO at 1/8 filling, there are clear indications of a magnetic-ordered and charge-ordered spatial configuration within the CuO_2-plane (see, e.g., [9, 10, 11, 12, 13]).

In the present work, the phase diagram is experimentally examined from the highly underdoped to the overdoped side. This work therefore relies on highly characterized, structurally-undisturbed single-crystals. In experiments of the hole-doped, high-temperature superconductors, two single-crystal systems are typically used: One is LSCO and the other is the two-layer cuprate $Bi_2Sr_2CaCu_2O_{8+\delta}$ (Bi2212). LSCO has a three dimensional crystalline structure of the charge reservoirs, whereas Bi2212 has a layered structure. Because of its structure, LSCO is better to synthesize and available in very high quality but it is not commonly used for surface-sensitive methods as it has no dedicated cleaving-plane. In the last decade, the synthesization quality of all HTSC single crystals has improved. This has led to surface-sensitive methods no longer being restricted to Bi2212. $Bi_2Sr_{2-x}La_xCuO_{6+\delta}$ (La-Bi2201) can also be used, which is a descendant of $Bi_2Sr_2CuO_{6+\delta}$ (Bi2201) - the first [14] discovered member of the series of so-called 'Bi-cuprates'.

This Bi2201 material is a 'one-layer' HTSC with one CuO_2-plane per primitive unit cell and the advantage of weak inter-plane coupling. For example, this results in a low T_C which makes it possible to measure in angular resolved photoemission (ARPES) the normal-state properties above T_C with low thermal broadening and high experimental accuracy. In Bi2201 and Bi2212, the hole-doping is solely done by the extra Oxygen, whereas in La-Bi2201 the hole-doping can be structurally controlled more softly by Oxygen and Lanthanum. Compared to Bi2201 and Bi2212, the Lanthanum-substituted one-layer material has the advantage that nearly all hole concentrations can be obtained. Also, it is worth noting that as for Bi2212, a modification can be grown where Lead is substituted on Bismuth positions: $Bi_{2-y}Pb_ySr_{2-x}La_xCuO_{6+\delta}$ (Pb-Bi2201). With high enough amounts of Pb, this substitute is structurally cleaner, i.e. free of one-dimensional superstructure.

In this work, single crystals of La-Bi2201, as well as Pb-Bi2201 are used. Before addressing the more complex question concerning the origin of superconductivity in the used compound, the structural change resulting from Pb substitution has to be examined in detail. In this work, this will be done by topographic scanning tunneling microscopy (STM). The aim of this study is therefore exclusively to explore the upper limit of current achievable perfection for the experimental realization of the theoretical CuO_2-plane.

With the realization of the CuO_2-plane, the physical properties measured within the phase diagram might turn out to be well-suited for clarifying the choice of theoretical models of the HTSC's. In my view, there exist some important questions connected to the discussion of the origin of pairing, which can be seen as the starting point for the examinations described in this thesis:

- *Does the Bi2201 system also show depression of T_C at certain hole doping fractions? What is the shape of the T_C-vs-doping curve?*

  These questions implicate the possibility that the previously mentioned depressions in T_C might be a generic feature within the phase diagram of the CuO_2-plane. Explicitly, here the word 'generic' means: (i) A certain feature depicted in this phase diagram exists for all the hole-doped cuprates, and (ii) this feature is caused only by the electronic structure within the single, undisturbed CuO_2-plane - not by the structural environment, e.g. the crystalline structure of the charge reservoirs.
  If these depressions are generic, they might be worth considering within the theoretical models of pairing, or at least can be used for the construction of the ground state in the absence of pairing. The questions are answered here by using basic characterization results of AC-susceptibility measurements and energy dispersive x-ray analysis, giving respectively the T_C and the chemical composition. The characterization was done for the statistically relevant number of 299 single crystals.

- *Does the electronic structure within the CuO_2-plane of Bi2201 show a spatial order?*

  This question partly relies on the results of the first questions, as the existence of generic depressions like 1/8 may lead to a spatially magnetic- and charge-ordered configuration. But there is also an order found in Bi2212 by scanning tunneling spectroscopy/microscopy, called 'checkerboard order' (see, e.g., [15, 16, 17, 18]). This order might be connected to the 1/8-like order or could also be of different origin. For the consideration of theoretical models, it might be interesting to know whether the possible ordered structure shows any relation to superconductivity or represents a certain ground state of the system. In order to test the crystals for a charge-induced order and to reveal its nature, measurements from scanning tunneling microscopy will be shown.

- *Is the pseudogap different from the superconducting gap? For Bi2201, what is the shape of the T^*-vs-doping curve?*

  As already mentioned, the unusual pseudogap phase might play a central role in revealing the origin of superconductivity in the cuprate HTSC's. The first questions will be discussed with the help of angular resolved photoemission measurements. The answer is of interest for defining the dependence of the pseudogap phase relative to the superconducting phase. The second question is relevant for the choice of models of pairing. It can be more specified to the question of whether T^* cuts the superconducting dome near optimal doping or covers the whole superconducting dome (see, e.g., [19, 20]). This question will be answered using angular resolved photoemission and resistivity measurements. The use of two methods also gives the opportunity for comparison, as both basically are thought to probe the charge channel. Therefore, by the usage of almost identical samples one can control the consistence of the T^* determination of both. The need for this comparison is given, as in dependence of the methods used, there are reports for two different pseudogap crossover temperatures - called respectively the 'upper-' and the 'lower-pseudogap'.

Sometimes the gained results will be compared to the two-layer material Bi2212. Obviously, a rich variety of experimental methods is used here. Let me therefore note that, for enhanced readability, the brief description of the most commonly used experimental methods is given in Appendix A. More detailed descriptions of the analysis procedures, as well as tables for refined quantities, are given in the Appendix B.

II

Introduction

2.1 From conventional to unconventional superconductivity

The phenomenon of superconductivity became accessible due to the achievement of low temperatures. Based on the Joule-Thompson process [21], in 1895 Linde developed a method to liquify air in large amounts [22]. In 1908, Onnes reported liquified Helium [23]. Three years later, he showed that at 4.19 K the resistance of Mercury drops to zero [24]. This phenomena was not expected within the conduction theory of metals developed by Drude [25].

In 1933, Meissner and Ochsenfeld [26] showed that a superconductor cannot be explained by assuming only a 'perfect conductor'. When a superconductor is in an external weak magnetic field and cooled below the critical temperature, the magnetic flux is expelled from the bulk. To explain this effect, the London brothers assumed two kinds of conducting electrons: Normal-state and super-conducting electrons [27]. Within this theory, they defined the penetration depth λ, indicating the length that the magnetic field penetrates the bulk. Its value is proportional to the number of superconducting electrons.

In 1950, Ginsburg and Landau proposed a phenomenological theory based on Landau's theory of second order phase transitions [28]. This theory introduces a complex pseudo-wave function ψ as an order parameter. Its square is the local density of superconducting electrons. The Ginzburg Landau parameter $\kappa = \lambda/\xi$ was also defined. The ξ is called the coherence length and can be understood as the decaying length of the superconducting wave function. Abrikosov showed that the case $\kappa > 1/\sqrt{2}$ leads to a type II superconductor [29]. This was a theoretical explanation for an experimental observation; From early magnetization measurements, it was known that the superconductors can be 'hard' (type I) or 'soft' (type II) in their diamagnetic response (see [30] and references therein). In 1934, Shubnikov had already experimented with an alloyed system which could be transformed from type I to type II. The considerable difference between both types is that in a type I superconductor the increase of a magnetic field to a critical value abruptly destroys superconductivity. In a type II superconductor, there are two critical fields: H_{c1} and H_{c2}. At H_{c2} the superconductivity is destroyed; The lower H_{c1} describes the boundary between the 'Meissner phase' and the 'Shubnikov phase'. In the Shubnikov phase, the superconductor minimizes the effect of the penetrating magnetic field within the superconducting bulk by vortices carrying magnetic flux. These vortices are quantized by multiplies of $\Phi_0 = h/2e$.

In 1950, Maxwell [31] and Reynolds et al. [32] reported the so called 'isotope effect' in Mercury. They found that T_C is inversely proportional to $M^{1/2}$ where M is the isotope mass. Fröhlich predicted that the driving force for superconductivity is the electron-phonon interaction [33].

In 1957, Bardeen, Cooper and Schrieffer published their theory of superconductivity [4]. In this BCS theory, two Bloch electrons with opposite spin and momentum can balance out the Coulomb repulsion by interacting though a virtual phonon. The correlation of both these electrons represents a bosonic quasi-particle in its ground state, which is called a 'Cooper pair'. Within this state, the boson can carry a current without dissipation. All this considered, the condition for a Cooper pair is therefore that the matrix element for electron-phonon interaction (Λ) is stronger than the electron-electron interaction (μ): $-V = -\Lambda + \mu < 0$. The formation energy of the Cooper pair and its thermodynamics can be calculated within the weak coupling limit. This limit means that the matrix element V is for the Bloch electrons in an interval around the Fermi energy $E_F \pm \hbar\omega_D$ isotropic (independent of the wavevector). This condition implicitly means that $T_C \ll \Theta_D$. Here $\Theta_D = \hbar\omega_D / k_B$ is the Debye temperature. Therefore, the superconducting transition temperature T_C can be calculated as:

$$T_C = 1.14\,\Theta_D\, e^{-1/N(E_F)V}\,. \tag{2.1}$$

Here, $N(E_F)$ is the electrons density of state at the Fermi energy. For the superconducting state it is also remarkable, that a gap opens below T_C. For T=0 the gap is given as

$$\Delta(0) = 3.52\, k_B T_C / 2 \tag{2.2}$$

The gap has an s-wave symmetry for weak-coupling, which means that the gap opens isotropically at the Fermi surface.

The predicted gap was found [34, 35] and the BCS theory was able to explain all phenomena in the superconductors, e.g. the isotope effect and the Josephson tunneling [36]. Further research led to the BCS weak-coupling case being expanded towards a strong-coupling including better understanding for the electron-phonon interaction by Migdal [37], Eliashberg [38], and McMillan [39]. McMillan determined that, in most conventional cases, the maximum critical temperature T_C^{max} could be estimated. In Nb_3Ge films, superconductivity[1] could be leveled up to 22.3 K [40], with improved conditions to 23.2 K [41]. In 1973, Bardeen stated that in the common alloys, T_C^{max} for normal phonon mechanisms is almost achieved and other mechanisms must be suggested for obtaining higher transition temperatures [42]. Since that time, T_C^{max} could not be increased further.

The situation changed in 1986 when Bednorz and Müller found the high-temperature superconductor $La_{2-x}Ba_xCuO_4$ (LBCO) with a T_C of about 30K [2]. This was the first high-temperature superconductor of the *hole-doped cuprate* family to be found. At this point the 'goldrush' for cuprate high-temperature superconductivity began: In January 1987, $La_{2-x}Sr_xCuO_4$ (LSCO) with T_C=36K was reported by Cava et al. [43], in February 1987,$YBa_2Cu_3O_{7-x}$ (YBCO) with T_C=93K by Wu et al. [44] - the first at temperatures warmer than liquid Nitrogen. In December 1987, $Bi_2Sr_2CuO_{6+\delta}$ (Bi2201) was reported by Michel et al. [14]: A high-temperature superconductor without rare earths. The events in January of 1988 may illustrate the excitement of the time: Maeda et al. found a 105 K phase in the Bi-Sr-Ca-Cu-O system [45]. The article was received by the Japanese Journal of Applied Physics on January 22 and accepted a day later. On January 26 of 1988, Chu et al. sent their report about superconductivity up to

[1] Historically, the superconductivity of this materials was already called 'high-temperature superconductivity'

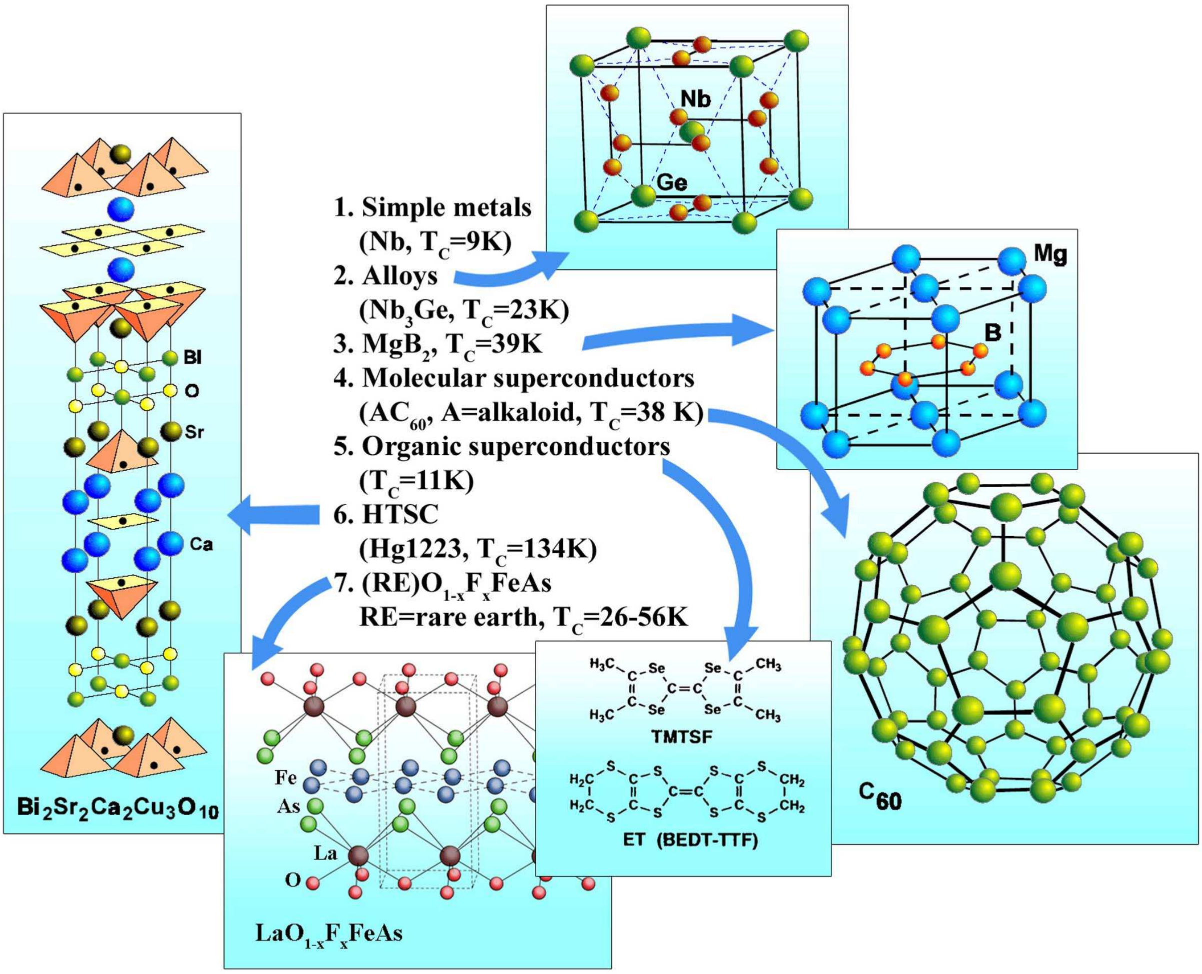

Figure 2.1: Composed from [49], [50] and [51]: Collection of some important superconductors.

114 K in the Bi-Al-Ca-Sr-Cu-O system to Physical Review Letters [46] and the phase identification followed later [47]. The material which was found by both was $Bi_2Sr_2CaCu_2O_{8+\delta}$, also called Bi2212 or BSCCO [2]. The discovery of other high-temperature superconducting cuprates followed. The highest transition temperature of all cuprates is observed for the Hg-family with the triple-layered Hg2223 having the maximum critical temperature of 134 K [48] under normal conditions. Under pressure of about 30 GPa, it can even reach 164 K [3]. Compared to the BCS-superconductors the remarkable difference is that the cuprates are bad metals in the normal-state and close to a metal-insulator transition. They are layered, quasi two-dimensional structures with a central CuO_2-plane. The superconducting order parameter (gap) has a d-wave symmetry. Most conventional, low-T_C superconductors have an s-wave symmetry and are normal-state metals.

Electron-doped cuprates also exist, e.g. $Pr_{2-x}Ce_xCuO_4$ (PCCO), $Nd_{2-x}Ce_xCuO_4$ (NCCO)

---

[2] More exactly it seemed to be a mixture of the two-layer Bi2212 and the three-layer Bi2223, with a contamination caused by the AlO_2-crucible, in the case of the latter.

[52, 53], and $Sr_{1-y}Nd_yCuO_2$ [54]. These materials possess the essential building block of the cuprate family: The CuO_2-planes. An important question is whether its superconductivity is the same as in the hole-doped cuprates. Further investigations that reach this conclusion could be very interesting for testing the mechanism.

The mechanism of cuprate high-temperature superconductivity is strongly debated. The most prominent theories will not be reviewed here, but will be addressed in a later section. In the following I would like to summarize briefly other known superconducting materials. The subjectively ordered collection of these materials is depicted in Fig. 2.1.

There are also organic superconductors. For a more detailed review, please see [55, 50]. They consist of a packed repetition of a building block, which is a donor molecule plus an acceptor complex. Certain packing produces a quasi two-dimensionality. The first superconductivity in this class of materials was reported in 1980 by Jerome et al. in $(TMTSF)_2PF_6$ [56]. Here, TMTSF is the donor and is fully written as tetramethyltetraselenafulvalene. The organic superconductors show some similarities to the cuprates; They are typically quasi two-dimensional and show indications of a d-wave superconductivity. They can be considered correlated materials, because they are Mott-insulating and antiferromagnetic. Under ambient pressure, the record is T_C=11.2 K for κ-$(ET)_2Cu[N(CN)_2]Br$ [57]. Here, ET is the donor and the short form of BEDT-TTF (bisethylenedithio-tetrathiafulvalene) and κ is one of three possible phases for the packing of the ET molecules.

The alkaloid-doped C_{60} is the most prominent member of the so-called 'molecular superconductors' or 'fullerene superconductors'. The first report of superconductivity at 18K was in K_3C_{60} as reported by Hebard et al. [58] in 1991. Until now, the highest T_C found is 38 K in Cs_3C_{60} [59]. It is widely believed that A_3C_{60} are s-wave, BCS-like superconductors, driven by the coupling to phonons and probably with some strong-coupling effects. But there is no conclusive evidence that this picture is correct or that another electronic mechanism is excluded [60].

Powdered MgB_2 has been used since the 1950s, but in 2001 Nagamatsu et al. [61] discovered that it is a high-temperature superconductor with a T_C of 39 K. This ignited a new 'gold rush'. Similar to high-T_C superconductors, MgB_2 is a layered material. However, while cuprates are bad metals or even insulators in their normal-state, MgB_2 is always a metal. The material is mainly considered to be a multigap superconductor. In this system two conduction bands are involved in a BCS-like phonon-mediated pairing and two superconducting gaps also evolve (see e.g [62, 63, 64]).

In 2006 it was not widely recognized that the Iron-based layered superconductor LaOFeP showed superconductivity up to 4 K [65]. In February 2008, Kamihara et al. reported that $La[O_{1-x}F_x]FeAs$ has a T_C up to 26K [66], then it was found to be 43 K [67]. Again a 'gold rush' ensued. The record is now (June 2008) T_C=56K for $Gd_{1-x}Th_xOFeAs$ [68]. I suggest that the superconducting series can be described by the formula $(RE)[O_{1-x}F_x]Fe(P)$, where RE is a rare earth and P a pentel. As the papers are published before the ink is dry, a discussion of a possible mechanism would only be premature.

2.2 The cuprate high-temperature superconductors

Here I would like to discuss the cuprate high-temperature superconductors, focussing on the hole-doped variety. All of the cuprates posses CuO_2-planes, which are the conducting planes where the holes reside. Fig. 2.2 shows the ideal tetragonal crystallographic unit cells of the Bismuth-cuprate series. The structure of Bi2201 will be discussed in Chapter 3 in more detail. Without going into the detail of the structure, one can see the CuO_2-planes marked in yellow. The series can be chemically described by the formula $Bi_2Sr_2Ca_{n-1}Cu_nO_{2n+4+\delta}$. Here n gives the number of CuO_2-planes per primitive unit cell. Other homologous members of the family of the cuprates are the series $Tl_1Ba_2Ca_{n-1}Cu_nO_{2n+3+\delta}$, $Tl_2Ba_2Ca_{n-1}Cu_nO_{2n+4+\delta}$, and $Hg_2Ba_2Ca_{n-1}Cu_nO_{2n+2+\delta}$.

All of the previously listed materials are high-temperature superconductors. It is interesting that the maximum critical temperature T_C^{max} scales with the number of CuO_2-planes per unit cell. This can be seen in the graph shown in Fig. 2.3, where T_C^{max} is plotted against the number of CuO_2-planes per primitive unit cell. For each family we see an increase in T_C with the number of CuO_2-planes and a maximum for three or four.

The basic knowledge about superconductivity in the cuprates is the following: Superconductivity in the cuprates originates from pairs of electrons (or holes), because e.g. in $YBa_2Cu_3O_{7-x}$ the flux through a superconducting ring is quantized by the fluxoid quantum $\Phi_0 = h/2e$ [73]. In contrast to conventional s-wave superconductors, the superconducting order parameter is dominantly d-symmetric (see [74] and references therein). Within the Ginzburg Landau theory, the cuprates are type-II-superconductors [71]: In the ab-plane, the coherence-length (ξ_{ab}) is small with typi-

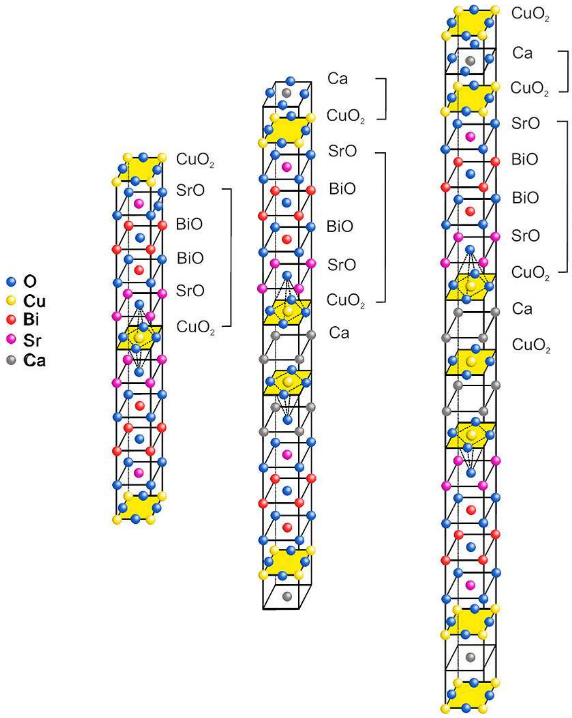

Figure 2.2: Tetragonal crystallographic unit cells of the Bismuth-cuprate series. From left to right the one-layer, two-layer, and three -layer variations are shown.

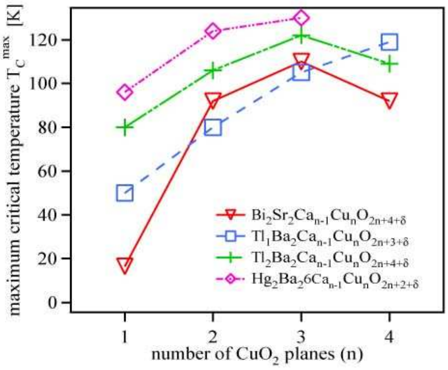

Figure 2.3: T_C^{max} of different HTSC-families as function of number of CuO_2-planes per primitive unit cell. Measurements from this study and [69, 70, 71, 72].

cal values around 20 Å and the penetration depth is large with $\lambda_{ab} \approx 6000$ Å. The out-of-plane coherence length (ξ_c) is about 3-4 Å and the penetration depth $\lambda_c \approx 1500$ Å. From the extremely high value of $\kappa = \lambda/\xi$, it follows that the upper critical magnetic field H_{c2} is much higher than in conventional weak-coupled superconductors.

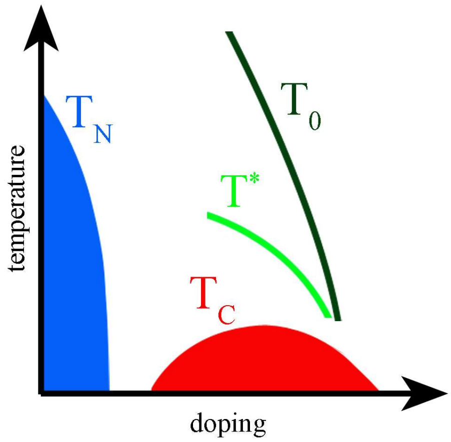

Figure 2.4: Adapted from [5]: Generic electronic phase diagram of the hole-doped cuprates including the two pseudogap crossovers T$_C$ (lower pseudogap) and T$_0$ (upper pseudogap).

Next, I will discuss the normal-state properties. Because of the quasi two-dimensionality of the materials, the normal-state resistivity is also strongly anisotropic; Common ratios of the in-plane and the out-of-plane resistivity ρ_c/ρ_{ab} are between 500 and 10^6 [71]. At around optimal doping and in the underdoped region, the cuprates are bad metals. It is remarkable that already below the Debye temperature ($\approx$ 400K), the normal-state resistivity scales nearly linearly with temperature (see, e.g., [75, 76, 77]). In angular resolved photoemission, the self-energy measures close to the Fermi-energy (E$_F$) linearly with temperature and energy. Also, other normal-state properties, such as the optical conductivity, the electronic Raman-scattering intensity, the thermal conductivity, various nuclear relaxation rates, the Hall conductivity and the magneto-resistance show an anomalous non-metal-like behavior (see [78] and references therein). Because of these unusual behaviors, the cuprates are often seen as 'strange metals'; marginal-Fermi-liquids or non-Fermi-liquids. Within Landau's Fermi-liquid theory [79], interacting electrons can be described as quasi-particles consisting of free electrons plus their (weak) interactions, which are adiabatically switched on.

Remarkable for the hole-doped cuprates is the pseudogap state. This state can be probed by resistivity measurements, nuclear magnetic resonance (NMR) relaxation time and Knight shift in NMR measurements (see [5] and references therein). In angular resolved photoemission, a gap can be observed below a characteristic temperature T*>T$_C$. This situation is depicted in Fig. 2.5: The dispersion of the lowest excitation shows above T* a hole-like Fermi surface. Below T*, the pseudogap with a d$_{x^2-y^2}$-symmetry forms. This behavior is quite unique as it means in principal that in one direction the electrons behave as they do in a metal, whereas in the other direction they are more semiconductor-like. The 'metal-like' direction is transversal to the in-plane Cu-O binding, while the gap is strongest along the in-plane Cu-O binding. As indicated in the phase diagram in Fig. 2.4, T* changes with doping. But there is no consensus about the shape - e.g., whether the pseudogap-temperature already drops close to optimal doping or covers the whole superconducting dome[3]. This uncertainty concerning the shape may have its origin in the different quality of the single crystals or in the different experimental methods probing different gaps (see, e.g., [20]). There are also reports of two different pseudogaps (see, e.g., [5]), the previously mentioned upper and lower varieties.

---

[3] For a more detailed discussion about the shape, please see Chapter 6 and references therein.

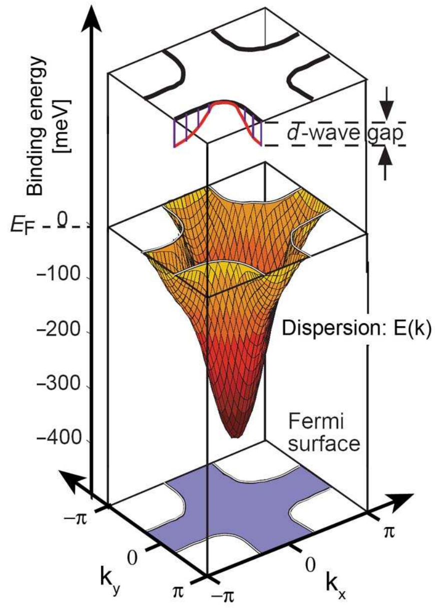

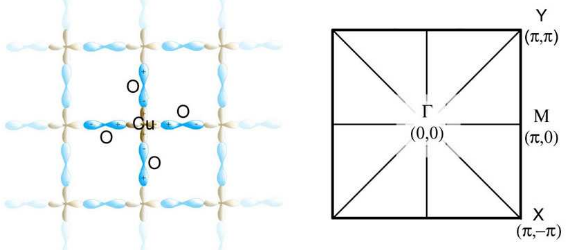

Figure 2.5: **Top:** Orientation of the Brillouin-zone relative to the CuO_2-plane. The ΓM-direction is along the CuO-binding.

Left: The dispersion of the lowest excitation in the cuprates (middle) gives a hole-like Fermi surface (lower). A gap of $d_{x^2-y^2}$-symmetry (upper) leaves the nodal direction $\Gamma \rightarrow X/Y$ unaffected while the excitation shows a large gap near M (composed under usage of [80]).

Both can be observed by the Knight shift in nuclear magnetic resonance, while other methods like ARPES only show one pseudogap. The lower pseudogap in Fig. 2.4 is marked by the crossover temperature T^*, the higher with T_0.

By using nuclear magnetic resonance (NMR), it can be observed that antiferromagnetic fluctuations are present within the pseudogap state. At low hole-dopings, the cuprates are antiferromagnetic insulators. Long range antiferromagnetic order was first found in the LSCO parent compound La_2CuO_4 by Vaknin et al. [82], using neutron powder diffraction. This long-range order is completely destroyed in $La_{2-x}Sr_xCuO_4$ at about 2% hole-doping [83]. But it is remarkable that at low temperatures a short range magnetic order survives upon hole doping. Fig. 2.6 shows results from neutron scattering on $La_{2-x}Sr_xCuO_4$ [81]: At hole doping of x=0, the long range antiferromagnetic order produces a peak at the $(1/2, 1/2)$ position in the Brillouin zone by the doubling of the magnetic cell. Upon doping, the antiferromagnetic peak splits into two incommensurate peaks; Above around 0.05 holes per Cu the incommensurate peaks are fourfold. In Fig. 2.6, the incommensurability ϵ of the two different regimes (x<0.05 filled circles, and x>0.05 open circles) is plotted in relative length units of the tetragonal cell. One can clearly see that the incommensurability scales linearly with doping.

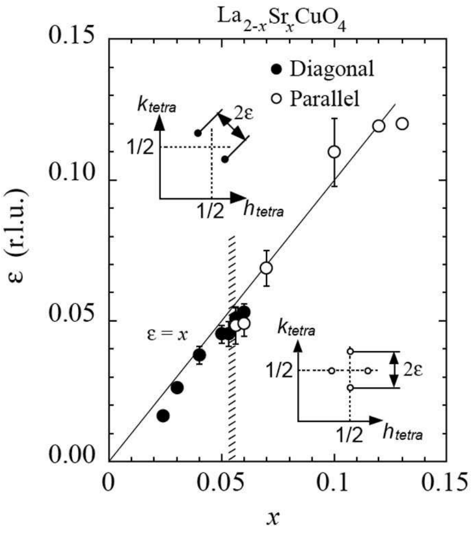

Figure 2.6: From [81]: Variation of the magnetic incommensurability ϵ (as defined in the insets) for lightly doped $La_{2-x}Sr_x$-CuO_4.

Overall, the antiferromagnetism in the parent compound seems to have a strong impact. To discuss the electronic structure of the cuprates, it is therefore good to start with the parent compound and then discuss the possible change due to additional hole-doping.

2.2.1 Electronic structure

The electronic structure of the parent compound

To discuss the electronic structure, I begin with the CuO_6-octahedron: Each Cu-atom has four O-atoms as nearest neighbors in the plane and two apical O-atoms. For Bi2201, the Cu-atom is covalently bound to the O-atoms in the plane with a bond length of about 1.9 Å. In apical direction, the CuO-bond is only weakly covalent with a typical bond length of about 2.3 Å [84]. A schematic picture of the CuO binding is shown in Fig. 2.7. From the atomic O-$p_{x,y}$ and Cu-$d_{x^2-y^2}$-orbits one accounts for the crystal field splitting and the Jahn-Teller distortion [85] and results in CuO-hybrids of pdσ -symmetry. According to this simple model, it is evident that the electronic structure of the region around the Fermi-energy is composed mainly of these CuO pdσ orbits. Because of this, the investigations have been concentrated on the CuO_2-plane. In principle, four steps are necessary to to illustrate the current level of knowledge about its electronic structure:

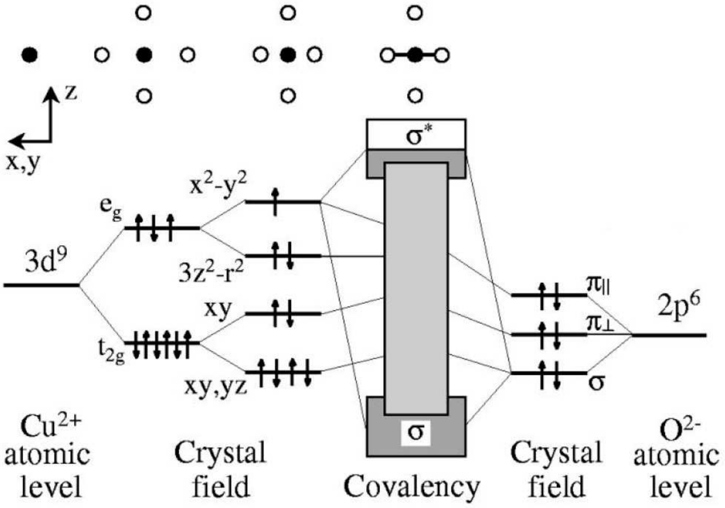

Figure 2.7: From [86]: Crystal-field splitting and hybridization produces CuO-hybrids of pdσ -symmetry. On the upper left a side view of the atomic placement due to the different processes is shown.

The first step is to calculate the electronic band structure within the local density approximation (LDA). In the case of an undoped CuO_2-plane, this will give an antibonding CuO_2 *pdσ*-hybrid band which is half filled. Thus, band structure calculations propose a metal shown by the density of states (DOS) in Fig. 2.8 (1). In contrast to this, it is well known that the undoped CuO_2-plane is an antiferromagnetic insulator. For example, in polycrystalline $Bi_2Sr_1La_1CuO_{6+\delta}$, the Néel temperature is approximately T_N=270K [87]. Although LDA model calculations obviously fail in this case, they propose for high temperatures and high hole-dopings quite realistic Fermi

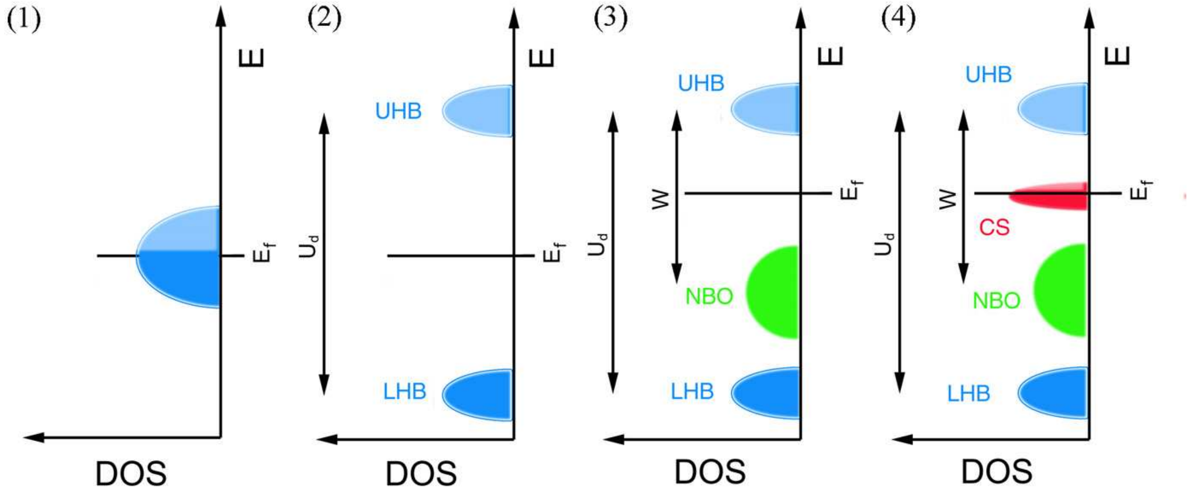

Figure 2.8: Qualitative overview of the density of states expected in different models for the electronic structure of a CuO_2-plane:

(1) The LDA band structure calculation produces a half-filled conduction band according to a metal.

(2) The DOS of a Mott-Hubbard insulator. The upper Hubbard band (UHB), which is empty when half-full, and the filled lower Hubbard band (LHB) are visible.

(3) The extension of the Mott-Hubbard model, taking into account also the O2p$_{x,y}$-orbits, is the three-band Hubbard model. An additional DOS peak between the UHB and LHB is produced. This peak is often associated with the non-bonding O2p band and denoted as NBO.

(4) Increasing the number of holes and including the interaction between the 2p- and 3d- holes, an additional correlated state (CS) splits off from the NBO band.

surfaces[4] in the normal-state (see, e.g., [89, 90]).

The reason why the LDA band structure calculations fail in describing the electronic character of the CuO$_2$-plane is because the correlations of the electronic system are not adequately taken into account. The strong correlations may be considered at first only on the Cu sites and not the Oxygen sites. This setup can be described within the Mott-Hubbard model [91, 92]. The electrons within the Cu-orbital at Cu-atom position i are constructed within the second quantization formalism by the operator $d^{+}_{i,s}$ and destructed by the operator $d_{i,s}$. The mean energy of each electron is represented by ϵ_d. The strong correlations due to Coulomb interactions for two electrons on the same Cu-site are included by the Hubbard interaction energy U_d. The hopping of an electron between different sites with position i,j is described by t_d. The Hamiltonian then

---

[4] Let me note here that in the case of the Bi-cuprates the LDA derived Fermi surfaces show BiO-pockets, which until now could not resolved by ARPES. A good starting point for the 'BiO-pocket problem' is [88].

yields

$$\mathcal{H} = \epsilon_d \sum_{i,s} n^d_{i,s} + t_d \sum_{<i,j>,s} d^+_{j,s}\, d_{i,s} + \frac{U_d}{2} \sum_{i,s} n^d_{i,s}\, n^d_{i,-s}\,, \tag{2.3}$$

where $n^d_{i,s} = d^+_{i,s} d_{i,s}$ is the number of electrons on site i with spin s. The symbol $< \cdots >$ indicates summation only over next neighbors. At half-filling (Cu3d^9-configuration) this model produces two bands split by the energy gap U_d. The Fermi energy of this hypothetically correlated Cu 3d^9 system lies within the gap. Fig. 2.8 (2) shows the DOS of this *Mott-Hubbard insulator.*

The extension of the Mott-Hubbard model also including the O2p$_{x,y}$ -orbits is the *three-band Hubbard model.* In the same notation as above, the included p electrons are constructed by $p^+_{l,s}$ and destructed by $p_{l,s}$. The energy of each electron is ϵ_p. The Coulomb correlation within one O2p -orbital is U_p, while the correlation between next neighbor p- and d-orbits is given by U_{pd}. The hopping between different O 2p-orbits is described by t_p. The hopping between the O2p - and the Cu3d-orbits is represented by t_{pd}. The Hamiltonian can be written as

$$\begin{aligned}\mathcal{H} &= \epsilon_d \sum_{i,s} n^d_{i,s} + \epsilon_p \sum_{l,s} n^p_{l,s} + t_{pd} \sum_{<i,l>,s} d^+_{i,s}\, p_{l,s} + t_p \sum_{<l,m>,s} p^+_{l,s}\, p_{m,s} \\ &+ \frac{U_d}{2} \sum_{i,s} n^d_{i,s}\, n^d_{i,-s} + \frac{U_p}{2} \sum_{l,s} n^p_{l,s}\, n^p_{l,-s} + \frac{U_{pd}}{2} \sum_{<i,l>,s} n^d_{i,s} n^p_{l,-s}\end{aligned}$$

Based on the approximation by Zaanen, Sawatzky and Allen [93], it became possible to determine the character of the DOS as a function of the ratio U_d/W. Common parameters for the CuO$_2$-plane are [94]:

$U_d \approx 6$ eV, $U_{pd} \approx 0$ - 2 eV, $U_p \approx 3$ eV,
$t_{pd} \approx 1.3$ - 1.5 eV, $t_p \approx 0.5$ eV, and $W \approx 1$ - 3 eV.

In the case of $W < U_d$, the system is called a *charge transfer insulator.* The model produces an additional peak in the DOS between the lower occupied and the upper empty Hubbard band, which is associated with the valence band composed mainly of non-bonding O2p-orbits (NBO). This is shown in Fig. 2.8 (3). As a consequence of the charge transfer insulating regime, hole doping from the antiferromagnetic insulator energetically favors the Oxygen sites. Double occupancy of holes on the Cu site is impeded due to the strong intersite exchange interaction U_d. This behavior of the holes is also known from experiments [95, 96, 97].

For theoretical calculations, instead of the Hubbard model, the tJ-model is often used, which can be derived from the Hubbard modell by second order perturbation theory (see, e.g., [98]). Let me now come to the last point of discussing the electronic structure, which is the change caused by doping the holes in the charge-transfer insulator:

Change of the electronic structure due to hole-doping

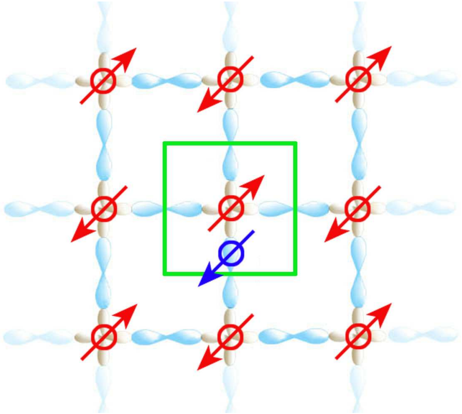

Figure 2.9: A Zhang-Rice singlet located within a CuO_2-plaquette (green square) is formed by the interaction of the doped holes on Oxygen- and Copper-site.

There were several models discussed for the changes of the electronic structure upon hole-doping. Often discussed is the Zhang-Rice singlet. This construction can be seen as a mapping of the topmost excitations of the system to an effective one-band Hubbard model. Zhang and Rice[99] started from a two-band Hubbard Hamiltonian and added the hybridization introduced by the interaction of a hole on an O 2p site with the neighboring Cu^{2+} ion. This strong coupling results in a singlet and a triplet state. Increasing the doping of holes splits off spectral weight from NBO into the charge transfer gap yielding a correlated state (CS) at the Fermi energy which has no analogue in the band structure. This can be seen in Fig. 2.8 (4). This feature can be interpreted as the singlet state (band) due to interactions between the Cu hole and the doped O hole [94]. This Zhang-Rice singlet is sketched in Fig. 2.9. In addition to the singlet states band, a triplet state also appears, which is located at higher binding energy near the bottom of NBO. Taking into consideration several models for the doping-dependent electronic structure, this model seems to be in closest correspondence with the experiment [100].

2.2.2 Models for high-temperature superconductivity of the cuprates

Before I come to the models for high-temperature superconductivity, let me critically discuss the view on electronic structure I presented before. The need for this is obvious, as the models must explain the occurrence of superconductivity by the electronic structure. The complete multi-particle Hamiltonian consists of a kinetic term, an electron-electron interaction, but also other interactions. In the case of the one-band Hubbard model, the electron-electron interaction is reduced to a nearest-neighbor interactions, which was already justified for atomic d-wavefunctions by Hubbard himself. It remains for me to question, how effective a reduction to nearest-neighbor interaction is, e.g., in the case of a long-range potential caused by periodic charge-order like in a Wigner crystal. However, I am not a theoretician: Let us assume the reduction to nearest-neighbors is allowed and the Hubbard model effectively describes the electronic structure. Unlike the one-dimensional case [101], the general analytical solution of the Hubbard model on the two-dimensional CuO_2-plane is not known. It follows that the Zhang-Rice singlet described above can best be seen in a certain view as the local configuration near low hole dopings and temperatures.

Among the models of pairing, different views also exist concerning the electronic structure. What was described above is based solely on the strong correlations, implicitly meaning that these are also dominant between 5% and 25% hole doping, which is the region where superconductivity occurs. Not all other views necessarily refute that with some accepting the importance of other interactions. Another important question is, whether the doping region of superconductivity can be described by a strong renormalized Fermi-liquid-like approach or by new particles produced by the strong correlations. The former method produces quasi-particles having in principle the same conserved quantum numbers as the free electrons, the latter produces particles which have different abilities and quantum numbers than the free electrons[5], e.g., so called 'holons' and 'spinons'.

The models used to explain high-temperature superconductivity or the phase diagram can be divided into microscopical models and phenomenological models. The microscopical models can be further divided into two groups [102]: The first group regards bosonic interactions as the 'glue' for Cooper pairs whereas the second group considers the Cooper pairs to be caused only by the electronic interactions due to the strong correlations. It is impossible to list all theories of high-temperature superconductivity. Therefore, I will provide only some examples:

◇ A model containing phonon-mediated pairing is provided by Abrikosov [103]. This model accounts for the 'extended saddlepoint singularity'; In comparison with Fig. 2.5 one sees the fact that the density of states near the M-point (at the saddle) is very high. Already in the weak-coupling case of Eq. (2.1), one can see that a large density of states near E_F increases T_C. Using strong coupling BCS, the T_C is even more enhanced. The d-symmetry is caused by the additional spin fluctuations or Coulomb repulsion on a Cu site. The existence of the pseudogap is, to my knowledge, not treated as relevant for pairing.
Another model dealing with phononic interactions is the 'Bi-polaron' theory. When a hole is put into the charge transfer-insulator and its kinetic energy is much smaller than the phonon energy, it can be dressed by a phonon cloud and its effective mass is enhanced - This dressed particle is the polaron. There is the possibility that two of them can build a bosonic Bi-polaron, which can be in singlet-state or triplet-state. The Bi-polarons can reach their ground state via the Bose-Einstein condensation. Alexandrov et al. [104] stated that the binding energy of the Bi-polarons, as well as the singlet-triplet Bi-polaron exchange energy, are thought to be the origin of the normal-state pseudogaps.

◇ Some models exist in which a spin-mediated pairing occurs near ferromagnetic and antiferromagnetic instabilities (for a review see [105]). Scalapino et al. [106] showed already in 1986 that in the almost half-filled Hubbard model near the antiferromagnetic wavevector $Q=(\pi,\pi)$ an attractive d-wave pairing interaction occurs. At low hole concentrations - nearly half-filled, electrons on neighboring sites tend to align antiferromagnetically to lower their energy by the exchange interaction $J = 4\ t^2/U$. A spectrum of spin excitations is produced which is typically around 40 meV in energy. This is similar to BCS-theory but applies a spin-excitation instead of a phonon-excitation. In this model a pairing interaction evolves for the electronic system which is lower than the spin excitation energy. The pairing seems to favor in most cases d-wave singlet states. The pseudogap is mostly discussed as a spin gap.
Also the 'marginal Fermi-liquid' described by Varma et al. [78] highlights the existence of mo-

---

[5] It is often said in the second case: 'the mapping breaks down', which means that the interaction can no longer be adiabatically switched on.

mentum independent spin and charge fluctuations which scatter the fermions. This model is based on the experimental findings and therefore the normal-state properties where these fluctuations renormalize the Fermi-liquid and leads in many experimental quantities to linear energy and temperature behavior. Questioning the origin of the fluctuations leads to a quantum critical point scenario, as I will discuss later.

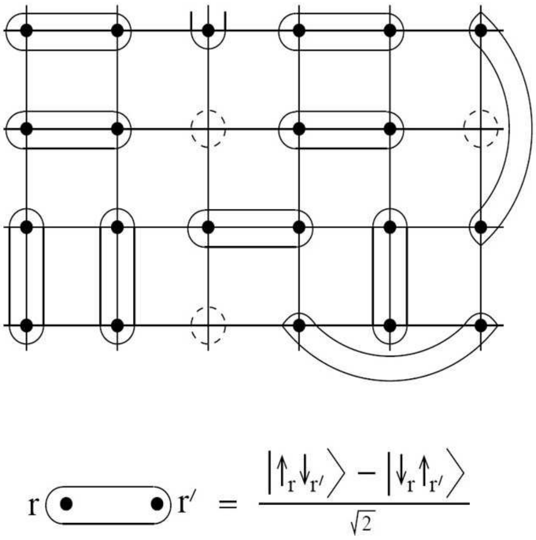

Figure 2.10: From [107]: Snapshot of a resonating valence bond (RVB) configuration showing singlet pairs of electrons and, in addition, a fraction x of doped holes. The many-body ground state wavefunction is a linear superposition of such configurations.

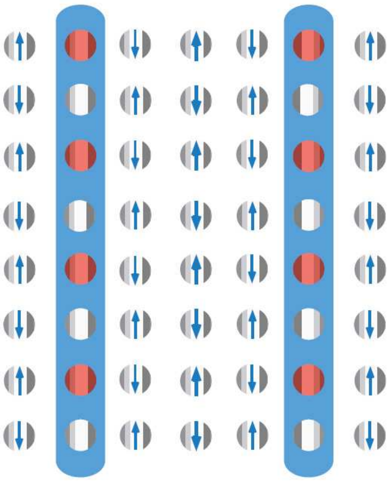

Figure 2.11: Sketch of a stripe ordering [9]: Each disc represents one plaquette. The charge runs like a river in the blue shaded stripes. The average charge density along the stripe of 1e per two sites is indicated by alternating red and silver circles. Blue arrows indicate the magnitude of the magnetic moment on sites containing spins. The stripe is an antiphase boundary for the antiferromagnetic order.

⋄ The most prominent non-glue model is the resonating valence bond (RVB) -theory by Anderson [108]. The RVB ground state at low hole dopings on a square lattice can be described as liquid containing a superposition of singlets as its basic building block. Fig. 2.10 shows a snapshot of the RVB configuration. A d-wave superconductor can be derived when looking at the stability of these singlet correlations. Stable configurations can Bose-Einstein condensate. The pseudogap is treated as a spin gap.

Another model assumes the existence of so called ’stripes’. A view of a striped state is sketched in Fig. 2.11. Early mean-field results by Zaanen and Gunnarson [109] already supported the idea that there are stripes within the CuO_2-plane. These are derived from holes expelled on the domain walls of antiferromagnetic regions. The spin charge separation model by Emery and Kivelson et al. [110, 111] expects that within the dynamic stripes running though the square lattice, a form of a one-dimensional liquid develops. In one-dimension, there is separation of spin and charge which leads to two kinds of quasi-particles moving at different speeds through the system ('holons' and 'spinons'). Under certain conditions, in each of the stripes a spin gap arises which is connected with superconducting correlations [112]. Global superconductivity in the sense of phase coherence is produced by Josephson-coupling between neighboring stripes. The superconductivity is then mainly d-wave with a possible weak s-wave mixing. The model has two crossover temperatures. The crossover at higher temperatures is the onset of stripe formation, the lower pseudogap is basically treated as a spin gap but also as the onset of local superconducting fluctuations. Here, T_C marks the phase coherence.

◇ A common aim of the phenomenological models is to explain the rich phase diagram without necessarily stating a microscopic model for the appearance of d-wave superconductivity. Two prominent models are the 'SO(5)-theory' and the theory of 'quantum criticality':

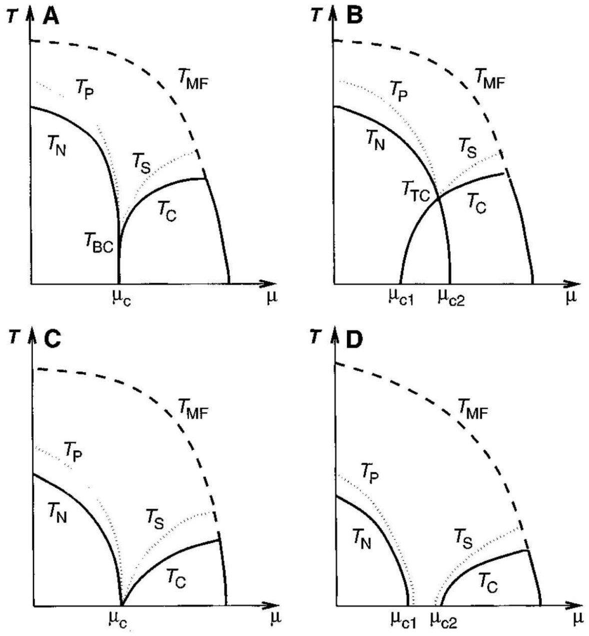

Figure 2.12: Possible phase diagrams in the SO(5) model by Zhang et al. [113]: T_{MF} is the temperature below which electrons bind to form singlet pairs. It corresponds to a finite magnitude of the superspin and is interpretable as the pseudogap-temperature. There are four possible types of transitions from the AF to SC state. (A) There is a direct first-order transition that terminates at a bicritical point T_{bc}. (B) There are two second-order phase transitions with an intermediate phase. The four second-order lines merge at a tetracritical point T_{tc}. (C) There is a single second-order phase transition at a quantum critical point. (D) There are two second-order quantum phase transitions with an intermediate quantum-disordered phase.

The SO(5)-theory [114, 113, 115] somehow straddles the border between microscopical and phenomenological models as it can be motivated by a projected tJ-model. It locally groups the three-component symmetry of the antiferromagnetic phase and two-component symmetry of the superconducting phase in a five dimensional vector - the so-called 'superspin'. The superconducting state is therefore nothing but the antiferromagnetic state rotated by a certain phase and vice versa. The rotation is defined by a symmetry group, which is obviously the SO(5) group. The generators of this symmetry group can be regarded as coupled bosonic gauge fields and can be used to build a Lagrangian and therefore, an effective Hamiltonian: One can disregard the fermions and concentrate on the collective degrees of freedom and map the whole problem into an 'effective magnetic problem' involving the SO(5) superspin [113]. Because of the absence of the sign problem (see, e.g., [116]) the bosonic picture of the SO(5) model has the great advantage that Quantum Monte Carlo simulations can be efficiently used. Also, its thermodynamics can be solved using a mean-field approach. Depending on the coupling constants, four possible phase diagrams can occur in the μ-T plane. These are shown in Fig. 2.12. The pseudogap-temperature in this model is interpretable as the mean field temperature below which the length of the superspin is fixed, i.e. the temperature below collective bosonic spin-excitations and charge-excitations exist.

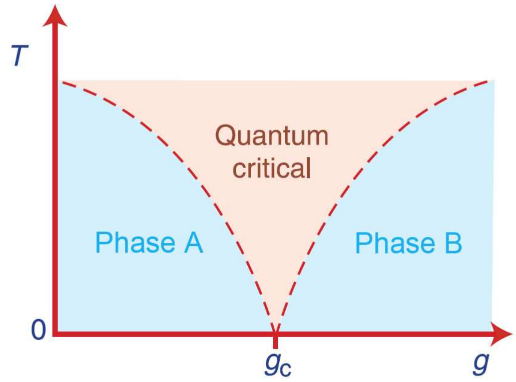

Figure 2.13: Adapted from [117]: Sketch of a phase diagram including a quantum critical point.

The theory of 'quantum criticality' [117] assumes a quantum critical point as in Fig. 2.12 (C) or Fig. 2.13, which indicates a second order phase transition at T=0. A quantum critical point occurs at a critical parameter g_c, e.g., a doping or a magnetic field where two ordered phases compete. For the cuprates, the parameter is the doping; and in most of these models the critical doping is typically suggested to be around 19% of holes per Cu. Unlike in classical systems, the critical fluctuations driven by Heisenbergs uncertainty principle are larger than the characteristic Boltzmann thermal energy k_BT. In the quantum critical region above the critical point the excitations of the system can no longer be described as excitations of Phase A or B (see Fig. 2.13), but follow a universal scaling law. For example, the extension of the marginal Fermi-liquid theory by Varma [118], a quantum critical point arises due to the competition of a 'circulating current phase' (A) at low dopings and a Fermi-liquid phase (B). Unlike the SO(5) model describing the region where a competition between antiferromagnetism and superconductivity occurs, this model tends to explain the existence of the non-Fermi-like region between the underdoped and optimally doped region observed in many experiments. However, both of the above mentioned phases have Fermi-like defined quasi-particles. Because the quantum criticality follows the existence of momentum independent spin-fluctuations and charge-fluctuations, it is meant to justify the early formulation of the marginal Fermi-liquid theory [78] described above. Here, the pseudogap-temperature is the crossover between the marginal Fermi liquid critical phase and the 'circulating current phase', which has a well-defined spin gap.

This concludes the the list of examples for theories of superconductivity in the cuprates. The reader experienced in the field of the HTSC's might notice that some models are missing [119], but I hope to have discussed the most prominent examples. Within the context of this work, it will be important to highlight some theories of the ground state which support the existence of spatial ordered nonsuperconducting configurations at certain hole fillings in addition to the superconducting state.

Models favoring a spatially ordered electronic structure

A good example of a spatial ordered state is the one-dimensional 'stripe' order. The spin charge separation model predicts static stripes at certain hole fillings. Unlike the dynamic stripes, these static stripes are nonsuperconducting (see, e.g., [9]). The clearest experimental indication of static stripes near 1/8 filling was found in $La_{1.48}Nd_{0.4}Sr_{0.12}CuO_4$ by Tranquada et al. [10]. $La_{2-x}Ba_xCuO_4$ [11, 12, 13] also shows a magnetic and charge ordered configuration at the 1/8 depression.

Another order which has drawn much attention in recent years is the 'checkerboard' order: For the high-temperature superconductor $Bi_2Sr_2CaCu_2O_{8+\delta}$, a two-dimensional '4x4 order' [17] was found using scanning tunneling microscopy (STM). Ordered patterns of similar dimensions are also present in the nonsuperconducting compound $Ca_{2-x}Na_xCuO_2Cl_2$ [16]. Here it is important to note that these findings led to many theories (see, e.g., [115, 120, 121] and references in [16]). All these theories commonly propose a crystal of holes, where in some theories the holes are paired and in others they are not. Also the mechanisms for achieving the crystalline electronic state differ. Detailed descriptions can be found in the citations provided.

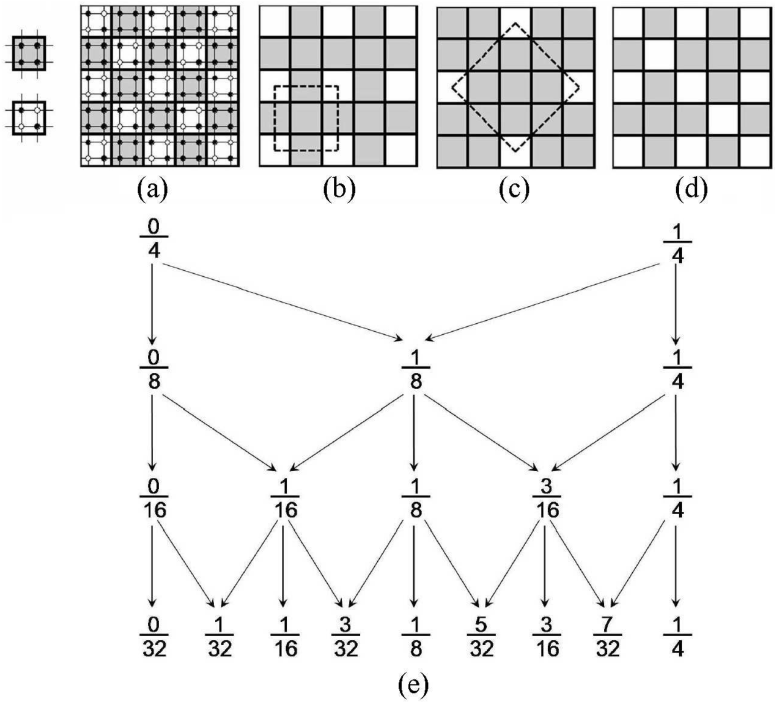

Figure 2.14: From [8]: Hierarchical construction schema for the 'magic doping fractions'. For details see text.

The SO(5) theory as expanded in the publication of Chen et al. [122] could be relevant in this work. One starts with a lattice, where the sites are composed of CuO_2-plaquettes. These sites are grouped into larger plaquettes with even sites, e.g., typically in a 2x2 site plaquette. On these grouped larger plaquettes, the lowest excitations are grouped into the SO(5) bosonic schema. In the next step, interactions are allowed between the bosons on different plaquettes . One order occurring in the system is the so-called 'PDW-order', which is seen as a charge density wave formed by pairs of holes that are equal to Cooper-pairs. For me, the reason is not clear but this PDW-order is insulating and non-superconducting. Due to a more or less geometrical hierarchical construction, the authors were able to find the doping values where these insulating

PDW-orders develop. The construction schema as shown in [8] is depicted on the left side of Fig. 2.14: A checkerboard like covering of the plane is created by black and white squares. Electrons are denoted by black circles, while holes are left uncolored; The black square is therefore formed by from undoped CuO_2-plaquettes containing in principle only RVB-states. The white square contain two holes in the PDW-order. The construction (a) on the upper left of Fig. 2.14 shows the 1/4 state. At the next level of the hierarchy, consider only the lattice of white squares, and alternately color half of them black. Such a state has a hole doping of x = 1/8 (b). At the next level, one can either consider the lattice of the white squares and alternately color half of them black, thus obtaining a state with x = 1/16 (c), or one can consider the lattice of the newly colored black squares and alternately color half of them white, thus obtaining a state with x = 3/16 (d). This hierarchy construction can be iterated ad infinitum, generating a binary tree of 'magic doping fractions' as shown in (e).

III

Bi2201: Crystal structure, growth, and structural analysis

This chapter aims to discuss the high-temperature superconductor Bi2201 in detail. This material exhibits one CuO_2-plane per primitive unit cell. As a one-layer material, Bi2201 has the advantage of a low T_C: For ARPES this low T_C makes it possible to probe the transition into the superconducting state with high energy resolution. Also, this material can be seen as a nearly perfect realization of the single CuO_2-plane with only weak inter-plane coupling. This is because the distance between the planes is quite large. However, Bi2201 has some special problems:

Fig. 3.1 is a repetition of the already shown dependence of T_C on the number of CuO_2-planes for the different homologous families. We see that the one-layer material $Bi_2Sr_2CuO_{6+\delta}$ does not follow the general trend: Its T_C^{max} is lower compared to other one-layer materials. The origin for this reduction lies in the fact that this material exhibits structural distortions. The structural problems can be reduced by the substitution of Lanthanum for Strontium which leads to $Bi_2Sr_{2-x}La_xCuO_{6+\delta}$; and T_C^{max} increases from 16.5 K [69] to 29K. Furthermore, the La substitution makes it possible to achieve nearly arbitrary hole-doping levels. This makes this descendant of Bi2201 interesting for examining generic features within the phase diagram. By additionally substituting of Pb for Bi the reduction of T_C in the Bi2201 system can be even more removed. The transition temperature of $Bi_{2-y}Pb_ySr_{2-x}La_xCuO_{6+\delta}$ reaches 38 K. With this substitution, one sees that the slope of the Bi-cuprates is quite the same as the slope for the other homologous series. The difference in interception might be attributed to the strength of the inter-plane coupling.

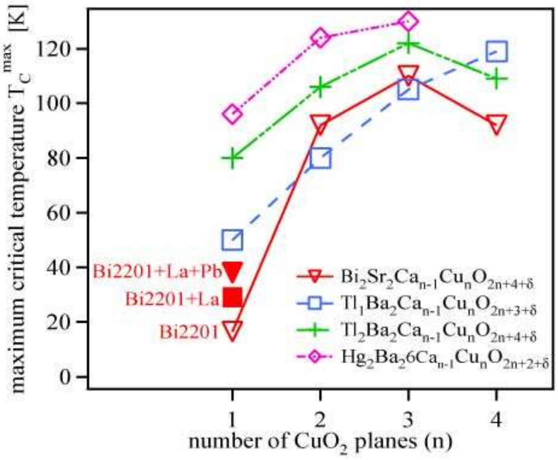

Figure 3.1: T_C^{max} of different HTSC-families as function of number of CuO_2-planes per unit cell. Measurements from this study and [69, 70, 71, 72].

In this thesis, I show experimental results of single crystals of the Pb- and La -substituted $Bi_{2-y}Pb_ySr_{2-x}La_xCuO_{6+\delta}$ system. The Lead substitution in single crystals of Bi2201 is not often addressed in the literature; therefore, much care was taken to characterize the crystals. For this, a phase analysis by scanning tunneling microscopy was carried out. Based on these results, I will show in great detail the change of the sub-microstructural properties due to Pb substitution. Also, the similarities to the two-layer compound $Bi_{2-y}Pb_ySr_2CaCu_2O_{8+\delta}$ will be revealed. The question of the microstructural properties is connected with a better realization of the single undisturbed CuO_2-plane which is important for the search for the origin of high-temperature superconductivity. The purpose of this chapter will have been fulfilled, when I am able to define a basically microstructural clean series of $Bi_{2-y}Pb_ySr_{2-x}La_xCuO_{6+\delta}$ based on the phase analysis. Measurements for this series will be used during all of the following chapters.

3.1 Ideal crystal structure

In the literature there is no uniformly used space group of $Bi_2Sr_2CuO_{6+\delta}$ and its substituted descendants mentioned above [123]. Some authors prefer the tetragonal I4/mmm space group, while others account for the small orthorhombicity by using the Amma space group[1]. A representation of the structure is shown in Fig. 3.2. This representation is not a unit cell, but instead the hybris between the orthorhombic and tetragonal crystallographic unit cell. The tetragonal cell was shown in Fig. 2.2 of the last chapter. The hybris shown has the chemical formula $(Bi_2Sr_2CuO_{6+\delta})_2$ like the tetragonal cell; the orthorhombic cell has $(Bi_2Sr_2CuO_{6+\delta})_4$. The a,b-lengths are of the orthorhombic cell. In tetragonal representation they would be $\sqrt{2}$ shorter. The c-axis length is in both cases the same. The sketch of Fig. 3.2 does not show the extra Oxygen δ as the exact position is still controversial. The recent theoretical considerations by He et al. [88] point to a larger amount of interstitial Oxygen between the BiO- and SrO-plane. However, what can be seen well in this hybris is that the structure consists of two structural sets, one being the inner CuO_6-octahedron together with the surrounding Sr forming a perovskit structure. This structure is expanded in both c-directions by a rocksalt component which is formed by the SrO-plane and the BiO-plane. This stacking is then repeated in the c-direction but with a shift of a/2. The BiO-planes are weakly van der Waals bound. This makes the material convenient for surface-sensitive investigation methods since it always cleaves between these BiO-planes. For completeness, it shall be mentioned that the stoichiometric $Bi_2Sr_2CuO_6$, without any extra Oxygen, is non-superconducting and has a monoclinic C2/m [124, 125, 126] shear [127] structure (see Fig. 3.3). Because of the different structure of the stoichiometric $Bi_2Sr_2CuO_6$, some authors do not use the term 'Bi2201-phase' for

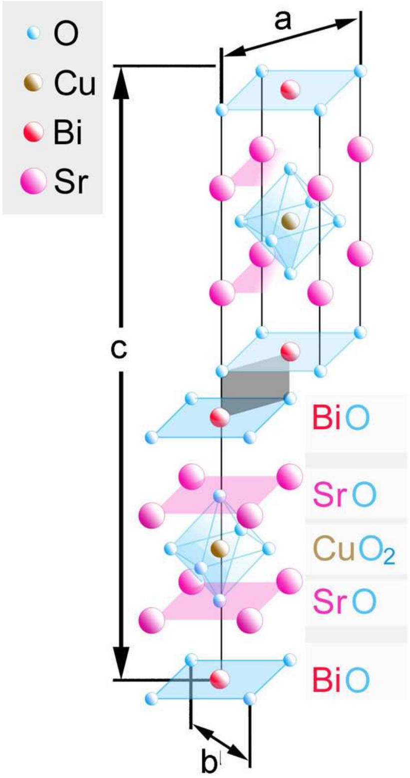

Figure 3.2: Representation of the Bi2201 structure of $Bi_2Sr_2CuO_{6+\delta}$. The lattice parameter a,b,c are shown for the orthorhombic Amaa space group.

---

[1] This is a nonconventional setting of Cccm, No. 66 in the international crystallographic tables.

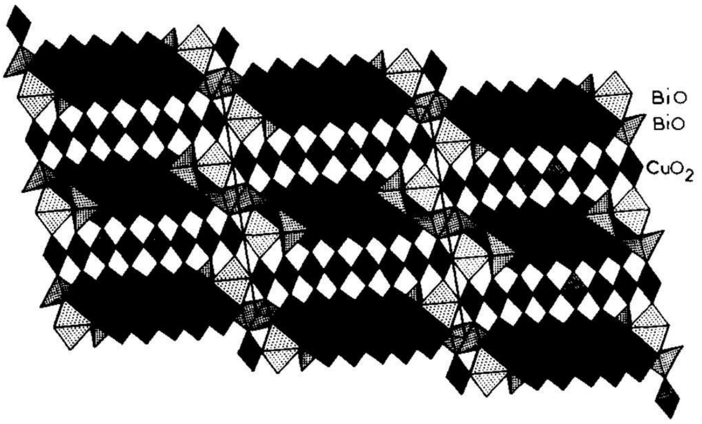

Figure 3.3: From [127] : Representation of the monoclinic C2/m shear structure of the stoichiometric $Bi_2Sr_2CuO_6$-phase. This phase is nonsuperconducting.

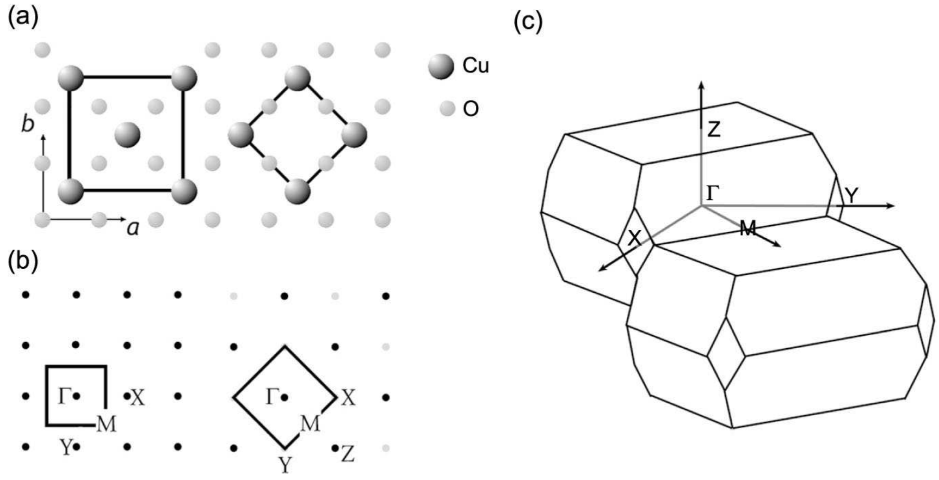

Figure 3.4: From [128], who adapted (c) from [129]: (a) Comparison of the Wigner-Seitz cells for the 2d orthorhombic (left) and pseudotetragonal (right) description of the CuO_2-plane. (b) First Brillouin zone of the 2d orthorhombic (left) and pseudotetragonal(right) description. (c) 3d orthorhombic Brillouin zone. The c-axis direction (ΓZ) is strongly expanded in this visualization.

the superconducting crystals, but instead refer to it as the Raveau phase (see e.g [124]). However, in this work Bi2201 refers to the superconducting phase unless the term stoichiometric is specifically stated.

3.1.1 Reciprocal structural description

The reciprocal structure will now be discussed; The three-dimensional Brillouin zone is shown in Fig. 3.4(c). Because of the extreme length of the c-axis of about thirty Ångström compared to the in-plane length of around five, the Brillouin zone can be regarded as almost two-dimensional. The two-dimensional Brillouin zone is often reduced to the tetragonal symmetry and called pseudo-tetragonal. One reason for this redefining lies in the convenience for theoretical calculations to have the Cu-O bond directions along the basic vectors of the coordinate system because the CuO_2-plane is often seen as the only and most important part of the crystal. The pseudo-tetragonal Brillouin zone is $\sqrt{2} \times \sqrt{2}$ larger than the orthorhombic and rotated by 45°. In Fig. 3.4(b) the two-dimensional pseudo-tetragonal Brillouin zone is compared to the corresponding orthorhombic Brillouin zone. In Fig. 3.4(a) the orientations to the real space CuO_2-plane are shown.

3.2 Crystal Growth

To introduce the crystal growth of high-quality single crystals of the Bi2201-phase, it is appropriate to start with the equilibria ternary phase diagram. The superconducting Bi2201-phase exists only in a very narrow composition range. This can be seen in Fig. 3.5 where as an example, a part of the pseudo-ternary phase diagram for $Bi_{2+z}Sr_{2-z}CuO_{6+\delta}$ at T≈ 900 °C is shown. This is shown relative to the composition of the elements SrO-1/2 Bi_2O_3-CuO. One competition in the growth is the existence of the above-mentioned non-superconducting stoichiometric phase next to the Bi2201-phase [130] (phase 2:2:1 in Fig. 3.5). The $Bi_{2-y}Pb_ySr_{2-x}La_xCuO_{6+\delta}$ pseudo-ternary phase diagram is in principle the same as the one shown. The difference is that one has to replace 1/2 Bi_2O_3 by 1/2 Bi_2O_3 + LaO. Because the La has a higher melting temperature compared to Bi, the shown diagram may reassemble the one for $Bi_{2-y}Pb_ySr_{2-x}La_xCuO_{6+\delta}$ at slightly higher temperatures. The effect of Pb substituting Bi is very weak in this diagram. An important feature of the Bi2201-phase is that it can only be reached from the melt via a peritectic point. This situation is depicted in Fig. 3.6 by an experiment-based pseudo-binary phase diagram [131]. In this diagram, x=0 represents $Bi_2(Sr,Ca)O_4$ and $x=\infty$ is $(Sr,Ca)O_2$. As illustrated, the phase can be solely reached via the peritectic point at x≈0.85 and T≈835°C.

Among the methods existing for growing the Bi2201-phase as single crystals, the floating zone technique (e.g., [132, 133]), and the flux method (e.g., [134, 135]) are often applied. Here, the growth was achieved using a flux method. In my opinion, the advantage of this method is that the crystals grow without any extra strain because of a small temperature gradient within the crucible. Also, the risk of producing intercalations between the BiO-planes might be reduced because possible pollution will be concentrated on a certain crystallization region. The flux method can be applied with or without solution (then also called 'stoichiometric growth'). The solution can be an additional transport material such as KCl [136, 137, 138], or possibly also Li and Sb (done for the Bi2212-phase by [139]), or an element of the final composition weighted in a higher amount. With the latter type of solution, the method is then called 'self flux'. For this growth of Bi2201, theoretically Cu, Pb and Bi can be used. Because Cu does not seem appropriate as solution [140], and Pb is not wanted in La free crystals, here, Bi is used in typical additional amounts of 10% of the total Bi formula unit. The use of Bi as a solvent has the additional advantage of lowering the melting temperature. In the following I would like to describe the processing steps of growing the $Bi_2Sr_{2-x}La_xCu_{1+w}O_{6+\delta}$ and $Bi_{2-y}Pb_ySr_{2-x}La_x$-$Cu_{1+w}O_{6+\delta}$ single crystals used here. The process can be roughly summarized by the following:

The total mass must be more than a critical mass (> 50g). The dependence of the La starting composition and the resulting average La content for the crystals used here is shown in Fig. 3.7.1. The starting composition is also often called the 'nominal composition' whereas the resulting

La content is the 'actual composition'. Interestingly, the curve is quite similar to that published by Yang et al. [135]. The first process step is divided between crystals with Lead and for those without:

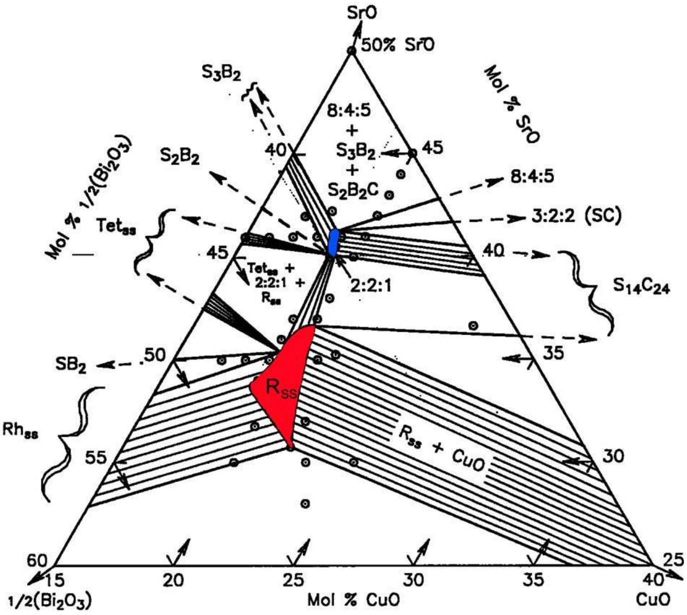

Figure 3.5: From [124]: Enlarged portion of the subsolidus pseudo ternary phase diagram in equilibria of the system SrO-1/2 Bi_2O_3-CuO at T≈ 900 °C. The two phases Bi_2Sr_2-CuO_6(2:2:1) and $Bi_{2+z}Sr_{2-z}$-$CuO_{6+\delta}$(R_{SS}) can be seen. The bunches of thin lines represent the tie lines.

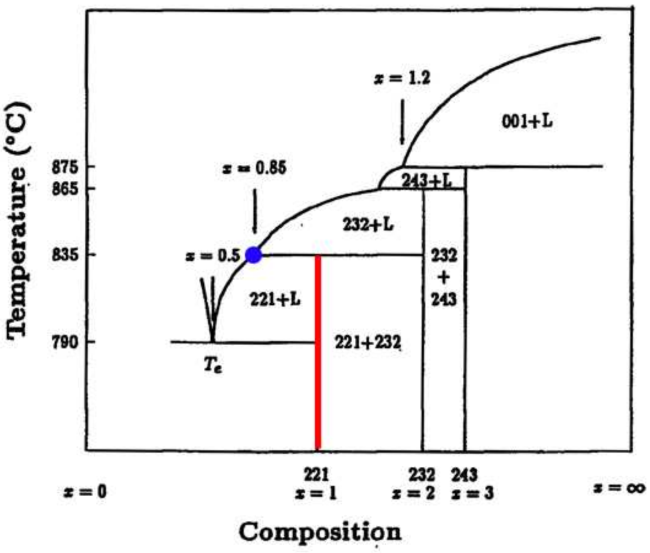

Figure 3.6: By [131] proposed pseudo-binary phase diagram: x=0 is $Bi_2(Sr,Ca)O_4$ and x=∞ is $(Sr,Ca)O_2$. The Bi2201-phase is here denoted as '221' and at x=1. Please note the peritectic point at x ≈ 0.85 and T ≈ 835 °C.

(i) For crystals without Lead, the oxides Bi_2O_3, CuO, LaO and the carbonate $SrCO_3$ are composed. To get a homogeneous mixture, the composition is dissolved in ethanol and then grounded. It follows a calcination at T≈ 800 °C to decompose the Strontium-Carbonate: $SrCO_3 \rightarrow SrO + \uparrow CO_2$, afterwards the composition is again dissolved in ethanol and grounded.

(ii) For crystals containing Lead, first the oxides Bi_2O_3, CuO and the carbonate $SrCO_3$ are

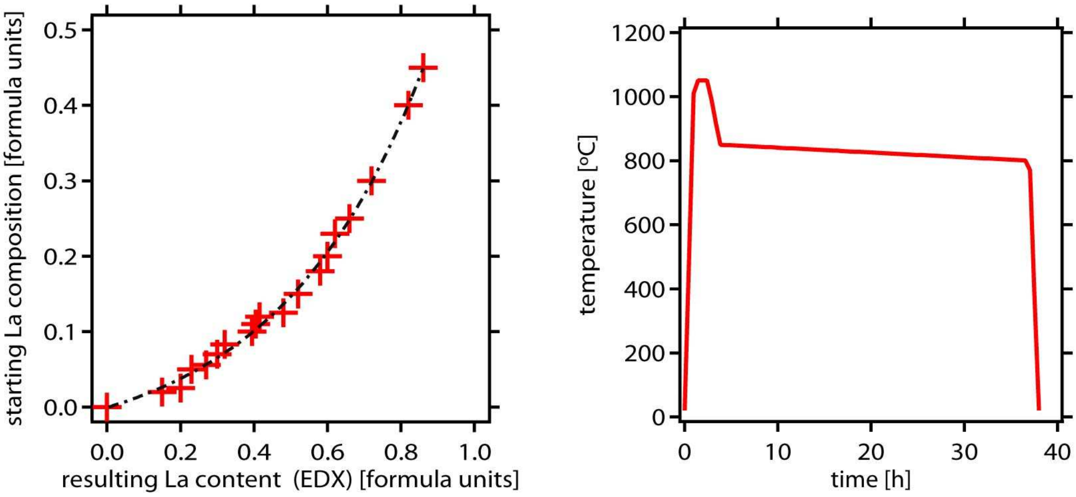

3.7.1: Dependence of the La starting composition and the resulting La content measured by EDX.

3.7.2: Typical temperature-time dependence of the growing steps in the oven.

composed, dissolved in ethanol and then grounded. This composition is compared to the procedure without Lead calcinated at higher temperatures of T≈ 930°C. After the calcination, LaO and PbO are added and the composition is dissolved in ethanol and grounded.

The composition is placed in an oven and melted beyond the liquidus temperature T_m in a zirconium oxide crucible. T_m is approximately in the range from 950°C to 1050°C. This temperature is maintained for 1-2 hours to thermally homogenize the melt. The typical temperature-time dependence of the growing steps in the oven are shown in Fig. 3.7.2. For crystals with Pb concentration y>0.3 formula units, additional air is supplied. After the homogenization, the system is cooled down to the upper crystallization temperature T_2. For Bi2201 with x=0.4 and y=0 formula units, $T_2 \approx 850$°C. In the crystallization temperature range $[T_1,T_2]$ the system is cooled down very slowly at a rate of 1-2 K/h to allow the system only to form a few crystallization nuclei. For Bi2201 with x=0.4 and y=0, $T_1 \approx 800$°C. As already mentioned, the system is peritectic and therefore must be cooled down very slowly in the crystallization process. With the help of additional Oxygen, it is then possible to reach the solely Bi2201-phase (please compare Fig. 3.6). After the system is stable and depending on the number of crystallization seeds desired, it is rapidly quenched to room temperature.

Photographs of the crystals in the zirconium crucible after the growth process are shown in Fig. 3.7. It is then necessary to prepare some crystals from the mixture of slightly different phases and La concentrations in the crucible to get a true one-phase crystal of Bi2201. As a rule, the crystal properties vary from the center of the crucible to the surface. The cleave requires some manual skill but can be handled quite well because the crystals cleave easily between the BiO-layers due to their weak van der Waals bonds. Typically, the samples are flat with a thickness of about 300 μm and a typical size of about 2 x 1 mm^2. The longer side is in most cases the growth direction, which is the a-axis.

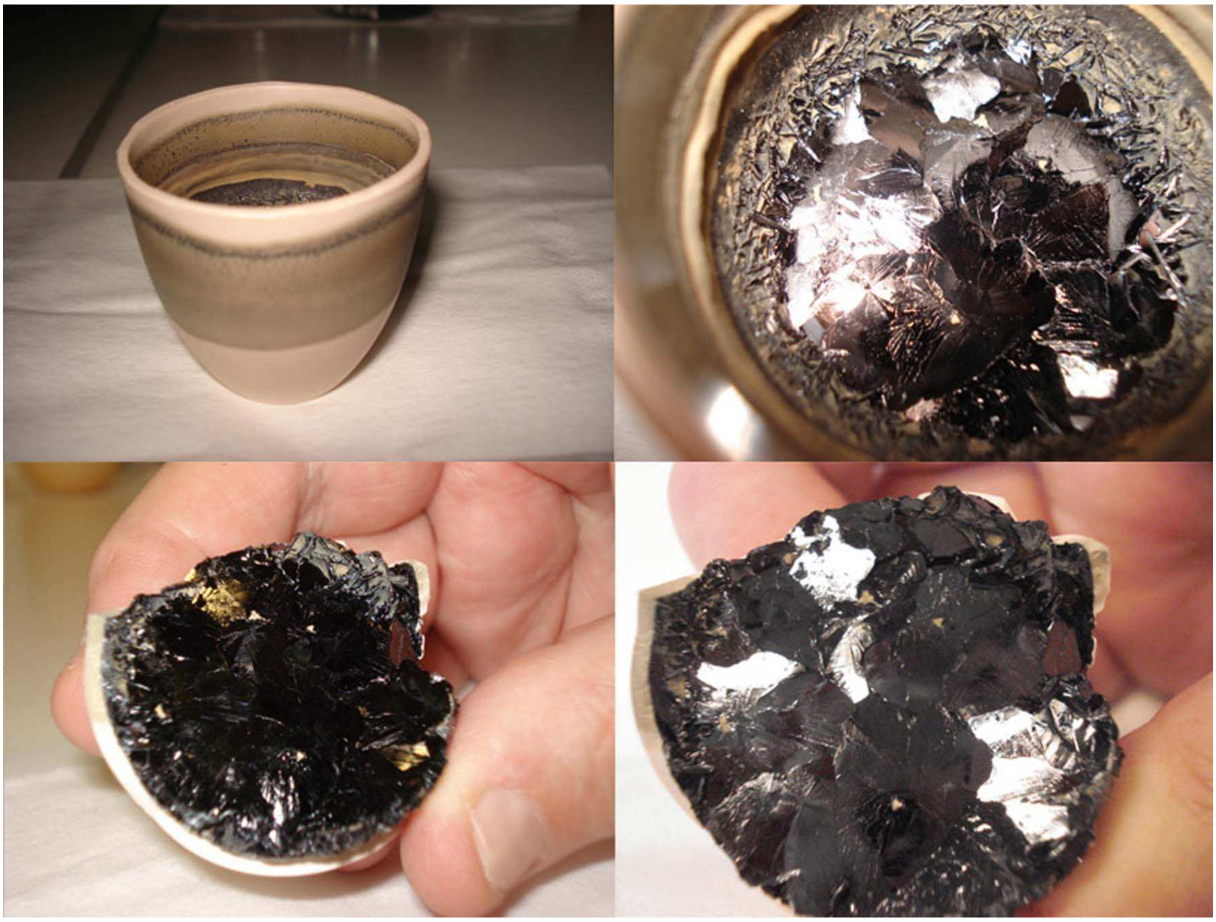

Figure 3.7: The crystals in the zirconium oxide crucible after the growth process. Single-phase crystals are obtained by crushing the crucible and preparing small monophasic crystals under the microscope from the slag.

3.3 Doping mechanisms and the structural response

The substitution behavior within the Bi2201-phase is very complicated and must be fully understood in order to control it. This complicated behavior is caused by the fact that the unit cell has so many atom-positions inside. Currently, all possible substituted structures can be described as $Bi_{2-y+z}Pb_ySr_{2-x-z}Ln_xCu_{1+w}O_{6+\delta}$, where δ is the amount of extra Oxygen, Ln is a (typical trivalent) rare earth in composition x, w is the number of extra copper and z describes the tendency of the crystal to set Bi atoms on Sr sites.

Obviously, by the substitutions it is possible to change the number of holes. In an ionic model this can be achieved by changing the extra Oxygen content δ of the system, substituting $Bi^{3+,5+}$ by Pb^{2+} or the substitution where Sr^{2+} is populating Bi sites. The other way is to 'shovel electrons into the holes', which can be achieved by La^{3+} substituting Sr^{2+} or also by $Bi^{3+,5+}$ atoms populating Sr sites. For example, this can also happen when Bi^{3+} is formally replaced by Pb^{4+}.

A deeper understanding of the HTSC's requires the construction of a generic phase diagram relative to the hole-content. Considering these many different methods to substitute and dope the Bi2201-phase above, it is questionable whether a reduction to only the holes can be done. I will do this in Chapter 4, but it should be kept in mind that some information is lost due to this reduction and the role of the structural surrounding is important. It is absolutely necessary to realize that in the cuprates the term 'doping' has another meaning than in semiconductor physics. Doping in the cuprates means always substituting a very large amount of atoms. In the introduction to this chapter, I pointed out that by using the different substitutions one can produce different T_C^{max}. For the Pb-substituted system, Jianwu et al. [141] showed that ceramics of $Bi_{1.6}Pb_{0.4}Sr_{1.65}La_{0.35}CuO_{6+\delta}$ had an impressive[2] $T_C{}^0$ of 39 K. In this work, the enhancement of T_C due to Pb substitution for single crystals up to 38K is shown. To understand this increase in T_C^{max} the structural surrounding must be discussed. Let me therefore list some views on the properties and problems of the structure:

The first point to consider is the adaption. Many of the structural features of this material are related to the adaption of the perovskit structure to the rocksalt structure. To understand this, a comparison between the crystallographic distances and the sum of the Shannon ionic radii in the correct coordination [143] is helpful. For $Bi_2Sr_2CuO_{6+\delta}$ and δ=0.1 the cell parameters are a=5.382Å, b=5.365Åand c=24.67Å [69]. For example, the sum of the ionic radii in the BiO-plane is equal to $2\ r^{Bi^{3+}}+2\ r^{0^{2-}}=4.76$ Å, which is smaller than the measured a or b parameter. This also holds for the SrO-plane where $2\ r^{Sr^{2+}}+2\ r^{0^{2-}}=5.06$Å. But for the CuO_2-plane $2\sqrt{2}r^{Cu^{2+}}+2\sqrt{2}\ r^{0^{2-}}=5.88$Å is much larger than the measured a or b parameter. Of course, the ionic radii will not reassemble the real binding lengths, but within this naive calculation it is intuitively understandable that the structure favors any kind of inhomogeneities which can be used to reduce the misfit between the planes. These inhomogeneities are, e.g., the extra Oxygen δ which may be favorably inserted in or around the BiO-plane as in the comparison of the a,b parameter with the ionic radii, there appears to be plenty of room.

---

[2] In accordance with Schneider et al. [142] for comparing susceptibility and resistivity measured T_C, I here use $T_C{}^0$. This is the temperature at which the resistivity drops to zero.

The next point to consider is the covalency of the Cu-O binding; The system cannot be oversimplified to only the adaption problem. The planar Oxygen 2$p_{x,y}$-orbits and the cooper 3$d_{x^2-y^2}$-orbits form a pd-σ-hybrid. When this hybrid is hole-doped, this means that electrons are removed from antibonding Cu-O bonds [144, 145]. That means that the system is more bonding and the planar Cu-O distance decreases. This is a means for the structure to reduce the stress in the CuO_2-plane with the help of 'well chosen' inhomogeneities by removing electrons from the CuO_2-plane and thus residing holes in this plane. This behavior is the Pauling-type contraction and it is expected to reduce the planar area by 1 - log(m) when the degree of covalency (m) is increased upon hole doping [146]. Also, with regard to the covalent view, the behavior of the apical Oxygen-binding produced by the Cu 3d_{z^2}-orbits and the O 2p_z-orbits belongs here. With no extra hole in the $3d^9$ filled CuO_6-octahedron, a Jahn-Teller distortion is energetically favored. In fact, the expected strong Jahn-Teller distortion in $La_{2-x}Ba_xCuO_4$ was the reason why the material was examined and the high-temperature superconductivity was found [2].

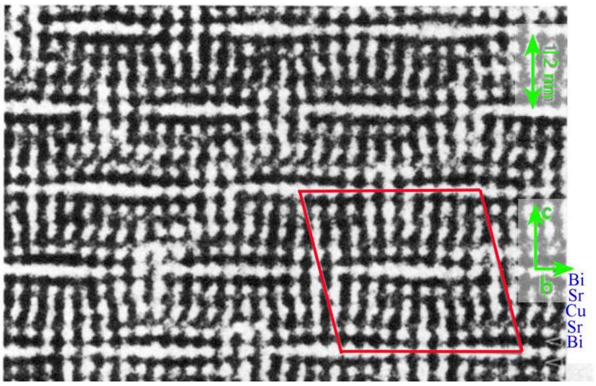

Figure 3.8: From [147]: Image of the bc-plane in $Bi_2Sr_2CuO_{6+\delta}$ as processed by a transmission electron microscopy (TEM) experiment

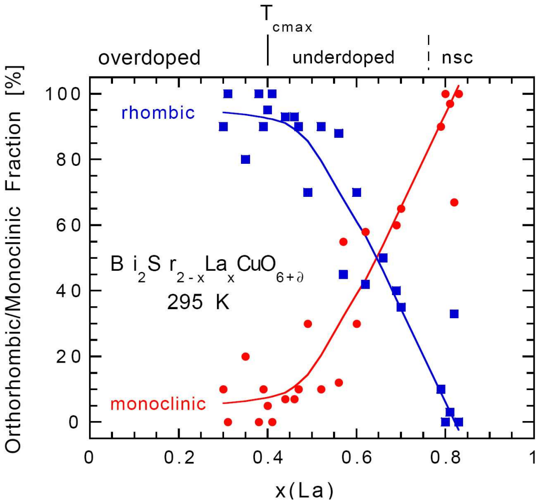

Figure 3.9: From [145], who adapted from [148]: Orthorhombic and monoclinic fraction of $Bi_2Sr_{2-x}La_xCuO_{6+\delta}$ dependent on the Lanthanum content.

One can also assume that the CuO_2-plane must pucker or tilt when it cannot fit into the surrounding structure but wants to retain its binding distance. In samples of $Bi_2Sr_{2-x}La_xCuO_{6+\delta}$ a puckering can be shown [145]. Perhaps more insight about the octahedral tilting can be gained by comparison with the orthorhombic perovskites where an amazing kaleidoscope of tilting configurations is possible (see, e.g., [149, 150]). In general, it can be expected that all substitutions and dopings cause a change in the central CuO_6-octahedron. In order to explore this, some substitution situations exist which seem to be primarily dedicated: This can be achieved in a relatively soft way by substituting Ba on Sr sites, e.g., in polycrystalline $Bi_2Sr_{2-x}Ba_xCuO_{6+\delta}$ [151], or in a more direct way by producing Sr vacancies, e.g., in polycrystalline $Bi_{1.8}Pb_{0.2}Sr_{2-z}$-$CuO_{6+\delta}$ [152]. In a more offensive approach, it can be achieved by replacing Cu by Mn [153], for example.

When it comes to substitution or doping to form a superconducting material, in all substituted descendants of $Bi_2Sr_2CuO_{6+\delta}$ a structural deformation remains. In $Bi_2Sr_2CuO_{6+\delta}$ and $Bi_2Sr_{2-x}La_xCuO_{6+\delta}$ these deformations result in an incommensurate superstructure along the b and c axes. The left side of Fig. 3.8 shows the image of the bc-plane in $Bi_2Sr_2CuO_{6+\delta}$ as processed by a transmission electron microscopy (TEM) experiment by Eibl [147]. The monoclinic superstructure is clearly visible. The red box represents the super-cell. In $Bi_2Sr_{2-x}La_xCuO_{6+\delta}$, the superstructure consists of an orthorhombic and monoclinic fraction [148]. The fractions dependent on the Lanthanum content are depicted on the right side of Fig. 3.9.

These kinds of structural modulations are also present in the two-layer material $Bi_2Sr_2CaCu_2O_{8+\delta}$ (Bi2212). The origin for these modulations gives rise to several models [154], e.g., 'the extra Oxygen model' [155, 156] and 'the crystal misfit model' [157, 151]. These models might be deduced from the views above.

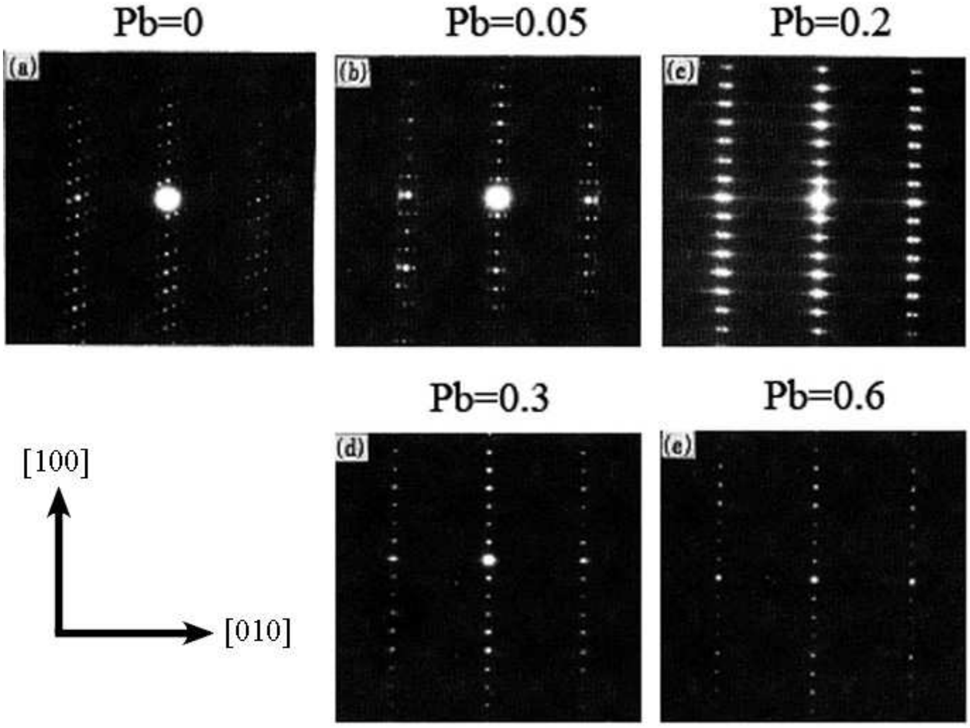

Figure 3.10: From Zhiqiang et al.[151]: Electron diffraction patterns on ceramics of $Bi_{2-y}Pb_ySr_2CuO_{6+\delta}$. From (a) to (e) the Pb content is increased. The monoclinic superstructure disappears around 0.2 Pb substitution and only the so-called 'Pb-type' orthorhombic superstructure is present. For samples with a Pb substitution of about y=0.6, no superstructure is detectable.

In the $Bi_{2-y}Pb_ySr_{2-x}La_xCuO_{6+\delta}$, it is possible to remove the superstructure via Pb substitution. I would like to illustrate the change resulting from Pb substitution in Fig. 3.10 from Zhiqianq et al. [151]. Electron diffraction patterns of grains of polycrystalline $Bi_{2-y}Pb_ySr_2CuO_{6+\delta}$ at different Pb substitution levels are shown. From these photographs it can be clearly seen that the monoclinic superstructure of this Pb-free sample is superimposed in the gently Pb-substituted sample by an orthorhombic superstructure. Here, the monoclinic superstructure disappears and only the 'Pb-type' called orthorhombic superstructure is present. For samples with a Pb substitution of about y=0.6, no superstructure is detectable. One may conclude that because enough Pb is substituted into the system, the superstructure is absent. The effect of Pb substitution will be examined in the following.

3.4 Submicroscopical behavior due to Pb substitution

In the following, the sub-microstructural behavior upon changing the level of Pb substitution in $Bi_{2-y}Pb_ySr_{2-x}La_xCuO_{6+\delta}$ will be examined. For this purpose, measurements by topological scanning tunneling microscopy (STM) and low-energy electron diffraction (LEED) will be shown. For details of those methods, I refer the reader to Appendix A.3 for STM and the book by Ertl and Küppers for LEED[158]. A review for STM on cuprate high-temperature superconductors is provided by Fischer et al. [15].

Here, the vanishing of the superstructure will be examined with surface-sensitive methods. Because the bulk is not examined, no difference can be determined between an orthorhombic or monoclinic superstructure - the difference is only visible along the c-direction. From this point of view, the following can be seen as a qualitative phase analysis. A motivation for this comes from the existence of characteristic lamellar structures in single crystals of $Bi_{2-y}Pb_ySr_2CaCu_2O_{8+\delta}$ [159]. These lamellae consist of Pb-poor and Pb-rich regions, which were called α- and β -phase, respectively. Hiroi et al. [160] initiated for $Bi_{2-y}Pb_ySr_2CaCu_2O_{8+\delta}$ a phase diagram to describe the appearance of the α- and β -phases upon varying the Pb content. Recently, these kinds of lamellae were also shown to be present in single crystals of $Bi_{2-y}Pb_ySr_{2-x}La_xCuO_{6+\delta}$ [161]. In the following, the evolution of the microscopic structure upon Pb substitution is shown in more detail than in previous studies. This is presented in Section 3.4. In Section 3.4.3, the existence of the α- and β -phases in $Bi_{2-y}Pb_ySr_2CaCu_2O_{8+\delta}$ is evaluated. In Section 3.4.4, a phase diagram is constructed to achieve an adequate description of the $Bi_{2-y}Pb_ySr_{2-x}La_xCuO_{6+\delta}$-system.

3.4.1 Sample characterization

I will show the analysis of eight samples used for the measurements. To characterize these samples, the average composition relative to the average Pb content is shown in Fig. 3.11.1. The composition was established through energy dispersive x-ray analysis, briefly explained in Appendix A.1. The dotted lines in Fig. 3.11.1 represent the linear least square fits to each composition dependent on the Pb substitution y. The fits yield

$$c(Bi) = (1.95 \pm 0.02) - (1.01 \pm 0.07)y \quad ; \quad \chi^2 = 0.0069 \tag{3.1}$$

$$c(Sr) = (1.49 \pm 0.02) + (0.03 \pm 0.06)y \quad ; \quad \chi^2 = 0.0050 \tag{3.2}$$

$$c(La) = (0.40 \pm 0.02) + (0.01 \pm 0.05)y \quad ; \quad \chi^2 = 0.0039 \tag{3.3}$$

$$c(Cu) = (1.15 \pm 0.01) - (0.02 \pm 0.03)y \quad ; \quad \chi^2 = 0.0011 \tag{3.4}$$

Apparently, in the chosen samples only the Bi content significantly changes due to the substitution. The Lanthanum content is almost constant with 0.4 formula units. The T_C's of the STM measured samples relative to the average Pb content are shown in Fig. 3.11.2. The T_C's were extracted by AC-susceptibility measurements as described in Appendix A.2. Also shown is an averaged T_C over a large number of characterized samples with a certain stoichiometry (compositional restriction). The averaging will be more precisely specified in Chapter 4.1. Here it is sufficient to state that the T_C's of the STM measured samples follow the general trend.

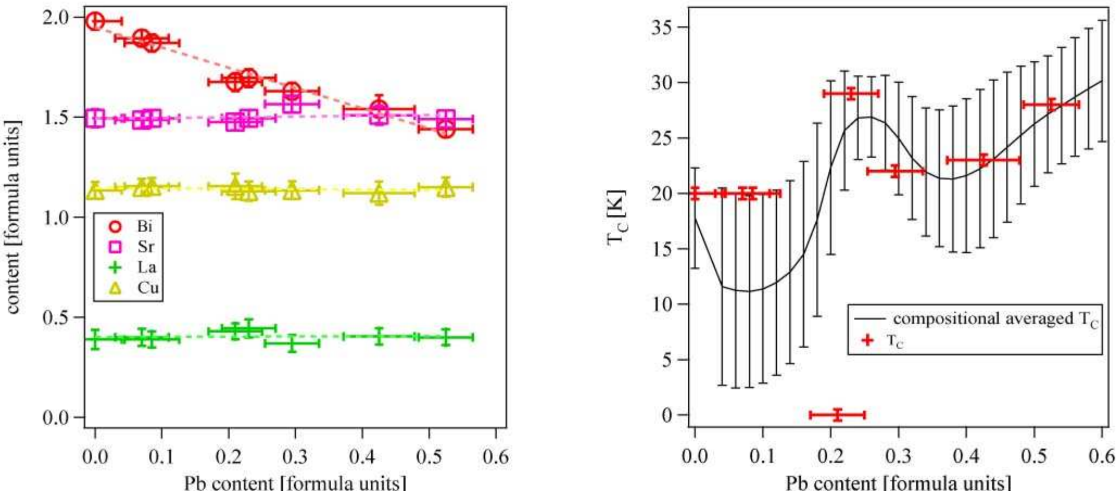

3.11.1: The average composition of the STM measured samples dependent on the average Pb content. The dotted lines represent the linear fits to each composition dependent on the Pb substitution y. Practically only the Bi content changes are visible due to the substitution. The Lanthanum content is almost constant with 0.4 formula units.

3.11.2: The T_C of the STM measured samples dependent on the average Pb content. Also shown is the averaged T_C of the compositional restriction for the constant La content of x=0.4 dependent on the Pb content.

Only the sample with y=0.21 deviates significantly from the area spanned by the standard error of the averaged curve. We will soon see that this might not be incidental as the region around 0.2 to 0.3 is a structural instable region.

3.4.2 STM measurements and interpretations

In this paragraph, I will present some selected STM patterns of the samples characterized above. By changing the Pb substitution, the samples will show an amazing kaleidoscope of phases. At low Pb level, we will see only some Pb atoms which orientate themselves along the present superstructure. The Pb atoms will clump together and form bright linear objects. The superstructure vanishes in the region between 0.2 and 0.3 formula units of Pb substitution. But the most exciting morphologies are also produced within this region as the system evolves into a two-phase system. This evolution goes through two precursor phases, called here α^* and β^*. At the higher Pb side of the region, these precursor phases develop into two clear distinguishable phases: The α- and β -phases. At Pb substitution levels higher than this region, the β-phase appears to dominate.

A collection of typical STM patterns for the samples of $Bi_{2-y}Pb_ySr_{2-x}La_xCuO_{6+\delta}$ with y=0; 0.07; 0.09; and 0.21 is shown in Fig. 3.12. For y=0.23; 0.3; 0.43; and 0.53 the patterns are shown in Fig. 3.13. The size of the probed area, the current and the bias are written below each pattern. All samples were measured at room temperature. If available, a LEED photograph of the same sample is depicted in the inset. In the following, I will describe and comment on the evolution visible in the STM patterns upon Pb substitution.

Let us begin the series with the Lead-free sample $Bi_{1.98}Sr_{1.5}La_{0.39}Cu_{1.14}O_{6+\delta}$. The STM and LEED patterns are shown in Fig. 3.12.1. In the STM pattern for the Pb-free samples, the well-known $\approx 1\times5$ superstructure is visible. This can also be seen clearly in the LEED pattern by the beads of additional reflexes. Topographic STM patterns often include dark atomic rows on the ridge of the superstructure (see, e.g., [163]). It might be that these are missing atoms [164]. It is also possible that these rows are caused by atoms which lie more deeply below the surface [165]. However, the dark atomic rows do not seem to be generally characteristic for the superstructure since there are also reports about an absence (for Bi2201 see [166], for Bi-2212 see [167]). In the samples examined here, no such rows were found.

I will now discuss the mildly Pb-substituted sample with y=0.07 formula units. In the STM patterns, the substitution leads to some brighter points. A typical STM pattern of this kind of sample is shown in Fig. 3.12.2. The bright spots represent a higher unoccupied density of states and seem to be oriented along the superstructure. In reference to other STM measurements for $Bi_{2-y}Pb_ySr_2CuO_{6+\delta}$ [168] and for $Bi_{2-y}Pb_ySr_2CaCu_2O_{8+\delta}$ [169], it is assumed that the bright spots are the substituted Pb atoms. The superstructure is present in the STM pattern as well as in the LEED photograph shown in the inset. Mildly increasing the Pb substitution further (y=0.09) leads to Fig. 3.12.3. There, the bright spots already visible in the y=0.07 sample seem to cluster linearly along the superstructure. These kinds of bright linear objects appear to represent the energetically most favorable position. The 1×5 modulation is still present.

The STM pattern for a Pb substitution of y=0.21 is shown in Fig. 3.12.4. The density of the bright linear objects is significantly increased compared to the sample with y=0.09. It is remarkable that these bright linear objects themselves seem to cluster, denoted as the β^*-phase in Fig. 3.12.4. The clustered bright linear objects are interrupted by a phase denoted as the α^*-phase. This phase consists of bright linear objects in a lower density than in the β^*-phase. Since the bright linear objects may represent ordered Pb atoms, the α^*-phase has a lower Pb content compared to the β^*-phase. The bright linear objects seem to orient themselves along the direction of the $\approx 1\times5$ superstructure. The STM pattern of a sample with y=0.23 is shown in Fig. 3.13.1. The bright linear objects within the β^*-phase seem to be more pronounced. The $\approx 1\times5$ superstructure is only weakly detectable.

A sample with a Pb-content of y=0.3 is shown in Fig. 3.13.2. Within the STM pattern, there are areas where no bright linear objects are present. It is reasonable to assume that these areas evolved out of the β^*-phase which is smooth and bright. It is assumed that this phase is Pb rich. This assumption is supported by a report by Hiroi et al. [160], where this topology was examined in $Bi_{2-y}Pb_ySr_2CaCu_2O_{8+\delta}$ by doing EDX using a focused electron beam (30 nm in diameter) produced by a high-resolution electron microscope (HREM). The β-phase is interrupted by a rough α-phase consisting of bright linear objects that look like lamellae. An $\approx 1\times5$ superstructure is not detectable. Increasing the Pb substitution further, to y=0.43 (Fig. 3.13.3) or y=0.53 (Fig. 3.13.4) for example, results in no new topological features. The STM patterns consist of the α- and the β -phase. The fraction of the α-phase decreases when the amount of Pb is increased. The $\approx 1\times5$ superstructure remains absent.

Figure 3.12: Measurements from [162]: STM patterns for samples of $Bi_{1.95-y}Pb_ySr_{1.49}La_{0.4}Cu_{1.15}O_{6+\delta}$ with y=0; 0.07; 0.09; and 0.21.

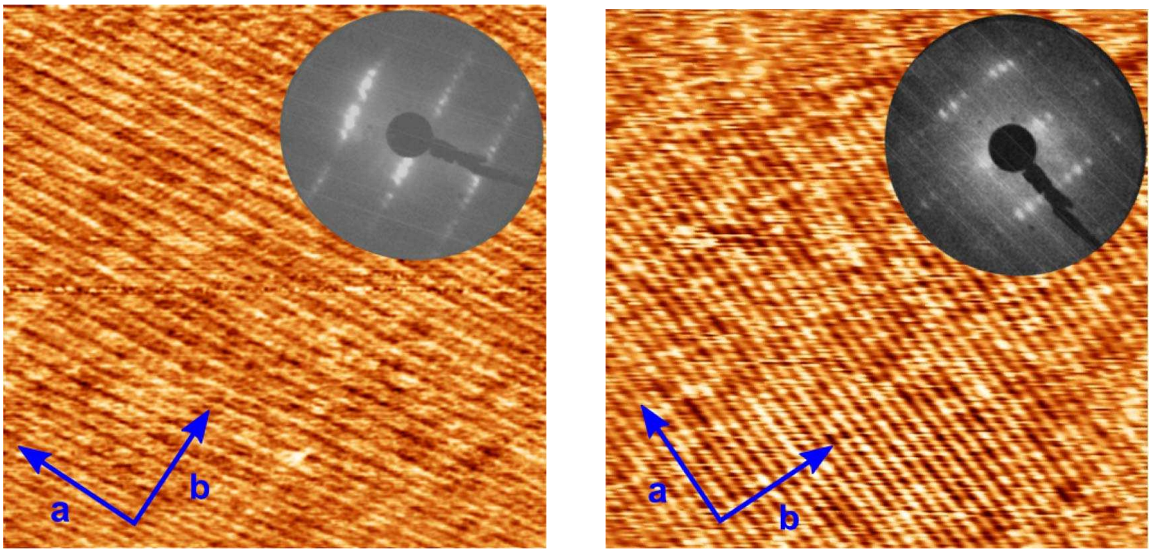

3.12.1: $Bi_{1.98}Pb_ySr_{1.5}La_{0.39}Cu_{1.14}O_{6+\delta}$ with y=0: (70×70) nm^2, RT, 1.0 V, 0.50 nA. The well-known ≈ 1×5 superstructure is well visible.

3.12.2: $Bi_{1.9}Pb_ySr_{1.49}La_{0.4}Cu_{1.15}O_{6+\delta}$ with y=0.07: (100×100) nm^2, RT, 1.9 V, 0.16 nA. Some brighter spots appear which seem to be oriented along the superstructure.

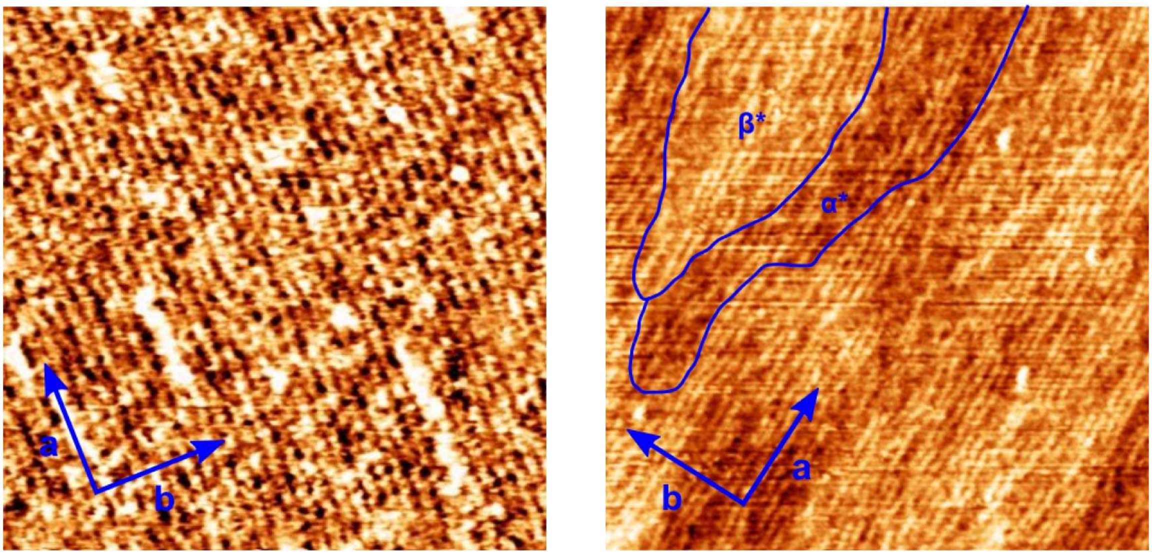

3.12.3: $Bi_{1.87}Pb_ySr_{1.5}La_{0.39}Cu_{1.16}O_{6+\delta}$ with y=0.09: (80×80) nm^2, RT, 0.9 V, 1.53 nA. The bright spots already visible in y=0.07 samples seem to cluster and form bright linear objects which are orientated along the superstructure.

3.12.4: $Bi_{1.68}Pb_ySr_{1.48}La_{0.43}Cu_{1.16}O_{6+\delta}$ with y=0.21: (450×450) nm^2, RT, 0.7 V, 1.43 nA. The density of the bright linear objects is compared to the sample with y=0.09 significantly increased. The bright linear objects themselves seem to cluster into a β^*-phase. The β^*-phases are interrupted by a phase denoted as the α^*-phase which has a lower density of bright linear objects than in the β^*-phase.

Figure 3.13: [162]: STM patterns for samples of $\mathrm{Bi}_{1.95-y}\mathrm{Pb}_y\mathrm{Sr}_{1.49}\mathrm{La}_{0.4}\mathrm{Cu}_{1.15}\mathrm{O}_{6+\delta}$ with y=0.23; 0.3; 0.43; and 0.53.

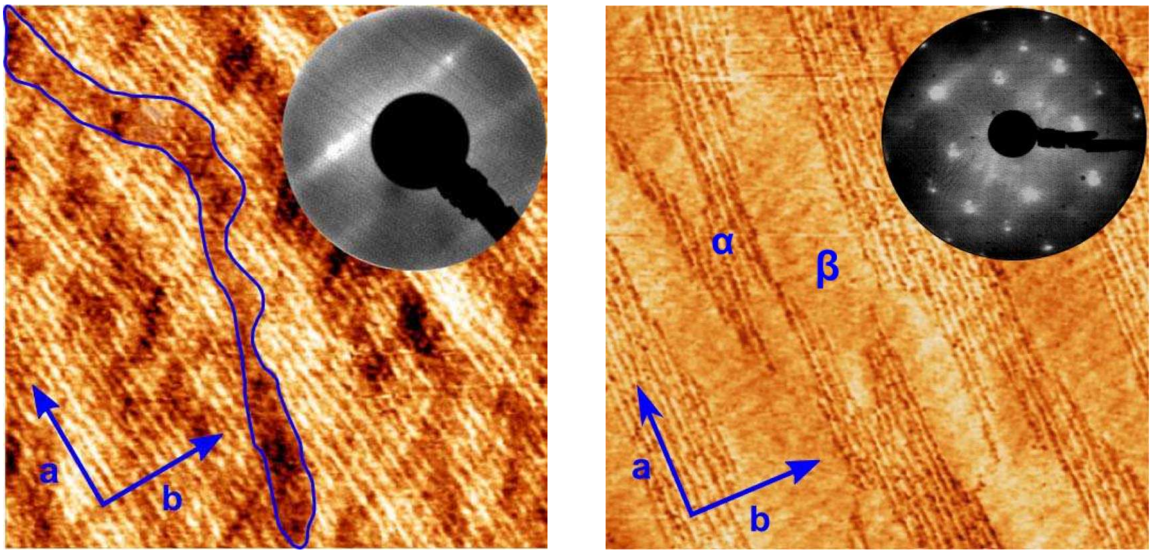

3.13.1: $\mathrm{Bi}_{1.7}\mathrm{Pb}_y\mathrm{Sr}_{1.5}\mathrm{La}_{0.45}\mathrm{Cu}_{1.13}\mathrm{O}_{6+\delta}$ with y=0.23. (300×300) nm^2, RT. 0.3 V, 0.10 nA. The clustering of the bright linear objects within the β^*-phase of Fig. 3.12.4 seems to be more pronounced. The about 1×5 superstructure is only weakly detectable.

3.13.2: $\mathrm{Bi}_{1.63}\mathrm{Pb}_y\mathrm{Sr}_{1.57}\mathrm{La}_{0.37}\mathrm{Cu}_{1.14}\mathrm{O}_{6+\delta}$ with y=0.3. (300×300) nm^2, RT, 1.0 V, 1.08 nA. A β-phase which looks smooth and bright is clearly detectable. The β-phase is interrupted by an α-phase consisting of bright linear objects, which ordering looks like lamellas. An ≈ 1×5 superstructure is no longer detectable.

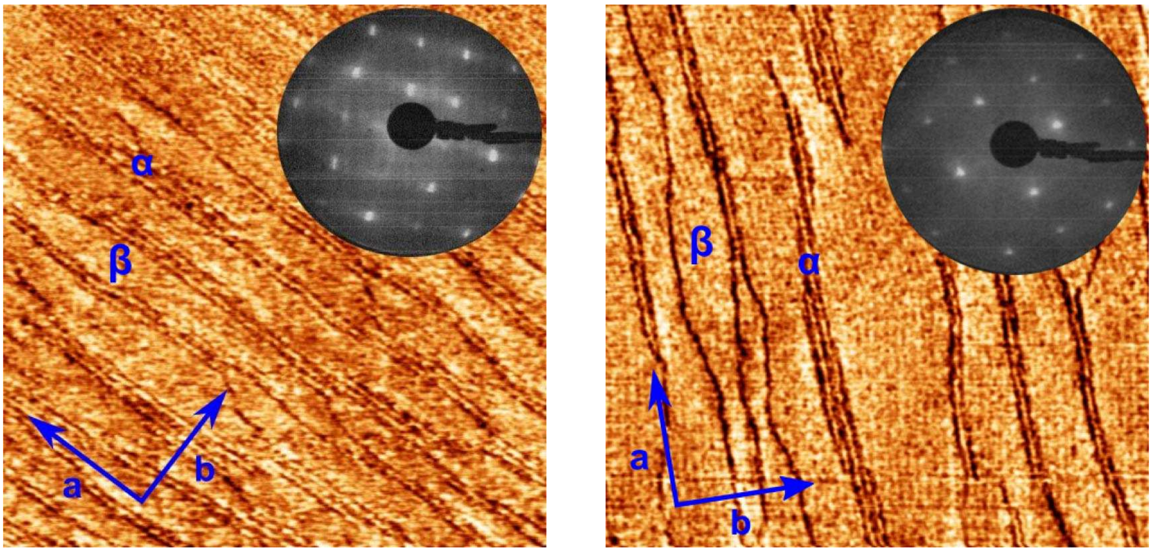

3.13.3: $\mathrm{Bi}_{1.54}\mathrm{Pb}_y\mathrm{Sr}_{1.51}\mathrm{La}_{0.41}\mathrm{Cu}_{1.12}\mathrm{O}_{6+\delta}$ with y=0.43: (300×300) nm^2, 0.5 V, 0.10 nA. The topology consists of the α- and the β -phase. The fraction of the α-phase is lower than in the sample with y=0.3. The ≈ 1×5 superstructure remains absent.

3.13.4: $\mathrm{Bi}_{1.44}\mathrm{Pb}_y\mathrm{Sr}_{1.49}\mathrm{La}_{0.4}\mathrm{Cu}_{1.15}\mathrm{O}_{6+\delta}$ with y=0.53: (300×300) nm^2, 0.6 V, 1.19 nA. The topology consists of the α- and the β -phase. The fraction of the α-phase is lower than in the sample with y=0.43. The ≈ 1×5 superstructure remains absent.

We may conclude that a small amount of Pb substitution does not change the structure dramatically because the superstructure remains. Increasing the Pb substitution up to the region between 0.2 and 0.3 formula units results in a strong phase mixture. Above approximately 0.3 formula units of Pb substitution we observe a rough α- and a smooth β -phase. The β-phase dominates at a high enough Pb level. This is consistent with results on $Bi_{2+z}Pb_ySr_{2-z}CuO_{6+\delta}$ from Nishizaki et al. [161]. In Fig. 3.14, the quantitative analysis of the distances found between the bright linear objects at low Pb, the bright linear objects within the α-phase, as well as the superstructure wavelength, are shown. The periodicity was averaged over many patterns. For computing, the b-length was set to 5.4 Å. According to this graph it becomes clear that the ≈ 1×5 superstructure remains nearly constant. This is in contrast to the results of Nishizaki et al. [161]. The distance between the bright linear objects reduces when the Pb substitution level is increased and its lengthscale appears to evolve into the lengthscale of the bright linear objects within the α-phase. It can be suggested that the distances of the bright linear objects cause the Pb-type superstructure. As will be recalled, this superstructure was shown in the electron diffraction patterns in Fig. 3.10 and discussed in Section 3.3.

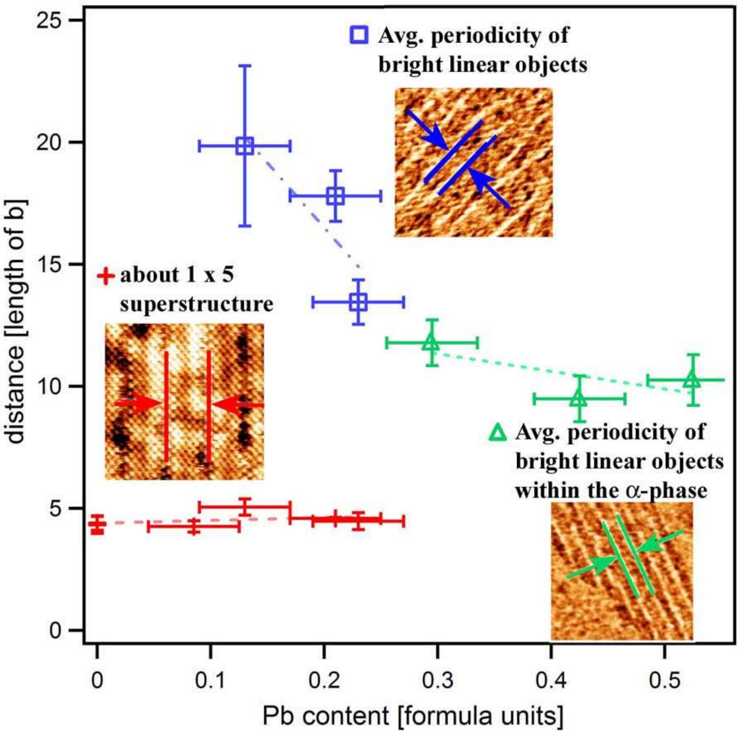

Figure 3.14: Quantitative length found by averaging over many patterns. Shown are the characteristic lengths which are produced by the superstructure wavelength, the distances of the bright linear objects at low Pb and the distances of the bright linear objects within the α-phase. For computing the length in units relative to b, the absolute length was divided by 5.4 Å.

3.4.3 Comparison to Bi2212

In this section, the behavior upon Pb substitution is briefly discussed for the two-layer $Bi_{2-y}Pb_ySr_2CaCu_2O_{8+\delta}$. This is to be compared with the one-layer material. As for these two-layer samples, only the nominal composition of Pb was given; the actual composition of Pb is only estimated. In this way, the comparison is qualitative. Some STM patterns of $Bi_{2-y}Pb_ySr_2CaCu_2O_{8+\delta}$ with nominal composition y=0; 0.04; 0.12; 0.27 are shown in Fig. 3.16 [170]. The

Figure 3.16: [170, 162]: A collection of typical STM patterns for samples of $Bi_{2-y}Pb_ySr_2CaCu_2O_{8+\delta}$ with nominal composition y=0; 0.04; 0.12; 0.27. The size of the probed area and the current and bias are written below each pattern. The estimated actual Pb composition is written in brackets behind the nominal composition.

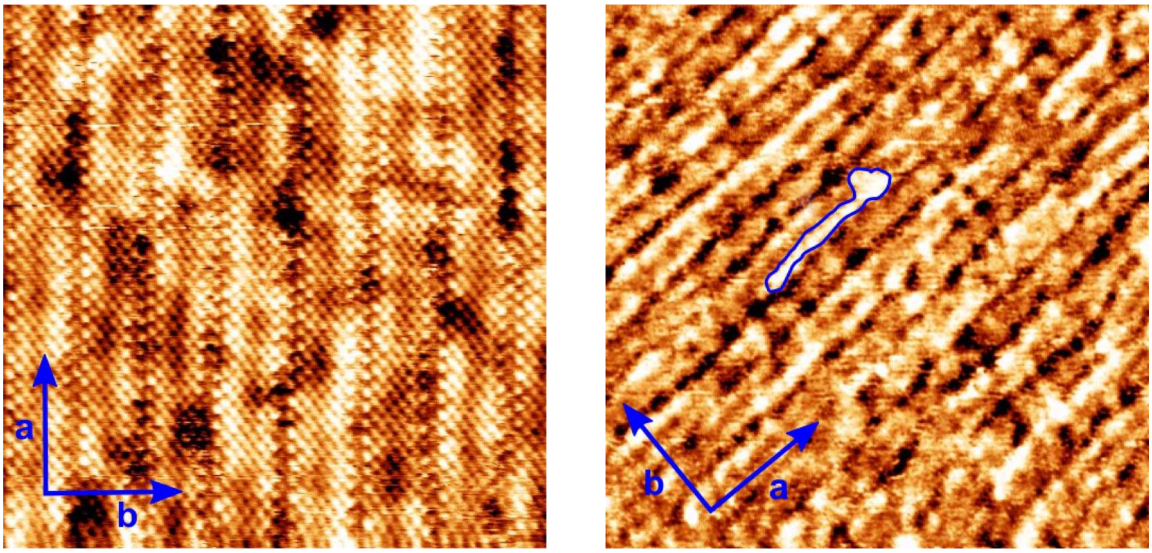

3.16.1: $Bi_2Sr_2CaCu_2O_{8+\delta}$ (20×20) nm^2, RT, 0.15 V, 0.50 nA.

3.16.2: $Bi_{2-y}Pb_ySr_2CaCu_2O_{8+\delta}$ y_{nom}=0.04 (y≈0.1). (50×50) nm^2, RT, 0.50 V, 0.50 nA.

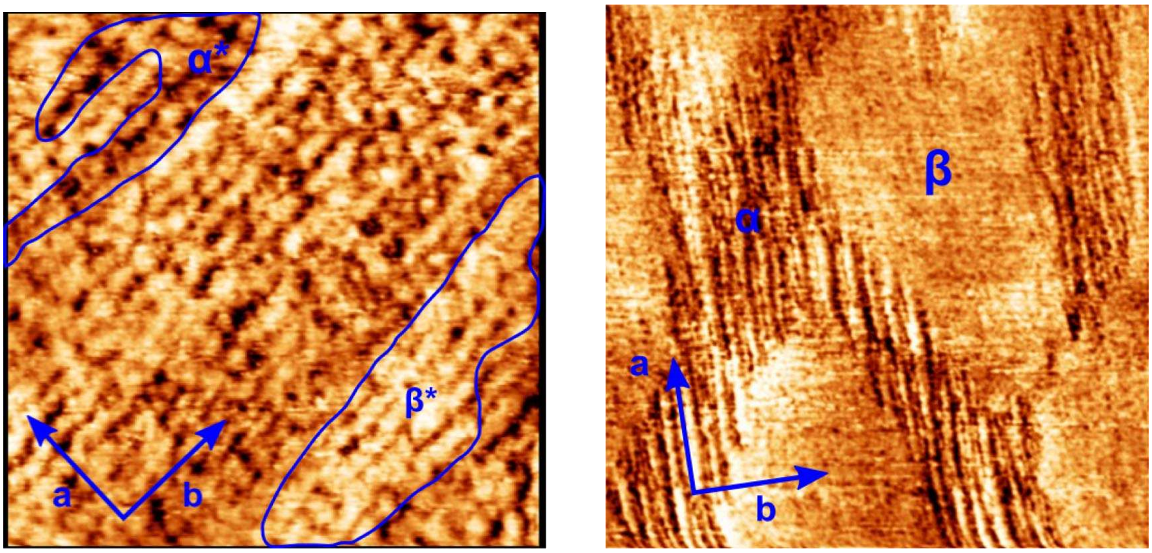

3.16.3: $Bi_{2-y}Pb_ySr_2CaCu_2O_{8+\delta}$ y_{nom}=0.12 (y≈0.2). (100×100) nm^2, RT, 0.30 V, 0.40 nA.

3.16.4: $Bi_{2-y}Pb_ySr_2CaCu_2O_{8+\delta}$ y_{nom}=0.27 (y≈0.3). (200×200) nm^2, RT, 0.50 V, 0.50 nA.

size of the probed area and the current and bias are written below each pattern. The estimated actual Pb-composition is written in brackets behind the nominal composition. All samples were measured at room temperature.

The STM pattern of a Pb-free sample $Bi_2Sr_2CaCu_2O_{8+\delta}$ with T_C=92 K is shown in Fig. 3.16.1. As expected, the ≈ 1×5 superstructure is visible. In this sample, the dark atomic rows on the ridge of the superstructure are present. An STM pattern of a sample of $Bi_2Sr_2CaCu_2O_{8+\delta}$ with nominal Pb substitution of 0.04 is shown in Fig. 3.16.2. Similar to the one-layer samples (please see Fig. 3.12.3), bright spots accumulate along the ≈ 1×5 superstructure, cluster and form bright linear objects. The bright spots here are also assumed to be Pb atoms. In comparison to the one-layer material, the actual Pb substitution is roughly estimated as y=0.1. A sample with the nominal composition y=0.12 is shown in Fig. 3.16.3. This sample should be compared with the STM pattern of the one-layer sample with y=0.21 shown in Fig. 3.12.4. The last STM pattern of Fig. 3.16.4 shows a sample with nominal composition of y=0.27. Because of the existence of the rough α- and the smooth β -phase, it is assumed to have an actual Pb content of $y \approx 0.3$. This pattern should be compared with the one-layer material at 0.3 Pb substitution as shown in Fig. 3.13.2.

Through this comparison, we see that the behavior upon Pb substitution for the one-layer and the two-layer material is quite similar. The estimation of the Pb content in the two-layer material is questionable, as it is derived from a comparison. For example, Hiroi et al. [160] found that the region of strong phase mixture was also present in Pb-Bi2212 crystals with a starting (nominal) composition of 0.4 formula units. But overall, we can deduce that there is a similar trend for the two-layer material and for the one-layer material.

3.4.4 Evaluating a phase diagram for the microscopic behavior

Based on the previous two sections, the following general behavior due to Pb substitution for Bi2201, and also for Bi2212, can be stated: At low Pb substitution the Pb atoms orient themselves along the superstructure. Increasing the substitution leads to the formation of bright linear objects along the superstructure. More Pb substitution further results in an increase in the density of bright linear objects. There is an intermediate region with a strong phase mixture where the bright linear objects are partly clustered. At a critical Pb-level, the clustered bright linear objects become the smooth β-phase which is intersected by the rough α-phase. The α-phase is in principle the same topology as at substitution levels before the bright linear objects started to cluster. At higher substitution levels, the topology does not change dramatically but the fraction of the α-phase lowers when increasing the amount of Lead. At a high enough Pb substitution, the β-phase is the dominant phase. It is important to notice that up to the critical Pb level, the wavelength of the superstructure remains about the same. When reaching the critical Pb level, the superstructure is no longer detectable.

In this paragraph I want to evaluate a phase diagram for the behavior upon Pb substitution which is observable by STM. First, we have to discuss what the driving force of the change in morphology is. The change due to Pb substitution at constant La is examined here. In Chapter 4.2 I will show that the hole concentration at Pb content y=0 is given as p=0.24 - 0.21 x, while for Pb content y=0.4 it is p=0.23-0.15 x. Here, the x denotes the Lanthanum content. For our structural discussion this means that changing the Pb content from 0 to 0.4 formula units at constant Lanthanum of x=0.4 would result only in a hole concentration difference of approximately 0.015 holes per Cu. In Chapter 3.3 I discussed that the structural change due to substitution is mainly influenced by two views on the structure: (i) the misfit between the perovskite structure and the BiO-layer (adaption) and (ii) the binding conditions in the CuO_6 octahedra. For nearly constant hole doping, it can be suggested that the binding conditions within the octahedra remain the same. Therefore, here the driving force in the change of morphology is suggested to be the mismatch of the (Bi,Pb)O layer and the perovskite block. When the β-phase present at high Pb levels is considered, it might be that this phase represents a structure where the (BiPb)O-plane is perfectly adapted to the perovskit block. The STM patterns suggest that the adaption in $Bi_{2-y}Pb_ySr_{2-x}La_xCuO_{6+\delta}$ will occur around 0.5 formula units of Pb substitution. We can further simplify and consider a two-component system: One component is the nearly static perovskite block while the other is the (BiPbO)-layer. The latter component can be assumed to have its size determined by the Pb an Bi ratio. Therefore, to account for the morphologies here, we can design a pseudo-binary phase diagram for $Bi_{2-y}Pb_y$-$Sr_{2-x}La_xCuO_{6+\delta}$ relative to the Pb-level. As nearly the same morphologies were present in the two-layer material, this diagram might only be slightly modified to account for the Bi2212-phase.

What we see in Fig. 3.17 is a phase diagram which is dependent on temperature and Pb substitution level. The vertical axis marks the temperature and starts at room temperature (RT). The Pb substitution level is on the upper horizontal axis and given as a percentage and on the lower vertical axis in formula units. The region at high Pb substitution is drawn only schematically. The lines are the phase boundaries and the points are critical points. When we look at the phase present in the system, the upper phase is the melt (liquid). At low Pb

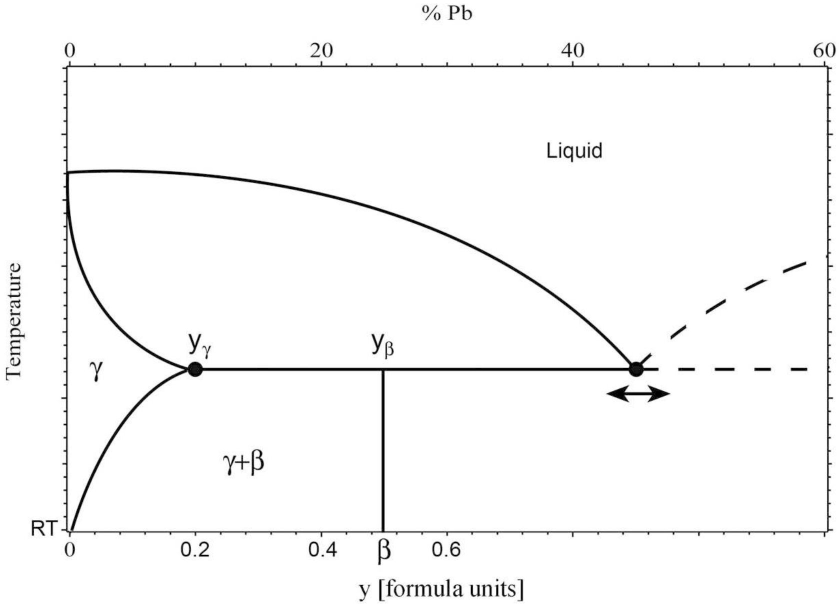

Figure 3.17: Pseudo-binary phase diagram to explain the found topologies: The γ-phase is the Lead-free crystal of $Bi_{2-y}Pb_ySr_{2-x}La_xCuO_{6+\delta}$ with the stoichiometry x=0.4 and y=0, exhibiting the ≈ 1×5 superstructure. The peritectic β-phase is at around y=0.5. In this phase, the (BiPb)O-plane is probably perfectly adapted on the perovskite block. An eutectic point in this phase diagram might be around y=0.9.

substitution (on the left side) the γ-denoted-phase is present. This phase is considered to be the Lead-free crystal of $Bi_{2-y}Pb_ySr_{2-x}La_xCuO_{6+\delta}$ with x=0.4 and y=0. As we know, this phase exhibits the ≈ 1×5 superstructure. The optimally adapted, smooth β-phase is at about y=0.5. This phase has no superstructure. Also, we see an area where the γ- and the β-phases mix. This area is called $\gamma + \beta$. We see also that the β-phase cannot be reached directly from the melt because another phase is present between the liquid and the β-phase. This means that the β-phase is depicted here as a peritectic phase.

It is important to note some details at this point. The shown phase diagram is characterized by an eutectic point. As the arrow implies, the exact position of this eutectic point is not certain. In the (pure) three-dimensional phase diagram of only Bi and Pb, an eutectic point is at 45% Pb and 125°C. As we expect this system to also have an eutectic point, it was set on the same substitution level as in the three-dimensional (pure) system. Further studies might be necessary to find its exact position. This is also because the phase diagram is based on STM measurements up to a Pb substitution of about 0.5 formula units. Some features above this concentration might not be exact and no exact temperatures can be given. In principle, the optimally adapted β-phase could be either peritectic or eutectic. For the topological behavior at substitution levels up to y=0.5, this uncertainty is of minor importance in this basic view.

After this basic description of the evaluated phase diagram, I would like to explain the development of the different topological phases. For this purpose, some interesting starting compositions are depicted in Fig. 3.18.

We start with the melt at around y=0.04 formula units. This composition is denoted as 1 in Fig. 3.18. Lowering the temperature of this composition leads to the splitting of the system at the solidus line. One part crystallizes in the γ-phase (at point A) whereas the rest of the system follows the solidus towards the eutectic point. A soft reduction of the temperature will enable

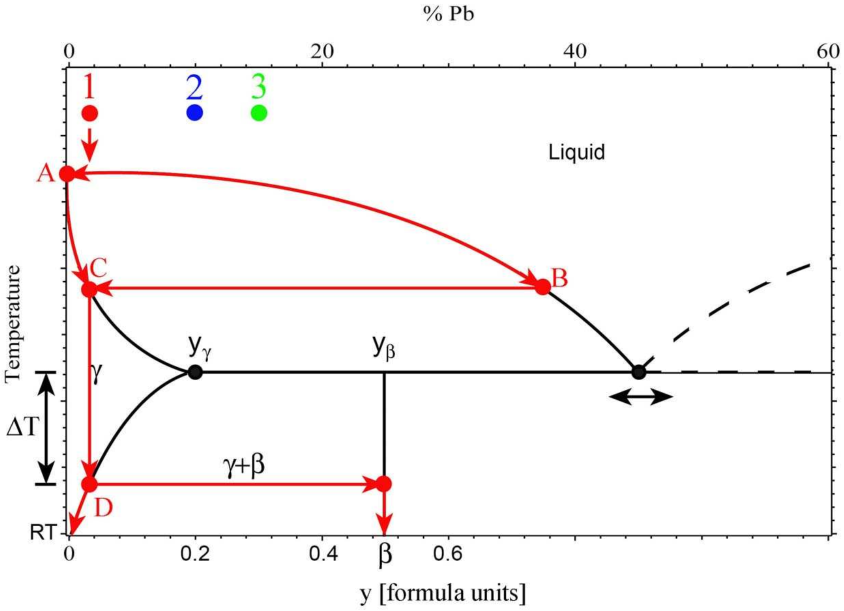

Figure 3.18: The same pseudo-binary phase diagram as Fig. 3.17. To further explain the topologies found by STM, three interesting starting compositions (1,2,3) are plotted within the phase diagram. Also, the crystallization process for starting composition 1 is depicted. For details, see the text.

the γ-phase to grow on the cost of the melt. This growth can be achieved until point C is reached and the concentration in γ is identical to the starting composition. Lowering the temperature further leaves the system stable within the γ-phase until point D is reached. At this point, the β-phase decomposes from the γ-phase. Because the system is strongly supercooled (ΔT), the decomposition of the β-phase will be sudden: The Pb atoms crystallize at local inhomogeneities. These local inhomogeneities are given by the superstructure. Therefore, in the STM patterns at low substitution levels, bright spots appear which are located near the superstructure (see Fig. 3.12.2).

Changing the starting composition in the direction of composition 2 will increase the condensed amount of Pb near the superstructure. At a certain composition, bright linear objects will be formed. The Pb concentration relevant for the appearance of the bright linear objects is roughly determined by the exact shape of the (γ)-$(\gamma + \beta)$ -phase boundary, the diffusion velocity of the elements, the supercooling ΔT, the ability of the superstructure to attract Pb atoms and geometrical factors.

Let us now assume a melt with the composition 2 in Fig. 3.18. This is at $y_\beta \approx 0.2$ formula units. For the crystallization process, point B in Fig. 3.18 moves onto the eutectic point. This means that above concentration 2, the β-phase can be stabilized without supercooling. The previous statement might be clearer when realizing that points C and D in Fig. 3.18 will merge for concentration 2 at y_γ. But the above-mentioned stabilization of the β-phase without supercooling will only be possible in adiabatic conditions, e.g., with an infinitesimally slow cooling rate near the temperature of the eutectic line. What will typically happen is the formation of two topologies: One topology would be the very locally stabilized β-phase and the other topology would be quite similar to the bright linear objects (see Fig. 3.12.4 and Fig.3.13.1).

The stability of the β-phase is dependent on the cooling rate and the Pb level. In the case of the results from the crystals shown here, the level seems to be at about point 3 in Fig. 3.18 with y<0.3. At this composition it is possible to *define* the α-phase. The α-phase is a phase-mixture produced by the part of the system which crystallizes at point y_γ into the γ-phase and decomposes further in the γ- and β -phase. The α-phase can be seen in the STM patterns depicted in Figs. 3.13.2 to 3.13.4. Please note that this explanation of the α-phase is the difference and extension of the phase diagram given for $Bi_{2-y}Pb_ySr_2CaCu_2O_{8+\delta}$ by Hiroi et al. [160].

This explanation of the α-phase as a phase mixture is quite interesting as it means that in the compositional region y≈0.2-0.5 in one and the same sample, two (metastable) phase mixtures are present. One phase-mixture is produced by the decomposed γ- and β-phase at the eutectic line and the other is the decomposed γ-phase at temperatures lower than the eutectic line. The latter process results in an α- phase mixture. In principle, it should be that around the eutectic line the later α-phase mixture and the β-phase order themselves perpendicular to the growth direction. The growth direction for Bi2201 is the a-direction. The bright linear objects in the α-phase mixture should order at local inhomogeneities present in the already crystallized γ-phase.

Overall, it can be stated that a strong inhomogeneity is present in the Pb-region, where a strong decomposition of the γ-phase occurs. This also applies for the region where the β-phase starts to form. The formation occurs within the Pb-substitution range from y=0.2 to 0.3 formula units. For crystal growth, crystals in this region are hard to grow because there is an attempt to reach a metastable state there. This is interesting for the superconducting properties as the inhomogeneities may influence or even destroy superconductivity. Therefore, it may be speculated that the reduction of T_C visible around y=0.2 in the averaged T_C curve, as well as the T_C of the here-examined samples, may have this underlying physical reason. The T_C's were shown in Fig. 3.11.2.

3.4.5 Discussion

From the preceding section, the evolution of the morphology of crystals of $Bi_{2-y}Pb_ySr_{2-x}La_x$-$CuO_{6+\delta}$ at fixed Lanthanum upon varying the Pb substitution was shown. It turned out that the superstructure is suppressed in samples with Pb substitution above 0.3. In the region from 0.2 to 0.3, a strong inhomogeneous phase mixture is present. Within this region, the superconducting properties might be strongly influenced. In the examined system, above the 0.3 Pb substitution level the system *always* exhibits two components: One component is a smooth β-phase and the other component is not a true phase, but instead a *phase mixture*. Here and in the literature it is called the α-phase (see, e.g., [159, 160, 161]), but it might be more appropiately referred to as a α-mixture. By a comparison with the two-layer $Bi_2Sr_2CaCu_2O_{8+\delta}$, I showed that the same phases are present there. I proposed a phase diagram which explains all appearing phases and is, in my view, a reasonable extension of the phase diagram presented by Hiroi et al. [160].

Considering the consequences of the found phase mixtures for other experimental methods, I would like to briefly discuss a problem for angular resolved photoemission (ARPES). For basic knowledge about ARPES see Appendix A.5. From the 1x5 superstructure it is well known that it causes diffraction replicas of the photoemission signal [171]: The measured photoelectrons, e.g., at wavevector k, also consist partly of photoelectrons emitted from the wavevector k±n q_{SS}. Here, n is an integer and q_{SS} the wavelength of the superstructure. For the wavelength of a periodic structure which is known and much larger than the k-resolution of the ARPES experiment, this is not a significant problem. However, in the case of the other periodical structures described above, it might occasionally be a problem, especially when the characterization of the crystals is not done by STM or equivalent methods. For low energy diffraction (LEED), we can see by the pictures above that it can no longer detect periodicity larger than about 100 Å. This is due to the finite transfer-width[3] of LEED. In [172], I showed the results for a sample of $Bi_{2-y}Pb_ySr_{2-x}La_xCuO_{6+\delta}$ with x=0.4 and y=0.4: Beside a 2d periodicity which I will discuss later, there was a diffraction in the photoemission signal produced by the one-dimensional 1x32 periodic arrangement of the α- and β-phase. From this analysis, it follows that the extraction of many quantities gained in a photoemission experiment - like the self energy - are questionable under certain circumstance.

However, the way the superconducting properties are affected should also be addressed. Because of this sub-microstructural analysis we know that crystals with high enough Pb are dominantly in the smooth β-phase. For the influences of the α-phase on the superconducting properties, it is useful to compare the superconducting coherence length in the plane $\xi_{ab} \approx$ 20-30Å [71] with the lengthscales produced by the mixing of the α-phase within the β-phase. According to Fig. 3.14, the lengthscale is about 10 times b, which is 54 Å$> \xi_{ab}$. It can therefore be concluded that, at least from a sub-microstructural view, the system is clean. Therefore, for the following measurements on Pb substituted crystals I will use the series $Bi_{2-y}Pb_ySr_{2-x}La_xCuO_{6+\delta}$ with y=0.4 formula units.

---

[3] The transfer-width acts in principal like a coherence length; More detailed knowledge can be found, e.g., in [158]

IV

Superconducting properties and depressions in T_C

In the motivation, the first figure I showed was the generally accepted generic phase diagram of the hole-doped high-temperature superconductors. There, the superconducting dome was illustrated: A parabola which exhibits a maximum at around 16% of hole doping. This parabola is also often called the 'Presland curve' [7] or 'universal curve'. This curve is suggested to fit for every hole-doped high-temperature superconductor. This means that superconductivity should occur at the same hole-doping range. The structural differences of the system are accounted for by scaling the maximum T_C of this parabola.

I am of the opinion that the 'universal curve' is oversimplified. One interesting feature in the hole-doped cuprates is the possible generic existence of depressions within the superconducting dome: At certain hole-doping values, the T_C drops. For $La_{2-x}Ba_xCuO_4$ (LBCO), the famous 1/8 depression [6] is widely accepted. Also, $La_{2-x}Sr_xCuO_4$ has the 1/8 depression, but other fractional depressions can also be suggested for this material [8]. Even $YBa_2Cu_3O_{7-x}$(YBCO) shows a reduction in T_C, which was found early and often referred to as 'the 60K plateau' [173]. It can be assumed to be the 1/8 depression [174]. As will be recalled from the introduction, the depression at 1/8 can be explained as a result of static stripes, for example.

But despite one report by Yang et al.[175], for the system examined here, the knowledge about the existence of such depressions is very poor. In my view, this is also due to problems in estimating the hole doping in this cuprate. As I pointed out in the last chapter, there are numerous possibilities for doping holes into this system. Because the superconducting phase diagram of $Bi_{2-y}Pb_ySr_{2-x}La_xCuO_{6+\delta}$ will be examined experimentally in this work, I require the T_C vs. hole-doping curve. Only by achieving this curve will it be possible to discuss generic features of hole-doped high-temperature superconductors. From the preceding, there are two goals in this chapter: One is to find the number of holes for the system, while the other is to show that - like for the other cuprates in the $Bi_{2-y}Pb_ySr_{2-x}La_xCuO_{6+\delta}$ system - there are also depressions in T_C.

To fulfill these goals, I start by showing results of energy dispersive x-ray analysis (EDX) and AC-susceptibility. Based on these basic characterization results, I will discuss two series: One is the system without Lead ($Bi_2Sr_{2-x}La_xCuO_{6+\delta}$) and the other is $Bi_{2-y}Pb_ySr_{2-x}La_xCuO_{6+\delta}$ with Pb substitution of y=0.4. As we know from the last chapter, both these systems are structurally different. I will show that in both these systems depressions of T_C at certain - but for both series different - La substitution levels are present. As these series both show depression at different La content, it means that the depressions cannot be a feature of the La. Therefore, we can already suggest that the depressions are only dependent on the holes. But, before coming to the determination of the hole content, the possible influence of the extra

Oxygen for the T$_C$ vs La/Pb curve must be considered. The question is whether the La and Pb in the system determine the amount of excess Oxygen. If this is the case, it is in principle possible to determine the hole concentration by determining the amount of Pb and La. In a further section, an overview of recent experimental methods to extract the hole concentration is presented. In reference to other work [142, 176], the goal for finding a hole scaling is reached by looking in the literature. In principle, the chapter could end there.

But one important aim of this thesis is to prove that the depressions in T$_C$ are a generic feature of the cuprate high-temperature superconductors. Therefore, to discuss the existence of the depressions, I will put the cart before the horse by first presenting the existence of depressions for LSCO. In $La_{2-x}Sr_xCuO_4$, the hole concentration is directly proportional to the Strontium substitution x. Therefore, the hole concentration of the depressions in LSCO can be used to assign the depressions of T$_C$ in $Bi_{2-y}Pb_ySr_{2-x}La_xCuO_{6+\delta}$, which were found relative to the Lanthanum (and Lead) substitution level. In this way, a scaling between the La and Pb concentration relative to the hole-concentration can be constructed. This hole scaling equals the one obtained by x-ray absorption spectroscopy (XAS) [142, 176]. Because the opposite can be argued it is therefore shown that depressions at certain hole dopings also exist in the single-layered Bi-cuprate.

4.1 Superconductivity in relation to the Lanthanum and Lead content

To achieve a phase diagram relative to the content of the elements of the samples and the superconducting characteristics, energy dispersive x-ray analysis (EDX) and AC-susceptibility (ACS) were conducted. EDX probes the chemical composition for each crystal at two 'typical' points on the surface. ACS provides an onset-T$_C$ and a ΔT$_C$ derived by the 10% - 90% criterium. For a brief description of ACS and EDX please see the Appendix A. The whole dataset contained 299 crystals which were optically preselected under a microscope. Only samples with a growth time between 37 - 90 hours were taken. The growth time is defined here as the time the melt was above 830 °C. This restriction was to ensure structural equality, e.g. comparable insertion of Oxygen and Bi-Sr exchange. Superconducting samples were chosen with the restriction that they must have only one peak in the imaginary part of ACS. No distinction was made between small or broad transition width as long as the imaginary peak looked like one Gaussian-like peak and the real part downturn looked smooth. The samples can further be chosen by the following *compositional restriction*:

The chemical composition of La is written x and the chemical composition of Pb is y. For each element of the composition an average[1] content for each sample j can be defined. For example, for La it is written as

$$\overline{x}^j = \frac{1}{2}(x_0^j + x_1^j)\,, \tag{4.1}$$

---

[1] When having only two data points in stochastically terms there is of course no reason to speak of an 'average' or neither a 'standard error'. In any case, it might be an appropriate number.

where x^0, x^1 are the two EDX measurements and $j = 0, 1, \cdots (J-1)$ is the index of the J measured samples. A standard error can also be defined:

$$\sigma_x^j = \sqrt{\sigma_{Fit}^2 + \frac{1}{2}(x_0^j - x_1^j)^2}\,. \tag{4.2}$$

σ_{Fit} describes the systematic error of EDX within the PUzaf correction [177], e.g., the fitting routine to extract the composition from the spectrum. It was taken as 0.04 formula units. For La and Pb, this is about the average value but Cu typically exhibits a higher one. For the restriction, the standard error as defined above for each element should not exceed 0.07 formula units. Samples with a larger error were removed.

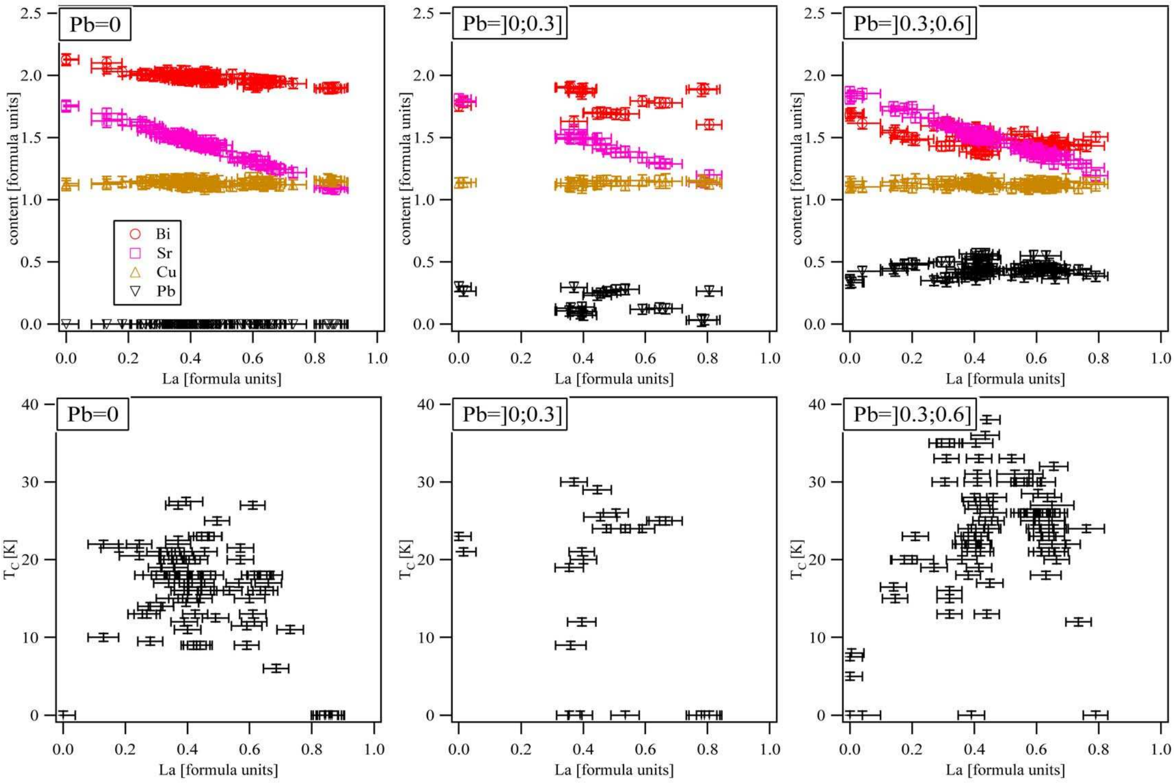

Figure 4.1: **Upper panel:** The average chemical composition of Bi,Sr and Cu vs the average Lanthanum content in slices of Pb=0, Pb=]0;0.3] and Pb=]0.3;0.6] for the dataset with the compositional restriction. **Lower panel:** T$_C$ vs the average Lanthanum content for the dataset with the compositional restriction. From left to right the dependence of the Pb content is shown in slices of Pb=0, Pb=]0;0.3], and Pb=]0.3;0.6].

The average chemical composition was then fitted by a linear dependence. The Pb content and the La content were assumed to be independent of each other. If the average chemical composition of Bi, Sr and Cu is written as c(Bi), c(Sr) and c(Cu), the linear dependence of

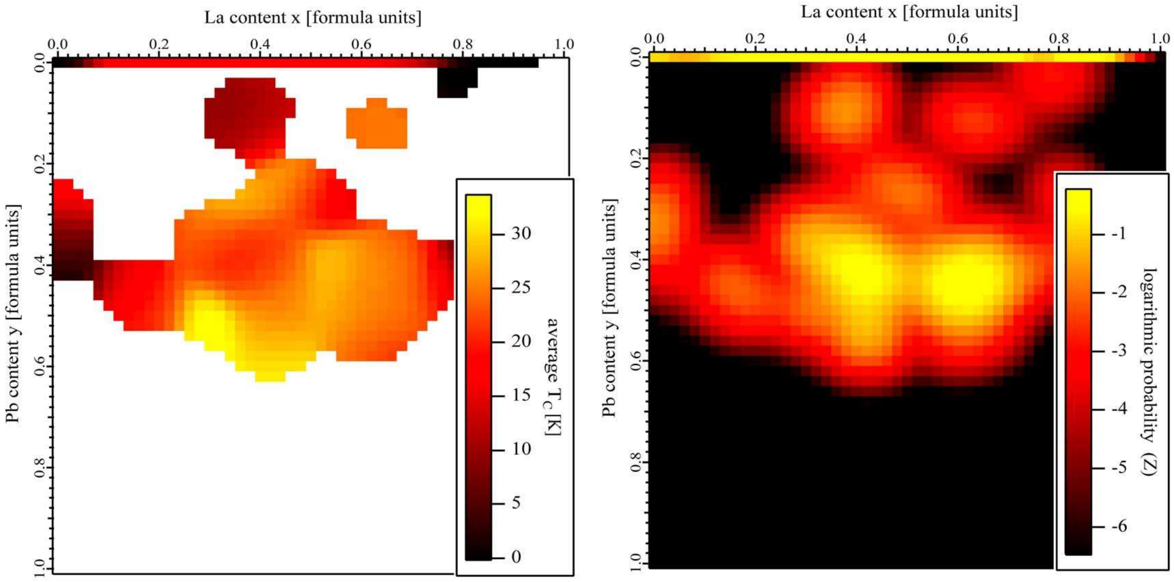

Figure 4.2: **Left panel:** Average T$_C$ for the filtered dataset. For details of the averaging algorithm please see Appendix B.1. Here Δx,Δy= 0.02. **Right panel:** The probability Z in logarithmic scale of having a sample with the content (x,y) in the dataset of size J=208.

these 299 samples is given by

$$\begin{aligned}
c(Bi) &= (2.08 \pm 0.01) - (0.21 \pm 0.01)x - (1.12 \pm 0.01)y \quad ; \quad \chi^2 = 0.70246; \\
c(Sr) &= (1.79 \pm 0.01) - (0.78 \pm 0.01)x + (0.12 \pm 0.01)y \quad ; \quad \chi^2 = 0.55005; \\
c(Cu) &= (1.13 \pm 0.01) - (0.01 \pm 0.01)x + (0.01 \pm 0.01)y \quad ; \quad \chi^2 = 0.60479\,.
\end{aligned}$$

Here all values are given in formula units. Crystals with a derivation of the average Bi, Sr or Cu composition from the linear dependence larger than 0.05 formula units were removed.

By applying this restriction, the size of the dataset was reduced to 208. In the upper panel of Fig. 4.1, the average chemical composition of Bi, Sr and Cu vs the average Lanthanum content is shown. The resulting T$_C$ relative to the average Lanthanum content for the compositional-restricted dataset is shown in the lower panel of Fig. 4.1. There, the data is shown in slices of Pb=0, Pb=]0;0.3] and Pb=]0.3;0.6]. From Fig. 4.1, it is obvious that T_C^{max} increases by increasing the amount of Pb. Typically, the curve T$_C$ vs La content is described as a parabolic curve (see, e.g., [178]). But here the data points appear strongly scattered or irregular although the compositional dependence of Bi, Sr, and Cu vs the average Lanthanum content looks smooth. For Pb concentrations higher than y=0, this can be best observedwhen looking at the Bi curve and the Pb curve, which have to be complementary in its gradient. At y=0 a strong scattering of T$_C$ values takes place in the region around x=0.25, 0.4, and 0.6 formula units. At y=]0;0.3], no definitive values can be found because the statistic is very poor; maybe there is a center of scattering around x=0.4 formula units. At y=]0.3;0.6], a strong scattering is visible in the region of x=0.4 and 0.65 formula units. In the following, I will discuss the assumption that the T$_C$ vs La curve might only be describable in the first or zeroth order by a parabolic curve, but actually exhibits a finer structure upon close investigation.

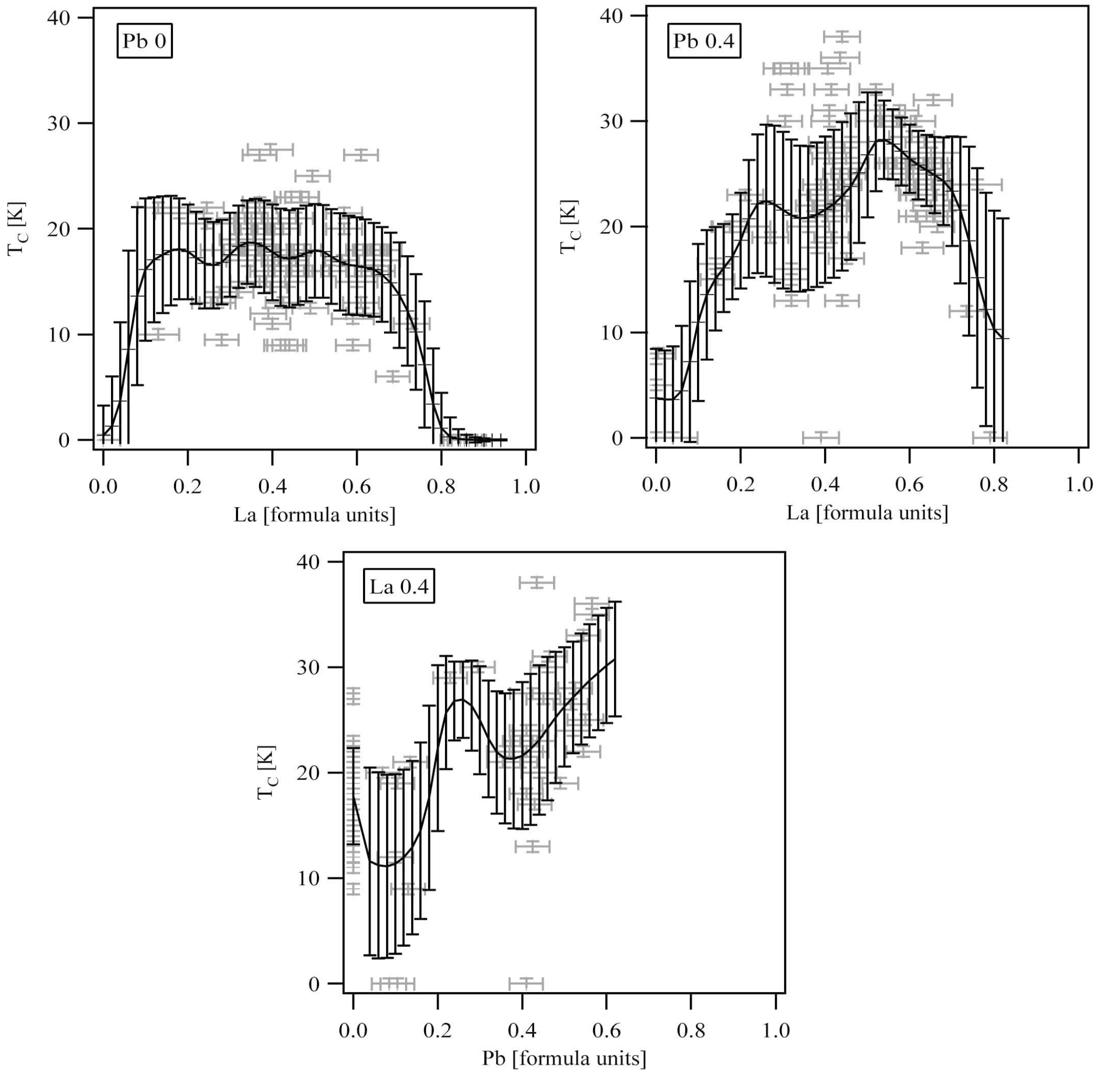

Figure 4.3: Averaged filtered dataset for the regions Pb0 **(upper left)**, Pb0.4 **(upper right)** and La0.4 **(lower middle)** together with the original data (light grey).

4.1.1 Depressions in T_C

Because of the high number of data points, it is possible to apply some statistical routines to gain a deeper insight into the true three-dimensional T_C vs La and Pb phase diagram. The relevant averaging algorithm relies on a Gaussian probability distribution and is described in Appendix B.1. For the compositional-restricted dataset, Fig. 4.2 shows the average T_C and the probability Z in logarithmic scale of having a sample with the content (x,y) in the dataset. The higher the value for Z, the more samples were characterized in this region. I will now define three series. There are strongly statistic-relevant data in the series {y=0} (Pb0). The series {y≈0.4} (Pb0.4) has a weaker statistic. For the series {x≈0.4 ; y≈0-0.5} (La0.4), the weakest statistic relevance can be expected. The question of which way the structural quality of the series La0.4 is affected by the Pb substitution level was discussed in Chapter 3.4. There it turned out that, in around 0.2 to 0.3 of Pb substitution, a high inhomogeneous phase mixture is present. In the mentioned chapter it was also shown that the Pb0.4 region represents its own structural system and can be viewed from the microstructural analysis as an almost undisturbed system.

Fig. 4.3 shows the averaged compositional-restricted dataset for the series Pb0, Pb0.4 and La0.4 together with the original data. From La0.4 (right), it is quite clear that the T_C^{max} increases generally with increasing Pb content. Note that in La0.4 the region of Pb content y≈0.1-0.3 has low probability (see right panel of Fig. 4.2). Reminiscent of the inhomogeneous phase mixture around this region, this resembles the fact that the crystals are not likely to grow in this region. From the averaged T_C of Pb0 (left) and Pb0.4 (middle), a reduction of T_C, but still not a strict parabolic curve, is visible. The reduction takes place for Pb0 at La concentration of x≈ 0.25±0.02; 0.43±0.02 and 0.58±0.02 formula units. For Pb0.4, a depression can be seen at x≈ 0.4±0.02 and 0.62±0.02 formula units and possibly at x≈ 0.28±0.04. These are, of course, the same Lanthanum contents; the strong scattering was seen in the original data. But because of the high variance, it cannot be easily concluded that a finer structure exists in the parabolic curve.

The following only deals with samples without Pb as this dataset allows more reliable statistical interpretation. The dataset in this region filtered by the compositional restriction contains 82 samples. One interesting question is whether the form of the curve on the upper-left side of Fig. 4.3 is strongly dependent on the ensemble. Whether the ensemble is representative or not can, of course, never be determined. What can be done is to change the magnitude of the dataset representing an ensemble and compare the changes based upon that. On the left side of Fig. 4.4, the dataset, which was sorted by a 'best' ΔT_C-criterium in addition to the compositional reduction, is shown. This 'best' ΔT_C-criterium is performed by selecting the sample with the lowest transition width ΔT_C compared to the other samples present in the same La-content slot. The slots had a width of $\Delta x = 0.02$ formula units. In this way, the dataset is reduced to 27 samples[2]. One large contribution in the transition width ΔT_C comes from the level of uniformity for the composition. It might therefore be reasonable to assume that samples with a sharper transition width are structurally better and have a better compositional uniformity also below the scale of the typical area measured by EDX. In a way, it might be that by this restriction the samples have the best superconducting properties. On the right side of Fig. 4.4,

---

[2] Please note that not all slots could be populated in the high and very low La region

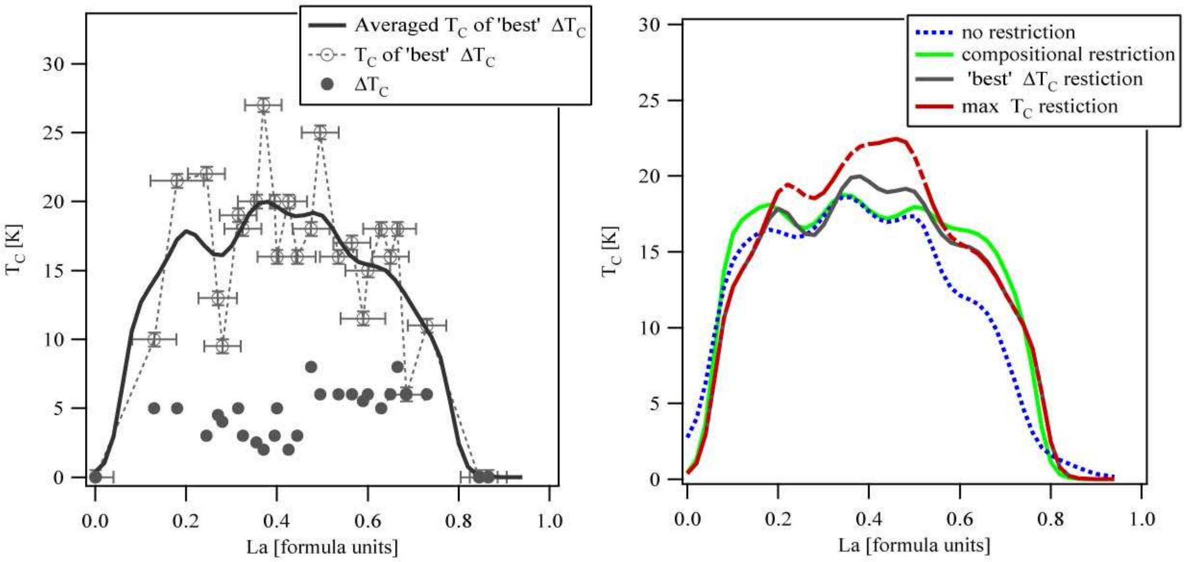

Figure 4.4: **Left:** The ΔT_C-criterium reduced dataset. The solid line represents the averaged T_C. The open symbols indicate the T_C's and the filled circles the ΔT_C's. **Right:** Comparison of the averaged T_C for the dataset without any restriction (blue dotted line), the dataset with the compositional restriction (green solid line), the 'best' ΔT_C reduced dataset (dark grey solid line) and the maximum T_C reduced dataset (red dashed line).

the averaged T_C for the ΔT_C-criterium reduced dataset can be compared to the dataset with the compositional restriction. Also shown there is the averaged T_C for all characterized samples without applying any restrictions. For comparison, this dataset contains 139 samples. Lastly, also shown is the averaged T_C of reducing the dataset with the compositional restriction further by taking only the samples with the maximum T_C in each slot of the width of $\Delta x = 0.02$ formula units, which is another way to guarantee good superconducting properties within the samples. From all the averaged T_C-curves on right side of Fig. 4.4, it can be seen that the La-T_C-curve changes slightly but *always* shows depressions at about the same Lanthanum concentrations.

4.1.2 The influence of the extra Oxygen

When accepting these depressions as real, it is necessary to discuss the changes which result from extra Oxygen content. This Oxygen might be non-uniformly distributed and is an uncontrollable parameter. The answer is complicated by the fact that until now the extra Oxygen content and its influence on the structural behavior has barely been detectable. But a strong indication that the form of the T_C vs La curve is at least not strongly influenced by non-uniform-distributed Oxygen comes from the author's own heat treatment tests. Generally, for samples of Bi_2Sr_{2-x}-$La_xCuO_{6+\delta}$, it appears that a heat treatment at T=650°C under flowing Oxygen up to 50h typically affects the transition width ΔT_C the most and only slightly affects the T_C. Only in crystals with low La concentration < 0.3 is the T_C changed strongly due to the heat treatment. This is suggested to be the reason why in Fig. 4.1 at Pb=]0;0.3] and Pb=]0.3;0.6] for x=0 some samples with higher T_C exist. It might also be that, for the 'as grown' samples used here, at 'high enough' La concentrations the incorporation of extra Oxygen is solely determined by the defective structure produced by the La concentration and can only be changed very slightly by the heat treatment. It might be that this heat treatment can only reduce 'non-artificial' defects, i.e. defects other than the inherent superstructure.

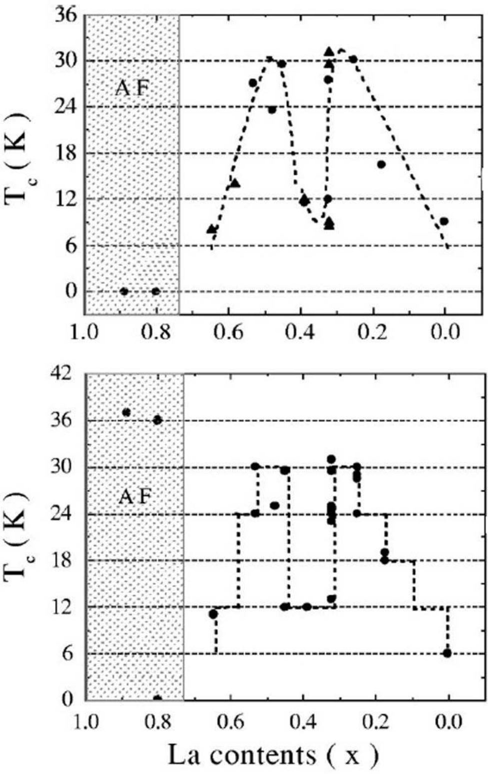

Figure 4.5: From Yang et al. [175]: **Upper panel:** Doping dependence of T_C for deoxidized $Bi_2Sr_{2-x}La_xCuO_{6+\delta}$ crystals. The circles and upward triangles are T_C values measured on samples that are annealed in flowing N_2 at 700°C for 360 h and Ar at 680°C for 40 h, respectively. **Lower panel:** Doping dependence of T_C for oxidized samples that are annealed in flowing O_2 at 680°C for 10 h. Please note the drop of T_C at $x \simeq 0.4$.

In thin films of $Bi_2Sr_{2-x}La_xCuO_{6+\delta}$ Li et al. [179] found that the supermodulation wave vector component q_b only changes remarkably at low La-concentrations due to different oxygenation. The supermodulation wave vector component q_b can be seen as directly proportional to the Oxygen content [155, 156, 180]. For single crystals of $Bi_2Sr_{2-x}La_xCuO_{6+\delta}$, there is an interesting contribution by Yang et al.[175]. The result is depicted in Fig. 4.5. It shows the T_C vs La curve for single crystals of $Bi_2Sr_{2-x}La_xCuO_{6+\delta}$. The T_C was determined by measuring the dc magnetic susceptibility and taking the onset T_C definition. The La was calculated from the nominal La content using the relation given in [135]. This dependence is equal to the dependence of the samples used here. Referring back to the figure, two interesting features are visible; First, there is also a drop in T_C at about La concentrations of x=0.4. Second, there is a change of the T_C vs La curve upon heat treatment. The upper panel shows the T_C vs La concentration curve for 'deoxidized' $Bi_2Sr_{2-x}La_xCuO_{6+\delta}$ crystals. Here, deoxidization means that the samples were annealed in flowing N_2 at 700°C for 360 h or in flowing Ar at 680°C for 40 h. The lower panel shows the T_C vs La concentration curve for oxidized samples which were annealed in flowing O_2 at 680°C for 10 h. As shown, the form of the curve and also the drop at x=0.4 do not change dramatically. It can be concluded here that indications exist from which it may be reasonable to treat the changes made by a non-uniform extra Oxygen as minor changes when talking about La concentrations in the region of x=[0.3;0.7].

4.2 Consideration of the hole content

4.2.1 Overview of recent methods

The methods for determining the exact value of the hole content of the CuO_2-plane shall be discussed in more detail. For the hole-doped high-temperature superconductors $La_{2-x}Sr_xCuO_{4\pm\epsilon}$ (LSCO), the method to determine the hole-content is very simple. Under correct annealing conditions (see, e.g., [181]), this material has nearly a stoichiometric amount of Oxygen. Therefore, merely determining the value of x gives the hole content p. In the Bi2201 system, the situation is more complicated because the extra Oxygen cannot be easily determined, e.g., by energy dispersive x-ray analysis (EDX). It can be measured by titration measurements (see, e.g., [182, 183, 184]), thermogravimetry and gas chromatography (see, e.g., [185] for $YBa_2Cu_3O_{6.5+\delta}$), but these methods require high amounts of clean single-phase material. The mixed valence of Bi and Pb is also a problem when determining the true hole content of the CuO_2-plane. In the two-layer compound $Bi_2Sr_2CaCu_2O_{8+\delta}$, indications were found [186] that Bi exists in the reduced valence $Bi^{(3-\epsilon)+}$ and, therefore, the crystal may *self-dope* the CuO_2-plane by the amount of ϵ holes. Within this context, it also important to note that, in polycrystalline $Bi_{2.12}Sr_{1.86}Cu_{1.02}O_y$ [187], not only the Cu valence changes with the Oxygen content y, but also the Bi valence.

In principle, two methods exist for determining the hole content: One involves measurements relative to the composition and comparing these measurements afterwards. The comparison can either be done with a 'universal curve' or a material where the results of the measurements can be directly related to a hole content. The other method is to measure the valence of the Cu itself or its response in a more direct way.

The first method often uses a 'universal bell-shaped curve' found for $La_{2-x}Sr_xCuO_{4\pm\epsilon}$ by Presland et al. [7]. This curve is given by the formula $T_C/T_C^{max}=1-82.6\,(p-0.16)^2$. For thermopower measurements, the comparison with this curve leads to the Obertelli-Cooper-Tallon (OCT) law[188], where for all cuprates the room-temperature thermopower vs T_C/T_C^{max} should fall on the same curve. Unfortunately, the OCT law is not a consensus; in LSCO itself, reports of violation already exist [189]. Also, in thin films and ceramics of $Bi_2Sr_2CuO_{6+\delta}$ the OCT law does not appear to be completely accepted [190]. In single crystals of $Bi_2Sr_{2-x}La_xCuO_{6+\delta}$ there is also a controversy; One report by Ando et al. [178] informs that the OCT law does not hold, while the study by Dumont et al. [191] showed a partial adherence. The latter found two branches in the thermopower vs La substitution graph where one branch follows the OCT law and the other does not. However, in the publication of Ando et al. [178], the hole content in single crystals was estimated by comparing the normalized Hall-coefficient of $Bi_2Sr_{2-x}La_xCuO_{6+\delta}$ to LSCO. This comparison also leads to a 'bell-shaped curve' for $Bi_2Sr_{2-x}La_xCuO_{6+\delta}$, but not the 'universal bell-shaped curve'. The curve shows a faster drop in the underdoped and overdoped regime. Therefore $Bi_2Sr_{2-x}La_xCuO_{6+\delta}$ is already non-superconducting below $p < 0.1$ holes per Cu, which is in this scaling equal to an La content of about $x = 0.8$. The authors give the dependence $p = 0.21 - 0.13\,x$ for $Bi_2Sr_{2-x}La_xCuO_{6+\delta}$ in the substitution range $0.23 \leq x \leq 0.84$. To complete the description of this method, it is important to add that differences exist between the hole-content per CuO_2-plane and the three-dimensional hole-content as pointed out by Honma et al. [192].

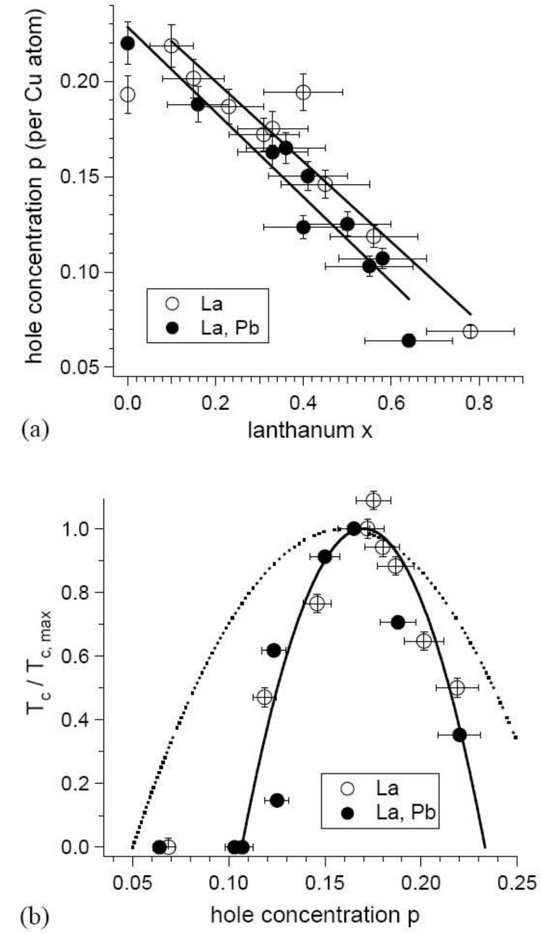

Figure 4.6: From Schneider et al. [142]: **(a)** Hole concentration p vs La content of $Bi_2Sr_{2-x}La_xCuO_{6+\delta}$ and $Bi_{2-y}Pb_ySr_{2-x}La_xCuO_{6+\delta}$, as determined by XAS from the Cu-L_3 absorption edge. **(b)** Relationship between $T_C/T_C^{max}$and the hole concentration p of $Bi_2Sr_{2-x}La_xCuO_{6+\delta}$ and $Bi_{2-y}Pb_ySr_{2-x}La_xCuO_{6+\delta}$. With respect to the 'universal curve' (dashed line) of Presland et al. [7], a faster drop for the samples on the underdoped and overdoped sides can be seen.

The second method might be more straightforward and can be implemented by analyzing the Cu-L_{III} absorption edge measured by the fluorescence or the electron yield in an x-ray absorption spectroscopy (XAS) experiment. Although this method has a problem with the estimation of the correct background, which is very sensitive in affecting the desired result, it has been successfully used for LSCO by Ronay et al. [193], and Merrien et al.[194]. It also works for the two-layer $Bi_2Sr_2CaCu_2O_{8+\delta}$[186, 195, 183] and also for the three-layer compound $Bi_2Sr_2Ca_2Cu_3O_{10+\delta}$[196]. Also, for polycrystalline $Bi_2Sr_{2-x}La_xCuO_{6+\delta}$ and $Bi_{2-y}Pb_ySr_{2-x}La_xCuO_{6+\delta}$, this method was applied by M. Schneider et al. [142], where a 'bell-shape curve' - but not the 'universal bell-shaped curve'- was also found for $Bi_2Sr_{2-x}La_xCuO_{6+\delta}$. The hole scale there differs from the scaling determined by the comparison with the normalized Hall coefficient by Ando et al. [178]. From XAS measurements of [142], Fig. 4.6 shows the hole concentration p vs La content curve of $Bi_2Sr_{2-x}La_xCuO_{6+\delta}$ and $Bi_{2-y}Pb_ySr_{2-x}La_xCuO_{6+\delta}$ and their relationship between T_C/T_C^{max} and the hole concentration p. The relation was given there as $p = (0.24 - 0.21\,x)$ for $Bi_2Sr_{2-x}La_xCuO_{6+\delta}$, and $p = (0.23 - 0.22\,x)$ for $Bi_{2-y}Pb_ySr_{2-x}La_xCuO_{6+\delta}$. It should be noticed here that the Pb-substituted ceramics had a large unsystematic variation in the Pb-content. Recently, the scaling for single-crystals could be obtained by XAS. The crystals used had a more defined Pb substitution level. The scaling of the hole-concentration relative to the La-content for $Bi_{2-y}Pb_ySr_{2-x}La_xCuO_{6+\delta}$ with y≈0.4 was evaluated by Ariffin et al. [176] as $p = (0.22(9) \pm 0.02) - (0.15(6)x \pm 0.05)$

It should also be noted that, as for other cuprates (see, e.g., [197, 198]), it should be generally possible to calculate the hole doping by the normal-state Fermi surface as measured by ARPES. This method accounts for the validity of the Luttinger theorem [199], by which, in the case of no symmetry change of the ground-state, the Fermi surface area for free electrons equals the surface area of interacting electrons. For $Bi_{2-y}Pb_ySr_{2-x}La_xCuO_{6+\delta}$, this method was applied by Kondo et al. [200] and the normal-state Fermi surface area gives a value of holes which is too high. This is in accordance with the author's own results [172], and Hashimoto et al. [201].

4.3 The existence of depressions at certain hole concentrations

In the following, I will show the existence of depressions of T_C. I will start here with a collection of T_C data for LSCO. From this, I will show that depressions are present. Then I will compare the hole positions of these depressions with those from the series Pb0 and Pb04, which were obtained relative to the La-content. I can thereby construct a hole scaling for the unknown amount of holes in $Bi_{2-y}Pb_ySr_{2-x}La_xCuO_{6+\delta}$.

4.3.1 Depressions of T_C in LSCO

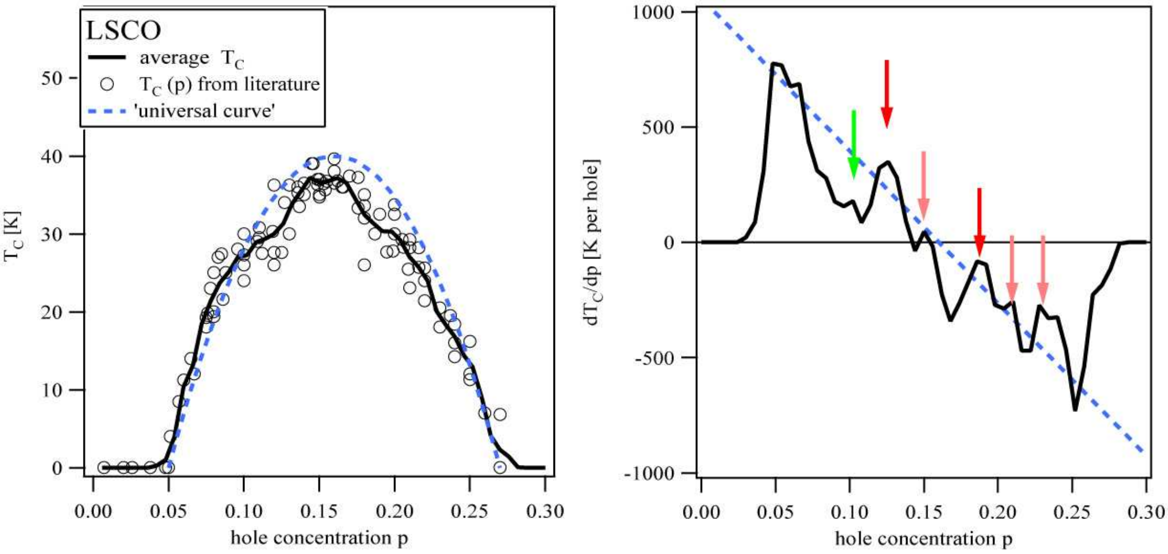

Figure 4.7: **Left:** Experimental T_C and hole doping values for LSCO [202, 203, 204, 205, 206, 207, 208, 209, 210, 211, 8, 212]. The solid line is the averaged curve for all the 98 experimental data points. The dashed curve represents the 'universal curve' [7] with T_C^{max}=40K. **Right:** The first derivative of the average T_C vs p curve. The depressions of T_C at hole dopings of about x=0.1; 0.125; 0.15; 0.185; 0.21; and 0.235 are marked by an arrow. The dashed line is the derivative of the 'universal curve'.

The T_C values for LSCO were derived by resistivity measurements and are taken from [202, 203, 204, 205, 206, 207, 208, 209, 210, 211, 8, 212]. The collected data is shown on the left side of Fig. 4.7. Also depicted is the averaged T_C vs p curve for all the 98 data points. To generate the curve, additional four data points at p=0.27; 0.28; 0.29; and 0.30 with T_C=0 were used. These extra points are used to improve the visualization and can be justified; As for p>0.26 , then no superconductivity is detectable. The average algorithm described in the appendix was used with $\Delta p = \Delta x$ =0.01 and σ_x=0≈0.001. The most remarkable feature of the T_C vs p curve is that it is also not a simple parabola for LSCO. This can be seen compared to the 'universal curve', which is also depicted in the figure and calculated for T_C^{max}=40K.

At certain doping concentrations, a depression of T_C can be seen. The first derivative of the averaged T_C vs p curve is shown on the right side of Fig. 4.7. These depressions can be seen as maxima of $\partial T_C/\partial p$. Specifically, Fig. 4.1 reveals that the depressions manifest themselves as a strong scattering which is artificial for an instability. Due to the fact that, in the literature, typically the maximum T_C achievable is given and due to the assumption of a Gaussian distribution in the averaging algorithm, these singularities are smeared out. In both graphs of Fig. 4.7, the depressions are marked by an arrow. They occur at hole dopings of approximately p=0.98; 0.126; 0.15; 0.188; 0.21; and 0.228. The maximum T_C (T_C^{max}) is reached at a doping of about 0.156. The error is estimated at about ±0.005. The depressions at p=0.98; 0.15; 0.21 and 0.228 are weaker and the exact position more uncertain, while the depressions at p=0.126 and 0.188 are more pronounced. There might be even more depressions at the highly underdoped and overdoped sides but the statistic is not sufficient. The bounce visible in the T_C curve, and also in the derivative as an upturn around 0.26, is due to the additionally inserted non-experimental data points. It is worth noting that these depressions are well known; The depression of T_C at hole concentrations of about 1/8 [6] was the first found and is widely accepted. The other depressions agree mostly with the 'magic doping fraction' found in LSCO by Komiya et al. [8]. The construction schema for the 'magic doping fraction' was given by Chen et al. [115] and is based on an SO(5) model. The construction schema was briefly described here at the end of Chapter 2.2.2. These magic doping fractions follow the law $p = (2m+1)/2^n$ where n and m are integers. By comparing with this formula, it might be that the hole doping of the depression can also be written as 3/32;1/8; 5/32; 3/16; 7/32; and 15/64. A comparison for that issue is given in Tab. 4.1. It is important to note that other laws for determining the hole-doping concentrations of the depressions may also be possible.

4.3.2 Scaling by the depressions for Bi2201

As shown in Section 4.1, the Bi2201 crystals used here also exhibit depressions. These depressions are visible in the T_C vs La curve and can be used to scale the hole concentrations. This scaling is, of course, based on the assumption that these depressions must occur at the same doping concentrations as those for LSCO. Fig. 4.8 shows the derivative of the average T_C vs hole concentration curve for LSCO and the derivatives of the average T_C vs Lanthanum concentration curves for $Bi_{2-y}Pb_ySr_{2-x}La_xCuO_{6+\delta}$ for the Pb contents of y=0 and y=0.4. The averages used for the derivatives are the compositionally-restricted average and the max. T_C-restricted average. The max. T_C-restricted average is used because it might better resemble the features produced by a resistivity measured T_C-curve. This is because, in the case of heterogenous samples, by resistivity the path with the highest T_C will be probed. However, by a comparison, the maxima of the derivative of the average T_C-curve of $Bi_{2-y}Pb_ySr_{2-x}La_xCuO_{6+\delta}$ were assigned to these depressions. The assignment is indicated by arrows in Fig. 4.8 and also listed in Tab. 4.1. Due to a low statistic for the Pb content of y=0.4, some maxima of the derivative are more uncertain.

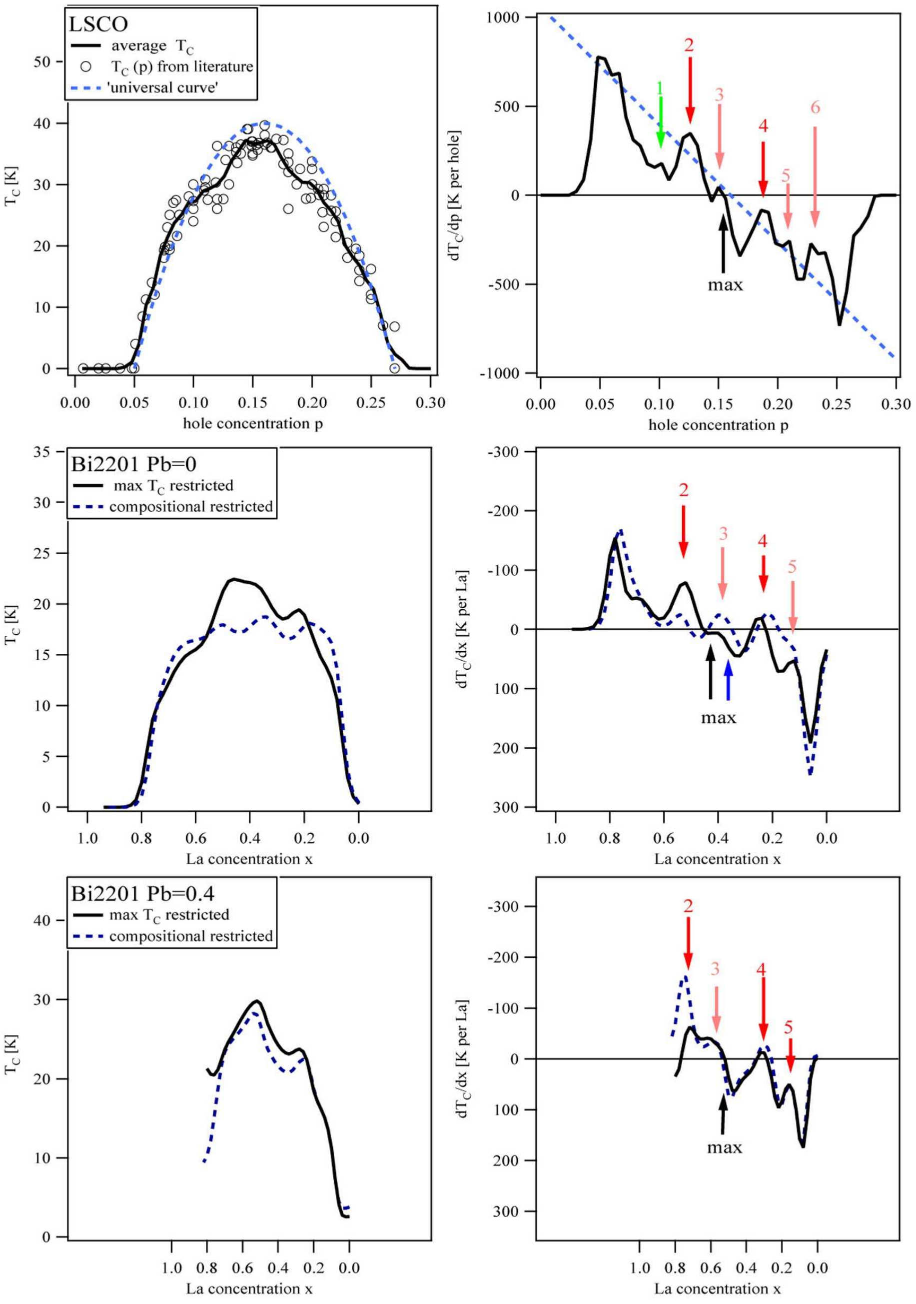

Figure 4.8: The derivative of the average T_C vs hole concentration curve for LSCO **(upper panel)**, and the derivatives of the average T_C vs Lanthanum concentration curves for $Bi_{2-y}Pb_ySr_{2-x}La_xCuO_{6+\delta}$ for the Pb contents of y=0 **(middle panel)** and y=0.4 **(lower panel)**. The derivative of the max. T_C-restricted average is the solid line and the derivative of the compositional restricted average is the dashed line. The assignment to the depressions is indicated by arrows. Also included is the maximum position of the T_C curve. Please compare also with tab. 4.1.

description	label of the maxima of the 1st. derivative						T_C^{max}
	1	2	3	4	5	6	position
LSCO x [holes/Cu] †	0.98	0.126	0.15	0.188	0.21	0.228	0.156
magic fractions [8]	3/32	1/8	5/32	3/16	7/32	15/64	-
as floats:	0.094	0.125	0.156	0.188	0.219	0.234	-
	La content x [formula units]						
Bi2201 y=0 content ‡	-	0.54	0.39	0.22	0.14	-	0.44
Bi2201 y=0 maxT_C‡	-	0.53	0.41	0.25	0.13	-	0.36
Bi2201 y=0.4 content ‡	-	0.75	0.58	0.30	0.16	-	0.53
Bi2201 y=0.4 maxT_C‡	-	0.72	0.58	0.31	0.16	-	0.52

Table 4.1: From top to bottom: The depressions found in LSCO. For the labels, please compare with Fig. 4.8. The comparison to the 'magic doping fractions'. The positions in La content of the depressions found in $Bi_{2-y}Pb_ySr_{2-x}La_xCuO_{6+\delta}$ for the different averaging methods. On the right column the T_C^{max} position of every curve is written.
†: error estimated as ± 0.005 holes/Cu. ‡ for individual error estimation please compare with Fig. 4.9,

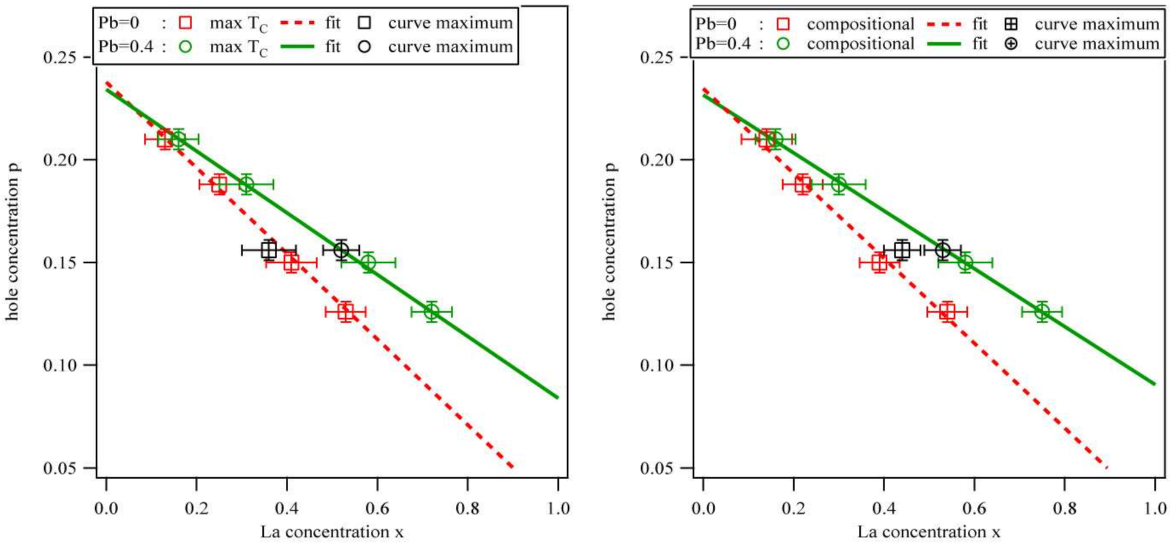

Figure 4.9: The Lanthanum concentration of the maxima in first derivatives for both restricted averages vs the hole doping of the maxima found in LSCO. Please compare with Tab. 4.1. On the left side, the maximum $T_C$restricted average is shown for Pb content of y=0 (boxes) and 0.4 (circles). On the right side, the same is done for the compositional-restricted average. Also, the positions of the maximum T_C (T_C^{max}) for y=0 and y=0.4 and both averages vs the T_C^{max} position in LSCO are shown. Also included are the linefits for the four restricted averages.

From the different methods described above for considering the hole concentration, one should realize the fact that the Lanthanum-hole scale of M. Schneider et al. [142] and Ando et al. [178] for $Bi_2Sr_{2-x}La_xCuO_{6+\delta}$ differ greatly, but are both linear. It is not a simple question of whether the dependence must be linear or not. This is because the insertion of Oxygen relative to the La concentration is not well examined. For example, in the report by Yang et al. [175], a non-linear dependence is used. For Pb content of y=0 and 0.4, Fig. 4.9 shows the Lanthanum concentration of the maxima of the first derivative for both restricted averages vs the assigned depressions. In consensus with M. Schneider et al. and Ando et al., a linear behavior is also assumed. A linefit yields the following relations for the Pb content y=0:

$$\begin{aligned} p_c &= (0.23(6) \pm 0.01) - (0.20(9) \pm 0.02)\,x, \text{ and} \\ p_m &= (0.23(9) \pm 0.01) - (0.21(4) \pm 0.01)\,x\,. \end{aligned} \tag{4.3}$$

The first formula is the linefit of the maxima of the first derivative of the compositional average while the second is by the max T_C average. p is given in holes per Cu and x is in formula units. Please note the perfect agreement with the measurements of M. Schneider et al. (upper panel of Fig. 4.6). There, the dependence $p = (0.24 - 0.21\,x)$ was obtained for $Bi_2Sr_{2-x}La_xCuO_{6+\delta}$. For Pb content y=0.4, the relations are

$$\begin{aligned} p_c &= (0.23(2) \pm 0.01) - (0.14(1) \pm 0.01)\,x, \text{ and} \\ p_m &= (0.23(4) \pm 0.01) - (0.14(8) \pm 0.01)\,x\,, \end{aligned} \tag{4.4}$$

for the compositional and the max T_C average, respectively. Here, the measurements do not concur as well with Schneider et al. is not so good. As already mentioned, the discrepancy might have its origin in the unsystematic variation of Pb in the ceramics of Schneider et al. [142]. The agreement with the more homogenous single crystals of Ariffin et al. [176] is good. There, the

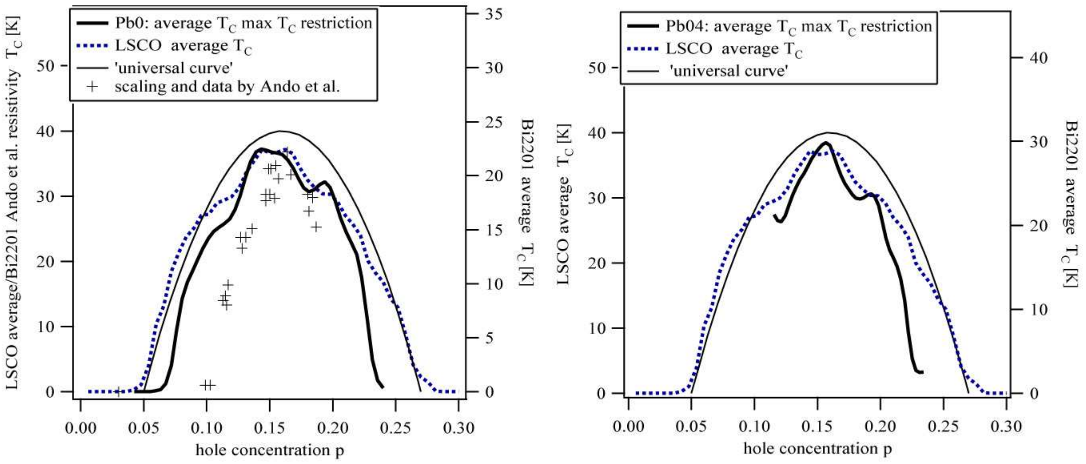

Figure 4.10: Lanthanum hole scaling by the fit from the max T_C average (p_m). **Left:** The scaling of the max T_C average of $Bi_{2-y}Pb_ySr_{2-x}La_xCuO_{6+\delta}$ for Pb content y=0. Also included is the comparison with the scaling and data of Ando et al. [178]. **Right:** The scaling of the max T_C average of Bi_{2-y}-$Pb_ySr_{2-x}La_xCuO_{6+\delta}$ for Pb content y=0.4. For both graphs the T_C-curve for LSCO and the 'universal curve'[7] are also shown.

scaling for Pb content y≈0.4 was given as $p = (0.22(9) \pm 0.02) - (0.15(6)x \pm 0.05)$.

In Fig. 4.10, the T$_C$ vs hole concentration curves achieved by this scaling are shown. The scaling used is the fit from the max T$_C$ average (p_m). The left side of Fig. 4.10 shows the scaling of the max T$_C$ average of $Bi_{2-y}Pb_ySr_{2-x}La_xCuO_{6+\delta}$ for Pb content y=0 whereas the right side shows the same for the Pb0.4 series. Also included for Pb content y=0 are the comparisons with the scaling and data of Ando et al.. For both Pb concentrations, the T$_C$-curve for LSCO and the 'universal curve' are also shown. With respect to LSCO and the 'universal curve', the curve for $Bi_{2-y}Pb_ySr_{2-x}La_xCuO_{6+\delta}$ with Pb content y=0 shows a faster drop at the underdoped and overdoped sides. For y=0.4 over the region of obtained data, nearly the same picture holds.

4.4 Discussion

To conclude, it was shown that the phase diagram for $Bi_{2-y}Pb_ySr_{2-x}La_xCuO_{6+\delta}$ with y=0.4 and $Bi_2Sr_{2-x}La_xCuO_{6+\delta}$ exhibit depressions at certain Lanthanum concentrations. It was also shown by an analysis of the present data in the literature for $La_{2-x}Sr_xCuO_4$ that depressions of T$_C$ at certain hole dopings exist. The dopings agree mostly with the the 'magic doping fractions' found by Komiya et al. [8]. The depressions were unambiguously proved in the $Bi_2Sr_{2-x}La_xCuO_{6+\delta}$ and in the $Bi_{2-y}Pb_ySr_{2-x}La_xCuO_{6+\delta}$ by assigning the depressions visible in the T$_C$ vs Lanthanum graph to certain dopings. Then it turned out that this assignment gives nearly the exact hole doping vs Lanthanum scaling measured by XAS by Schneider et al. [142] and Ariffin et al. [176]. It is, of course, possible to turn this argumentation around, because a measurement of the hole doping should have more weight than an assignment.

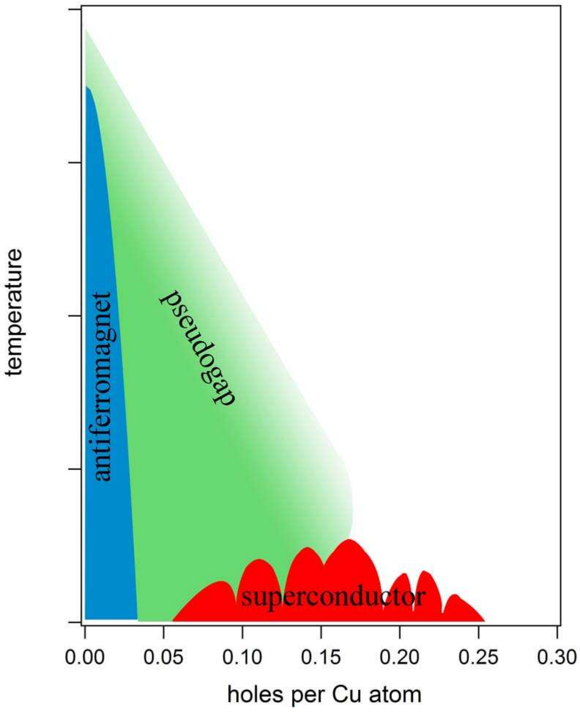

Figure 4.11: Possible generic phase diagram of the hole doped cuprates with the inclusion of the depressions in T$_C$.

Therefore, the existence of depressions is proved for two cuprate systems: LSCO and Bi2201. Considering the fact that the CuO_2-plane in $Bi_{2-y}Pb_ySr_{2-x}La_xCuO_{6+\delta}$ with y=0.4 exists in a different structural environment than in $Bi_2Sr_{2-x}La_xCuO_{6+\delta}$, we might state that two-and-a-half cuprate systems show depressions. It is known that in $YBa_2Cu_3O_{7-x}$(YBCO) the '60K plateau' and a '90K plateau' exist [173]. The first one can be associated with 1/8 hole doping [174]. Also, the cuprate $La_{2-x}Ba_xCuO_4$ has the 1/8 depression. Therefore, I strongly suggest that the existence of depressions is generic within the phase diagram of the hole-doped cuprates.

Fig. 4.11 depicts the purposed generic behavior within the superconducting phase. The attentive reader may have noticed that compared to $La_{2-x}Sr_xCuO_4$, for Bi2201, the T_C vs hole concentration curve is narrow. We will see by resistivity measurements discussed in Chapter 6 that in the underdoped region there might be a suppressed superconducting phase. I suggest that the suppression occurs due to structural factors. Therefore, this feature is a speciality of Bi2201 and not incorporated into the generic phase diagram. Here, it is important that the depressions show up within the accessible superconducting region.

For discussing the ground state at the depressions, it is known that near 1/8 the magnetic properties of $La_{1.6-x}Nd_{0.4}Sr_xCuO_4$ [10] and $La_{2-x}Ba_xCuO_4$ [11] are consistent with static stripes. It is important to note that this evidence of stripes was achieved by neutron scattering. Because neutrons have no charge, they do not scatter directly from the modulated electron density. Instead, they are scattered by the ionic displacements induced by the charge modulation. Results on $La_{2-x}Ba_xCuO_4$ by charge-sensitive resonant soft x-ray scattering (RSXS) revealed that the charges also order at 1/8 [12, 13]. It can therefore be suggested, that each of these depressions describes a charge-ordered and spin-ordered ground state whereas it does not seem certain to me whether this electronic ground state is two-dimensional or one-dimensional, e.g. a kind of Wigner hole crystal or that of static stripes (see also discussion in [13]). Because the doping values of the depressions agree well with the 'magic doping fractions' given in [115, 8], I suggest a two-dimensional pattern of the ground state. In any case, these ordered structures are static; I do not propose that they are conducting or even superconducting. For stripes, perfect static charge order can be shown to be incompatible with the metallic behavior of the cuprates [111, 9]. For the superconducting properties, this is exactly what we see in the T_C vs hole concentration curves: A non-superconducting ground state at a depression. As T_C was derived here by the onset of diamagnetic behavior, let me add that, at a depression, the in-plane resistivity shows for $T \rightarrow 0$ an insulating behavior. This will be shown in the context of the pseudogap in Chapter 6.

It can now be asked whether it is possible to directly see this ordered state and which characteristic temperature belongs to the onset of ordering. Also, what the existence of these depressions means for the superconducting state of the cuprates is an important question which must be addressed.

V

Nanoscale two-dimensional modulations as probed by STM

In the last chapter, I showed the existence of depressions within the superconducting dome. In the conclusion it was suggested that, at the dopings of the depressions, a kind of static order exists within the CuO_2-plane.

One interesting feature in the Bismuth-cuprates is the existence of an inhomogeneous background in STM data (see, e.g., [213, 15]). This background measured at low temperatures is ordered. This was found for $Bi_{1.75}Pb_{0.37}Sr_{1.86}CuO_{6+\delta}$ measured at T=4.6K [18], for example. For the optimally doped two-layer $Bi_2Sr_2CaCu_2O_{8+\delta}$, a nondispersive '4x4 order' was found at low bias and at temperatures below the pseudogap-temperature [17]. Findings of ordered patterns of similar dimensions in the non-superconducting compound $Ca_{2-x}Na_xCuO_2Cl_2$ supported the idea that electrons within the pseudogap phase organize themselves into checkerboard patterns [16]. Therefore, this kind of electronic ordering might present a fascinating possibility for explaining the existence of the found depressions.

In this chapter, I will discuss results of topological scanning tunneling microscopy (STM) on a nanoscale. The background in $Bi_{2-y}Pb_ySr_{2-x}La_xCuO_{6+\delta}$, as well as in $Bi_2Sr_2CaCu_2O_{8+\delta}$, is examined at a rather high temperature - at room temperature. Chapter 6 will show that, for the samples used here, room temperature is well above the (lower) pseudogap-temperature. It can be argued that, at the high measured temperatures, electronic ordering is suppressed. Nevertheless, I will show that two-dimensional modulations are present in the local density of states and characterize them. It will be strongly suggested that these modulations are comparable in their dimensions to the modulation found for $Bi_{1.75}Pb_{0.37}Sr_{1.86}CuO_{6+\delta}$ at T=4.6K [18]. The two-layer compound $Bi_2Sr_2CaCu_2O_{8+\delta}$ probed here also shows a two-dimensional modulation which exhibits similarities to the one found in Lead-free $Bi_2Sr_{2-x}La_xCuO_{6+\delta}$. I will argue that this two-dimensional modulation is congruent to the nondispersive 4x4 order which was found at low bias and temperatures.

Therefore, a dependency between the 2d nanoscale modulations found here and the nondispersive 4x4 order can be speculated. In the discussion at the end of this chapter, I will give a suggestion about the origin of the nanoscale 2d modulations found here. It will be proposed that they are not due to an electronic ordering but an interesting structural phenomenon which is possibly caused by dopant-atom ordering. I will also provide a suggestion as to how these modulations can be used to manipulate the ground state at the depressions.

5.1 The nanoscale modulations in Bi2201 due to changing the Pb substitution

5.1.1 Sample characterization

For the STM measurements, samples where taken with a nearly constant Lanthanum content of x=0.4 and the Pb substitution was varied. The compositions relative to the average Pb content of the seven samples discussed here are shown in Fig. 5.1.1 [1] The dotted lines in Fig. 5.1.1 represent the linear least square fits to each composition relative to the Pb substitution y. The fits yield

$$c(Bi) = (1.97 \pm 0.01) - (1.06 \pm 0.05)y \quad ; \quad \chi^2 = 0.0026 \tag{5.1}$$
$$c(Sr) = (1.49 \pm 0.03) + (0.02 \pm 0.11)y \quad ; \quad \chi^2 = 0.0123 \tag{5.2}$$
$$c(La) = (0.40 \pm 0.02) + (0.06 \pm 0.08)y \quad ; \quad \chi^2 = 0.0078 \tag{5.3}$$
$$c(Cu) = (1.15 \pm 0.01) - (0.01 \pm 0.03)y \quad ; \quad \chi^2 = 0.0008\,. \tag{5.4}$$

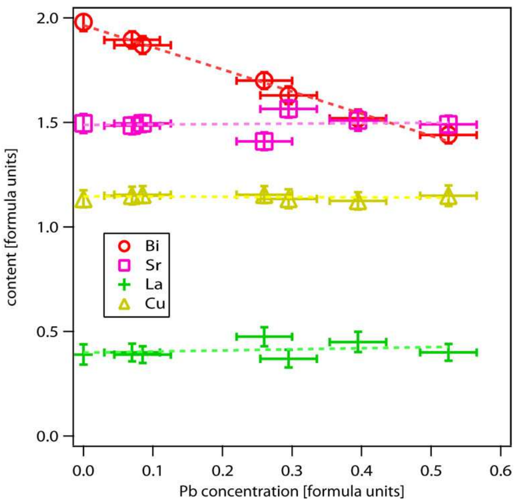

5.1.1: The average composition of the STM measured samples used for the harmonic analysis relative to the average Pb content. The dotted lines represent the linear fits to each composition relative to the Pb substitution y.

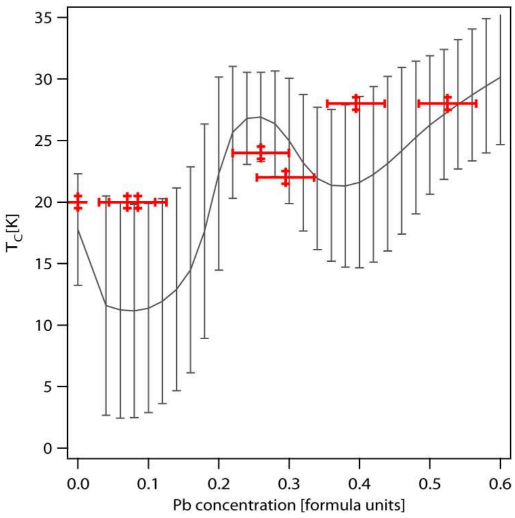

5.1.2: The T$_C$ of the STM measured samples relative to the average Pb content. Also shown is the averaged T$_C$ of the compositional restriction for the constant La content of x=0.4 relative to the Pb content (please compare with Chapter 4.1)

From the fits it is clearly visible that the restriction to a Lanthanum content of x=0.4 formula units is sufficiently achieved. Due to Pb substitution, practically only the bismuth changes while all other compositions remain nearly constant. The T$_C$'s of the samples are shown in Fig. 5.1.2. It can be seen that the samples represent the average T$_C$'s expected within the standard error. Therefore, a highly representative series could be examined.

---

[1] The average composition depicted here is according to Eq. (4.1). The error denoted in the graph is the one calculated according to Eq. (4.2) of Chapter 4.1.

5.1.2 STM data and harmonic analysis

For revealing the existence of two-dimensional modulations, I will show topographic STM data. It will turn out that, in every measured sample, a two-dimensional modulation is present. After some remarks, I will discuss the appearance of this modulation in an example. Then I will comment on and discuss the results of the performed harmonic analysis for all samples.

Sometimes during the measurement a 2d modulation was not pronounced and therefore the bias was changed. The aim of the study was not to find a bias dependency, but to show the presence of 2d charge modulations. For the bias, it can therefore only be stated that it reflects a stochastic value in the region of best visibility of the 2d modulations. However, a suggestion on the probed density of states can be provided. As the measurements were taken typically at high positive bias around 1V, a large contribution comes from the (semiconducting) BiO-plane (see, e.g., [214, 15]). These 2d modulations are existent in the inhomogeneous background. When focussing on subatomic resolution, on the BiO-lattice, the appearance of the modulation was weak. Therefore, I suggest the 2d modulations to be localized below the BiO-plane.

As the two-dimensional modulations were found to be buried in the low background beside the atomic lattice, no samples could be used within the Pb substitution range from y=0.1 to 0.26 formula units. Compared with the previous findings as discussed in Chapter 3.4, this is because the distortion of the STM signal by the 'bright linear objects' is very high in the Pb region from 0.1 to 0.3. These bright linear objects were produced within the BiO-plane by the substituted Pb atoms. For Pb substitutions higher than y=0.26, the topological STM data comes from the smooth β-phase where effects of the topmost BiO-plane are expected to be low.

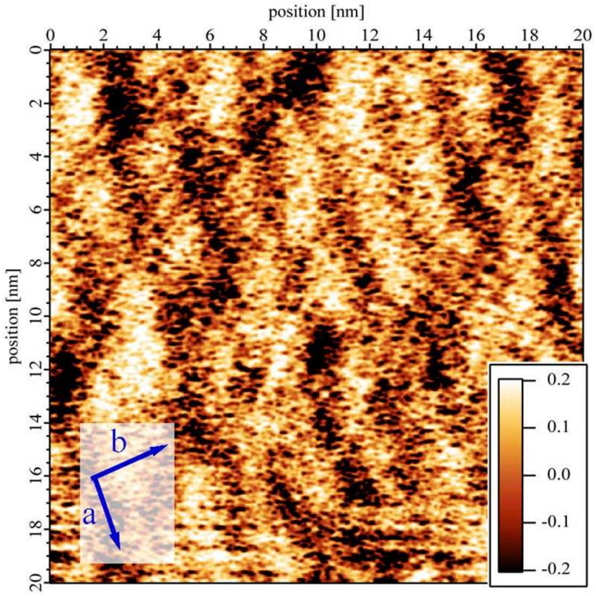

Figure 5.1: Topographic STM measurement of $Bi_{1.98}Sr_{1.5}La_{0.39}Cu_{1.14}O_{6+\delta}$, (20x20)nm^2, RT, 1 V, 0.5 nA. Black lines representing the superstructure are visible. Additional blurred bright 'bubbles' are present.

I will present an example of the 2d modulations. Fig. 5.1 shows the normalized topological data of a Pb-free sample. The parameters are written below the figure. The normalization is described in Appendix B.2. We can see black lines running along the a-axis. These black lines are the ridges of the one-dimensional ≈1x5 superstructure. However, we can also see blurred pale 'bubbles' near these ridges. An order of these bubbles can already be suggested.

For examining the periodic corrugation of the data, results of a harmonic analysis will be shown in the following. Here, the analysis was done by the unbiased autocovariance which can also be called the correlogram technique. For basic definitions, please see Appendix B.2. The autocovariance is a normalized convolution of the spatial data with itself but shifted by a distance. Plotting the resulting autocovariance vs this shifting, the modulations will reveal themselves by maxima at multiples of its wavelength.

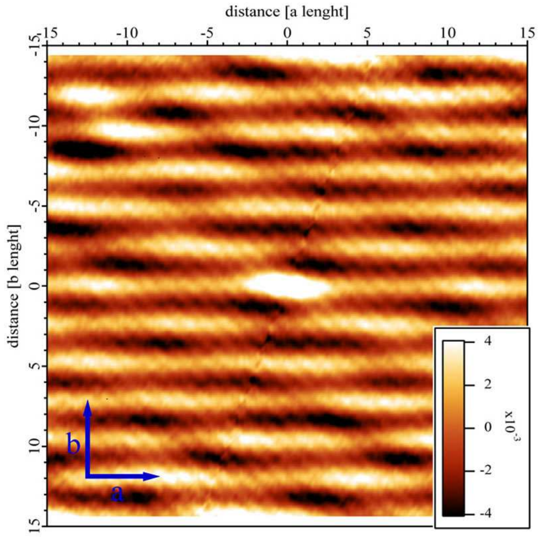

5.2.1: Fragment of the unbiased autocovariance of Fig. 5.1. When counting from (0,0) the horizontal lines, every even line represents the ≈1x5 superstructure. However, odd horizontal lines are also present. On the horizontal lines, bright bubbles appear. These bubbles represent the two-dimensional modulation.

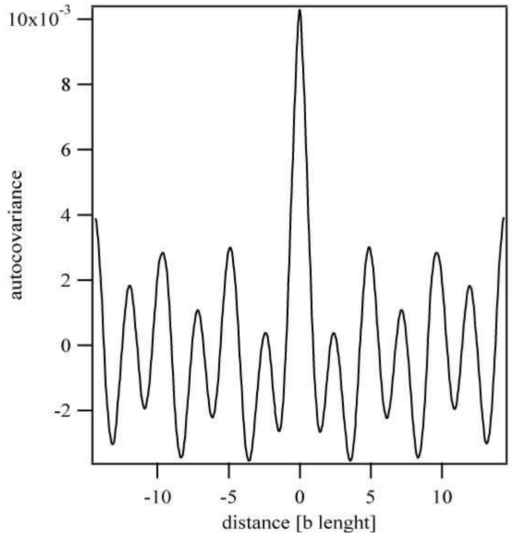

5.2.2: The autocovariance of Fig. 5.2.1 averaged over the a-direction.

Fig. 5.2.1 shows the autocovariance processed on the STM pattern of Fig. 5.1. In addition to a weak atomic grid[2], bubbling horizontal lines are visible. Counting from (0,0), every *even* horizontal line represents the one-dimensional superstructure which is well known from x-ray diffraction experiments. Here, the distance between two even horizontal lines is given as $\vec{r}_{SS}$=4.8$\vec{b}$ which fits well with the known value of the superstructure (see, e.g., [215]). However, the additional *odd* horizontal lines are particulary remarkable. These have about half the distance of the superstructure but a wavelength corresponding to this superstructure was not refined in other experiments like x-ray diffraction or transmission electron microscopy. It is important to point out that half a distance in autocorrelation cannot be simply produced as a kind of higher order. In fact, the horizontal lines are a product of two kinds of modulation. To reveal the differences more clearly, Fig. 5.2.2 shows the autocovariance of Fig. 5.2.1 averaged over the a-direction. One sees two different intensities of the shown pattern. The odd peaks are produced by a modulation with about half the wavelength of the even peaks. It is reasonable to explain the pattern by two modulations, which merge their intensities at the even peaks. From the existence of bright bubbles and horizontal lines in Fig. 5.2.1, it can be concluded that the modulation structure consists of a one-dimensional and a two-dimensional modulation. They can

[2] The atomic grid can be seen by thin lines running at an angle of 45 degrees from the a-axis.

be described as the well-known one-dimensional 4.8×b superstructure plus a two-dimensional modulation with lattice vectors $\vec{r}_1$=-5.4$\vec{a}$+ 2.4$\vec{b}$ and $\vec{r}_2$=-6.5$\vec{a}$-2.4$\vec{b}$. Here $\vec{a}$ and $\vec{b}$ are the vectors of the unit cell. The evaluation of the 2d lattice vectors can be done in Fig. 5.2.1 by taking the connecting line from (0,0) to the next two linear independent 'bubbles'. Please note that, for this analysis, phase information is lost due to the autocovariance. That means that this picture does not provide the placement of the two modulations relative to each other. From Fig. 5.1, it can already be suggested that the 2d modulation is produced by the pale bubbles lying around the ridge of the superstructure. We will later see that, for Bi2212, the relation is more pronounced as a bias adjustment was achieved where the 2d modulated background, as well as the atomic lattice, can be reproduced.

In the following, I will present the harmonic analysis for all measured samples. I first want to discuss the analysis qualitatively, then I will quantify and discuss the results. All autocovariances of the applied STM data are shown in Fig. 5.2 and Fig. 5.3. Below each figure is the Pb level, the size of the original STM pattern and the bias. In every autocovariance, a two-dimensional modulation can be stated. Let me comment on the autocovariances upon changing the Pb substitution:

For low Pb content, the 2d modulation was found to be well-ordered. Its prototype is the crystal without Lead which was already shown here. Its autocovariance is repeated in Fig. 5.3.1. As discussed, one can see clearly the 1d superstructure as horizontal lines. However, the 'bubbles' are also present which indicate a 2d modulation. For the Pb-free sample, the bubbles are oval. When we go to slightly higher Pb substitution, e.g., as depicted in Fig. 5.3.2 or Fig. 5.3.3, we see circle-like shapes. An interpretation of this behavior is that the spread of the 2d modulation along the ridges of the superstructure (along the a-direction) is energetically favored. In the b-direction, the 2d modulation is more localized and its spots somehow pinned. For the pinning, let me again refer back to Chapter 3.4 where it was shown that, at low Pb substitutions, the superstructure is decorated with Pb atoms. This decoration forms the 'bright linear objects' along the superstructure. It may be that these bright linear objects smear out the ridges and it might be that the pinning of the 2d modulation on the superstructure is thereby reduced. This reduction causes more circle-like bubbles. Overall, I conclude that, for no Pb substitutions, the 2d modulation is orientated by the ≈1x5 superstructure. This is also the case for low Pb substitution. But as more Pb clusters, the more the dependency of the 2d modulation on the superstructure is reduced.

In the case of higher Pb substitution levels than around 0.25, it is known from Chapter 3.4 that the one-dimensional superstructure is no longer present. The absence of an order-introducing superstructure allows the 2d modulation to equalize their lattice vectors; In the low-Pb autocovariances the order is rectangular, whereas in higher Pb-substituted samples the order is nearly quadratic. An example is the comparison of the autocovariance at y=0.08 in Fig. 5.3.3 to y=0.4 in Fig. 5.4.1. At these high substitution levels, the 2d modulations are not necessarily oriented along the a-axis and b-axis. This can clearly be seen in Fig. 5.3.4. Furthermore, since the modulations represent a 'crystalline state', it sometimes appears if there are twins or more than one phase. A good example for this is the autocovariance of the sample with y=0.5 as depicted in Fig. 5.4.3. There, at least two bubble patterns of different intensities exist, which indicates more than one 2d modulation. Overall, the behavior is clearly a continuation of the behavior at low

Figure 5.2: Results of the harmonic analysis I

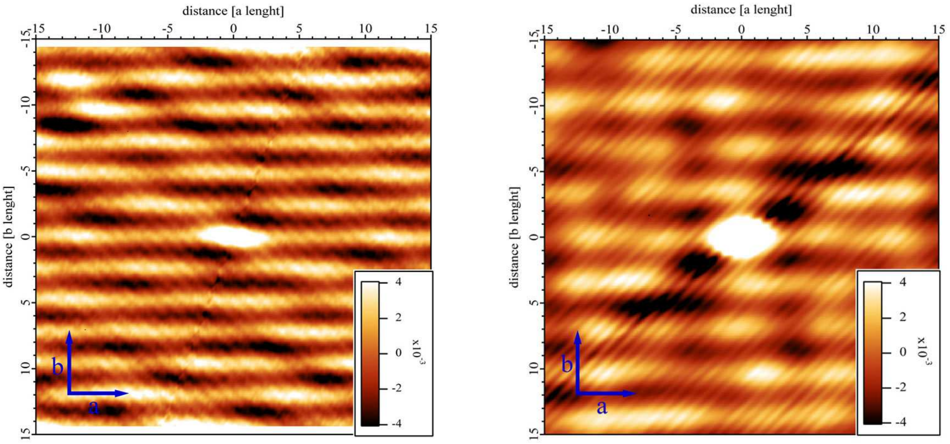

5.3.1: Pb y=0, (20x20)nm^2, 1 V

5.3.2: Pb y=0.07, (30x30)nm^2, 1.816 V,

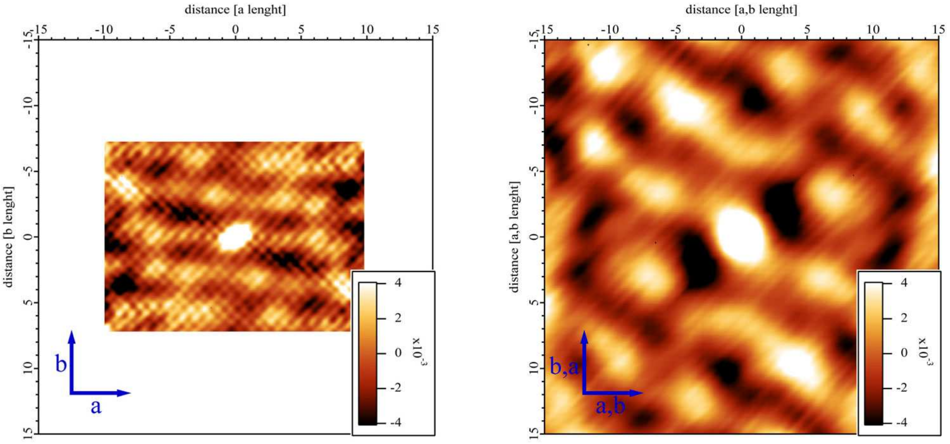

5.3.3: Pb y=0.09, (10x10)nm^2, 0.929 V

5.3.4: Pb y=0.26, (20x20)nm^2,1.071 V

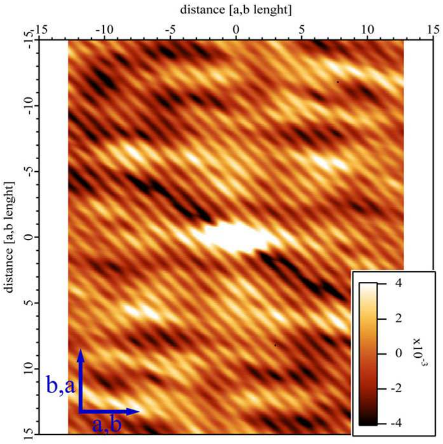

5.3.5: Pb y=0.30, (20x20)nm^2, 1.286 V

Figure 5.3: Results of the harmonic analysis II

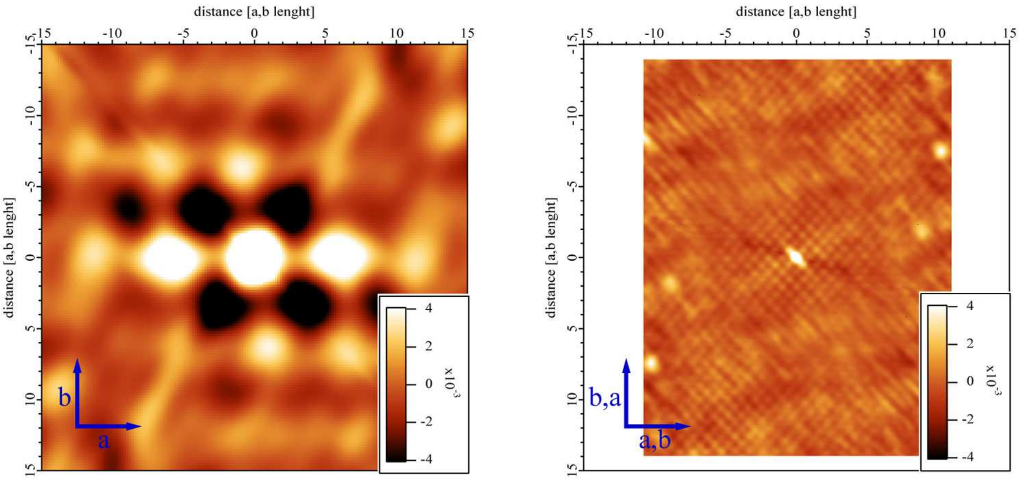

5.4.1: Pb y=0.40, (50x50)nm^2, 0.500 V

5.4.2: Pb y=0.40, (20x20)nm^2,0.027 V

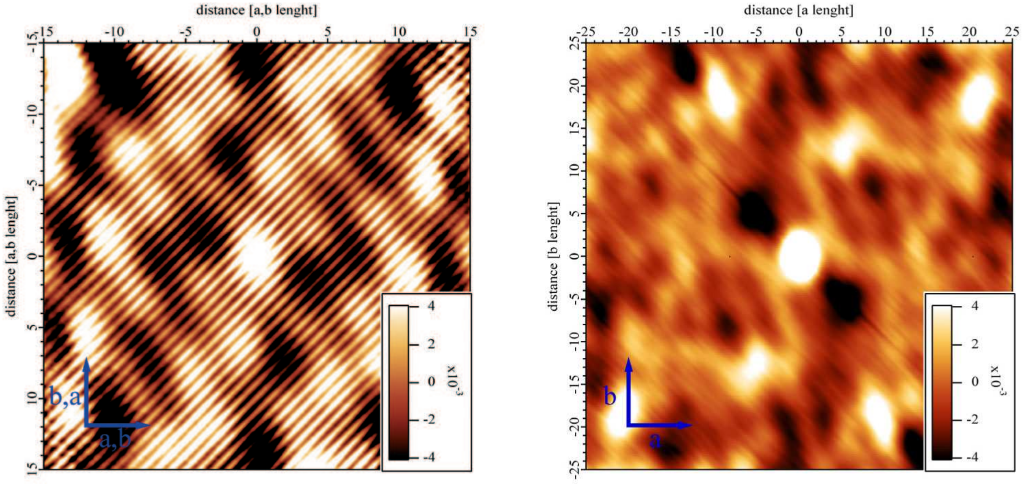

5.4.3: Pb y=0.53, (20x20)nm^2,1.185 V

5.4.4: Pb y=0.53, (50x50)nm^2,1.185 V

Pb; The ordering superstructure is absent, and therefore the tendency to disorder is enhanced. The orientation in respect to the a-axis and b-axis might be determined in this concentration range by other crystallization seeds than the superstructure.

Let me sum up these qualitative findings: At low Pb substitution we found a well-ordered 2d modulation which is controlled by the superstructure. In samples of high Pb substitutions, the present 2d modulation(s) is/are poorly ordered.

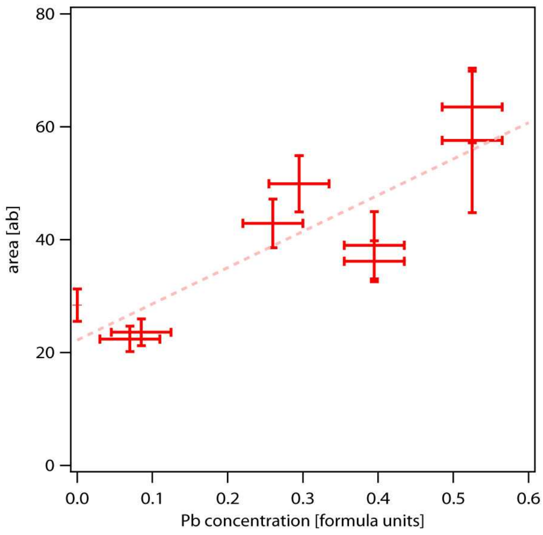

Figure 5.4: The area spanned by the lattice vectors of the 2d modulations vs Pb substitution.

Here, I will provide a quantification of the 2d modulations; Let us think of them as being produced by a crystalline state. It is possible to evaluate the lattice vectors. As the orientation of the 2d modulations changes, the best quantity is the area spanned by the lattice vectors. This area can be considered as the primitive unit cell of the crystalline state. For the purpose of calculating the area, let me note that there is no back-transformation from the autocovariance to the STM patterns. For example, this means that, when there are two modulations in two well-separated regions of the STM pattern, its autocovariance may look the same as the autocovariance of two modulations merged in one and the same region. For the samples with y=0.08 and y=0.30, it could be verified that the two 2d modulations come from different regions of the STM pattern. In the case of these two modulations being present and distinguishable, the average area was calculated by weighting each area with the relative intensity of the two modulations.

The evaluated areas of the 2d modulations relative to the Pb level are shown in Fig. 5.4. The table in Appendix B.3 subsumes all results of the harmonic analysis. The area is given as multiplies of the atomic unit cell area. The error was roughly estimated as 10 % of the area in the cases where an atomic lattice is present and 20 % in cases where it is not. From this graph, we see a clear trend: The area increases with an increasing Pb substitution.

The origin of the 2d modulation can be questioned. In the introduction, I wrote about the possibility of measuring a kind of crystalline hole state by STM - holes somehow ordered within the CuO_2-plane. Here, we are at room temperature and an electronic ordering at high temperatures is not expected. The measurements were taken at positive bias, therefore maxima in the STM patterns would represent high unoccupied density of states. I will argue in the following that the 2d modulations observed here are not produced by holes: In Chapter 4.2, I showed that the hole concentration at Pb content y=0 is given as p=0.24 - 0.21 x, while for Pb content y=0.4

it is p=0.23-0.15 x. Here, the x denotes the Lanthanum-content in formula units. Assuming the hole content is linear with Pb substitution, for the average La content of x=0.40, we get p=0.15(6)+ 0.03(5) y. Therefore, the Pb substitution changes the samples from optimally-doped to slightly overdoped. If we think of our area as the primitive unit cell of a crystalline state, the reciprocal area is the density of crystallized 'particles'. The results show that, with increasing Pb substitution, the density reduces. This is opposite to the behavior we would expect when the 2d modulations are due to holes as the density of holes increases due to Pb substitution. Also, the visibility of the modulations at high bias of about 1V would point in that direction.

Besides the Pb content itself, the quantity which is known to change due to substitution is the Oxygen content. Fig. 5.5 shows the result of an Oxygen content determination by titration on ceramics of $Bi_{2-y}Pb_y$-$Sr_{2-x}La_xCuO_{6+\delta}$ at x=0.4 as a function of Pb content y from Zhang et al. [216]. The total Oxygen content for quenched samples and N_2 annealed samples is depicted there. The curve of the single crystals used here is assumed to be roughly around both these curves. As we can see, the Oxygen content reduces at constant La content due to Pb substitution. Therefore, I strongly suggested that the above-described 2d-modulations are due to excess Oxygen dopants. However, one can easily calculate that the proportionality of the density to the excess Oxygen is not one to one. This could mean that only a certain part of the excess Oxygen forms the 2d modulations. It can be further suggested that the 2d modulations are created by dopant complexes near the SrO-layer. These complexes might be substituted La plus Oxygen, written as $(LaO)^+$ [215, 145], or Bi on Sr sites: $(BiO)^+$. Because of structural and/or electrostatic reasons, these complexes may tend to order.

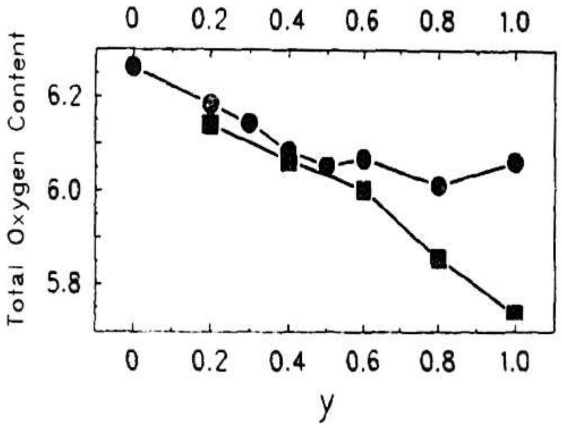

Figure 5.5: From [216]: Total Oxygen content of ceramics of $Bi_{2-y}Pb_ySr_{2-x}La_xCuO_{6+\delta}$ at x=0.4 as a function of Pb content y as determined by iodometric titration. The circles are for quenched samples and the squares for N_2 annealed samples. The solid lines are visual guides.

To briefly summarize the findings here, it can be stated that 2d modulations within STM patterns of the inhomogeneous background are present at room temperature in all examined samples. These modulations are more ordered when the superstructure is present and otherwise tend to disorder and form multiple phases. The 2d modulations were quantified by the area spanned by their lattice vectors. For a crystalline state, the area equals that of the primitive unit cell. The reciprocal of the area is the density of condensed particles. As the density of the modulations decreases and the hole density increases by Pb substitution, the 2d-modulations are not due to the holes. As the density is proportional to the excess Oxygen, it is more likely that the 2d-modulations are produced by dopant complexes involving the Oxygen.

5.1.3 Comparison to other work concerning 2d modulations in Bi2201

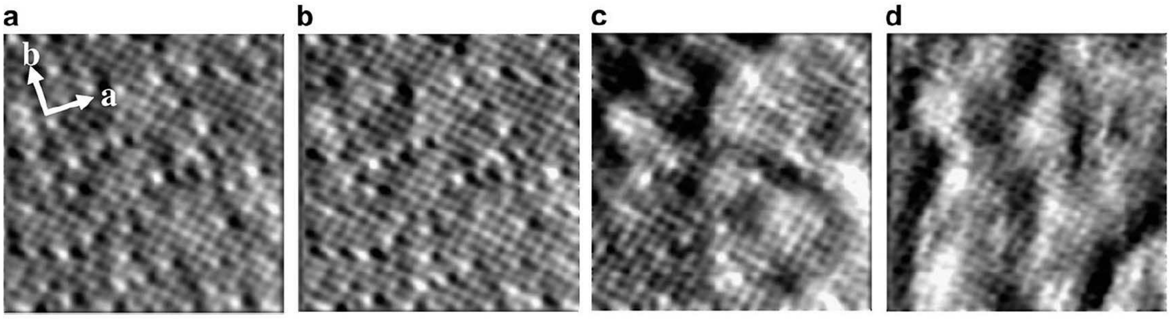

Figure 5.6: From [217]: STM images of the Bi(Pb)–O plane in $Bi_{1.79}Pb_{0.37}Sr_{1.86}CuO_{6+\delta}$ with T_C= 7 K under the bias-voltage (a) 600 mV, (b) 300 mV, (c) 150 mV and (d) 50 mV at T = 4.6 K. The tunneling current is 40 pA. Each image shows an area of 9 nm × 9 nm.

An important question is, whether STM measurements exist which also show 2d modulations on a comparable scale. Most of the topological STM measurements are done at low temperatures. Therefore, in the following I will compare different temperature scales. For most order phenomena within the same phase, we would expect the high-temperature behavior to be superior to the low temperature behavior; As long as no phase transition occurs, a present order stays upon cooling.

Fig. 5.6 shows STM measurements at T = 4.6 K by Kudo et al. [217]. The sample was overdoped $Bi_{1.79}Pb_{0.37}Sr_{1.86}CuO_{6+\delta}$ with T_C= 7 K. The patterns from (a) to (d) were measured at the same position but at a different bias voltage. A bias dependence of the inhomogeneous background relative to the atoms of the BiO-plane is clearly visible. The authors point out that the inhomogeneous background becomes suppressed at higher positive bias. Although it is questionable, whether a comparison between $Bi_{2-y}Pb_ySr_{2-x}La_xCuO_{6+\delta}$ and $Bi_{2+z}Pb_ySr_{2-z}CuO_{6+\delta}$ is reliable, it supports the finding of the previous section; The states of the atomic lattice and the modulated background are not at the same energy.

In another publication by the authors [18], it was shown that this sample exhibits a 2d modulation within the background. This was proven by the autocorrelation of the pattern obtained at a bias of 50 mV and depicted in Fig. 5.6(d). The characteristic lengths of the 2d modulation are given there as $(5.3a_0) \times (10.5a_0)$ where a_0 is the Cu-O-Cu distance. In the notation used here, the area of the lattice vectors can be calculated at about 25 $\vec{a}\vec{b}$. For an optimally doped sample of $Bi_{1.75}Pb_{0.32}Sr_{1.91}CuO_{6+\delta}$ with T_C= 22 K, the characteristic length scales were evaluated by the same authors in [18] as 15.6 Å ($\approx 4.1a_0$) and 23.2 Å ($\approx 6.1a_0$), respectively. In the notation here, the modulation spans an area of about 12 $\vec{a}\vec{b}$.

In conclusion, it can be stated that in $Bi_{2+z}Pb_ySr_{2-z}CuO_{6+\delta}$ there are also two-dimensional modulations present. The difference to the modulations shown before is the type of substitution used and the temperature at which the modulations where measured. The similarities are given in the comparable order of magnitude of the area. Unfortunately, the bias-dependency cannot be compared. However, overall I highly suggest that the modulations are of the same origin. Otherwise one might question how many different modulations within the same lengthscale can be expected in the Bi2201 compound. When we compare the area of the optimally doped $Bi_{1.75}Pb_{0.32}Sr_{1.91}CuO_{6+\delta}$ with the one of the nearly optimally doped $Bi_{1.98}Sr_{1.5}La_{0.39}Cu_{1.14}O_{6+\delta}$ of the last section, we must compare 12 $\vec{ab}$ with 28 $\vec{ab}$. Since both modulations are due to the same origin, they cannot be due to electronic-ordering because both are optimally doped. However, when assuming the modulation is due to dopant-ordering, the area will be different because the method of substitution is different.

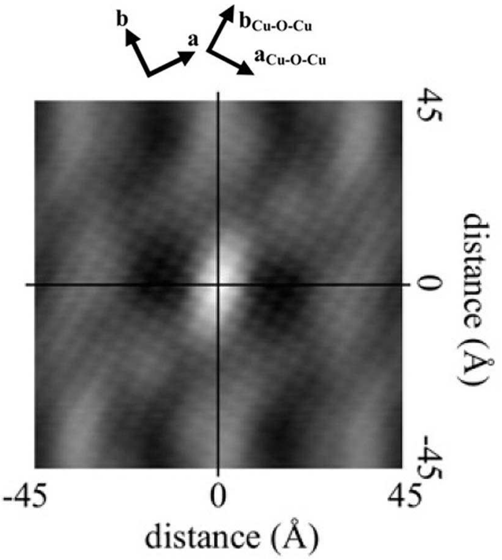

Figure 5.7: From [18]: Autocorrelation of the data shown in Fig. 5.6 (d).

5.2 Comparison to the 2d modulations in Pb-free Bi2212

In the last section, the evolution of the 2d modulation in the one-layer Bi2201 upon Pb substitution was shown. It turned out that the simplest and clearest modulation could be detected in the case where an order-inducing one-dimensional superstructure is present. In this section, I will show the results of the Pb-free two-layer $Bi_2Sr_2CaCu_2O_{8+\delta}$. This material also exhibits a one-dimensional superstructure which is highly comparable to the one-layer material without Lead. Therefore, in the case where 2d modulations are present, we expect them to be highly ordered. This expectation will be fulfilled. In the following, I will first show that the STM pattern at room temperature exhibits 2d modulations. This will be done by discussing its autocovariance, similar as already done with the one-layer material. For a later comparison with 2d modulations in Bi2212 at low temperatures, it is necessary to discuss the appearance of this 2d order in reciprocal space, i.e. in power spectral density calculated by the periodogram. Previously, the harmonic analysis was achieved by using the correlogram technique. For a harmonic analysis, the correlogram is more reliable, in most cases. However, here I will use the periodogram technique as it is often used in the literature and a comparison will be more convenient.

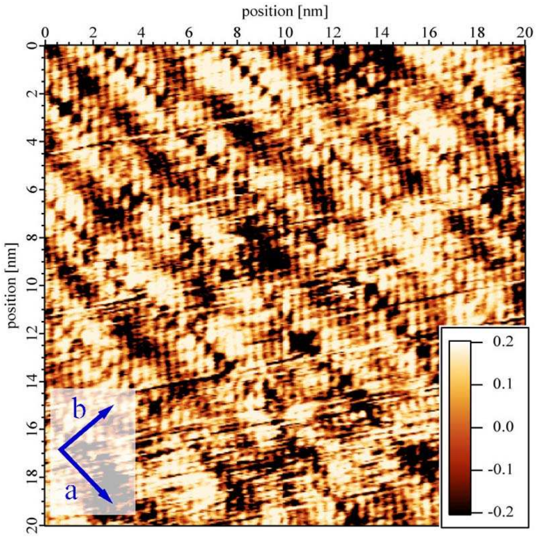

5.8.1: Topographic STM measurement of optimally doped $Bi_2Sr_2CaCu_2O_{8+\delta}$ with T_C=92 K, (20x20)nm^2, 0.6 V[170]. The pattern is raw data only normalized by the routine described by Eq. (B.11) of Appendix B.2.

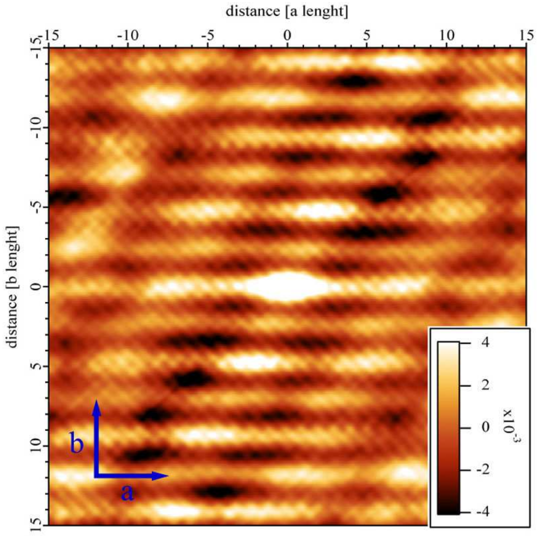

5.8.2: Fragment of the unbiased autocovariance of (a).

A normalized STM pattern of a sample of $Bi_2Sr_2CaCu_2O_{8+\delta}$ with T_C=92K at room temperature is shown in Fig. 5.8.1. At a bias of 0.6 V, clearly either the atomic lattice or the inhomogeneous background is resolvable. The ridges of the 1d superstructure can be observed as black lines. Pale light bubbles are also visible beside the ridges. From the middle region of the pattern, it is already suggestible that the 2d modulation is formed by these bubbles.

The autocovariance of this pattern is shown in Fig. 5.8.2. As in the autocovariance of the one-layer material of Fig. 5.2.1, two independent modulations are present: One is the one-dimensional about 1x5 superstructure and the other is a two-dimensional modulation. Also, the atomic lattice is very visible which is represented by the thin grid turned by 45 degrees from the a-direction. The lattice vector of the one-dimensional superstructure is evaluated as $\vec{r}_{SS}$=4.7$\vec{b}$. The 2d modulation exhibits the lattice vectors $\vec{r}_1$= 0.8$\vec{a}$ +2.3$\vec{b}$ and $\vec{r}_2$=-7.2$\vec{a}$. The area is given as 17 $\vec{a}\vec{b}$.

The repetitions of the autocovariances are shown in Fig. 5.8.3 and Fig. 5.8.4. To guarantee a high comparability, the colorscale and also the shown size of the fragment are exactly the same. Clearly an overall similarity of the modulations in both systems can be noted. It can therefore be suggested that the two modulations are of the same origin. The area spanned by the lattice vectors of the 2d modulation in the two-layer material is about 60 % of the area in the one-layer compound. Let me recall here that both crystals have a comparable number of holes per CuO_2-plane. Therefore, it is again shown that the 2d-modulations are not produced by an ordering of the electronic structure. On the other hand, we know that at comparable holes per CuO_2-plane, the Oxygen content in $Bi_2Sr_2CaCu_2O_{8+\delta}$ must be much more than in the one-layer material.

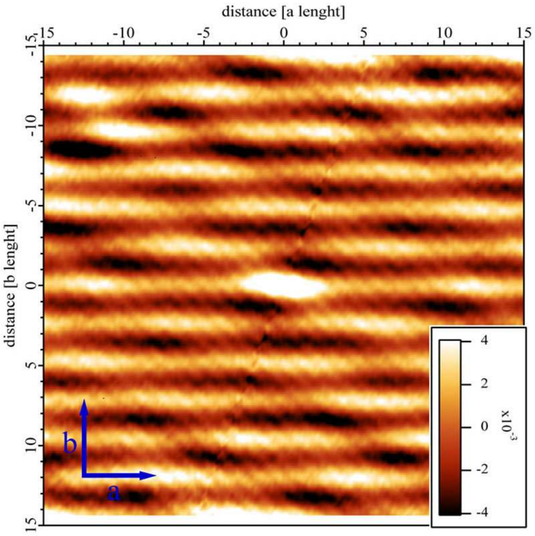

5.8.3: Autocovariance of nearly optimally-doped $Bi_{1.98}Sr_{1.5}La_{0.39}Cu_{1.14}O_{6+\delta}$.

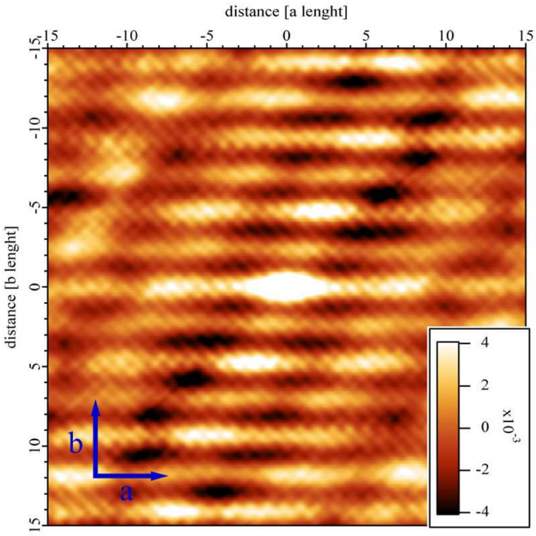

5.8.4: Autocovariance of optimally-doped Bi_2Sr_2Ca-$Cu_2O_{8+\delta}$.

5.2.1 The modulations in reciprocal space

In the following paragraph, I would like to illustrate the modulations in reciprocal space. The easiest method for this is to calculate the power spectral density (PSD) in the periodogram approach. For details please see Appendix B.2. Fig. 5.8.5 shows the square root of the power spectral density (equal to the structure factor) for the two-layer $Bi_2Sr_2CaCu_2O_{8+\delta}$. The power spectral density can be practically seen as both the Fourier-transformed autocovariance and the squared absolute value of a Fourier transformation of the original STM pattern. Therefore,

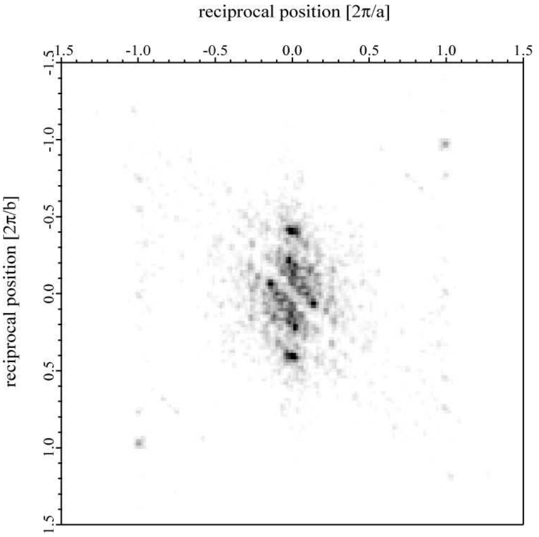

5.8.5: Square root of the PSD of the measurement of optimally doped $Bi_2Sr_2CaCu_2O_{8+\delta}$ with T_C=92 K, (20x20)nm^2, RT, as shown in Fig. 5.8.1. The PSD was evaluated by the periodogram technique.

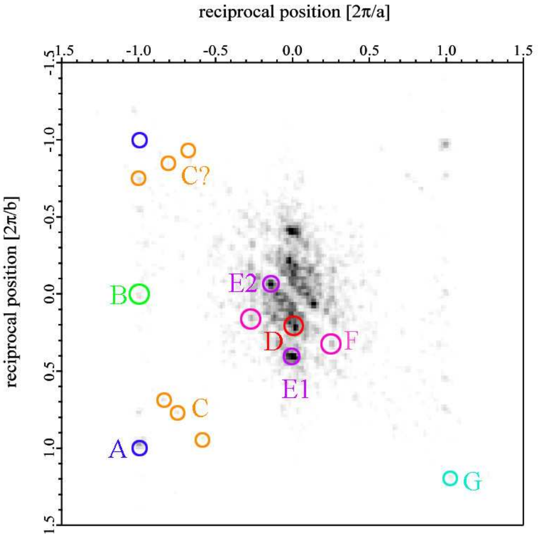

5.8.6: Same figure as Fig. 5.8.5, but with marks to explain the features found in the square root of the PSD. For details see text.

a modulation reveals them as peaks in the PSD. The position of the peaks will indicate its wavevector and the height of its oscillation strength. To increase the visibility of peaks with different intensities, the square root of the PSD can be used. What cannot be seen due to the normalization is the intensity of the constant STM background which corresponds to the undisturbed potential of the crystal. The constant signal is given as a broadened Kronecker delta at (0,0) whose width represents the uncertainty of the constant signal due to the finite probed area.

I would first like to discuss the straightening which must always be done in STM measurements because of the unequal attenuation of the piezos, for example. During this discussion, I will already highlight some features that are visible in the square root of the PSD. After that, I will calculate 'by hand' the transformation of the 2d modulation from real-space to reciprocal-space to explain some high-order features. This knowledge will be required in the next section.

The straightening was done by the points B and D. The reason for using these points will be explained in the following. To achieve this, the original data as depicted in Fig. 5.8.1 was rotated counterclockwise by 42 degrees and then sheared by the matrix:

$$S = \begin{pmatrix} 1 & 0.11 \\ 0 & 1 \end{pmatrix} \tag{5.5}$$

Here (1,0), is the horizontal direction. The points at A in Fig. 5.8.6 were assumed to be the spots produced by the Bi surface lattice. Here, a nearly quadratic Bi surface lattice might be assumed. It should be noted that the spots are not perfectly on their position and the spots at ($\pm 2\pi/a$,$\pm 2\pi/b$) are not visible. Instead, point G is clearly visible. Perhaps this is not accidental but has physical meaning. However, please note also that the spots of this lattice are distorted by the one-dimensional superstructure which results in replicas of the original lattice points at the length of about 1/5×2π/b. The point denoted as B is the result of a commensurate 2×a superstructure visible for Bi2201 and Bi2212 in diffuse x-ray diffraction [218]. It is, of course, also visible in LEED and for ARPES it produces the 'shadow band' [219]. In this work, for the one-layer $Bi_{1.44}Pb_{0.42}Sr_{1.44}La_{0.50}Cu_{1.20}O_{6+\delta}$, the visibility of this feature can be verified by LEED as shown in Fig. 5.8. There, the extra spot is visible at (1,0) while it is absent at (0,1). Point D in Fig. 5.8.6 represents the one-dimensional ≈ 1×5 superstructure in its first order and can be attributed to a wave vector of q_{SS}=0.21×2π/b (see, e.g., [220, 157]). Therefore, the straightening was done by points B and D, because the exact position for them is confirmed by the citations above.

The points at C represent the intersection of the Bi surface Brillouin zone with the bulk Brillouin zone. This is a typical phenomenon in surface condensed matter physics. The Bi-surface lattice produces the spots A, the bulk Brillouin zone produces the C-spots. Please compare also with Fig. 3.4 in Chapter 3. For the general description of an intersection of a surface lattice with a bulk Brillouin zone see, e.g, [221]. If the inequality in the symmetry of the points C and C? is confirmed, it may also represent the orthorhombicity. Point E1 is the combination of the first order of the wavevector q_{E1} of the two-dimensional modulation and the second order of the ≈1×5 superstructure. That is why the intensity is very high and comparable to the first order of the one-dimensional superstructure. This combination of the two modulations is also the reason why the peak looks broadened or doubled. Point E2 is then the second wave-vector of the two-dimensional modulation.

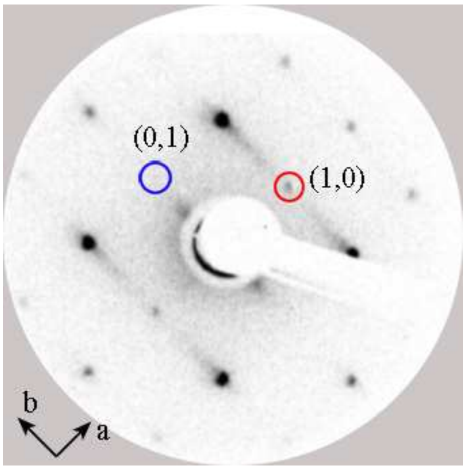

Figure 5.8: LEED pattern for $Bi_{1.44}$-$Pb_{0.42}Sr_{1.44}La_{0.50}Cu_{1.20}O_{6+\delta}$ at electron energies of 54 eV. Please note the spot at (1,0), which is absent at (0,1). The spot (1,0) is the same as spot B in Fig. 5.8.6.

For the preceding, I will show in the following that E1 and E2 are the positions of the reciprocal lattice vectors. As mentioned above, the 2d lattice vectors are $\vec{r}_1$= 0.8$\vec{a}$ +2.3$\vec{b}$ and $\vec{r}_2$=-7.2$\vec{a}$ and span the area of 17 $\vec{a}\vec{b}$. Their reciprocal vectors can be calculated with the help of a dummy vector, i.e. $\vec{c} \perp \vec{a}, \vec{b}$; $|\vec{c}| = 1$:

$$q_{E1} = \frac{\vec{r}_2 \times \vec{c}}{\vec{r}_1(\vec{r}_2 \times \vec{c})} = \frac{1}{17}\begin{pmatrix} 7.2 \\ 0 \\ 0 \end{pmatrix} \times \begin{pmatrix} 0 \\ 0 \\ 1 \end{pmatrix} = 0.424\,\vec{b}^*$$

$$q_{E2} = \frac{\vec{r}_1 \times \vec{c}}{\vec{r}_1(\vec{r}_2 \times \vec{c})} = \frac{1}{17}\begin{pmatrix} 0.8 \\ 2.3 \\ 0 \end{pmatrix} \times \begin{pmatrix} 0 \\ 0 \\ 1 \end{pmatrix} = -0.135\,\vec{a}^* + 0.047\,\vec{b}^*$$

Here, $\vec{a}^*$ and $\vec{b}^*$ are the reciprocal lattice vectors of the atomic lattice. In Fig. 5.8.6, there are also the points F. Although these points are of minor importance for the modulation structure, they must be addressed because of their significance to later shown findings. These points are produced by a combination of the present modulation wave-vectors

$$q_F = \pm 2q_{E2} \pm q_{SS} = \pm 0.27\,\vec{a}^* \pm (0.094 \pm 0.21)\,\vec{b}^* \tag{5.6}$$

5.2.2 Comparison to other work concerning 2d modulations in Bi2212

In the following, I want to discuss some results which can be found in the literature about 2d modulations in Bi2212. For a more detailed review, I refer to Fisher et al.[15].

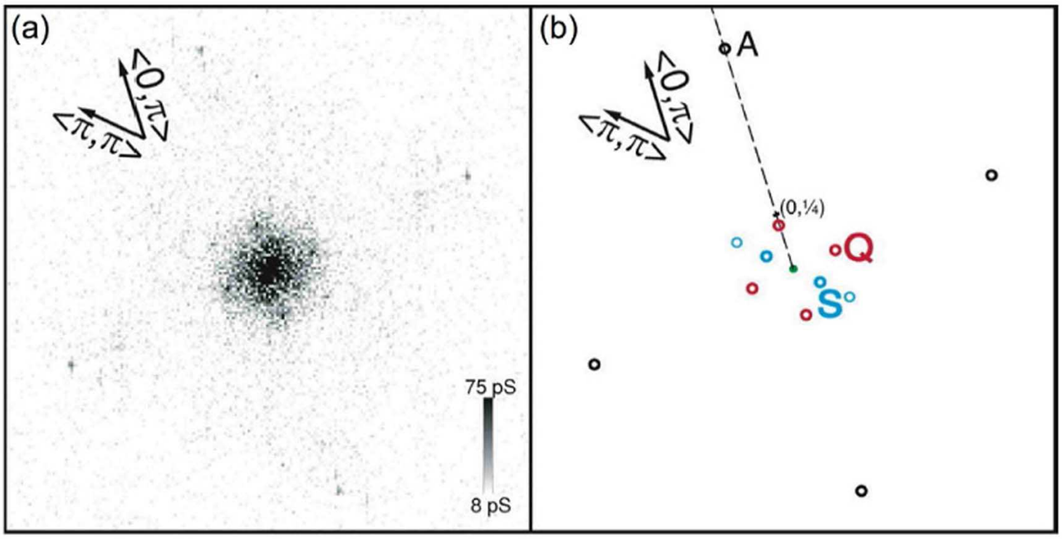

Figure 5.9: From [17]: Fourier analysis of DOS modulations. **(a)** Fast Fourier transform (FFT) of an unprocessed conductance map acquired over a 380 Å by 380 Å field of view (on a 200-square grid) at 15 mV. **(b)** The FFT has peaks corresponding to atomic sites (colored black and labeled A), primary (at $2\pi/6.8a_0$) and secondary peaks corresponding to the b-axis supermodulation (colored cyan and labeled S) and peaks at $2\pi/4.7a_0$ along the $<\pi, 0>$ and $<0, \pi>$ directions (colored red and labeled Q). The point $(0, 2\pi/4a_0)$ is also labeled for reference.

Fig. 5.9 shows a 'Fast Fourier transform' as published by Vershinin et al. [17]. The measurement for processing comes from an optimally-doped Bi2212 sample with T_C=92K. It was measured at 100K with a rather low positive bias of 15 mV. A 2d modulations is clearly visible which is evaluated as an about 4x4 order. In the referenced work, the coordinates were turned along the CuO-bond direction with $\vec{a_0} \approx 1/2(\vec{a} + \vec{b})$. The authors claim that the energy scale of the 2d modulations is connected to the pseudogap energy scale.

Inspired by this, Fig. 5.10.1 shows how the square root of the PSD of the sample examined here would look in another straightening. Starting from Fig. 5.8.1 this straightening is taken by the matrix

$$S = \begin{pmatrix} 1.18 & 0.02 \\ 0 & 0.96 \end{pmatrix} \tag{5.7}$$

Due to a better comparability, the PSD was turned 90 degrees counterclockwise. To put in the black circles representing the atomic lattice, the Bi surface lattice was assumed differently; In reference to Fig. 5.8.6, one point is the reflex G and the other is the visible point of A. In this assumption, the Bi surface lattice is rectangular with a side ratio of about 1.15:1. This is also similar to the case in the 'Fast Fourier transform' by Vershinin et al. [17]. In my processed PSD of Fig. 5.10.1, the about 1x5 superstructure is no longer exactly in the b-direction. This results in a second peak near the first order of the superstructure. This peak is produced, in the notation above, by the combination q_{E2}-q_{SS}. Note that, in Fig. 5.10.1, the reflex structure is not perfectly symmetric but looks nearly 4×4-like.

Let me conclude here that despite the small difference, the same structures as shown in [17] were found. The difference has something to do with the straightening here or there. It is important to state that, in the sample evaluated here, a 4×4 superstructure should not be mentoined. The spots visible in Fig. 5.10.1 represent a higher order of the underlying about $(0.8\vec{a} + 2.3\vec{b}) \times (7.2\vec{a})$ modulation. The higher order are the points at F in Fig. 5.8.6 and were explained in the last section. It can be assumed that, because of the nearly identical look of the structures, this change in nomenclature should also be applied to the measurement of [17] shown above.

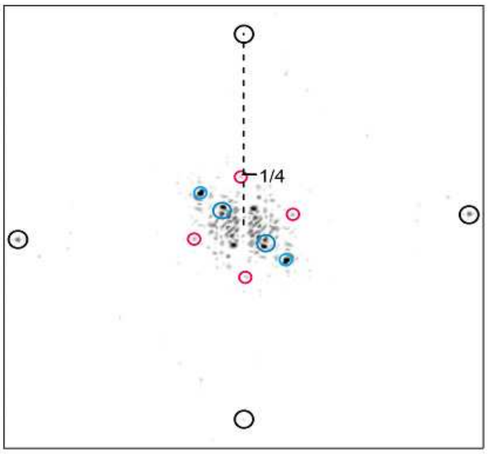

5.10.1: Square root of the PSD in another straightening.

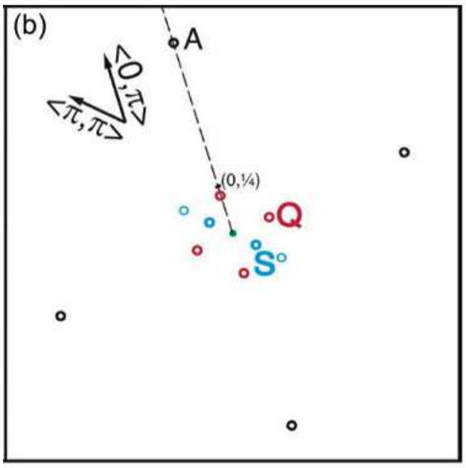

5.10.2: Same as Fig. 5.9 (b) for comparison.

I also want to point out the differences in the measurement of both examples of a 2d modulation in $Bi_2Sr_2CaCu_2O_{8+\delta}$. First, the patterns shown here were measured at a high positive bias of 0.6V while the measurement by Vershinin et al. was obtained at 16mV. The authors pointed out that the 2d modulation is only visible below the pseudogap energetic scale. The temperatures also differ; One STM pattern was obtained at room-temperature while the other was measured at 100K. It seems to be a common opinion [15] that 2d nanoscale modulations are only visible at low temperatures which are typically associated with the pseudogap-temperature T^*. However, a detailed examination of the literature concerning temperature dependencies of 2d modulations is so far lacking. Therefore, I suggest that the nondispersive 2d modulation at low temperatures is of the same origin as that shown here.

Although based on the argumentation above one should be careful about the exact nomenclature, another interesting result about the appearance of '4x4' modulations from McElroy et al. [222]

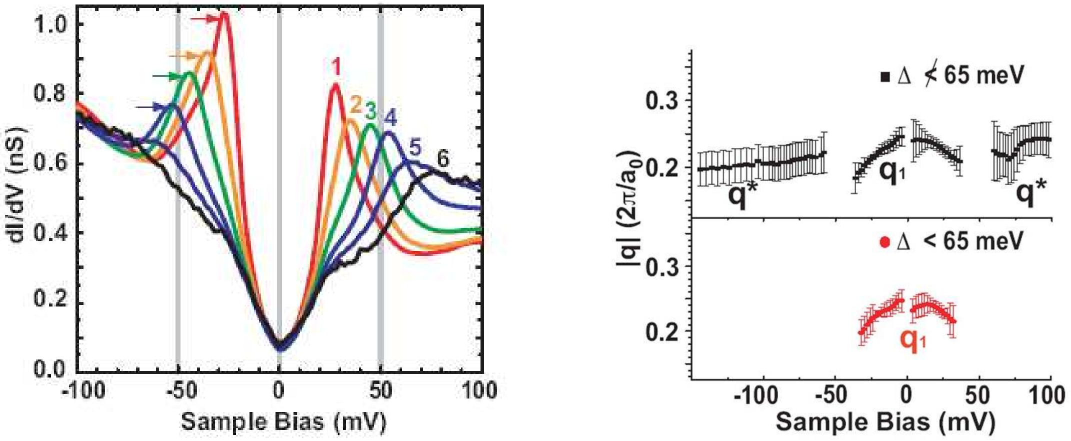

5.10.3: From [222]: Range of tunneling conductance spectra measured on inhomogeneous superconducting Bi2212

5.10.4: From [222]: Dispersion of the q-vectors observed in regions with 'SC coherence-peaked spectra' (red circles) and in regions with 'pseudogap-like spectra' (black squares). The vector q* has a length $4.5a_0 \pm 15\%$

Figure 5.10: The difference in modulation behavior in regions where a so-called 'SC coherence-peaked spectra' and where 'pseudogap-like spectra' were found in scanning tunneling spectroscopy (STS) measurements [222].

is shown in Fig. 5.10.3 and Fig. 5.10.4. In this publication, spatial resolved scanning tunneling spectroscopy (STS) was implemented. The authors divide the obtained spectra in regions where 'superconducting (SC) coherence-peaked spectra' and 'pseudogap-like spectra' were found. The SC coherence-peaked spectra are characterized by a sharp peak near zero bias whereas the pseudogap-like spectra do not have a sharp peak. In Fig. 5.10.3, a typical SC coherence-peaked spectra is notated as '1' while a typical pseudogap spectra is notated as '6'. The authors defined all spectra with a gap of < 65 mV as a typical SC coherence-peaked spectra. By this criterium, the spatial STS maps were divided into SC and pseudogap regions. As depicted in Fig. 5.10.4, both regions exhibit modulations at a bias lower than about 50 meV but the 'pseudogap-like spectra' also show non-dispersive modulations at higher bias. From this finding, it may be justified to apply the terms *dispersive* and *nondispersive* modulations.

Comparing the two reports by McElroy et al. and Vershinin et al., Fisher et al. [15] conclude that "the non-dispersing square pattern observed in the pseudogap phase above Tc in a nearly optimally doped sample is strongest at low energies. On the other hand, in the strongly underdoped samples investigated at low temperature an apparently different behavior is found. Here a non-dispersing pattern is found at high energy while a dispersing quasiparticle interference pattern is found at low energy". According to this statement, the difficulties in finding a characterization for this behavior may be seen. I think we can at least state that the appearance or visibility of the 2d modulation changes somehow with the bias. For the one-layer Bi2201, this was shown by Kudo et al.[217] and briefly discussed in Section 5.1.3.

5.3 Discussion

To conclude this chapter, I first want to summarize and then provide some suggestions and comments which also relate to the depressions found in the last chapter.

From the measurements shown here, the following statements can be made; Two-dimensional modulations on the nanoscale are present at room temperature in $Bi_{2-y}Pb_ySr_{2-x}La_xCuO_{6+\delta}$ as well as in $Bi_2Sr_2CaCu_2O_{8+\delta}$. With respect to the bias, their visibility may change. By varying the Pb substitution level in $Bi_{2-y}Pb_ySr_{2-x}La_xCuO_{6+\delta}$, the evolution of the modulations could be examined. These modulations are more ordered when the superstructure is present and otherwise tend to disorder and form multiple phases. Also, in Lead-free $Bi_2Sr_2CaCu_2O_{8+\delta}$ the modulations were found. Although the area is different, the overall shape of the modulations is similar to the modulations found in the one-layer material.

The 2d modulations found in $Bi_{2-y}Pb_ySr_{2-x}La_xCuO_{6+\delta}$ exhibit similarities to the 2d modulations found in $Bi_{2+z}Pb_ySr_{2-z}CuO_{6+\delta}$ at low temperatures by Kudo et al.[18]. I suggest that both modulations are of the same origin. The modulations found in $Bi_2Sr_2CaCu_2O_{8+\delta}$ are highly similar to the nondispersive 4x4 order presented in the publication by Vershinin et al. [17].

I will now address the thesis that the nanoscale 2d-modulations are due to the ordered electronic structure of the CuO_2-plane. My arguments against are: (i) The measurements shown here were obtained at high bias and temperatures. (ii) When assuming the probed modulations are due to holes, $Bi_{2-y}Pb_ySr_{2-x}La_xCuO_{6+\delta}$ scaled in the wrong direction. (iii) The two different optimally doped materials - Bi2201 and Bi2212 - should have the same area in the case where the cause is the ordered electronic structure.

A possible explanation for the modulations are some kinds of dopants or combination of dopant atoms which are required to control the hole-concentration. For the modulation structure of $Bi_{2-y}Pb_ySr_{2-x}La_xCuO_{6+\delta}$ with y=0.41 and x=0.44, it can be shown [172] that LEED and x-ray diffraction detect a perfect lattice whereas STM reveals periodic modulations. For LEED, this behavior results because it is not sensitive to periodic arrangements of low corrugation, especially when the corrugations are not directly in the surface layer but below it. Also, by x-ray diffraction not all possible periodic arrangements can be detected, i.e. the ordering of Oxygen in an otherwise perfect lattice. This is due to the small atomic form factor of O. Oxygen ordering within the CuO-chains of the high-temperature superconductor $YBa_2Cu_3O_{7-x}$ is quite common [223]. Thus, for a further interpretation of the origin of the modulations, it might be useful to compare the Oxygen levels of the samples. Also, the examination of possible dopant complexes might shed light on the origin of the modulations.

In the following, I want to assume that the modulations are caused by the dopant-atoms i.e. by inhomogeneities. Here, it is necessary to discuss possible consequences for the electronic structure of the CuO_2-plane. For an ideal 3d metal with an ideal surface, the influence on the electronic structure is that the electronic system will perfectly screen the inhomogeneities. However, the layered Bi-cuprates are not ideal metals. In the case of $Bi_2Sr_{2-x}La_xCuO_{6+\delta}$, the dielectric constant may be around ϵ=30. It might be good to compare the calculation within the local density approximation (LDA) by He et al. [88] where for $Bi_2Sr_2CaCu_2O_{8+\delta}$, a strong impact of Oxygen dopants on the local density of states was shown. The dopants were in this calculation located between the BiO- and SrO- layers.

For the differences in nondispersive and dispersive modulations found in STM, I suggest that the dispersive modulations are the interactions of the electronic structure with the inhomogeneities. It could also be the interaction of the tunneling-electrons with the inhomogeneities. Let me clearly state here that the high possibility that the nondispersive 4x4 order is caused by dopant atoms does not mean that electronic order is absent. It might only require more effort and shows that examining the cuprates means having to deal with inhomogeneities. These inhomogeneities might be required and could even be beneficial:

For the previous statement, I will now refer back to the ground state of the depressions and review some interesting findings about dopant order and a depression. As mentioned above, Oxygen ordering within the CuO-chains of $YBa_2Cu_3O_{7-x}$ is common [223]. These chains are located away from the superconducting CuO_2-plane and act as charge reservoirs. The 60K plateau in $YBa_2Cu_3O_{7-x}$ - the 1/8 depression - can be reduced by Oxygen order within these chains. The possibility of reducing the plateau gave rise to discussions about the origin of the plateau. On the one hand, there is the thesis that the Oxygen is the cause of the 60K plateau (see, e.g., [224, 225, 226]). On the other hand, there is the antithesis that the electronic structure is the cause (see e.g [227, 174]). My synthesis would be the following: Let us assume that exactly at the hole doping of a depression the electronic ordering is the most undisturbed and cleanest. But the ordering can be suppressed by an ordering of the dopant-atoms which is incommensurate with the electronic ordering. The electronic order will not be strongly affected when the dopant-atoms are disordered and represent only a 'white noise potential' for electrons in the CuO_2-plane. In the case that the dopant order is commensurate with the electronic one, it might be possible to increase the crystallization temperature of the ground state of the depressions, i.e. the crystallization temperature for electronic ordering. The question then arises: What, in my view, is this crystallization temperature.

VI
The pseudogap

One of the most interesting properties of the hole-doped cuprate superconductors is the existence of a pseudogap state. An experimental review of the pseudogap is given by Timusk and Statt [5]. This review should be extended by the review by Tallon and Loram [228]. Also, I would like to recommend the discussion by Norman et al. [19], Hüfner et al. [20] and the introduction in the publication by Sadovskii [229].

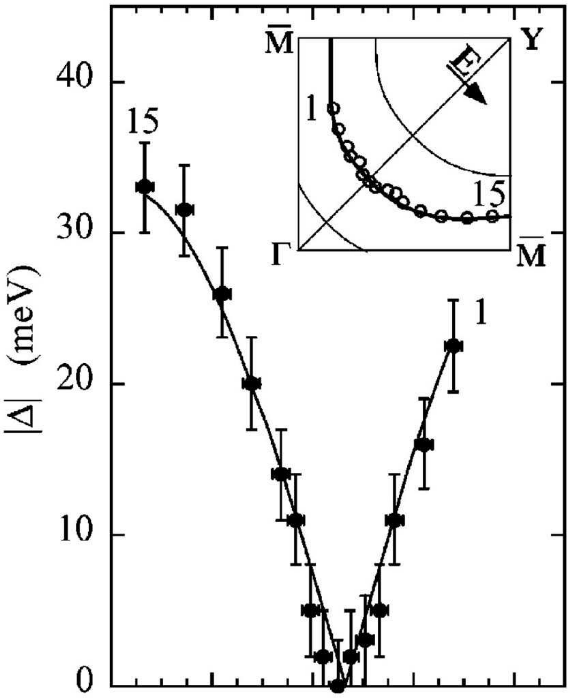

Figure 6.1: From Ding et al. [230]: Superconducting gap as extracted by spectra measured at 13 K on Bi2212 with T_C= 87 K. The gap is plotted vs the angle along the normal-state Fermi surface (see the Brillouin zone in upper right). Also included is a d-wave fit.

The question whether it is possible in angular resolved photoemission (ARPES) to differ between the pseudogap and the superconducting gap is not simple. Fig. 6.1 from Ding et al. [230] shows the fitting results of spectra measured along the Fermi surface of a Bi_2-$Sr_2CaCu_2O_{8+\delta}$ sample with T_C=87 K. There, one can see that the excitation in the vicinity of the Fermi surface exhibits a gap of $d_{x^2-y^2}$ symmetry; The state at zeroth Fermi-surface angle is strongly gapped while at 45° no gap is visible. When plotting the gap over the Fermi-surface angle, it has a 'V'-like shape. To account for this symmetry, the normal-state Fermi crossings along the line Γ(Y/X) are called 'nodal' while the Fermi crossings along the line M(X/Y) are 'antinodal'. Because this gap with the $d_{x^2-y^2}$ symmetry was measured at low temperatures $\ll T_C$, it was presumed to be the superconducting gap. The $d_{x^2-y^2}$ symmetry seems to be the dominant symmetry measured by phase-sensitive methods (see [74] and references therein) and is therefore incorporated into most theories of pairing. However, let me state here that photoemission does not necessarily measure the same properties as phase-sensitive methods (see, e.g., discussion in [20]). To discuss the pseudogap further, Harris et al. [231] showed a $d_{x^2-y^2}$ symmetry of a gap for an optimally doped $Bi_2Sr_{2-x}La_xCuO_{6+\delta}$ sample, as well as for an underdoped $Bi_{2+z}Sr_{2-z}CuO_{6+\delta}$ sample. This gap did not close at T_C and therefore is presumed not to be the superconducting gap but the pseudogap, at least at higher temperatures. No gap was found in a highly overdoped sample.

But even the $d_{x^2-y^2}$ symmetry of the gapped state measured in photoemission has been a topic of discussion for a long time. Often a 'U'-shape is seen for a gap, rather than the 'V'-shape shown in Fig. 6.1 (see [232] and references therein). This observation can be formulated by stating that the gap 'fills in' from the nodal direction. In order to account for this behavior, Mesot et al. [233] suggested that higher harmonics consistent with d-wave symmetry should be included in the expansion of the gap function. Recently, Kondo et al. [234] and Lee et al. [235] showed a non-pure $d_{x^2-y^2}$ symmetry in Bi2201 and Bi2212, respectively. These authors associated the filling of the gap with the closing of the superconducting gap. It can also been questioned whether the excitations near the antinode are due to the cooling reaching a coherent state faster than the excitations near the node. In most scenarios of the behavior of the pseudogap, the T^* is taken as a crossover rather than as a true phase transition [19]. It can be suggested that the d-wave symmetry is reached at $T \rightarrow T_C$ and the pseudogap is only a partly coherent state. For example, the pairing theory by Emery and Kivelson suggests that below T^* a precursor of the superconducting condensate exists which is long-range phase coherent below T_C [236]. This means that the superconducting gap equals the pseudogap but there are also arguments that the high-temperature superconductors are two-gap systems. This can be concluded by the review of different experimental methods as discussed by Hüfner et al. [20].

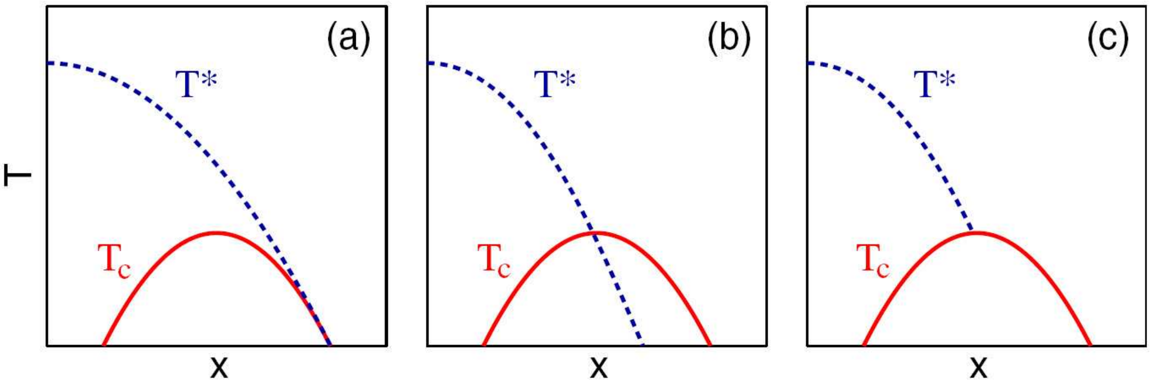

Figure 6.2: From [20] who adapted from [19]: Three commonly discussed possibilities for the behavior of the pseudogap-temperature upon hole doping. The red solid line is T_C, the blue dashed line is T^*.

The dependence of the pseudogap-temperature T^* upon hole doping is also under heavy debate. Fig. 6.2 show three commonly discussed ideal behaviors for $T^*(p)$. In (a), the pseudogap covers the whole superconducting region and merges with T_C on the overdoped side. In (b), it cuts through the T_C dome while in (c), it ends at T_C. (a) is typically associated with the assumption that the pseudogap phase is a precursor to the superconducting state, e.g. the above-mentioned theory by Emery and Kivelson [236, 110, 111]. The cut though the superconducting dome [237, 228] as depicted in (b) is expected from the theoretical side when two competing states are present. As described in the review by Sachdev [117], these competing states may then have a 'quantum critical point'. The third example is a reminder that there are even more possibilities and is given as an alternative in [19].

In the following, I will show that the behavior of the pseudogap-temperature is partly consistent with all three behaviors but also has important differences. The pseudogap also exists in the overdoped region and, in my view, the pseudogap-temperature can be understood as a crystallization temperature or as an onset of order in the electronic system. Consequently, the pseudogap-temperature has to react to the hole concentrations of the depressions. I will show this by angular resolved photoemission (ARPES) and resistivity measurements of the ab plane. I will also show indications that the purest pseudogap state is the eutectic ground state of the depressions and high-temperature superconductivity is caused by a defective ground state. Here, the term 'defective ground state' means that the spatial order within the electronic structure of the CuO_2-plane is not perfect and exhibits a certain level of inherent disorder.

The course of this chapter is the following: In the first part, the ARPES measurements of the temperature dependence of the Zhang Rice-derived band at the Fermi crossing near the M-point are discussed. I will first discuss the change in lifetime of the excitation. This will be done relative to the doping. From this, I will argue that the cleanest pseudogap state is at a depression. Then I will show that, by measuring the temperature dependence of the gap at this antinodal position, no significant superconducting gap can be seen. This confirms the suggestion that the pseudogap is dominant there. Then I will show that ARPES-accessible properties abruptly change at the doping of a depression.

To further examine the influence of the depressions on the pseudogap and the behavior of $T^*(p)$ in great detail, I conducted temperature-dependent resistivity measurements. From these, it is possible to derive a good estimate of the pseudogap-temperature relative to the hole doping. The analysis is performed by resistivity curvature mapping [238]. I will thereby confirm the finding of ARPES that, at doping value of a depression, a change in pseudogap-temperature T^* always occurs. At the end of this chapter, I will compare the obtained data of resistivity and ARPES.

6.1 T* and Δ* measured by ARPES

Here, the results from angular resolved photoemission (ARPES) are discussed. Basic knowledge can be found in Appendix A.5. Good reviews about ARPES on cuprates are provided by Damascelli et al. [232] and by Norman and Pepin [239]. A good book about ARPES in general is by Hüffner [221].

6.1.1 Sample characterization

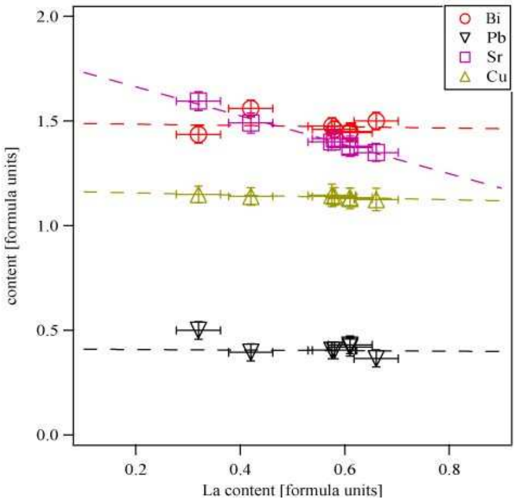

6.3.1: Composition of the samples used for ARPES relative to the the La content as measured by EDX. Also shown is a linefit for the chemical composition.

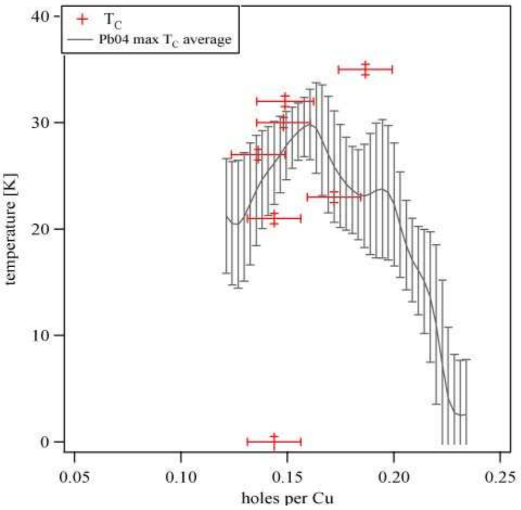

6.3.2: T_C's by AC-susceptibility of the samples used for ARPES relative to the hole doping as given by formula (4.4) in Chapter 4.3.2. Also shown is the max T_C average of all samples with y=0.4 as defined in Chapter 4.

For the ARPES measurements, samples of $Bi_{2-y}Pb_ySr_{2-x}La_xCuO_{6+\delta}$ with y≈ 0.4 were used. Fig. 6.3.1 and Fig. 6.3.2 show the characterization results. These results are additionally listed in Appendix B.4. In Fig. 6.3.1 the composition relative to the La content is shown. The least square line fits give

$$\begin{aligned} c(Bi) &= (1.49 \pm 0.09) - (0.03 \pm 0.11)x \quad ; \quad \chi^2 = 0.0115 && (6.1)\\ c(Pb) &= (0.41 \pm 0.08) - (0.01 \pm 0.14)x \quad ; \quad \chi^2 = 0.0025 && (6.2)\\ c(Sr) &= (1.80 \pm 0.03) - (0.69 \pm 0.05)x \quad ; \quad \chi^2 = 0.0009 && (6.3)\\ c(Cu) &= (1.17 \pm 0.01) - (0.05 \pm 0.02)x \quad ; \quad \chi^2 = 0.0002\,. && (6.4) \end{aligned}$$

As can also be seen from Fig. 6.3.1, only the sample with Lanthanum content of x=0.32 formula units has a larger derivation from the average. It has a higher Pb amount of y=0.5 formula units. For the linefit of the Pb content, this sample was not used. In Fig. 6.3.2, the T_C's by

AC-susceptibility are shown together with the max T_C average of all samples with y=0.4. The average was defined in Chapter 4. In the T_C curve, the samples' doping is calculated according to the formula (4.4) of Chapter 4.2.

From Fig. 6.3.2, it can be seen that the samples were chosen mainly around one depression in T_C. Compared with Chapter 4.3.2 and especially Tab. 4.1 and Fig. 4.8, the chosen depression is at x=0.58 which corresponds to a hole-doping value of about 0.15 holes per Cu. For comparison, the sample with T_C=0 has an average La content of x=0.61±0.04 formula units. The sample with Lanthanum content x=0.32 is already near the next depression. To indicate the samples in the following, they are named 'x' plus the Lanthanum content: x0.32, x0.42, x0.58-1, x0.58-2, x0.61, x0.62 and x0.66.

6.1.2 Experimental

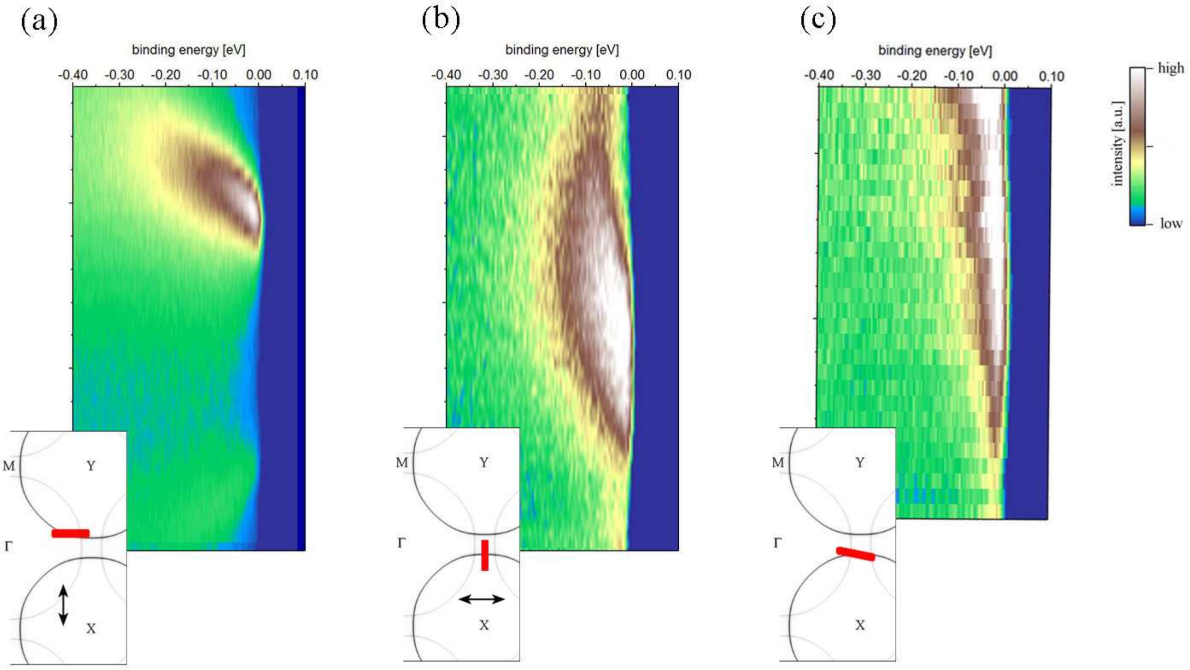

Figure 6.3: Geometries used for the ARPES experiments. Also included in the lower left of each geometry are the line of measurement and the plane of the electrical field vector.

The spectra were obtained near the M(X/Y) Fermi crossing. The measurement conditions are listed in Appendix B.4. The three geometries used are shown in Fig. 6.3. The line of measurement within the Brillouin zone is depicted in the lower left of each geometry. Also indicated by a black arrow is the plane of the electrical field vector. The photon energy was typically at around 22 eV. The angular resolution was typically at 0.2°. The energy resolution as determined by an evaporated gold film ranges from 10 to 22 meV; 16 meV was common.

The sample was cleaved at low temperatures (typically < 40K) on the manipulator at ultra-high

Figure 6.4: Selected temperatures of spectra at k_F for the samples

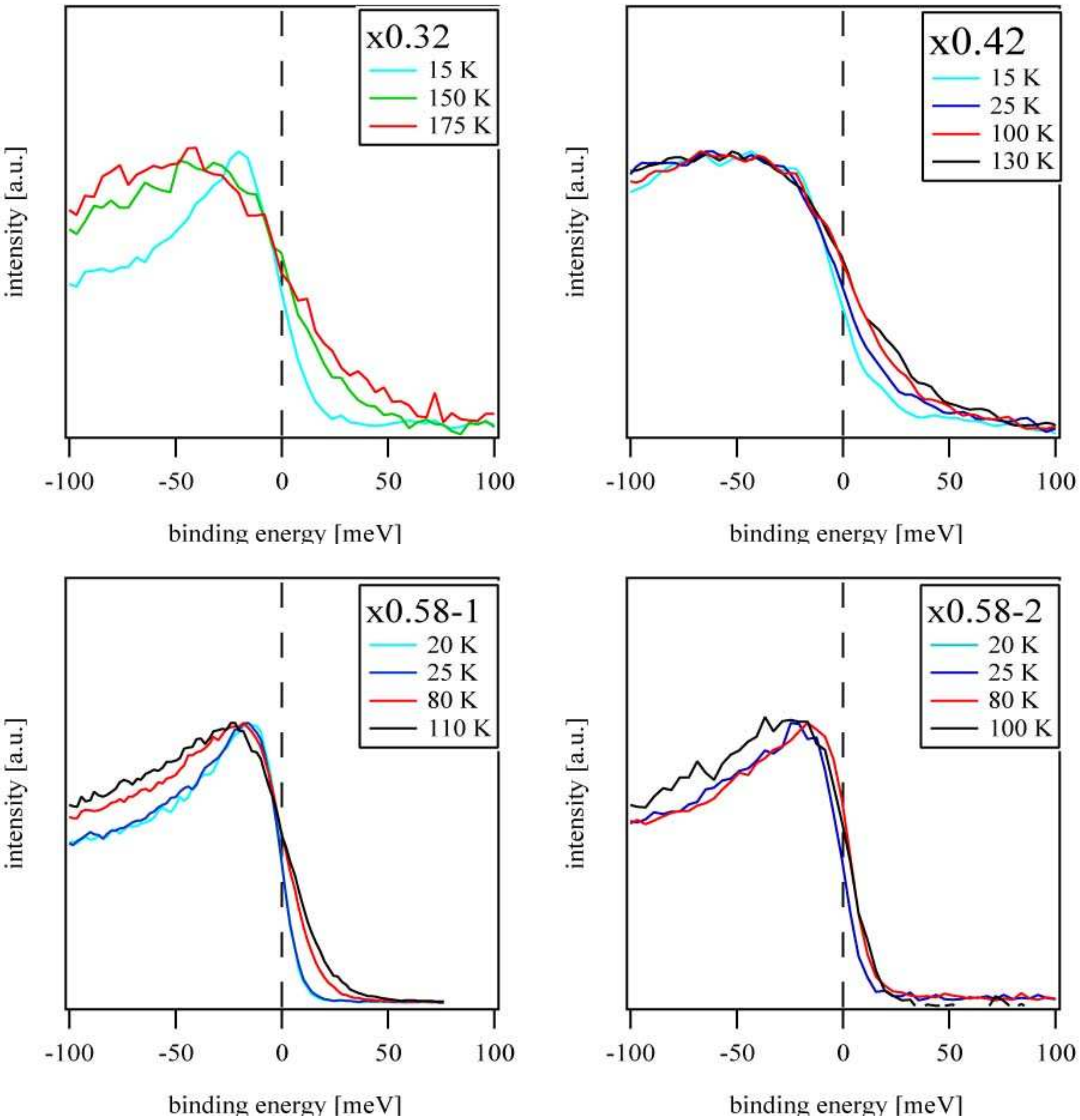

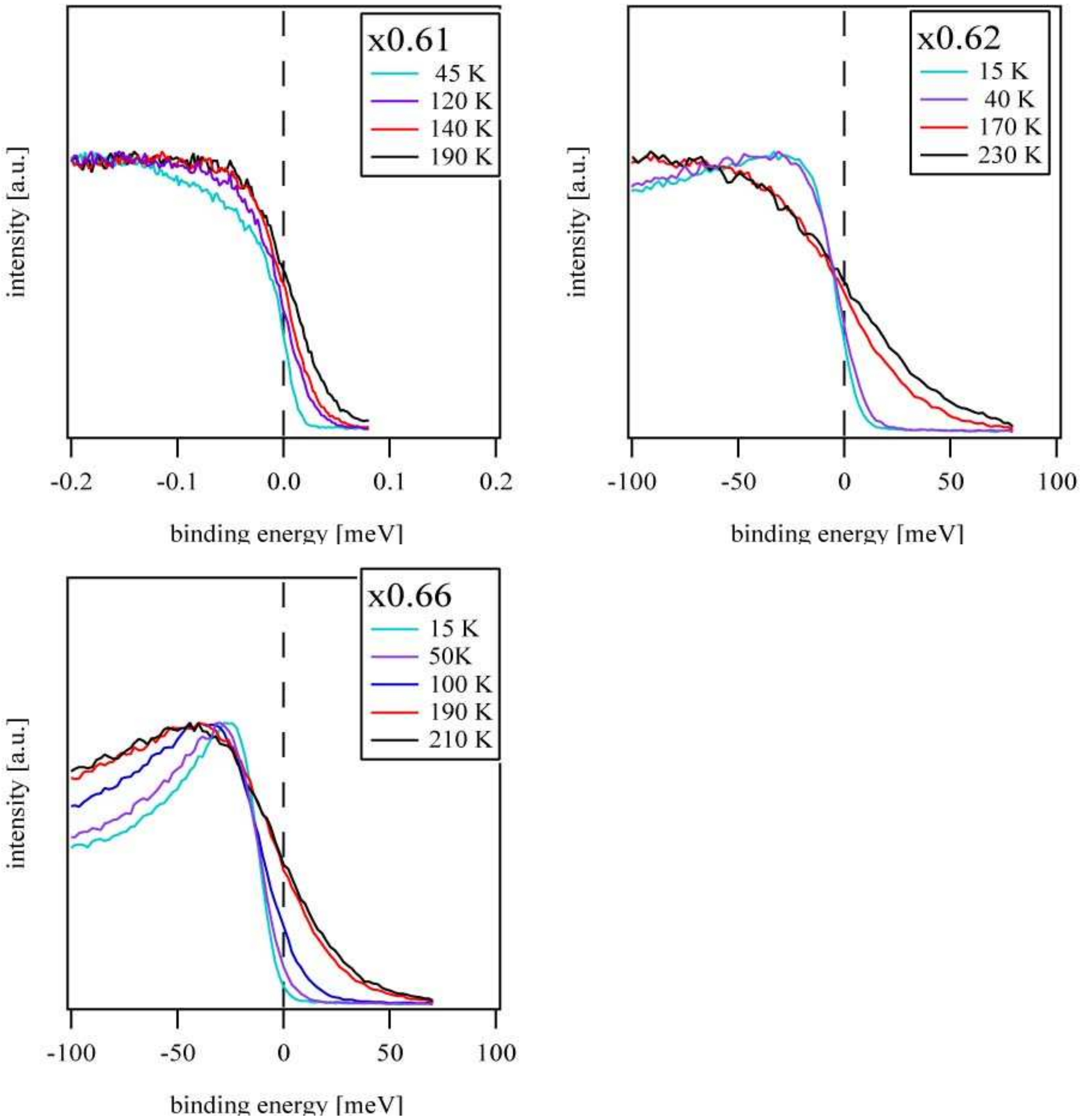
x0.61
45 K
120 K
140 K
190 K
intensity [a.u.]
-0.2
-0.1
0.0
0.1
0.2
binding energy [meV]
x0.62
15 K
40 K
170 K
230 K
intensity [a.u.]
-100
-50
0
50
100
binding energy [meV]
x0.66
15 K
50K
100 K
190 K
210 K
intensity [a.u.]
-100
-50
0
50
100
binding energy [meV]

vacuum ($< 1\times10^{-10}$ mbar) or cleaved by tape in the load lock ($< 8\times10^{-9}$ mbar) and then immediately transferred into the UHV measurement chamber onto the cold manipulator. The cleavage conditions are indicated in Appendix B.4 by 'M' for the manipulator cleavage and 'T' for the cleavage by tape in the loadlock. The photon source was either synchrotron radiation or a helium duoplasmatron (UVS 300). For measurements with the UVS 300, the base pressure increased from $\approx 1\times10^{-10}$ mbar to $< 3\times10^{-9}$ mbar when opening the valve to the lamp. Therefore, the higher pressure was only due to a higher partial pressure of inert helium gas which was also tested by mass spectrometry. After mounting the sample, it was then turned to the measurement position and measured in increasing temperature steps. Typically, the measurement position was not changed. Only very high temperatures sometimes required a change in height to account for the thermal expansion of the manipulator. After measuring at high temperatures, the gap was controlled at low temperatures to ensure no adsorbates had smeared the spectra around the Fermi energy. After that, the Fermi energy was determined by evaporated gold in the same measurement position at the lowest measured temperature. Thereby, a bending of E$_F$ in respect to the angle, most probably caused by a misalignment of the detector relative to the sample, could also be removed (see also [240], p. 43).

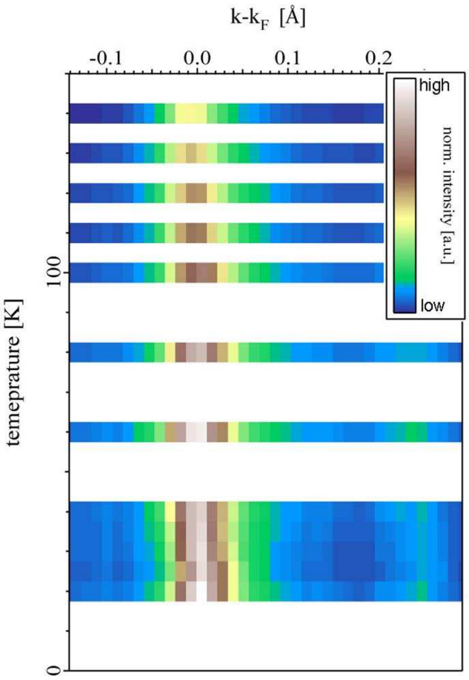

Figure 6.5: The normalized intensity around k$_F$ relative to the temperature (vertical axis). For achieving this plot, the spectra for sample x0.58-1 were integrated over ± 10meV around E$_F$.

EDC's at k$_F$

For processing, the normalization was chosen so that, in the energy distribution curves (EDC's), the unoccupied side is zero and the peak maximum near E$_F$ is one. Then the Fermi wavelength k$_F$ must be set. There are different methods to determinate k$_F$ from ARPES spectra. For a discussion of the methods see, e.g., [128] and the references [241, 242, 243, 244] therein. Here, the Fermi wavelength was chosen as the position where the spectrum at low temperatures near E$_F$ shows the maximum intensity. Fig. 6.5 shows the temperature evolution of the integrated spectra (± 10meV around E$_F$) for sample x0.58-1. At higher temperatures, the maximum intensity changes mainly due to the broadening of the Fermi function. Therefore, it is best to use the maximum intensity criterium at low temperatures.

Fig. 6.4 shows the change of the excitation at k$_F$ for some selected temperatures. Some of the following interpretations can be checked using these EDC's.

6.1.3 Doping dependency of the lifetime

Here, I want to discuss the width of the excitations at k_F for temperatures lower than the pseudogap-temperature and higher than T_C. The validation that these discussed EDC's are measured below the pseudogap-temperature will be provided in the next section.

What can be clearly stated from all the measurements is that the excitation sharpens at low temperatures. This sharpening is not so pronounced for the samples x0.42 and x0.61. A comparison of the linewidth relative to the doping is complicated by the use of different geometries. The comparison includes here only the samples x0.58-1, x0.61, x0.62 and x0.66. When referring to Appendix B.4, these samples were measured within the same conditions. The EDC's at T≈40K are shown in Fig. 6.6. For this comparison, the normalization was that the unoccupied part is zero and the 'background' at 0.5 eV binding energy is one. The excitation is quite well defined and more quasiparticle-like in the samples x-0.58-1, x0.62 and x0.66 while in sample x0.61 the excitation is very broad and ill-defined. Sample x0.61 was the non-superconducting sample which means that the sample sits exactly on a depression in T_C. From preliminary measurements on a 1/8 sample of $Bi_2Sr_{2-x}La_x$-$CuO_{6+\delta}$, a similar behavior was found; The excitation was very broad and ill-defined and the counting rate low.

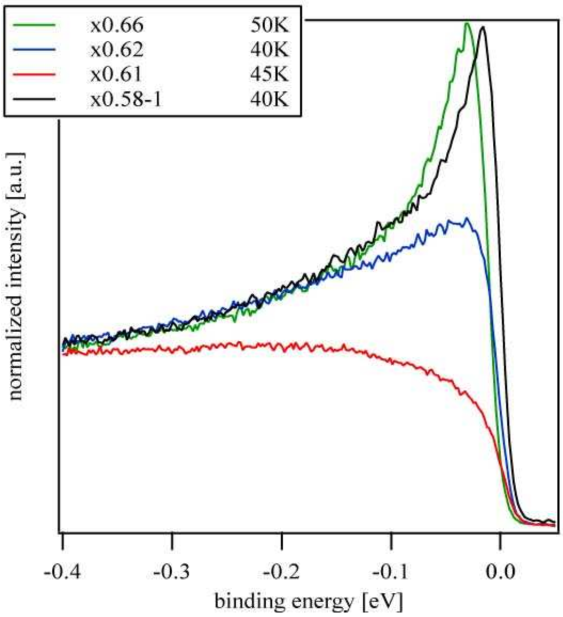

Figure 6.6: Comparison of EDC's of x0.58-1, x0.61, x0.62, and x0.66 at k_F for temperature T with $T^* > T > T_C$.

For understanding this broadening, the ordered state must be substantiated at a depression and a simple idealistic model must be created. I have already suggested that the most clean and pure ordering might be found at the hole doping of a depression, a suggestion which is supported near 1/8 by the magnetic ordering of $La_{1.6-x}Nd_{0.4}Sr_xCuO_4$ and $La_{2-x}Ba_xCuO_4$ [10, 11], and also the charge ordering in $La_{2-x}Ba_xCuO_4$ [12]. Due to the existence of the Zhang Rice singlet [99, 100], we might simplify the lowest excitation in this model as a hole on a CuO_2-plaquette moving in an antiferromagnetic background. In comparison with Fig. 6.7, an ordered insulating state is depicted by light-blue circles representing the holes and red arrows representing the electrons with spin. In this snapshot of Fig. 6.7, the antiferromagnetic spin fluctuations are simplified by an antiferromagnetic static order of the spins. What has been described so far is the state which might be expected at exactly the filling factor of a depression. The 1/8 case is shown here because it is a known configuration but the following will hopefully not rely on this depression. However, an electronic inhomogeneity within this ordered state can be produced by removing one electron. This extra hole is depicted in Fig. 6.7 as a dark-blue circle.

It can now be considered that the easiest way for this hole to move is a hopping along the transversal ferromagnetic grid as no spin flip occurs. This hopping is illustrated in the figure by the green arrows. Thus, in this transversal direction, a more metallic behavior can be expected due to the extra hole. This means that most intrinsic inhomogeneities within the perfect ordered state should be visible as nodal excitations in ARPES. Therefore, the cleanest pseudogap state can be probed near the antinode. Here, it is important to note that this kind of dual electronic structure is consistent with the detection of spectral weight along the nodal direction in 'stripe ordered' $\mathrm{La}_{1.4-x}\mathrm{Nd}_{0.6}\,\mathrm{Sr}_x\mathrm{Cu}\,\mathrm{O}_4$ [245]. It would also explain the 'U'-shape in the gap symmetry which was mentioned in the introduction.

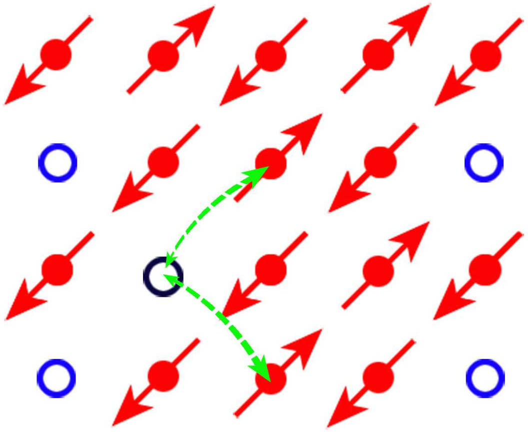

Figure 6.7: Cartoon of the ground state of the depressions plus one hole as inhomogeneity.

From the description above, one might think that the ARPES spectra at a depression should be quite well defined as there are no inhomogeneities. The state is stable and therefore the lifetime of the electrons in this state should be long. Thus, this would result in a sharp excitation. But there is a 'problem' and this is the fact that ARPES probes the one particle removal function. In a correlated system this means that the measured electron contains the information of the N-1 state. This N-1 state is depicted in Fig. 6.7. It is an otherwise perfectly ordered state with the flaw of having one hole too many. Therefore, the ordered state will never be probed by ARPES, but rather the decay of the photohole in this ordered system. By this consideration, it is understandable that the excitation near the antinode is broadened at the depression. This is because, in the nearly perfectly ordered ground state, the hole can decay by scattering away from the antinode to move along the transversal ferromagnetic grid, i.e. the nodal direction.

Now I will address the situation where there is more than one defective hole. In the case of a higher number of intrinsic defects, I can picture the system as being a superposition from the ordered ground state of the depressions plus an arrangement of a collective of defective holes. This arrangement can no longer be restricted on the nodal direction because no more density of states can be reserved there. The consequence is that the antinodal direction is also used. For the photoemission process, this means that a photohole produced at the antinode cannot decay in the nodal direction because this direction is filled. The lifetime of the photohole is therefore large. Thus, a sharp excitation is produced within the one particle removal function which is the notable fact for samples with hole-dopings different than the one of the depression.

The previous is admittedly a simple model but explains the change in linewidth quite naturally. The conclusion is that the broadening or scattering near the depression can be explained as a manifestation of a highly ordered state. Excitations with a long lifetime indicate a defective ordered state.

6.1.4 Extraction of the pseudogap temperature and magnitude

In the EDC's of Fig. 6.4, it is visible that a gap opens. For example, this can be seen in EDC's of sample x0.32 when looking first at the spectra on high temperatures. These spectra at T=175 K and 150 K rotate due to the Fermi function around one point, whereas the spectra at low temperature are shifted away from this point.

In the following, I will derive quantitative results for the dependence of the gap on temperature. Notwithstanding my suggestion above, in the following I must quantify a gap of unknown origin. To do this, I must choose a method of data processing which does not rely on a theory. In a case where the spectral function is known, one would be able to fit the spectra. Aside from a fitting routine, there are typically two methods to quantify the gap: One is by the *leading edge method* and the other is by the *symmetrization method* [246]. Both methods must be used because each has its own problems. For the examination of the temperature behavior, the leading edge method is adequate. After an introduction of the method, I will discuss some specialities in the temperature behavior. As the leading edge method gives the lowest boundary but not the real gap, the symmetrization method will be used for an estimation of the real gap magnitude. The results of both methods will then be compared and shown in the section thereafter.

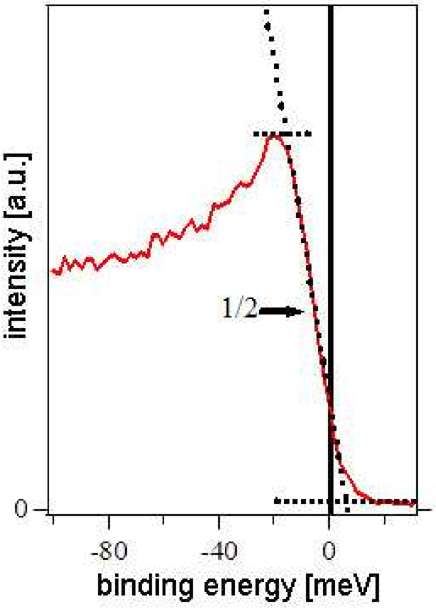

Figure 6.8: Directive of the leading edge midpoint: First determine the average intensity of the constant background on the occupied side and the height of the first maximum near E_F. Then the energetic position of half of the intensity between the background and the maximum must be chosen.

Pseudogap temperature and magnitude according to the leading edge method

The leading edge method can be seen as the air lever of gap determination in ARPES. It is simple and comparable but does not give the real gap magnitude but rather the shift of the spectrums leading edge. The used measurement directive of the leading edge midpoint (LEM) is illustrated in Fig. 6.8: The LEM is obtained by first determining the average intensity of the constant background on the occupied side and the height of the first maximum near E_F. The energetic position of half of the intensity between background and maximum must then be chosen. This position is found by a linefit using the points in an interval ± 3 meV around the position of half the intensity.

A good discussion about the quality and problems of the leading edge method is provided by Kordyuk et al. [247]. Let me note one problem of the leading edge midpoint. For this, I assume

Figure 6.9: The leading edge midpoint(LEM) in dependence of temperature

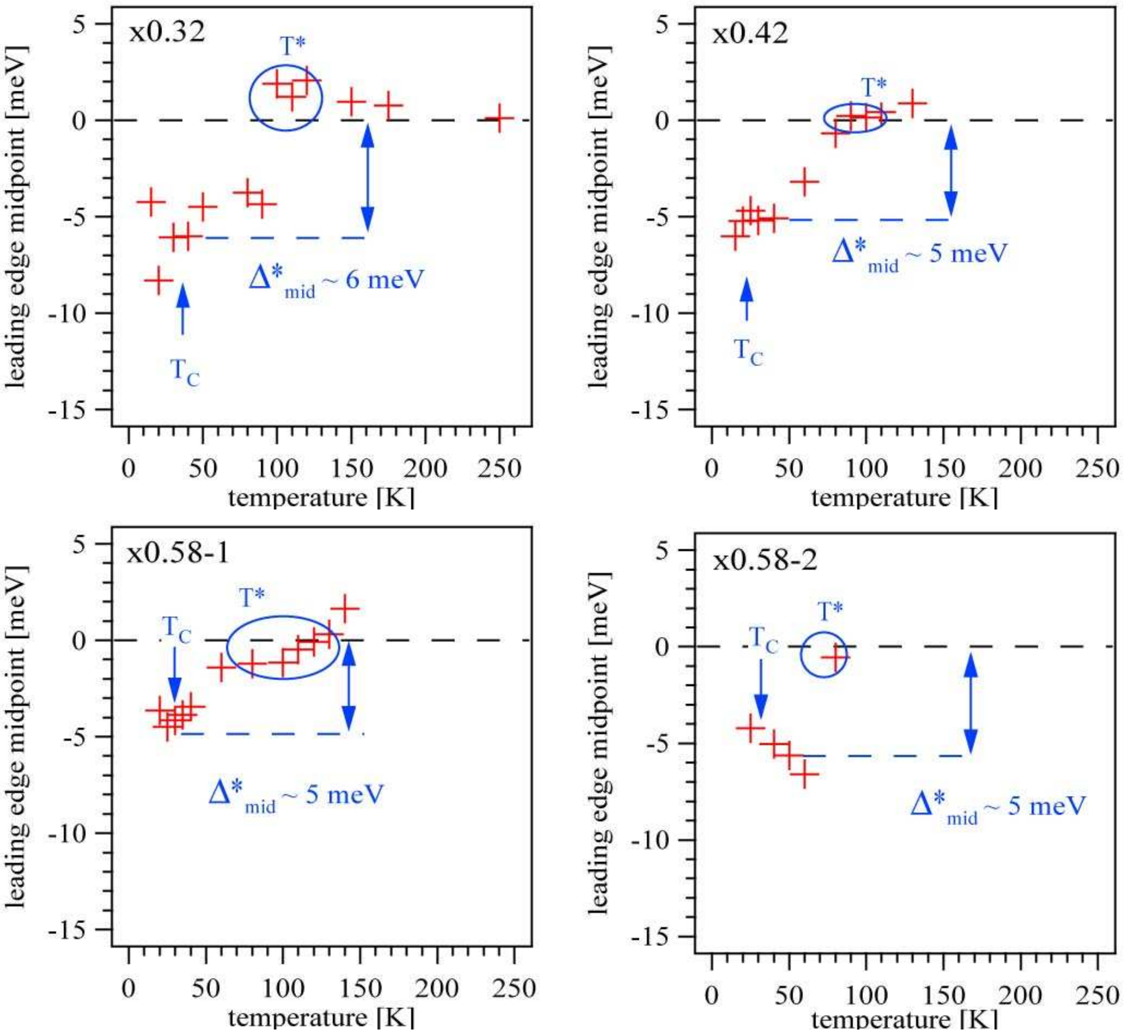

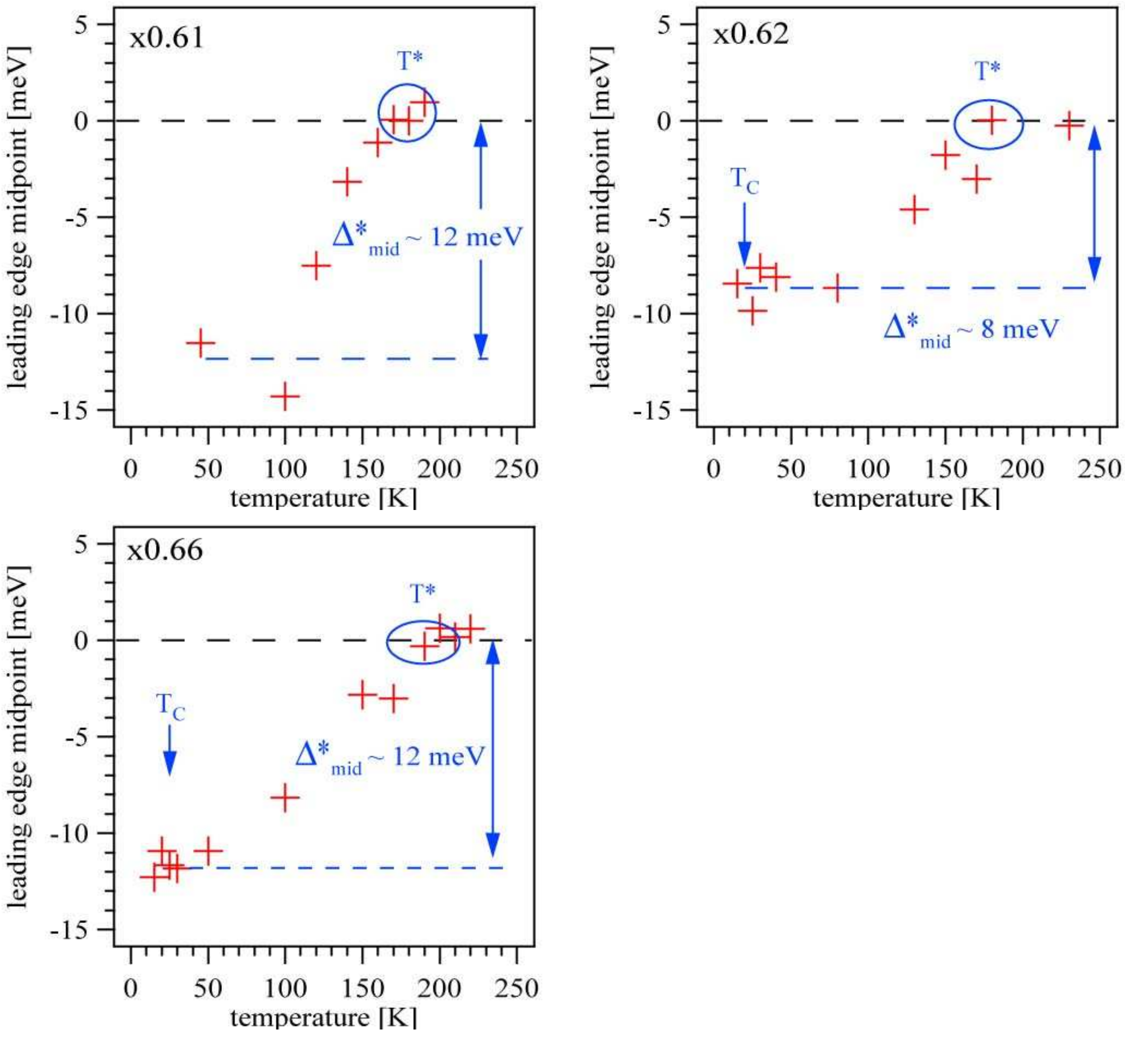
x0.61
T*
Δ*mid ~ 12 meV
leading edge midpoint [meV]
temperature [K]
5
0
-5
-10
-15
0
50
100
150
200
250
x0.62
T*
TC
Δ*mid ~ 8 meV
leading edge midpoint [meV]
temperature [K]
x0.66
T*
TC
Δ*mid ~ 12 meV
leading edge midpoint [meV]
temperature [K]

a non-gapped spectral function written in simple form as

$$A(\vec{k},\omega,T) \simeq \frac{\Sigma''}{(\omega - E(\vec{k}))^2 + \Sigma''^2}\,. \tag{6.5}$$

I now must assume a self-energy. One which fits well with the temperature dependency is the empirical spectral function of Kordyuk et al. [247]. There, the imaginary part of the self energy is given as $\Sigma'' = \sqrt{(\alpha\omega)^2 + (\beta T)^2}$. In principal, this spectral-function is nothing more than a simplified one of a marginal Fermi-liquid. However, basically the excitation, which will be measured by the leading edge, can be considered as a Lorentzian which broadens with temperature. But when this broadening occurs, the midpoint changes. Thus, the LEM not only gives the gap but is also sensitive to a change in width of the probed spectral function. As described in [248, 247, 249], the energy distribution curves (EDC) can be integrated over a finite momentum range around k_F to ensure that the leading edge midpoint of a non-gaped spectrum stays at the Fermi level. For the following analysis it was integrated over ± 0.06 $Å^{-1}$. This area is sufficiently large which might also be concluded from Fig. 6.5 as the area includes all significant changes in the maximum intensity due to temperature. It should be stated that this routine does not prevent the shifting of the LEM in a gapped spectrum due to change in the self-energy. Therefore, relative to the temperature, the LEM measures an opening of a gap but also a change in excitation width.

The reader may want to verify some of the following interpretations. Therefore, the resulting LEM's relative to the temperature are shown in Fig. 6.9.

In all measurements, the expected opening of the pseudogap can be seen by the shift of the leading edge midpoint. We see the LEM starting to move away from E_F and saturate at low temperatures. The saturation sometimes needs a large temperature interval as in sample x0.66 or, as in x0.32, an abrupt jump of the LEM instead of a saturation. For the quantitative analysis, the pseudogap-temperature T^* and a maximum LEM-pseudogap Δ^*_{mid} must be defined. The pseudogap-temperature is taken as the temperature where the LEM changes significantly. The LEM-gap Δ^*_{mid} was chosen as the difference of the Fermi energy E_F and a 'saturated' LEM position shortly above the superconducting transition temperature T_C. In some measurements - see x058-2 - this might not be a perfect description. I will discuss the qualitative results later. Here, it is enough to know how T^* and Δ^*_{mid} can be determined.

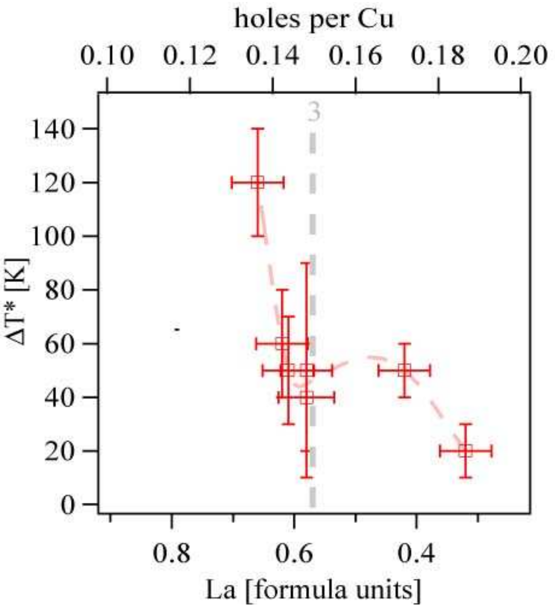

Figure 6.10: The temperature range where the LEM gap saturates ΔT^* vs doping and La concentration. Also included is the position of the 3rd depression and a cubic spline as guide to the eye.

What can also be observed by the figures is that there is no large contribution of a superconducting gap in respect to the limited temperature range. For BCS theory, the gap is proportional to T_C; When using the BCS-formula for Bi2201 we would expect a zero-temperature superconducting-gap of up to about 4 meV. Thus, I cannot state that there is no superconducting gap. What I can state is that, in respect to the resolution and the achievable temperature, in the antinodal direction there is no large contribution from the superconducting gap, but instead from the pseudogap.

When looking at x0.32, at T^*, a bounce in the LEM might also be observed. Let me note here that such behavior of the LEM-gap was recently found in Bi2212 [248]. From the previous discussion, we know that an increase or decrease in the leading edge midpoint does not necessarily mean that the gap changes. It could also be a broadening or narrowing of the excitation. Although more examination is necessary, I attribute a possible change in linewidth at T^* to an onset of ordering. For this ordering, I will now refer back to observations that I am able to quantify by my conducted measurements, e.g. that the LEM sometimes jumps and sometimes saturates. Let me refer back to the simple model described above; The model depicts that an ordered state exists at a depression and disorder occurs away from a depression. Let us further consider the onset of electronic ordering as a kind of crystallization process; An ordering from a high-temperature disordered state can be more easily achieved in a system with holes equal to the filling factor of a depression as in an electronic structure with (intrinsic) defects. In my opinion, exactly this behavior can be observed in the temperature range the LEM gap saturates. In the following, this temperature range is noted as ΔT^*. In the case where ΔT^* is small, the system is nearly clean, whereas if ΔT^* is large, many defects are present within the system. One can say that ΔT^* probes the population of antinodal defects which can be determined from Fig. 6.9 by a 10%-90% criterium as it is used for ΔT_C in AC-susceptibility (see Appendix A.2). This refined ΔT^* vs doping and La concentration is shown in Fig. 6.10. It can clearly be stated that, around the depression, ΔT^* is small. Note that the sample x0.32 is near the next depression.

In the case where the temperature range that the LEM needs to saturate is proportional to the number of defective holes, it can therefore be stated that the ground state at a depression is the cleanest pseudogap state.

The symmetrization method

For the final comparison of the gap magnitude, I will explain the symmetrization method [246] which I additionally use to quantify.

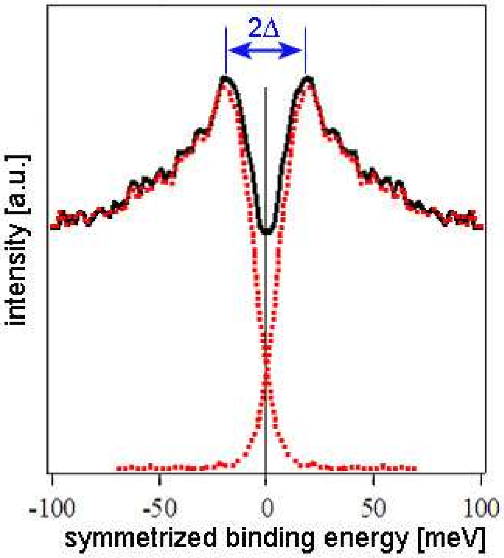

Figure 6.11: Directive of the gap estimation for the symmetrization method: Mirror the spectrum at E_F. The dotted lines are the spectra and its mirror image. The straight line is the addive of both. The gap is then given by the position of the peak maximum which is next nearest to zero binding energy.

The symmetrization directive is depicted in Fig. 6.11. By mirroring the spectrum at E_F, the contribution of the Fermi-function is basically removed. The gap is then given by the position of the next peak maximum nearest to E_F. The problem with the symmetrization method is its sensitivity to the correct determination of E_F. From a comparison of a fit of the gold spectra and the nodal direction for sample x.032, the uncertainty in E_F can be estimated as about ± 3 meV. This seems like a small value but let me point out that the symmetrization method is essentially a deconvolution where a small shift can produce a high error. From the directive of Fig. 6.11, the difference between the leading edge midpoint and the symmetrization gap can be seen; The leading edge gives a much smaller gap than the symmetrization.

The symmetrization gap was taken at the lowest temperature. For the sample x0.61, no result was obtained by the symmetrization method as the spectrum was very broad due to the enhanced scattering explained before. It can only be stated that a gap < 100 meV exists for that sample.

6.1.5 Pseudogap temperature and magnitude relative to the doping

Here, I want to finally show and discuss the results for T^* and the gap magnitude. A table with all results is presented in Appendix B.5. Also included there are -to my knowledge- all ARPES results on the antinodal LEM-gap in Bi2201 from [231, 234, 250, 251]. From these, one can conclude an overall good correspondence in the order of magnitude of the LEM-gap.

Fig. 6.12.1 and Fig. 6.12.2 illustrate the key results of the ARPES measurements. In Fig. 6.12.1, the pseudogap-temperature T^* as derived by the leading edge analysis is depicted. Also included is the position of the 3rd depression as derived in Chapter 4.3.2 which was found at a hole doping concentration of about 0.15 holes per Cu. Fig. 6.12.2 shows the leading edge midpoint gap Δ^*_{mid} and the symmetrization gap Δ^*_{sym}. Please note that the scale for the LEM gap is on the left while the scale of the symmetrization gap is on the right. One can see that there is a pseudogap in the overdoped region and it is clear that a change or jump occurs near the depression. As in both derived magnitudes Δ^*_{mid}, and Δ^*_{sym} this change is visible in the pseudogap-temperature T*.

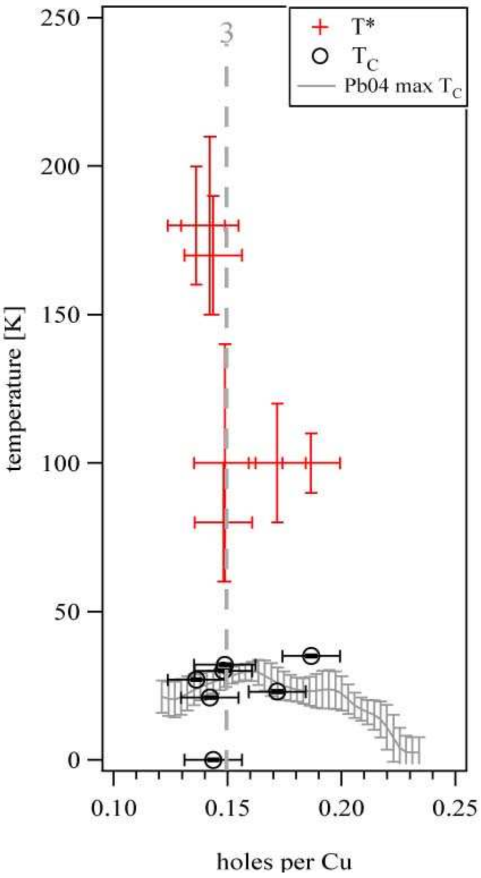

6.12.1: The pseudogap-temperature T* as derived by the leading edge analysis. Also included is the position of the 3rd depression which was found at a hole doping concentration of about 0.15. T* changes its value significantly near the depression.

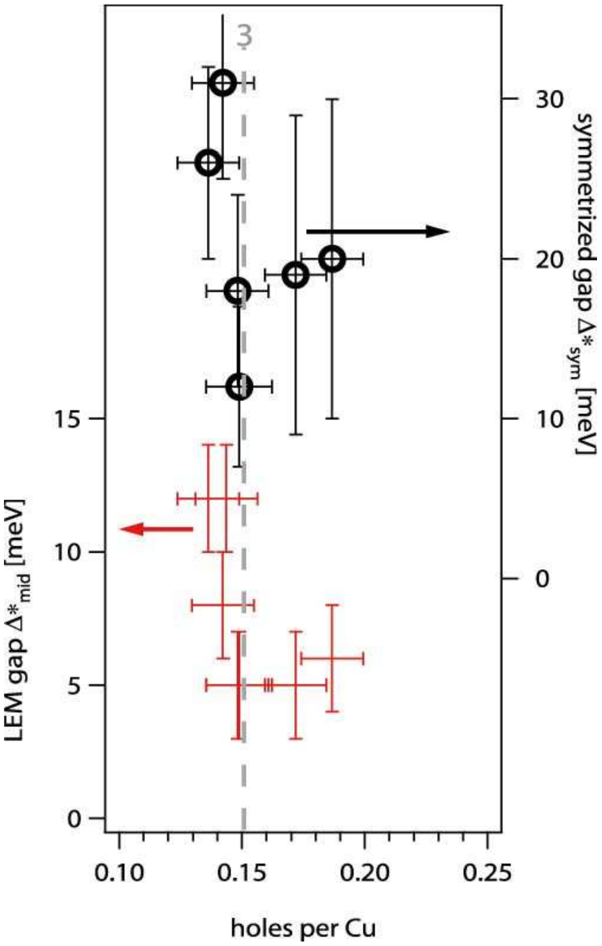

6.12.2: The leading edge midpoint gap Δ^*_{mid} as derived by the leading edge analysis is plotted with respect to the left scale. The symmetrized gap Δ^*_{sym} as derived by the symmetrization method is plotted with respect to the right scale. Please compare with tab. B.3. Again included is the position of the 3rd depression. Both gaps change strongly near the depression.

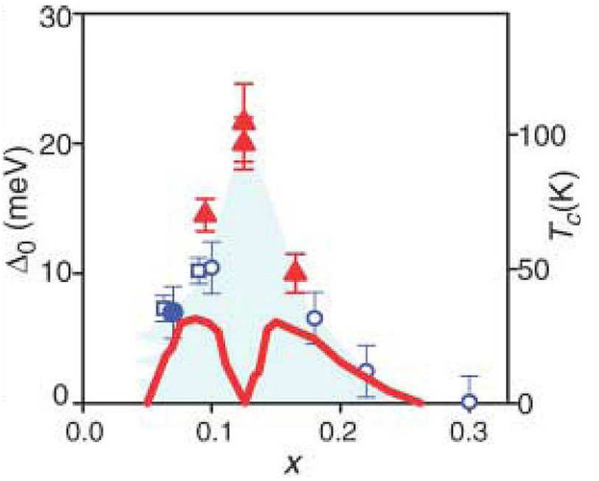

Figure 6.12: From Valla et al. [249]: Doping dependence of the antinodal leading edge midpoint gap Δ_0 in $La_{2-x}Ba_xCuO_4$(triangles) and $La_{2-x}Sr_xCuO_4$(circles and squares). Solid symbols are the study by Valla et al. [249]; open squares are from [252]; open circles are given in [232]. The red line represents doping dependence of T_C for LBCO from [6].

It might be interesting here to add comparison with an other publication: An interesting contribution about a change of ARPES-derived properties near the 1/8 depression comes from Valla et al. [249]. Fig. 6.12 shows the results for the gap magnitude. Depicted is the leading edge midpoint gap of $La_{2-x}Ba_xCuO_4$ (LBCO) and $La_{2-x}Sr_xCuO_4$ (LSCO) near the 1/8 depression. For $La_{2-x}Ba_xCuO_4$ and $La_{2-x}Sr_xCuO_4$ the pseudogap magnitude is not growing linearly when going to the underdoped side. For $La_{2-x}Ba_xCuO_4$, it can be clearly seen that the highest measured value of the gap is the value at the 1/8 depression. We see by this comparison that a change in gap magnitude near a depression is also present in $La_{2-x}Ba_xCuO_4$ and maybe as well in $La_{2-x}Sr_xCuO_4$.

Compared with the data in Fig. 6.12.2, here we see that the Bi2201 sample with T_C=0 is within the error on the depression and exhibits one of the largest gaps with 12 meV. This equals the finding in LBCO at the 1/8 depression by Valla et al. [249]. To avoid the risk of overinterpretation, let me state that not enough measurements at lower dopings are present here. As long as no more measurements are available, the shape of the derived quantities should be treated as moving over an instability at the filling factor of a depression. What I would expect in my model presented above is that the gap is not symmetric around a depression because the removal of a hole is not the same as the insertion of one.

6.1.6 Summary of the ARPES results

The following is a summary of this section about the ARPES measurements. It was shown that the presence of a depression leads to broad, ill-defined antinodal excitations in the vicinity of the Fermi surface. It was found that the temperature range, which the leading edge midpoint needs from T* to saturate, reacts to the doping value of a depression. At this doping value, it was also shown that the pseudogap-temperature and the gap change strongly. My interpretation was that an instability is present at this filling factor.

To understand most of these phenomena, I built a simple model. This model considers a perfectly ordered electronic structure at a depression. The clearest pseudogap state is at a depression. The pseudogap there reflects the formation energy for this ordered state. Dopings that are not near a depression result in defective holes. I suggest that the defective holes first produce density of states in the nodal direction. At a higher number of defective holes, density of states will also be available in the antinodal direction. The density of states in the measured k-space might be read by ΔT^* which is the temperature range the leading edge midpoint needs from T^* in order to saturate.

Along with this interpretation, it was also found that there is no significant contribution of the superconducting gap in the antinodal direction. It was further shown that the pseudogap exists in the overdoped region.

6.2 T* measured by resistivity

As it turned out in the last section, the pseudogap changes its properties strongly around a hole-doping value of a depression - a behavior which was also qualitatively found for LBCO [249].

It might be of interest to control and verify this behavior of the $Bi_{2-y}Pb_ySr_{2-x}La_xCuO_{6+\delta}$ system with another method. In order to do this, I will use resistivity measurements of the ab plane. Concerning resistivity measurements, it has long been known [253] that the opening of the pseudogap at T* leads to deviations from the high-temperature behavior. Therefore, we can identify a pseudogap-temperature but must identify a good extraction routine. The advantage compared to ARPES is that by this method a high number of samples can be measured. Using these numerous samples, I will clearly visualize the experimental phase diagram of Bi2201.

From this it can be unambiguously stated that the pseudogap-temperature exists in the overdoped region and changes significantly at the doping of each depression. Furthermore, I will clearly show that the ground states of the depressions are eutectic phases. Following this section, we will be able to compare the T* measured by ARPES with the T* achieved by resistivity.

6.2.1 Sample characterization

For the following, samples of two La-dependent series were used: One is the Pb0 series - Bi_2-$Sr_{2-x}La_xCuO_{6+\delta}$ without Lead and the other is $Bi_{2-y}Pb_ySr_{2-x}La_xCuO_{6+\delta}$ with Pb substitution of y≈0.4 formula units (Pb04). The latter can be directly compared to the series measured by ARPES. The set for the Pb0 series contained 31 crystals whereas 15 crystals were used for the Pb04 series. The chemical composition relative to the Lanthanum as gained by EDX is shown in Fig. 6.13.1 for samples without Pb and in Fig. 6.13.2 for samples with y≈0.4. A linefit relative to the La content(x) for Pb-free samples gives

$$\begin{aligned} c(Bi) &= (2.06 \pm 0.02) - (0.14 \pm 0.03)x \quad ; \quad \chi^2 = 0.028 && (6.6) \\ c(Sr) &= (1.82 \pm 0.02) - (0.88 \pm 0.03)x \quad ; \quad \chi^2 = 0.023 && (6.7) \\ c(Cu) &= (1.12 \pm 0.01) - (0.02 \pm 0.02)x \quad ; \quad \chi^2 = 0.014\,. && (6.8) \end{aligned}$$

The range of La goes from about 0.2 to 0.9 formula units. For Pb0.4, the linefit yields

$$\begin{aligned} c(Bi) &= (1.70 \pm 0.02) - (0.37 \pm 0.05)x \quad ; \quad \chi^2 = 0.011 && (6.9) \\ c(Pb) &= (0.37 \pm 0.02) + (0.08 \pm 0.04)x \quad ; \quad \chi^2 = 0.008 && (6.10) \\ c(Sr) &= (1.80 \pm 0.02) - (0.71 \pm 0.02)x \quad ; \quad \chi^2 = 0.010 && (6.11) \\ c(Cu) &= (1.13 \pm 0.02) - (0.00 \pm 0.02)x \quad ; \quad \chi^2 = 0.004\,. && (6.12) \end{aligned}$$

Here, the La-content ranges from 0.2 to 0.7 formula units.

From the graphic version of the characterization results of the Pb-free samples in Fig. 6.13.1, we see an overall well-defined system. The Pb04 series has a slight variation of the Pb content but this does not exceed ± 0.05 formula units from the average.

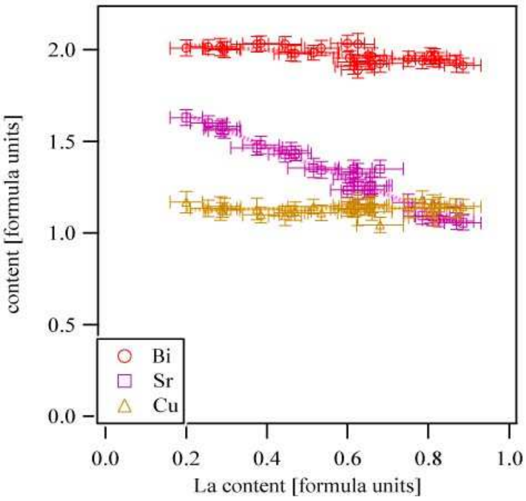

6.13.1: The chemical composition relative to the Lanthanum for the here used Pb0 series.

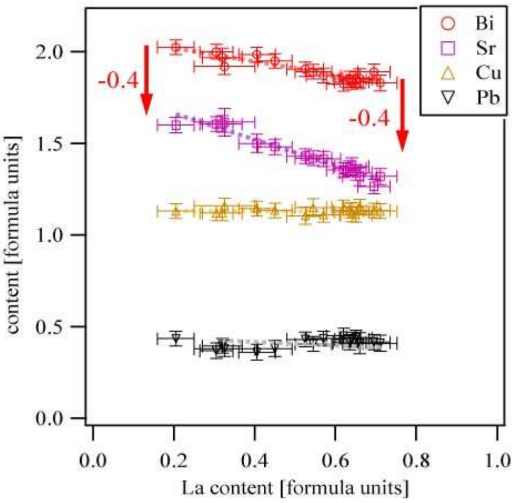

6.13.2: The chemical composition relative to the Lanthanum for Pb04. Please note the shift by 0.4 formula units of the Bi-content.

6.2.2 Resistivity measurements

With these well-defined samples, resistivity measurements using a standard AC four-probe technique were taken. For some details see Appendix A.4. In the following, I first describe the obtained curves and then explain the procedure for refining T*.

Fig. 6.13 shows a qualitative overview of the gained resistivity relative to the Lanthanum content and temperature. Here and in the following, the normalized resistivity is used. It is given as the value of the resistivity divided by its value at 250K, hence $\rho^N_{ab}(T) = \rho_{ab}(T)/\rho_{ab}(250K)$. The normalization makes it possible to compare the resistivity at different dopings and avoid the uncertainty of the specific resistivity due to geometric uncertainties of the contacts. Without the normalization and using the specific resistivity the error is assumed to be between 5% and 10%.

Here, I will describe the resulting resistivity curves of Fig. 6.13. On the left side, $\rho^N_{ab}(T)$ for the Lead-free series (Pb0) is shown while on the right side it is depicted for the y≈0.4 series (Pb04). The visualization is in the form of a waterfall plot where the normalized resistivity was shifted up according to the La content of the sample. I will first give a conventional description of the resistivity and later I will point out the specialities.

When we start with the Pb-free series at low Lanthanum substitution, we look at the lower left panel and the curve with x=0.2. This sample is superconducting which can be seen by the drop at low temperatures. Furthermore, it is overdoped and exhibits a doping of p=0.19(6)±0.015 holes per Cu according to Eq. (4.3). When we look at the curve, we see that at high temperatures the curve is nearly linear with a weak upturn at higher temperatures. It can be compared with higher overdoped samples, e.g., the sample of the Pb04 series with a La content of x=0.21. According to Eq. (4.4), this sample has a hole concentration of p=0.20(3)±0.015 holes per Cu. There, the more pronounced upturn at higher temperatures can clearly be noticed. This $\rho \sim T^{\alpha}$ behavior with $\alpha > 1$ verifies the expectation that a more overdoped system is more Fermi-liquid-like and more metallic. Let us now look towards optimally doped samples. There, we see that the T^{α} becomes a T-linear behavior. The linear behavior in the curves x=0.39 for Pb0 and for Pb04 by x=0.55 is quite pronounced. When we now focus on the underdoped side, we see that a low temperature upturn becomes stronger within the curves. This is clearly visible in the curves x=0.46 or 0.66 for Pb=0 and e.g. 0.71 for Pb04. This confirms our expectation that a more underdoped system is more semiconducting/insulating. The curves for the superconducting samples round and drop to zero after this upturn. The overall behavior of the resistivity curve is often called 'S-shape-like'. The drop or rounding above T_C was, to my knowledge, first reported by Vidal et al. [254] and associated with superconducting fluctuations which seems widely accepted today (see e.g [238, 255]). To continue with the description, in the Lead-free series we can also reach the non-superconducting/charge-transfer-insulating region. The curves for these samples are depicted in the upper box on the left side of Fig. 6.13. Due to the strong insulating behavior, these curves required a larger scaling range. At the end of this description, I would also like to point to the inset of the upper panel of Pb0. There, it is shown that, for low doping at about T=5K, a change occurs in the curves which points to a phase transition. The AC-susceptibility revealed the onset of diamagnetic behavior for one sample with x=0.89, but the signal did not saturate above 2K. It can be suggested that this is a superconducting phase. As discussed in the conclusion of Chapter 4, this superconducting phase has to be expected when believing that the width of the 'superconducting dome' is generic: As superconductivity of $La_{2-x}Sr_xCuO_{4\pm\epsilon}$ is detectable down to 0.05 holes per Cu, a superconducting phase should also be present for the Bi2201 system. However, perhaps for structural reasons, the superconductivity is suppressed in Bi2201. These structural reasons might be given by the dominant monoclinic superstructure present at the high La values which I discussed briefly in Chapter 3.3 (see Fig. 3.9). In the following I will call this phase 'suppressed superconducting phase' but it should be kept in mind that further examinations are necessary to determine the exact nature of this phase.

Despite the last point, what was described by the curves in the preceding paragraph can be regarded as a common consensus about the behavior of the resistivity upon doping. It can be summarized as follows: At the overdoped side a T^{α} behavior is present. From overdoped to optimally doped, the T^{α} becomes a T-linear behavior. Then, in the underdoped superconducting system, a low temperature upturn evolves which is followed by a downturn producing a curve which can be called 'S-shaped'. As can be taken from this summary, this behavior is often used for fast characterization: Samples with a low temperature upturn (a S-shape) are underdoped while samples with a linear behavior are optimally doped. In contrast to the former, a more detailed view of Fig. 6.13 reveals that the low temperature S-shape and the T-linear behavior

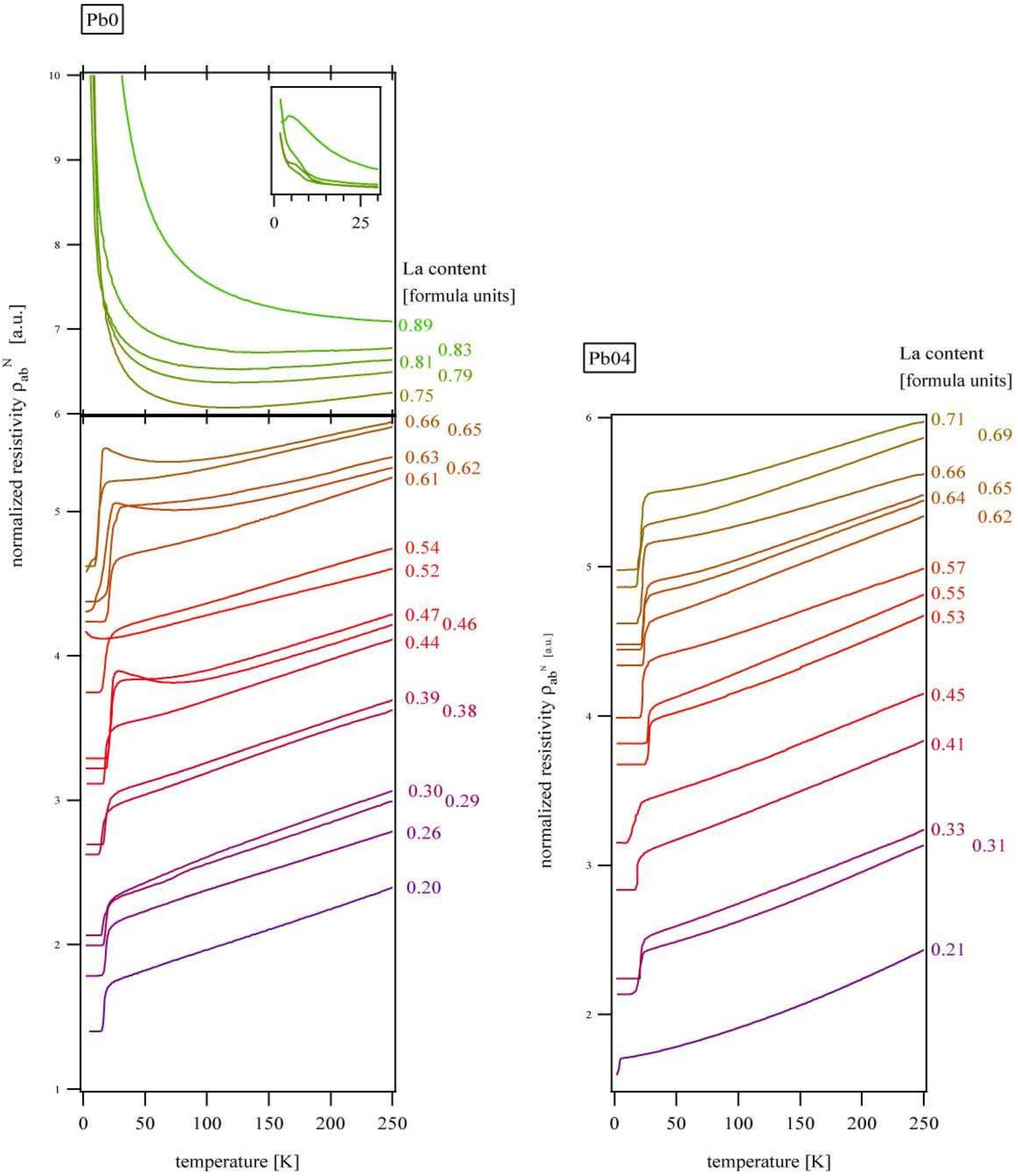

Figure 6.13: Overview of the resistivity measurements for $Bi_{2-y}Pb_ySr_{2-x}La_xCuO_{6+\delta}$. On left side, the curves of the samples without Pb are shown. On the right side, the curves are for $Bi_{2-y}Pb_ySr_{2-x}La_x$-$CuO_{6+\delta}$ with Pb substitution of y≈ 0.4 are depicted. The Lanthanum content is written beside each curve.

interchange. For example, this can be seen when looking at the behavior of the curves at Pb0 from x=0.46 over 0.52 to 0.62. The non-superconducting sample is at x=0.52±0.05. As evaluated in Chapter 4.3, this sample is at depression no. 2 at about x=0.53 formula units - in fractional holes this is the 1/8 depression. Around the depression, the curves are T-linear and further away from the depression they become S-shaped. Since the downturn in the S-shaped curves is associated with superconducting fluctuations, this means we see the influence of the depressions not only in non-superconducting samples, but also in superconducting samples. Therefore, the T-linear behavior would not be a sign for optimally doped samples, but a sign for for being near to a depression. In my view, it is only a fortunate circumstance that enough depressions are present around optimally doping.

6.2.3 Resistivity maps

Before coming to the derivation of the pseudogap-temperature from the curves shown, I will now show a possible means of visualizing the phase diagram using the obtained data. This is also to give the reader a general idea of the kind of visualization which I use in the following. Let me refer back to the generic phase diagram shown in Fig. 1.0 of the motivation of this thesis. Fig. 6.14 shows the resistivity data as processed by the Gaussian slotting algorithm of Appendix B.1. The parameters were Δy=3K and Δx=0.01 formula units (La-direction). The left graph shows the result for the Pb0 series and the right shows the result for the Pb04 series. Shown in each of the two graphs is the averaged normalized resistivity $\rho_{ab}^{N}(T)$ relative to the temperature (vertical axis) and Lanthanum-content (upper horizontal axis) or hole-concentration (lower horizontal axis). The hole concentration was calculated by means of Eq. (4.3) and (4.4). This type of diagram might be called a 'resistivity map' (RM). For Pb0, the region from 0.05 up to 0.20 holes per Cu can be visualized. The region Pb04 only reaches from 0.13 to 0.2 holes per Cu. The colorscale on the upper left indicates the value of $\rho_{ab}^{N}(T)$. The black crosses give the La content of the individual samples and, therefore, can be used to judge the statistical relevance of the averaged diagram.

When we look at the left RM for Pb0, we see a blue area with $\rho_{ab}^{N}(T) > 1$ at low hole doping. This area indicates the high insulating region. It is of course clear that the criterium $\rho_{ab}^{N}(T) > 1 = \rho_{ab}^{N}(250K)$ is not a very accurate criterium. Therefore, we should see this region only as a qualitative representation. Within the measured region of the resistivity map, we also see a white area which is the area with $\rho_{ab}^{N}(T) \simeq 0$. The white area qualitatively represents the superconducting region. Therefore, the crossing from white to brown marks T_C. The change in color from brown to yellow might then mark the superconducting fluctuations. Let me highlight again that these statements should be considered qualitatively and in respect to the normalization, the smoothing produced by the algorithm and the number of measured samples.

We can also see some depressions in the RM. Referring back to Chapter 4.3, the depression are expected at about 0.125;0.15 and 0.188 holes per Cu. For Pb0, these three depressions can be seen clearly. Due to the measured region, the 0.125 depression for Pb04 cannot be seen. The other depressions are less pronounced: Within the resolution, the 0.15 and 0.188 depression can be suspected. We will soon see them more clearly. With regard to the detection of the depressions within the superconducting dome, at high temperatures the influence of the depressions can also be seen in the RM. Let us focus now on the Pb0 graph: When staying at the temperature line of 120 K and looking at 0.15 hole doping, we have a brown-yellow color which corresponds to $\rho_{ab}^N(T) \approx 0.5$. Maintaining this temperature and moving to the underdoped side, we see a sudden change: The color become yellows which means $\rho_{ab}^N(T) \approx 0.7$. This happens around a hole doping of 0.125. The vertical line of this change can be seen up to 160K. This change is obviously caused by the T-linear behavior near a depression as explained above.

Furthermore, this last example again illustrates that the depressions have an impact on the high-temperature behavior, a fact we already know from the ARPES measurements. For the resistivity, this can be compared to the behavior found in LSCO by Komiya et al.[8]: There, the hole positions of the depressions were detected by a higher resistivity at high temperatures (>T$_C$).

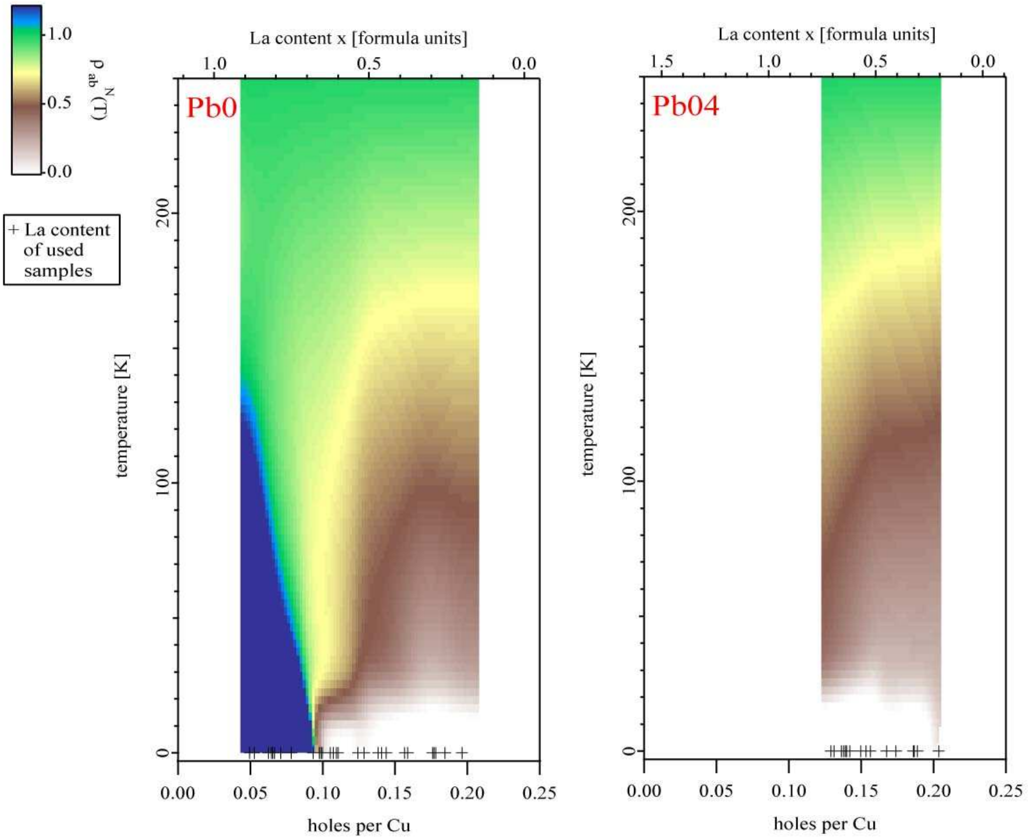

Figure 6.14: Resistivity maps: Averaged normalized resistivity $\rho_{ab}^N(T)$ relative to the temperature (vertical axis) and Lanthanum (upper horizontal axis) or hole concentration (lower horizontal axis). Left side is for $Bi_2Sr_{2-x}La_xCuO_{6+\delta}$(Pb0), the right for the $Bi_{2-y}Pb_ySr_{2-x}La_xCuO_{6+\delta}$with y=0.4 (Pb04). The colorscale on the upper left indicates the value of $\rho_{ab}^N(T)$. The black crosses represent the La content of the individual samples used for the averaging.

6.2.4 Definitions of the pseudogap-temperature

In the following, the pseudogap-temperature T* will be derived from the measurements. An early definition of the pseudogap-temperature was using the observation that the very high-temperature resistivity behavior was found to be linear [75, 76, 77]. Therefore, Ito et al. [256] used the deviation from the linear dependence in $YBa_2Cu_3O_{7-x}$ as a mark for T*. However, this definition poses a problem, since the linear dependency at high temperatures is typically found only in a very narrow region around optimum doping and in the underdoped side; Defining a pseudogap-temperature on the overdoped side by the linear behavior is problematic because, as shown before, in the overdoped region a more a T^{α}- behavior can be found. This is why the zero of the second derivative in respect to the temperature was recently used as a mark for T* [238].

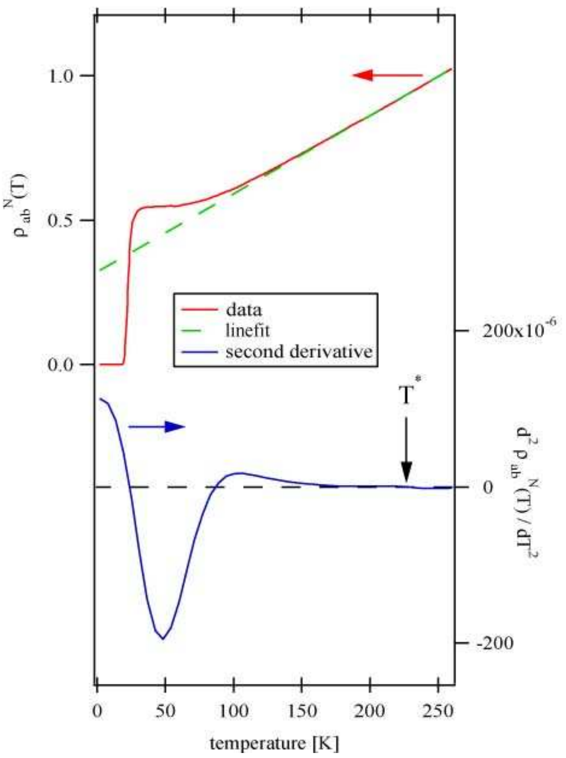

Figure 6.15: Graph to demonstrate the two methods for extracting the pseudogap: The upper half with the scale on the left shows the normalized resistivity curve ($\rho_{ab}^N(T)$) for $Bi_2Sr_{2-x}La_xCuO_{6+\delta}$ with x=0.47 together with a linefit. The lower half with the scale on the right side shows the second derivative: $d^2\rho_{ab}^N(T)/dT^2$.

Fig. 6.15 illustrates both definitions for a curve of $Bi_2Sr_{2-x}La_xCuO_{6+\delta}$ with x=0.47. This is a slightly underdoped sample. In the upper half of this figure $\rho_{ab}^N(T)$ is shown together with the linefit. Looking at the upper part, we can already see why it is hard to define T* by the linefit method; We see that it is difficult to objectively quantify a point where the resistivity deviates from the line because the deviation occurs gradually and continuously (see also [238]). On the lower half of Fig. 6.15, the second derivative in respect to the temperature is shown. It can be seen that defining T* by the zero should also be regarded with some caution because for the computation a soft smoothing must be applied. To give the routine, the derivative algorithm was taken as the central numerical derivative. The smoothing was achieved by the moving-average ('box smoothing') algorithm over 20K. Smoothing can be considered the most crucial parameter and great care was taken for this. Let me note that this sample represents the worst case as here the slope in the region of the pseudogap-temperature is one of the weakest found. A temperature-dependent lock-in technique would be beneficial when measuring these kind of samples.

Despite the above-mentioned problems, we can see that the smoothed second derivative reproduced all important features of the curve: (i) When comparing in the resistivity curve of the upper part of Fig. 6.15, we see the change in curvature between the onset T_C and the zeroth resistance ${T_C}^0$. In the smoothed derivative we see a zero in this temperature range which produces a kind of midpoint T_C definition. (ii) Focussing on the upper part of Fig. 6.15 on the up and downturn producing the 'S-shape' of the curve, we can see a zero in the derivative which resembles this feature.

Obviously, much information will be lost when using the linefit method and only a single value will be shown - the T* which is somehow extracted. But here in the following, the second derivative will be plotted in dependence on temperature and doping. Therefore, another advantage of this method is the low loss of information. When combining this method with a high number of measurements, we are able to discuss in great detail the phases and particulary the pseudogap-temperature relative to the doping.

6.2.5 Resistivity curvature maps

With the preceding, I hope to have made clear that the second derivative is a good quantity for examining and discussing the pseudogap-temperature T*. Thus, in the following, I will use the resistivity curvature mapping as proposed by Ando et al. [238]. Despite the higher detail here and the difference in hole scaling used, the resulting resistivity curvature map (RCM) for the Pb0 series is comparable with the map in [238].

I will first explain the computation process: To plot the RCM, the 2nd derivatives were calculated for each curve. After that, the derivatives were averaged by the Gaussian slotting algorithm over temperature and doping. The parameters of this algorithm were Δx=0.01 formula units (La-direction) and Δy=5 K. The changes in the quality of the visibility upon a variation of $\Delta\cdots$ were tested which resulted in the conclusion that it did not disturb the essential physical quantities. The resulting RCM's are shown in Fig. 6.16. On the left side, the RCM for Pb0 is shown while on the right side it is shown for Pb04. The vertical axis marks the temperature. The upper horizontal axis indicates the Lanthanum content while the lower is the calculated hole concentration[1]. The colorscale in the middle indicates the magnitude of $d^2\rho_{ab}^N(T)/dT^2$. Compared to the 2nd derivative of the sample depicted in the lower part of Fig. 6.15, we see that the region of magnitude shown here is very narrow around the zero. Also included for both series are the positions of the depressions and the La/hole values of the individual measurements (black crosses).

We can see a manifestation of the phase diagram in these resistivity curvature maps which is similar to the resistivity maps discussed before and shown in Fig. 6.14. The difference is, when plotting the curvature of the resistivity against temperature and doping, the influence of phase transitions can be seen more clearly. I will begin to explain the RCM's by using the Pb0 series on the left side of Fig. 6.16:

When we look at low temperatures and low dopings, we can see a blue area. With respect to the smoothing and the step width in temperature of 5K, this is the 'suppressed superconducting phase' mentioned above and also visible in the resistivity measurements themselves. These were

---

[1] The hole concentration was as usual calculated by use of Eq. (4.3) and (4.4).

shown in the upper left inset of Fig. 6.13.

When we keep the temperature around zero and go to dopings higher than about 0.1, we can see a red region which represents the superconducting phase. When it is in the red region and raises the temperature, the crossing from red to blue represents T_C. As explained above, the zero in the 2nd derivative is approximately the resistivity midpoint definition of T_C. Because of the already stressed smoothing and the step width in temperature, we cannot see any depressions at this phase transition and even the superconducting dome is not well shaped. Comparing the crossing (the T_C) for Pb0 and Pb04, we see the fact that for Pb04 the T_C is enhanced. These are all the qualitative statements one can make for the superconducting phase. The blue areas above the superconducting dome in the RCM's are the regions which are suggested to represent the superconducting fluctuations. Comparing the region for Pb0 and Pb04, we notice that this region goes to higher temperatures for Pb04. This resembles the behavior of T_C for both series.

I will come now to the interesting phase boundary which is the onset of the pseudogap. Let us first concentrate on the Pb0 series as depicted on the left side of Fig. 6.16. The pseudogap-temperature T^* can be clearly seen, when appearing in the underdoped region from the highest temperatures, i.e. by the crossing from blue to red. We can state the well-known, expected behavior of the pseudogap: Taken from optimally doped samples, the pseudogap-temperature increases when the hole doping decreases. What is remarkable is that the pseudogap has a continuation within the deeply underdoped, non-superconducting/supressed-superconducting region. Although the antiferromagnetic region is not reached in these samples, one can suggest that the pseudogap-temperature will merge with the Néel temperature. In polycrystalline $Bi_2Sr_1La_1CuO_{6+\delta}$, the Néel temperature was found to be around 270K [87]. The approximated linear continuation of T^* might be around 300K for Pb0.

When we focus on the overdoped side, we see nearly a thick vertical red line ranging to high temperatures. When compared with the black crosses indicating the single measurements, this line is only produced by two samples in Pb0. It appears that this phase transition has a high slope and already reaches a higher temperature than was measured here for optimally doped samples. As the statistic relevance of two measurements might not be enough to be convincing, for this feature it is also good to compare with the Pb04 series as depicted on the right side of Fig. 6.16. Based on the number of measurements there, it is safe to conclude that this phase is real. Within the Pb04 series it is also weakly visible that two phase transitions occur around 0.17 hole doping; One is at the high slope vertical feature at about 250K and the second occurs in the white area at about 150K. I suggest that the 'lower white area' in Pb04 is a continuation of the single T^*-line which is clearly detectable at lower dopings. The higher temperature's vertical line is suggested to be the same phase transition as is visible, e.g., in the Knight shift (see [5, 228] and references therein). This phase transition is called the 'upper pseudogap' and its characteristic temperature is marked as T^0. In this nomenclature, what is marked here as T^* might also be called the 'lower pseudogap'.

The most remarkable property visible in the RCM's is the change of the pseudogap in respect to the position of the depression. In the RCM's of Fig. 6.16, their positions are indicated by the vertical dashed lines. One clearly sees that the slope of T^* changes. In the Pb0 series, I had exactly one sample on the 1/8 depression. It can be strongly suggested from this depression that the depressions are minima of T*.

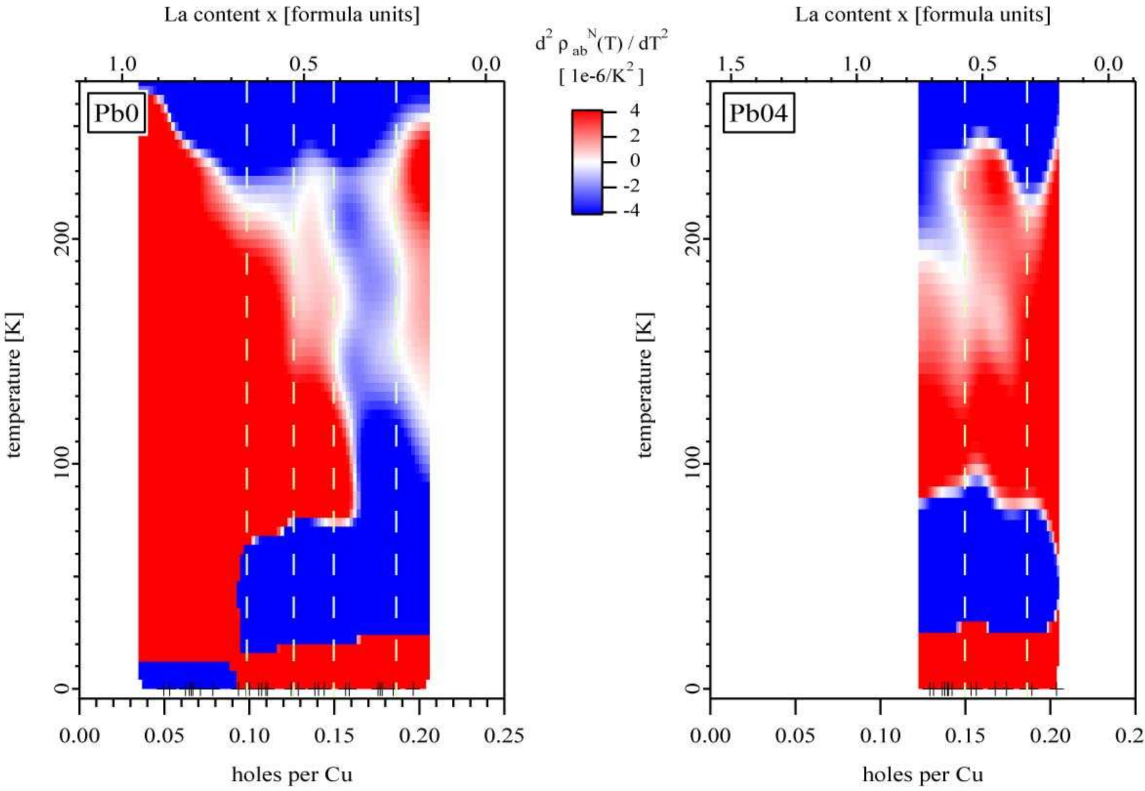

Figure 6.16: Resistivity curvature map (RCM) for $Bi_2Sr_{2-x}La_xCuO_{6+\delta}$(left) and $Bi_{2-y}Pb_ySr_{2-x}La_x$-$CuO_{6+\delta}$(right): The second derivative $d^2\rho_{ab}^N(T)/dT^2$ relative to the temperature (vertical axis) and Lanthanum content (upper horizontal axis) or hole doping (lower horizontal axis). The black crosses indicate the La content of the individual samples used for the averaging. The vertical dashed lines represent the positions of the depressions.

The shape of T* at each depression is asymmetric. This can be understood by expanding the model used and formulated in the ARPES discussion in section 6.1.3. Let us assume the ground state of the depressions itself is a highly ordered state. The next step is to note that, within the phase diagram, there is more than one depression. I suggest that, when destabilizing the system by inserting a few more holes, we get a ground state plus some extra defective holes. Insertion of many more holes results in an electronic system which better resembles the ordering of the next higher depression. Therefore, away from a depression the system always consists of two phases plus inhomogeneities as a result of the competition of these phases. This is also the case when lowering the number of holes. There, we get a system which partly consists of the ground state of the next lower depression. Note that this system is not symmetric upon the insertion and removal of holes. This is why we get the asymmetric shape at each depression in the derived T*. For the shape of the pseudogap-temperature relative to the doping, it might be that around depression 3, for example, the shape can be explained as follows: The pseudogap-temperatures with less holes than needed for depression 3 is the joint melting temperature of depression 2+3, the higher side the one of 3+4. What has been discussed here is an interesting similarity to crystallographic phase diagrams. If we can treat the pseudogap-temperature T* as a melting line, then eutectic phases are present at the depressions. Therefore, I come here to the same conclusion as with ARPES: The cleanest pseudogap phase can be found at a depression.

Let me with conclude the findings for the resistivity measurements: It was found that the low temperature T-linear behavior of the resistivity is strongest in samples near a depression. For the underdoped region, it can be speculated that the pseudogap-temperature merges with the Néel temperature. It was shown that two-phase crossovers exist in the overdoped region, one with the upper pseudogap-temperature T^0 and the other with T*. Furthermore, it was unambiguously shown here that the depressions change the pseudogap-temperature. The pseudogap-temperature T* is reduced near a depression. It can be suggested that the pseudogap state is the purest at a depression. The electronic ground states of the depressions are eutectic phases.

6.2.6 Comparison of T*

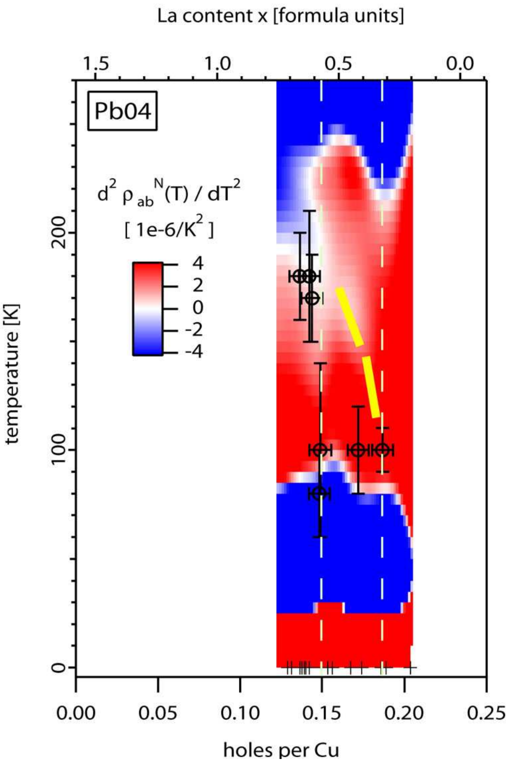

6.17.1: The comparison of the resistivity curvature map for Pb04 with the T* from ARPES (black circle). The yellow line is the estimated continuation of T* (the lower pseudogap).

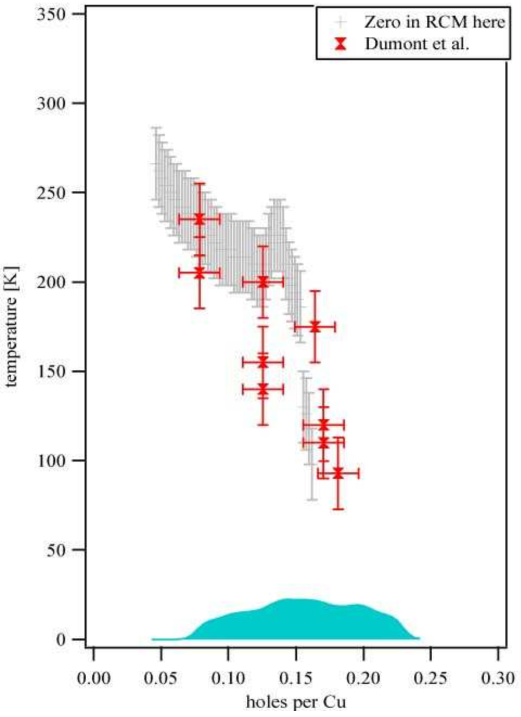

6.17.2: Comparison of T* from the zero of the RCM for Pb0 with the T* from Dumont et al. [191].

Figure 6.17.1 shows the resistivity curvature map for the Pb04 series in Chapter 6.2 together with the T* as derived by the leading edge midpoint analysis in Chapter 6.1. The T* from ARPES are the circles. For the more optimally-doped samples, the congruence between the T* of ARPES and resistivity is perfect. On the overdoped side, the correspondence between the two measurements appears, at first glance, not to be good. However, this is only due to the fact that the RCM has problems dividing the upper pseudogap from the lower. The yellow line is the estimated continuation of the lower pseudogap-temperature T^*. Thereby, we see that, within the error bars, it is reasonable that only the lower pseudogap was determined in the ARPES data processed here. It appears that this gap is not detectable by ARPES, at least in the antinodal direction. Further studies might be necessary to find out the effect of the upper pseudogap in ARPES. Let me point out that the upper pseudogap is - when considered - often seen as the onset of spin fluctuations. Therefore, T_0 might be marked by the onset of the linear (marginal Fermi-liquid-like) behavior of the self energy in ARPES.

One problem in the comparison of the ARPES measurements with the resistivity measurements is that samples at the depression should have the lowest T^*. In ARPES, the sample with T_C=0 has a high T^*. It can be argued that the perfect ground state itself is hard to measure, only an instability in the ARPES-derived properties is observed. It could be that the ARPES measurement is not as adiabatic as the resistivity measurement because photoemission was conducted here by an intense, focussed photon beam of about 22 eV. It could also be that the cleaving plane of this sample had a slightly different composition than the surface, e.g. because some Oxygen leaves the sample into the vacuum. But even when treating the results of this sample as an error, removing the datapoint from the curves results in the same shape of the curve overall. Referring to the comparison result between ARPES and resistivity, we can state that the correspondence between both T^*'s is astonishingly good.

To conclude this section, I want to compare the T^* as derived from the RCM of $Bi_2Sr_{2-x}La_x$-$CuO_{6+\delta}$ with thermopower measurements by Dumont et al. [191]. As these measurements were done on well-characterized single crystals of $Bi_{2.1}Sr_{1.92-x}$ $La_xCuO_{6+\delta}$, they are highly comparable to the crystals used here. For this purpose, I derived the T^* from the published thermopower curves by taking the temperature at which the linear behavior of the high-temperature thermopower changes. The La content was scaled in holes as given by Eq. (4.3). Fig. 6.17.2 shows the zero of the RCM together with the pseudogap-temperature as obtained from [191]. It can be seen that T^* is the same within the error.

6.3 Discussion

I will now summarize my findings about the pseudogap. At least in the antinodal direction, ARPES only detects the lower pseudogap; The resistivity measurements detect both crossovers. The pseudogap exists in the overdoped region. ARPES and resistivity show that the pseudogap-temperature and the gap change strongly near a depression. Resistivity measurements show more clearly that the depressions are minima of T*.

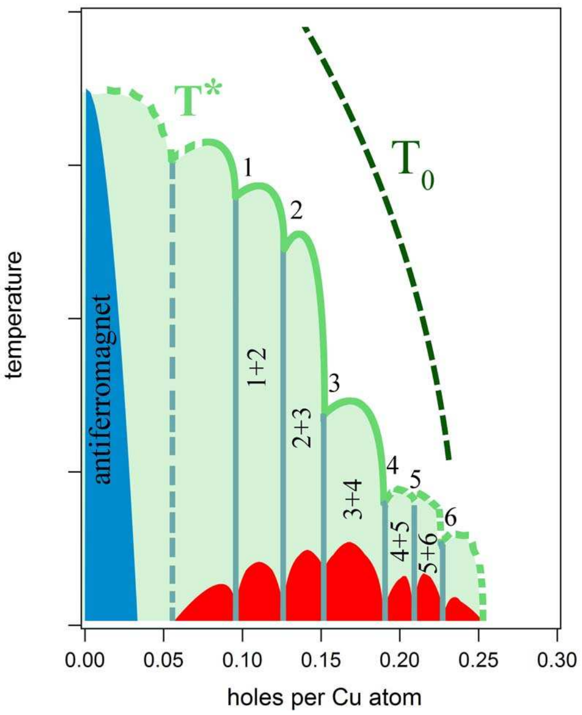

Figure 6.17: Suggested generic phase diagram of the hole-doped cuprates with the inclusion of the depressions in T_C and T*. T* is the lower pseudogap temperature, T_0 the upper one. The electronic structure within the lower pseudogap region may consist of phase mixtures of the electronic ground state at the depressions.

Using ARPES it was shown that the presence of a depression produces a broad, ill-defined excitation in the vicinity of the Fermi surface; away from a depression the spectra show a quasi particle-like peak. These phenomena were well explained in a model where a perfect spatially-ordered electronic-structure at a depression was considered. The broadening reflects the various possibilities for a photo-hole to decay in an otherwise perfectly ordered electronic structure. It is important to note here, that I showed no 'smoking gun' for an ordered state itself. Personally, I think that the circumstantial evidence in this work show that the existence of a spatially ordered electronic structure at each depression has a high probability. There are strong indications that the pseudogap-temperature T* is the melting temperature of this ordered state. These ordered states are the ground states of the depressions and are eutectic phases within the phase diagram. This means that the clearest pseudogap state is at a depression. Doping values away from a depression result in a phase mixture with defective holes. By the interpretation of the shown ARPES results, I suggest that the defective holes first produce density of states at the nodal direction. At a higher number, density of states will also be available in the antinodal direction. In ARPES, The density of states in the k-space direction might be deduced by the temperature range which the leading edge midpoint needs from T* to saturate.

The suggested sketch of the cuprates' phase diagram is shown in Fig. 6.17. It is of course interpretation. The dashed lines indicate a higher uncertainty because these features were not fully probed. The superconducting dome is cut by the depressions to smaller superconducting regions. The pseudogap-temperature also reacts on the depressions. The electronic structure between the depressions may consist of a phase mixture of the ground states at the depressions. When thinking about the microscopical origin of superconductivity, it might be that the pairing is driven by the existence of the defects. I can speculate about two mechanisms for pairing: (i) It could be that, similar to an atomic crystal, eutectic stripes form in the electronic structure of the CuO_2-plane. For the atomic crystal, we saw in this thesis something resembling eutectic stripes with the α- and β-phase mixture (see also Fig. 7.1 in the Conclusion). In the case discussed here, the two phases are created from the electronic structure. At the phase interfaces, one might expect a one-dimensional liquid. This speculation is therefore only a slightly epicyclical modification of the spin charge separation model by Emery and Kivelson [110, 111]. (ii) The second mechanism is not much different but slightly more general. It considers only the fact that defects exist in the electronic structure of the CuO_2-plane. The lowest energy state is achieved by the 'bosonization' of these fermionic defects because this bozonization allows the remaining electronic system to lower its energy. In this scenario, the number of Cooper-pairs would be proportional to the number of defects. Let me finally note that in a Wigner crystal, for example, defects can have an attractive interaction (see, e.g., [257]).

VII

Conclusion

This thesis dealt with the experimental exploration of the high-temperature superconducting Bi-cuprate system and mainly the one-layer $Bi_{2-y}Pb_ySr_{2-x}La_xCuO_{6+\delta}$. Many experimental methods were used which included low energy electron diffraction, scanning tunneling microscopy, four-probe resistivity measurements and angular resolved photoemission. All measurements shown were done on a statistically sufficient high number of single crystals. To ensure adequate comparability - particulary in relation to future work based on my findings, the crystals used were chosen very systematically and were thoroughly characterized. Among the multitude of findings, the most impressive results of this work are the following:

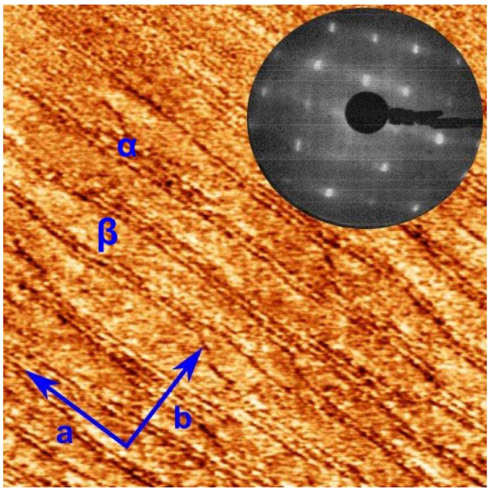

Figure 7.1: STM and LEED pattern of the (PbBiO)-plane of $Bi_{2-y}Pb_ySr_{2-x}La_xCuO_{6+\delta}$ with x≈0.4 and y≈ 0.4. One sees in the STM pattern the smooth β-phase which is intersected by the rough α-phase. The about 1x5 one-dimensional superstructure is absent.

I will now address the quality of the used Bi2201 single crystals. In Chapter 3, I showed the progress of this compound in single crystal synthesization, focussing mainly on the changes resulting from Lead substitution. The measurements shown by topological scanning tunneling microscopy (STM) and low energy electron diffraction (LEED) were done on a well-defined series: $Bi_{2-y}Pb_ySr_{2-x}La_xCuO_{6+\delta}$ with constant La-content of x=0.4 and the Pb substitution ranging systematically from zero to around 0.5 formula units. Because of the fine steps in Pb substitution levels, the morphologies could be examined in great detail. The about 1x5 superstructure of the Pb-free samples survives nearly unchanged up to around 0.2 formula units of Pb substitution. At higher Pb content, the superstructure is absent. In the intermediate region between 0.2 and 0.3 formula units of Pb, a very heterogenic phase mixture is present which affects the superconducting properties and makes them for experiments unlikely. However, at higher Pb levels, there are always phase mixtures which consist of the well known [159, 160, 161] rough α-phase and smooth β-phase. For y≈ 0.4, the STM and LEED patterns are shown in Fig. 7.1. I explained the morphologies in a pseudo-binary phase-diagram which also might roughly be applicable for the two-layer material and is a reasonable extension of the phase-diagram by Hiroi et al. [160]. The new finding was that the α-phase is not a true phase, but a phase mixture. At a Pb substitution larger than around 0.4 formula units, there is a large fraction of the smooth and Pb-rich β-phase and only a small amount of the α-phase mixture. For the superconducting properties, it was argued that for y>0.3 the lengthscales produced by the heterogenic phase mixtures are almost three times the superconducting coherence length ξ_{ab}. From this point of view, in Pb-Bi2201 it is possible to study the phenomenon of high-temperature superconductivity on the almost undisturbed CuO_2-plane.

Chapter 4 was dedicated to the T_C vs hole-concentration curve. Within this study, I showed the data of three structurally quite different high-temperature superconducting cuprates. The compounds were $Bi_2Sr_{2-x}La_xCuO_{6+\delta}$, $Bi_{2-y}Pb_ySr_{2-x}La_xCuO_{6+\delta}$ with y=0.4 and from the literature $La_{2-x}Sr_xCuO_4$. I showed that, in all these materials, the T_C vs hole-concentration curve is a parabola-like universal curve only in zeroth order. It was proven that depressions of T_C always occur at the same doping values. For $Bi_2Sr_{2-x}La_xCuO_{6+\delta}$ (La-Bi2201) and $La_{2-x}Sr_xCuO_4$ (LSCO), the curves are shown in Fig. 7.2. The values might be describable by the 'magic doping fractions' [122, 8]. It might be worth noting that before the present examination, the depressions were never shown to be in the Bi-cuprates system and the depression other than 1/8 were never shown to be existent in the T_C-curve itself. I strongly suggest that these depressions are generic and connected to the electronic ground state of the cuprates. It is well known that LBCO and LSCO show strong indications of a spatial magnetic-ordered and charge-ordered configuration within the CuO_2-plane at 1/8 doping [10, 11, 12, 13]. It can therefore be suggested that (i) this order is also existent in Bi2201 for 1/8, and (ii) an order is not only present at 1/8 but also at the other doping values of the depressions.

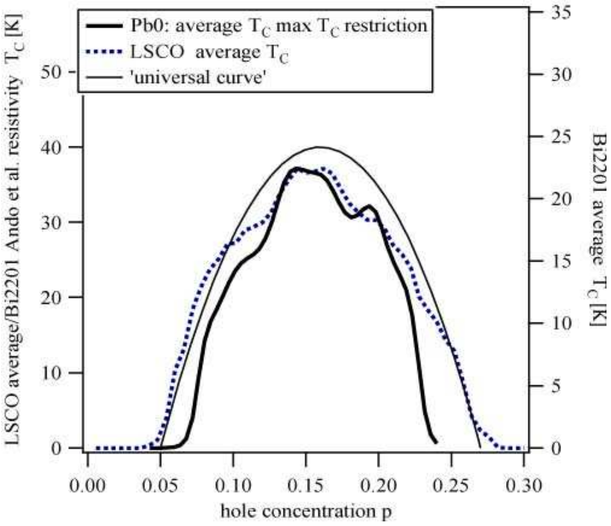

Figure 7.2: Averaged T_C vs hole concentration for La-Bi2201 and LSCO and the universal curve. The T_C curves are not parabola-like but exhibit depressions in T_C at certain dopings.

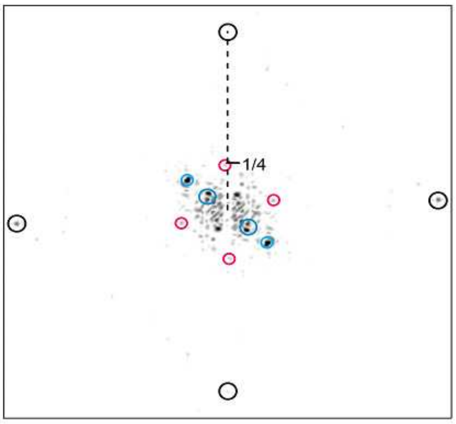

Figure 7.3: Squareroot of the power spectral density as processed by a straightened topographic STM pattern measured on $Bi_2Sr_2CaCu_2O_{8+\delta}$ at room temperature with U=0.6 V. A reciprocal order congruent to the nondispersive 4x4 'checkerboard order' is marked by the red circles which have a quarter of the length of the black circles.

Based on the suggestion of an electronic order within the CuO_2-plane, samples of Bi2201 and Bi2212 were probed by scanning tunneling microscopy. The measurements were done on a series of $Bi_{2-y}Pb_ySr_{2-x}La_xCuO_{6+\delta}$ single crystals with x=0.4 and y=0-0.5 and on optimally-doped Bi2212. All of the crystals probed exhibit a two-dimensional order with a periodicity around the nanoscale - roughly between three times and eight times the planar unit-cell size. For the one-layer material, it was shown that these modulations are quite similar to those found at low temperatures in $Bi_{2+z}Pb_ySr_{2-z}CuO_{6+\delta}$ by Kudo et al. [18]. A reciprocal representation of the modulation for Bi2212 is shown in Fig. 7.3. It is congruent to the nondispersive 4x4 order shown by Vershinin et al. [17]. This order was found in $Bi_2Sr_2CaCu_2O_{8+\delta}$ at low bias and at a temperature below the pseudogap-temperature. I reasonably argued that this 'checkerboard order' is **not** preferentially due to an ordering of the carriers in the CuO_2-plane i.e. not of the same origin as the above described electronic order within the CuO_2-plane, e.g., at 1/8 doping. In my interpretation, it is caused by dopant-atoms or dopant-complexes. The role of the Oxygen might be very particulary important.

Measurements concerning the pseudogap-phase were shown in Chapter 6. Using angular resolved photoemission (ARPES), it was found that the excitations in the antinodal direction exhibit no large contribution from a superconducting gap which is a gap that sets in at T_C; The dominant gap was found to set in at T^*. I showed the result of resistivity measurements on two well-defined series. The series were given by $Bi_2Sr_{2-x}La_xCuO_{6+\delta}$ varied over nearly the whole doping region (Pb0) and $Bi_{2-y}Pb_ySr_{2-x}La_xCuO_{6+\delta}$ with almost constant Pb substitution of 0.4 formula units (Pb04). A quite similar series with Pb content of 0.4 formula units was also probed by ARPES. The results of the measurement are shown in Fig. 7.4. Interesting results are:

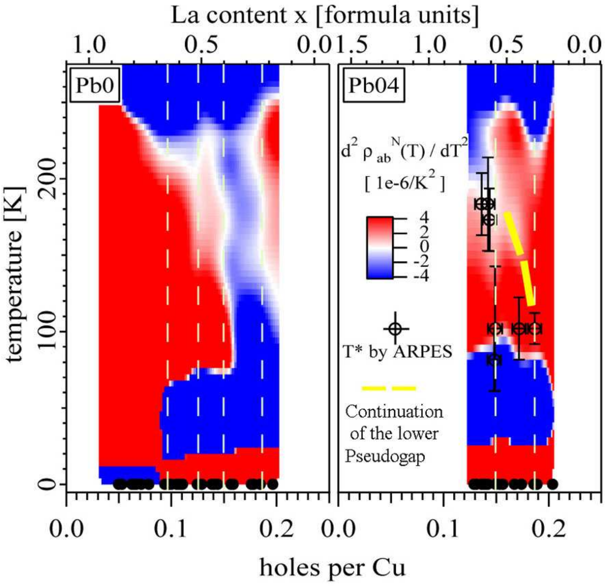

Figure 7.4: Resistivity curvature map for $Bi_2Sr_{2-x}La_xCuO_{6+\delta}$ (Pb0: left) and $Bi_{2-y}Pb_ySr_{2-x}La_xCuO_{6+\delta}$ with y=0.4 (Pb04:right). The pseudogap-temperature T^* is the zero (the upper crossover from blue to red). For Pb04, also included are the T^* as derived by ARPES. The T^* by ARPES is equal to the lower crossover for the overdoped side, marked by the thick yellow lines. The doping values of the depressions in T_C are marked by the white dashed lines.

(1) It can be stated that the pseudogap also exists in the overdoped region. Interestingly, while resistivity measurements detects two crossover temperatures, ARPES detects only the lower pseudogap-temperature T^*. It is remarkable that the correspondence of the T^* derived by the different methods is quite good.

(2) The most important finding about the pseudogap was that it also reacts on the doping values of the depressions; It was never shown before that T^* shows a local minimum at each of the depressions. The magnitude of the pseudogap Δ^* increases in the samples at the measured depression. In a certain way, this behavior supports the experimental finding at the 1/8 depression of $La_{2-x}Ba_xCuO_4$ by Valla et al. [249].

Overall, the findings in this thesis make a few models of high-temperature superconductivity less probable, e.g. the quantum-critical-point scenario or models which do not consider insulating states at the found depressions. The findings more likely support models as the SO(5)-theory or the spin-charge separation.

The impact of the depressions on the T^* was never considered before; Therefore, I would like to give some ideas and suggestions which should, in my view, be theoretically and experimentally checked:

There are indications that the cleanest pseudogap state is at the doping value of a depression. With respect to T^*, the whole phase diagram shows similarities to a phase diagram where eutectic crystalline phases are present and, in the present case, it is suggested that holes crystallize in an antiferromagnetic fluctuating background. This background sets in at the upper pseudogap-temperature. At T^*, a short range antiferromagnetic order is stabilized by the ordering of holes or vice versa. Superconductivity occurs in this picture when the 'crystallized'/ordered electronic system has mobile defective holes. These holes are suggested to be mainly in the nodal direction, but at a certain value of defects they are also in the antinodal direction. There, the defective holes pair first at T_C which allows the rest of the ordered electronic system to lower its energy.

The suggested ordering of dopant-atoms might prevent a possible self-organized electronic order within the CuO_2-plane- but also can force an ordering within the CuO_2-plane. In my view, an engineering of the dopant-atom order to be commensurate to the possible charge order in the CuO_2-plane is highly desirable as it might increase T^*. An increases in T_C can only be achieved when the dopant-atom order is perfect as defects in the dopant-atom order might pin the defective holes and make them less mobile. Putting the charge reservoir further away from the CuO_2-plane and trying to achieve a constant dopant field rather than 'periodic dopant-atom valleys' is the technologically simpler method but will not increase the T_C so much.

A

Experimental techniques

A.1 Energy dispersive x-ray analysis (EDX)

Energy dispersive x-ray analysis (EDX) is used to find the actual concentrations of the components of the samples. The basic concept of EM-EDX (electron microscope energy dispersive x-ray analysis) is as follows: A high-energy focused electron beam (typically $\approx 20keV$, $\Delta E \approx 135eV$), which is produced by an electron microscope, impacts on the sample surface. The electrons lose their energy in cascades of collisions by exciting electronic transitions in the sample. Here, the important process for the x-ray emission is the atomic excitation which competes against the Auger process. The measurement is a local probe of the sample characteristics because the penetration depth of the electron beam limits the volume of measurement. The emitted x-ray comes from a pear-shaped space volume of a diameter of approximately 2 μm. The resulting photon spectrum is measured energy dispersively with a semiconductor detector. Using a commercially available software tool based on the PUzaf correction [177], the elemental compositions can be computed by the height of the elementary characteristic x-ray peaks.

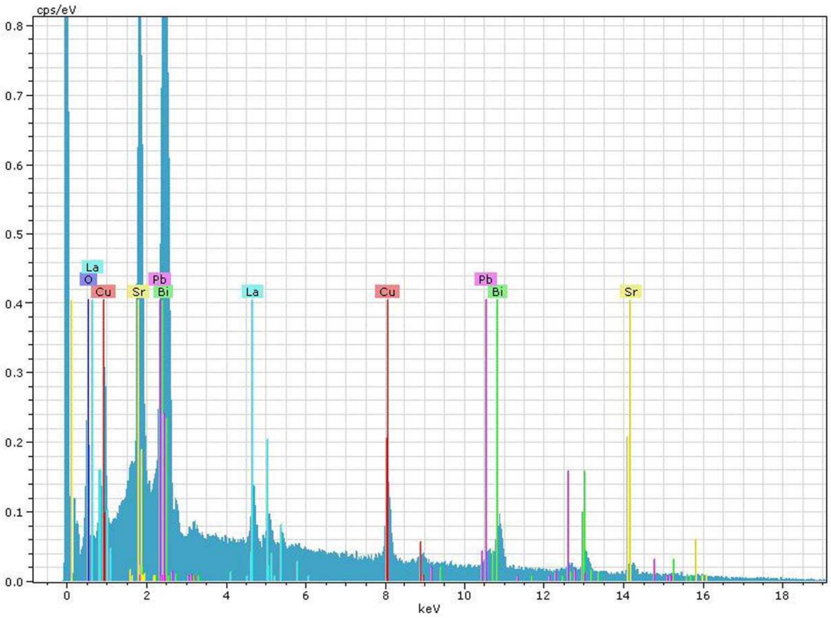

Figure A.1: Typical x-ray emission spectrum of $Bi_{2-y}Pb_ySr_{2-x}La_xCu$-$O_{6+\delta}$. The lines indicate the characteristic peaks for each element of the composition.

To compute the elementary composition for Cu, here the K_α duplet is used which is located around 8 keV. The location can be also seen in the example spectrum of a $Bi_{2-y}Pb_ySr_{2-x}La_x$-$CuO_{6+\delta}$ sample depicted in Fig. A.1. For La and Sr, typically the L-series is used which is located roughly around 4 keV to 6 keV and 1.5 keV to 2 keV for Sr. For Bi and Pb, the M series around 2-3 keV are used. Please note that this method is used without a standard, which means that the spectrum of the elements is not corrected by structurally dependent self-absorbtion.

A.2 AC-susceptibility (ACS)

With respect to the magnetic properties, Bi2201 and also all other HTSC's are type-II superconductors. The typical dependencies of the magnetization and the induced magnetic field are shown in Fig. A.3. Characteristic for a type-II superconductor are two critical fields, H$_{c1}$ and H$_{c2}$. Up to H$_{c1}$, the material behaves like a 'normal' type I superconductor. In the so-called 'Meissner-phase' the material is a perfect diamagnet. Above H$_{c1}$, the material is in the 'Shubnikov-phase' in which the field penetrates through the superconductor in the form of flux vortices. The upper critical field H$_{c2}$ describes the field above which the system becomes non-superconducting in a first-order phase transition. The aim of the AC-susceptibility measurements is to determine the complex susceptibility $\chi = \chi' - i\chi''$ which is defined by the relation between the alternating magnetic field $H(t) = H_0 + H_1 e^{i\omega t}$ and the magnetization $M(t)$. The relation can be given as $M(t) = M_0 + \chi H_1 e^{i\omega t}$, where χ' describes the static (DC) susceptibility of the sample and χ'' is connected with the energy absorbed by the substance due to magnetic phase changing. For the measurement, the commercial Quantum Design PPMS 6000 system was used. Typically, the susceptibility not is measured, but rather the susceptibility times the volume and a filling factor (χ'_v,χ''_v).

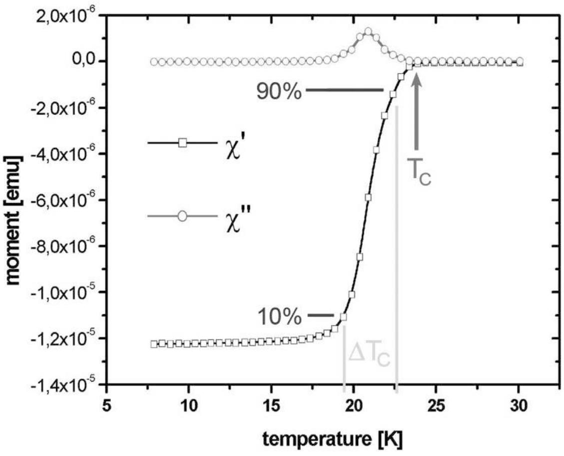

Figure A.2: Temperature dependent AC susceptibility curve of nearly optimally doped Bi2201.

The T$_C$-definition used in this work is the onset temperature i.e. the temperature point at which χ' begins to decrease. Another characteristic value is ΔT_c which describes the temperature range the crystal needs to become a superconductor from the paramagnetic state. Samples with a narrow ΔT_c are seen canonically as more clean. ΔT$_C$ is given by the difference in temperatures at 10% $\chi'_v(T = T_0)$ and 90% $\chi'_v(T = T_c)$. A typical χ'_v,χ''_v vs T for nearly optimally doped Bi2201 with T$_C$=24.5 K and ΔT$_C$≈ 3 K is shown in Fig. A.2.

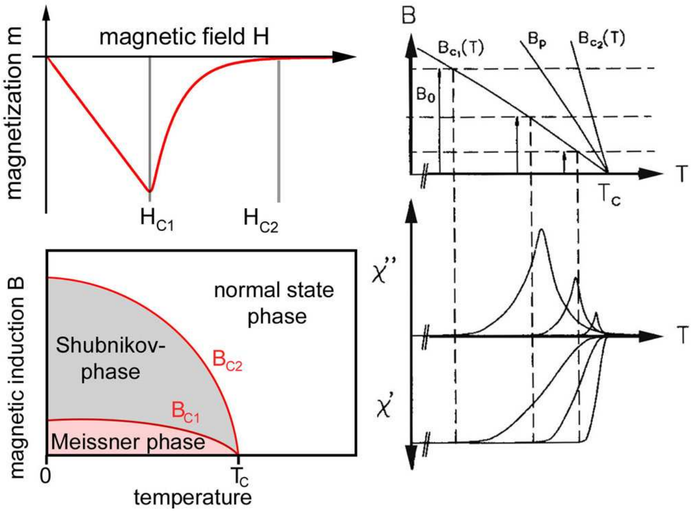

Figure A.3: Magnetization m as a function of the applied external field H (upper left), temperature dependence of the induced magnetic field (lower left) and real (χ') and imaginary (χ'') part of the AC susceptibility (right) of a type II superconductor.

A.3 Scanning tunneling microscopy (STM)

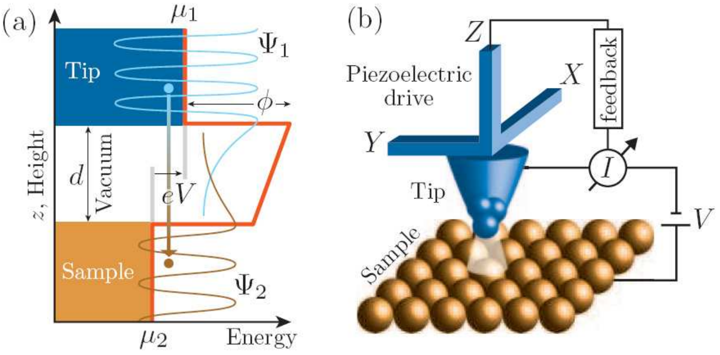

Figure A.4: From [15]: **(a)** Tunneling process between the tip and the sample across a vacuum barrier of width d and height Φ (for simplicity, the tip and the sample are assumed to have the same work function Φ). With a positive bias voltage V applied to the sample the electrons tunnel preferentially from the tip into unoccupied sample states. **(b)** Schematic view of the scanning tunneling microscope.

The scanning tunneling microscope uses the quantum tunnel effect which has been known about for some time. By using a characterized tip, a voltage current characteristic only depending on the barrier and the sample can be measured(see Fig. A.4 a). This setup makes it possible to study the local density of states with high resolution. The resolution is high enough to 'see' atoms because the measured tunneling current which is normal to the sample is extremely sensitive to the distance to the tip. It is proportional to the exponential function and written as

$$I \propto e^{-\frac{2}{\hbar}d\sqrt{2m_e\Phi}}\,. \tag{A.1}$$

Here, m_e is the electron mass and Φ the average barrier potential. As an example, when assuming an average barrier of $\Phi = 4\,eV$, increasing the distance by 1 Ångstöm leads to a reduction of the current by about a factor of 10. The technical realization of this simple and ingenious idea was already attempted between 1966 and 1971 by Young et al. [258]. But it took until 1981 when Binnig and Rohrer [259] developed the scanning tunneling microscope with atomic resolution by using a specially shaped three-dimensional piezoelectric actuator construction and a z-axis feedback control (see Fig. A.4 b).

The microscopical description of the tunneling process is done in the Bardeen formalism [260, 261]. A good derivation in real-space Green function formulation of the problem is given in [15]. The Bardeen formalism assumes that the Hamiltonian of the whole system can be written as $H = H_C + H_A + H_T$, where H_C and H_A are the Hamiltonians of the cathode and anode and H_T is the tunneling Hamiltonian which describes the tunneling process. For the derivation, one assumes that the Hamiltonians of both electrodes commutate. Other approximations used are the one-particle approximation and thermal equilibrium of both electrodes. An additional approximation often carried out is the Tersoff-Hamann approximation [262, 263]; At low temperature and low bias voltage, only the topmost atom of the tip is involved in the tunneling process and the tip material is assumed to be a simple metal with s-wave shaped states around the Fermi-surface. With the restrictions above, the normal-state tunneling current is then given as

$$I \propto \int d\omega \; [f(\omega - eU, T) - f(\omega, T)] \, \rho_A(x, \omega - eU) \rho_C(\omega) \, . \tag{A.2}$$

In this equation, $f(\omega, T)$ is the Fermi function, U the bias and $\rho_A(x, \omega - eU)$ is the local density of states (LDOS) of the anode which corresponds to the geometry depicted in Fig. A.4 a. $\rho_C(x, \omega)$ is the local density of states of the tip.

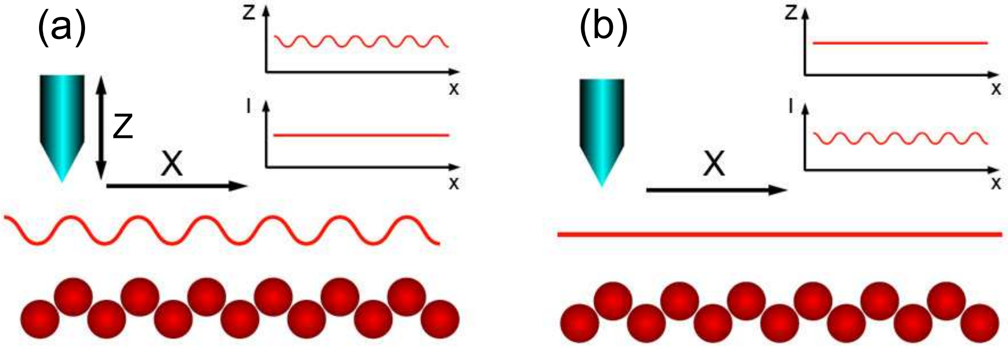

A.5.1: constant current mode A.5.2: constant height mode

Figure A.5: Adapted from [170]: Topographic STM operation modes.

In this work, the STM is used for topography where two operating modes are available. One is the constant current mode and the other is the constant height mode. The two modes are sketched in Fig. A.5. In constant current mode, the movement of the tip in the z-direction is controlled by the feedback control. In constant height mode, the feedback is turned off and the tip scans the surface of the sample at constant height. This is a risky mode in the case of a non-planar sample because the tip has the potential of crashing.

Experimental conditions

For the measurements, a commercial Omicron VT 25 SPM was used. The STM is decoupled from vibrations by air-vented buffers and by the built-in dynamic damper which works like an eddy current brake. The tips were mostly electrochemically etched tungsten wires or, when indicated, pinched-off platinum iridium wires. Most measurements were executed at room temperature in constant current mode. The samples were adhered to the holder using a two-component epoxide silver adhesive and heated for about one hour in an oven at $100°C$. They were cleaved by tape under vacuum conditions of $\approx 5 \times 10^{-7} - 5 \times 10^{-9}$ mbar inside a fast transfer lock. During cleaving, the samples were then transferred to a second stage lock ($p \approx 1 \times 10^{-9}$ mbar) and then into the measuring chamber with vacuum conditions of $\approx 1 \times 10^{-10}$ mbar.

A.4 Four-probe resistivity measurements

The sample used for resistivity measurements was grown rectangular with a smooth surface and typical dimensions of 2.5x0.5x0.3 mm^3. The setup of the contacts is shown for a sample of $Bi_2Sr_{2-x}La_xCuO_{6+\delta}$ with x=0.5 in the photograph on the right side where we can see the outer current contacts and the inner potential contacts. For the contacts, the four gold wires of 50 μm diameter were mounted with commercially available silver adhesive. The contacts were adhered over the full side of the sample to assure homogenous measurement conditions. To assure mechanical stability and good electrical contact the contacts were baked at 500 °C for one hour in air. Afterwards the resistance of the contacts was typically about one to five Ohm.

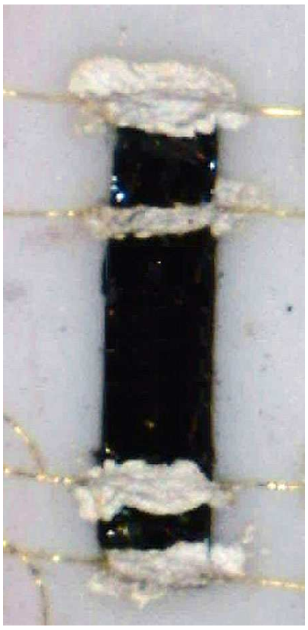

For carrying out the measurement using a standard 4-probe AC technique, the commercial Quantum Design PPMS 6000 system was used. The applied sinewave excitation was at a maximum 10mA. The resistivity was measured upon cooling from room temperature down to 2K with a rate of 2-6 K/min. The step width in probing the resistivity was around 0.4 K. The stability was given as 0.1 K at 300K and 0.01K at 5K.

A.5 Angular resolved photoemission (ARPES)

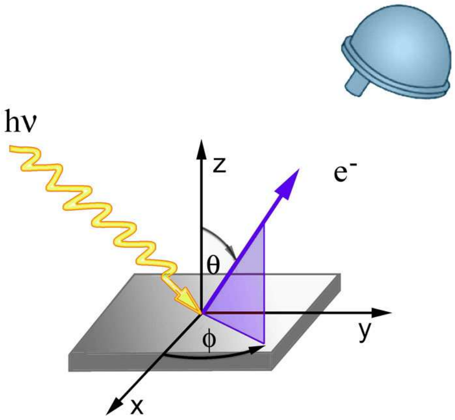

Figure A.6: Schematic view of angular resolved photoemission.

Photoemission accounts for the observation that when a nearly monochromatic photon beam impacts on a sample, electrons emit from the sample with a certain energy and a distinct angular distribution. It can be found that the maximum kinetic energy for the electron emission spectrum behaves as $E_{kin}^{max} = h\nu - \Phi$. Here, $h\nu$ is the energy of the photon and Φ the work function.

Let me specify the process: A photon beam with an energy of $E = h\nu$ impacts the sample. The photon interacts with the sample and after a certain length $1/\alpha(\nu)$, depending on the energy of the photon, the intensity of the photon beam is expected to be reduced to $1/e$ of the intensity of the incident beam, an assumption which can be written as $I = I_0 e^{-\alpha(\nu)x}$. Here, α is the absorption coefficient and may contain all of the interactions that a photon can be involved. Typical values of $1/\alpha$ are between 100 Å and 1000 Å. The important interaction for the photoemission process is the part in which the photon interacts with the electronic structure of the sample but only one electron leaves the sample. This is the one-particle approximation. After this approximation, one must find an equation of the dependence between the intensity of the outgoing photoelectrons and their kinetic energy and emission angle. For a better understanding, the emission process can be approximately divided into three processes. This is the so-called *three-step model*:

1. **Pure emission:** A photon of the energy $h\nu$ is absorbed into the bulk and exactly one electron with sufficient energy leaves the sample.

2. **Transport of the electron to the surface**. During this process, scattering can occur. This has two consequences: It determines the escape depth of the electrons and it is responsible for the inelastic background in the photoemission spectrum.

3. **Propagation through the sample surface**

In the following, each of these three steps will be described separately. This description will be phenomenological and does not attempt to derive the exact photocurrent.

1. Pure emission

It is common to calculate the photocurrent within the *sudden approximation* which negates the correlations of the escaping electron with the remaining system. The derivations of the photocurrent are intensively discussed in [221] and given by others [264, 265]. Within the approximation the photoemission intensity is

$$I(\vec{k},\omega) \propto |M(\vec{k})|^2\, f(\omega)\, A(\vec{k}\,,\omega) \tag{A.3}$$

where the momentum k gives the location in the Brillouin zone of the sample and ω is the energy of the initial state of the electron within the valence band measured with respect to the chemical potential. $f(\omega) = 1/(\exp(\hbar\omega/k_BT) + 1)$ is the Fermi function and $M(\vec{k})$ the matrix element. This includes all the kinematical factors and the dipole matrix element in the first order determin the selection rules which are extremely sensitive in the particular polarization geometry used in the experiment.$A(\vec{k},\omega)$ is the one-particle spectral function which is connected with the Greens function via

$$A(k,\omega) = -\frac{1}{\pi}\,\Im\left\{G(\vec{k},\omega - i0^+)\right\}\,. \tag{A.4}$$

2. Scattering within the sample

The escape depth of the electrons is determined by electron-electron and electron-phonon collisions. Except in special cases, electron-phonon scattering only plays a role at very low energies. If for the energies of interest the solid can be treated as a free electron gas, the inverse escape depth for the electron-electron process is a function of the mean electron-electron distance in the sample r_s. Then it can be given [221] as

$$\lambda^{-1} \approx \sqrt{3}\frac{a_0 R}{E_{kin}} r_s^{-3/2} \ln\left[\left(\frac{4}{9\pi}\right)^{2/3} \frac{E_{kin}}{R} r_s^2\right]\,,$$

where $a_0 = 0.529$ Å is the Bohr radius and $R = 13.6eV$ is the Rydberg energy. r_s is measured in units of a_0. This formula is nearly independent of material and is often called 'universal'. Fig. A.7 shows the typical escape depth for various metals and the evidence that the electron escape depth of photoemission is only a few Ångströms. It can be shown that the emission rate of the pure photoelectrons which leave the sample without being scattered is given in the first order by $D(E,\theta) \approx \alpha\lambda/(1+\alpha\lambda)$. Extensive descriptions and derivations can be found in [268, 221]. In principle, $D(E,\theta)$ can be used to remove the scattering part from the measured spectrum. Even if it was possible to remove all other processes from the spectrum, λ and α cannot be determined exactly enough. The background in the photoemission spectrum is caused by the e-e scattering and other forms of inelastic scattering. For the experimental analysis of wide energetic scaled spectra, this background must be subtracted to remove the energy dependence of the scattering process from the pure emission spectrum. A common form of modeling the background is the Shirley background [269].

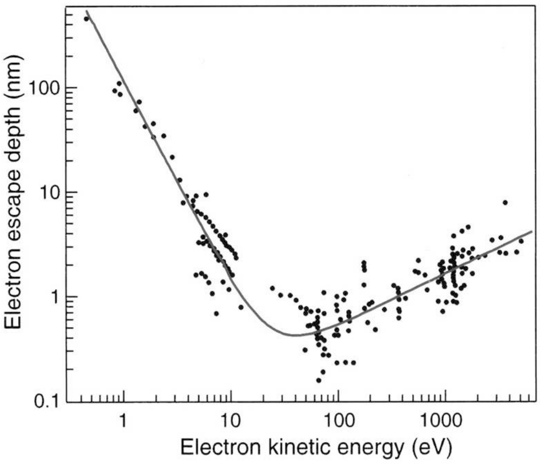

Figure A.7: From [266], who adapted from [267]: Electron escape depth in various elements and inorganic compounds as a function of the kinetic energy. The line is the so-called universal curve.

3. Propagation through the sample surface

While propagating through the surface, the electron is diffracted by the changing potential at the surface. I will explain the simple refraction model which leads to a conservation of the momentum. A more quantitative picture also describing the change in the photoemission current due to the influence of surface states can be found, e.g., in [221]. The simple model is illustrated in Fig. A.8. Consider that the change of the potential is only in the z-direction. Inside the sample the photoelectrons are moving in a constant potential V$_0$ in the conduction band. The momentum inside the crystal is $\vec{k_{in}}$. The escape condition is $(\hbar^2/2m)k^2_{in,\perp} \geq V_0$. The momentum of the escaping electrons parallel to the surface remains unchanged while propagating through the surface which means $K_{\|} = k_{in,\|}$. Because the momentum $K_{\|}$ outside the sample is the momentum of a free electron with the kinetic energy E_{kin}, it follows

$$k_{in,\|} = \sin(\Theta)\sqrt{\frac{2m}{\hbar^2}E_{kin}}\,. \tag{A.5}$$

The perpendicular momentum inside the sample is given by

$$k_{in,\perp} = \sin(\Theta')\sqrt{\frac{2m}{\hbar^2}(E_{kin}+V_0)} \tag{A.6}$$

It follows from Eq. (A.5) and Eq. (A.6) that for each energy, a maximum exists for

$$\Theta'_{max} = \sqrt{\frac{E_{kin}}{E_{kin}+V_0}}\,. \tag{A.7}$$

For $\Theta' > \Theta'_{max}$, the electron does not have the ability to leave the sample. The region $\Theta' > \Theta'_{max}$ is called the *first escape cone.* Theoretically, it is now possible to determine V_0 by measuring the escape cone for each energy. Commonly, for the cuprates the band structure is only shown in the $k_{in,\|}$ -direction because there is nearly no dispersion in z-direction. With photon-energy-dependent spectra and measuring across high-symmetric points, it is possible to derive the complete band structure $E(\vec{k_{in}})$.

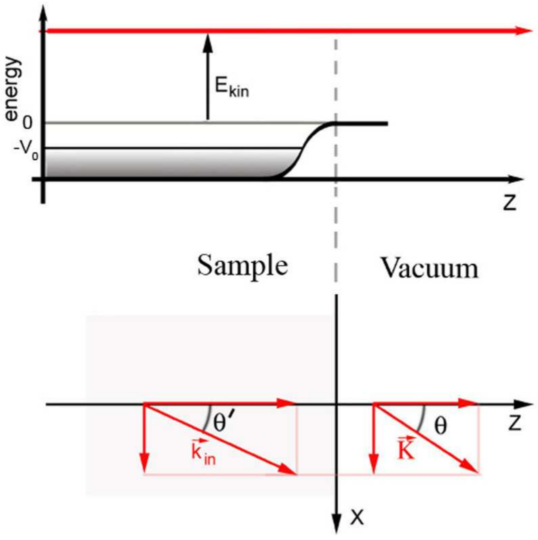

Figure A.8: Sketch of the derivation of the refraction of the electron by the sample surface

B

General remarks, analysis and data processing

B.1 Gaussian slotting algorithm

In this section, I want to describe the algorithm used for averaging. The advantage of the algorithm is that non-equispaced data can be used and that the data is weighted by its error.

It is important to recall that the chemical composition of La is written x and the chemical composition of Pb is y. For the La-Pb phase diagram there is the non-equispaced continuous sampled dataset of the form $\tilde{A}^j(x_i^j, y_i^j)$ where $i = 0, 1$ is the indicae of the two EDX measurements and $j = 0, 1, \cdots (J-1)$ is the indicae of the J measured samples. The letter A denotes the x,y-dependent data point and can be either T_C or $\Delta\mathrm{T}_C$. For each element of the composition, an average was defined in Eq. (4.1) of Chapter 4.1:

$$\overline{x}^j = \frac{1}{2}(x_0^j + x_1^j)\,. \tag{B.1}$$

Also, a standard error was defined in Eq. (4.2) of Chapter 4.1

$$\sigma_x^j = \sqrt{\sigma_{Fit}^2 + \frac{1}{2}\left((x_0^j - \overline{x}^j)^2 + (x_1^j - \overline{x}^j)^2\right)} = \sqrt{\sigma_{Fit}^2 + \frac{1}{2}(x_0^j - x_1^j)^2}\,. \tag{B.2}$$

σ_{Fit} describes the systematic error of EDX.

By using the definitions above, a data point for an average composition is generated and written as $\tilde{A}^j(\overline{x}^j, \overline{y}^j)$. Then, an equispaced discrete averaging function $A(p\Delta x, q\Delta y) = E[\tilde{A}^j(\overline{x}^j, \overline{y}^j)]$ with $p = 0, 1, \cdots (P-1)$, $q = 0, 1, \cdots (Q-1)$ can be constructed by weighting each $\tilde{A}^j(\overline{x}^j, \overline{y}^j)$ with a Gaussian probability with the width of the standard error at position into the slot $(p\Delta x, q\Delta y)$. Here, $p, q = 0..P-1, Q-1$ and $P\Delta x \times Q\Delta y$ is the compositional area of interest. This averaging reads:

$$A(p\Delta x, q\Delta y) = \frac{1}{Z(p\Delta x, q\Delta y)} \int\limits_{p\Delta x - \Delta x/2}^{p\Delta x + \Delta x/2} dx' \int\limits_{q\Delta y - \Delta y/2}^{q\Delta y + \Delta y/2} dy' \sum_{j=0}^{J-1} \frac{\tilde{A}^j(\overline{x}^j, \overline{y}^j)}{2\pi\sigma_x^j\sigma_y^j} \times \exp\left\{-\frac{(x' - \overline{x}^j)^2}{2(\sigma_x^j)^2} - \frac{(y' - \overline{y}^j)^2}{2(\sigma_y^j)^2}\right\}\,. \tag{B.3}$$

Here, Z can be treated as a probability and given as

$$Z(p\Delta x, q\Delta y) = \int\limits_{p\Delta x - \Delta x/2}^{p\Delta x + \Delta x/2} dx' \int\limits_{q\Delta y - \Delta y/2}^{q\Delta y + \Delta y/2} dy' \sum_{i=0}^{J-1} \frac{1}{2\pi\sigma_x^i\sigma_y^i} \exp\left\{-\frac{(x' - \overline{x}^i)^2}{2(\sigma_x^i)^2} - \frac{(y' - \overline{y}^i)^2}{2(\sigma_y^i)^2}\right\}\,.$$

It is easy to see that

$$\sum_{p,q=-\infty}^{\infty} Z(p\Delta x, q\Delta y) = J \approx \sum_{p,q=0}^{(P-1)(Q-1)} Z(p\Delta x, q\Delta y). \tag{B.4}$$

The largest error in this approximation comes from boundary effects of samples with $x - \sigma_x < 0$ or $y - \sigma_y < 0$. The standard error is calculated as usual:

$$\sigma_A = \sqrt{Var[\tilde{A}^j(\overline{x}^j, \overline{y}^j)]} = \sqrt{E\left[\tilde{A}^j(\overline{x}^j, \overline{y}^j)^2\right] - E\left[\tilde{A}^j(\overline{x}^j, \overline{y}^j)\right]^2} \tag{B.5}$$

Without losing to much accuracy, for $\Delta x, \Delta y \ll \sigma_x, \sigma_y$ the integrals above can be reduced to

$$A(p\Delta x, q\Delta y) \approx \frac{\Delta x\, \Delta y}{Z(p\Delta x, q\Delta y)} \sum_{j=0}^{J-1} \frac{\tilde{A}^j(\overline{x}^j, \overline{y}^j)}{2\pi\sigma_x^j\sigma_y^j} \times \exp\left\{-\frac{(p\Delta x - \overline{x}^j)^2}{2(\sigma_x^j)^2} - \frac{(q\Delta y - \overline{y}^j)^2}{2(\sigma_y^j)^2}\right\}. \tag{B.6}$$

This averaging function is expected to be asymptotically unbiased since the estimated function is analytical and harmless. The probability reads

$$Z(p\Delta x, q\Delta y) \approx \Delta x\, \Delta y \sum_{i=0}^{J-1} \frac{1}{2\pi\sigma_x^i\sigma_y^i} \exp\left\{-\frac{(p\Delta x - \overline{x}^i)^2}{2(\sigma_x^i)^2} - \frac{(q\Delta y - \overline{y}^i)^2}{2(\sigma_y^i)^2}\right\}. \tag{B.7}$$

From Eq. (B.5) it is clear, that the standard error will increase for slots with a low probability, e.g. with 'no samples' in the slot. For visualization of $A(p\Delta x, q\Delta y)$ of Eq. (B.6) it is therefore good to define a cutoff value. The function is not plotted below this value. Therefore, it should be that

$$Z(p\Delta x, q\Delta y) \geq Z^{\text{cutoff}} := \frac{1}{2PQ}. \tag{B.8}$$

From Eq. (B.4) it can be seen that this means that half of a sample's probability must be located in the slot.

B.2 Harmonic analysis

In the vicinity of possible modulations buried in the noise of the topographic STM signal, there is a need for an estimation of the true signal. This method takes the form of a harmonic analysis. More extended knowledge can be found in [270, 271] or elsewhere. The harmonic analysis is often done over the *power spectral density* (PSD). In this work, the name PSD is a bit misleading. Historically, this method was first used in 1898 by A. Schuster [272] for meteorological phenomena. Around the time of the Second World War, the technique was adapted for time-dependent signals in communications engineering where here it was used for two-dimensional position-dependent signals. Therefore, in the following, the PSD can also be called the *squared structure-factor* $F^2(\vec{q})$. However, the techniques remain the same. Among many existing methods, there are two nonparametric methods to estimate the PSD. The first is the *periodogram technique* and the second the *correlogram technique.* The periodogram is also often called the 'direct method'. Please note also that the PSD cannot give any information about phase shifts. In modern physics literature, the periodogram is sometimes called 'Fourier-transformation', 'Fourier map' or 'FFT'. However, although the periodogram technique is not consistent [273], it is more or less typically used when refining STM data also presented here in Chapter 5.2. But even though it is not consistent, the periodogram also has the advantage of easy and fast data processing when the failings of the technique are accounted for. In the following, I want to describe the steps which can be taken for the harmonic analysis:

The signal of the STM can be written as $\tilde{I}(x, y)$. We are dealing with a discrete signal measured with $N \times M$ data points which means that $x = n\,\Delta x$ and $y = m\,\Delta y$ with $n = 0, 1, \cdots (N-1)$ and $m = 0, 1, \cdots (M-1)$. The value of the STM scanned area is therefore $A = N\,\Delta x \times M\,\Delta y$. I assume that, due to the discrete recording of the data, no aliasing problems have been produced, e.g., the sampling distances Δx and Δy are 'well chosen' to record all harmonics which are important in the quasi-continuous system measured. The periodogram technique estimates the PSD at wavelength $(q_k, q_l) = \left(\frac{k}{N\,\Delta x}, \frac{l}{M\,\Delta y}\right)$ as the square of the discrete finite Fourier transformation of the signal:

$$F_P^2(q_k, q_l) = \left| \frac{1}{A} \sum_{n=0}^{N-1} \sum_{m=0}^{M-1} I(n\,\Delta x, m\,\Delta y)\; e^{2\pi i (q_k n\,\Delta x + q_l m\,\Delta y)} \right|^2 \tag{B.9}$$

The graph of the Fourier transformation vs the wavelength is called the periodogram. The periodogram is computed by use of the standard radix-2 FFT algorithm[274]. When using the technique it is assumed that the measured signal is produced by a cyclostationary process and has a mean squared ergodicity of the autocorrelation. The next assumption is that the signal is of the form

$$\tilde{I}(n\,\Delta x, m\,\Delta y) = I_{true}(n\,\Delta x, m\,\Delta y) + I_0(n\,\Delta x, m\,\Delta y) + I_N(n\,\Delta x, m\,\Delta y) \tag{B.10}$$

where I_{true} is the 'true signal' of the modulation of the sample, I_0 is a constant signal and I_N is the noise. By the normalization

$$I(n\,\Delta x, m\,\Delta y) = \frac{\tilde{I}(n\,\Delta x, m\,\Delta y)}{\frac{1}{N}\sum_{n=0}^{N-1} \tilde{I}(n\,\Delta x, m\,\Delta y)} - 1 \tag{B.11}$$

the constant signal is removed and the remaining signal is normalized to units of the average constant signal. This signal is used for the periodogram. The noise is assumed to be white or less colored because in the periodogram of the STM data only a small constant background is visible. Afterwards, the periodogram is smoothed by a Gaussian of 3x3 data points. In principle, this smoothing works like broadband windowing of the data. Older but good sources about windowing are [273],[275] and [276]. In order to control the estimation, it is better to compare the signal with the unbiased autocovariance i.e. the correlogram. The unbiased autocovariance is given by

$$\tilde{R}_{II}(o,p) = \frac{1}{(N-o)(M-p)} \sum_{n=0}^{N-o-1} \sum_{m=0}^{M-p-1} I(n\,\Delta x, m\,\Delta y)\; I([n+o]\Delta x, [m+p]\Delta y)\,. \tag{B.12}$$

As the name indicates, this estimator is unbiased but has a high variance, especially for large distances $o, p \rightarrow (N-1)$. Therefore, it is good to compare the correlogram. As long as all important modulations visible in the periodogram are also in the correlogram, they can be considered as real. In the case of ambiguous modulations, the correlogram should be treated as superior to the periodogram.

B.3 Results of the harmonic analysis

Pb/La content	**1d SS**	**2d modulations**						**figure reference**
		1st. modulation		2nd. modulation		relative Intensity	average Area	
y / x	$\vec{r}_{SS}$	$\vec{r}_1$	$\vec{r}_2$	$\vec{r}_1$	$\vec{r}_2$			
0 / 0.39	$4.8\ \vec{b}$	$-5.4\ \vec{a} + 2.4\ \vec{b}$	$-\ 6.5\ \vec{a}\ -\ 2.4\ \vec{b}$				$28.4\ \vec{a}\vec{b}$	Fig. 5.3.1
0.07 / 0.40	$6.2\ \vec{b}$	$-0.9\ \vec{a} + 3.6\ \vec{b}$	$-6.2\ \vec{a}\ -\ 0.1\ \vec{b}$				$22.4\ \vec{a}\vec{b}$	Fig. 5.3.2
0.09 / 0.39	$5.5\ \vec{b}$	$-1.5\ \vec{a} + 3.2\ \vec{b}$	$-7.2\ \vec{a} + 0.9\ \vec{b}$	$4.3\ \vec{a}\ -\ 3.7\ \vec{b}$	$2.9\ \vec{a} + 3.6\ \vec{b}$	5:4	$23.6\ \vec{a}\vec{b}$	Fig. 5.3.3
0.26 / 0.48		$0.4\ \vec{a} + 6.6\ \vec{b}$	$-6.3\ \vec{a} + 3.3\ \vec{b}$				$42.9\ \vec{a}\vec{b}$	Fig. 5.3.4
0.3 / 0.37		$-0.5\ \vec{a} + 5.5\ \vec{b}$	$-7.4\ \vec{a} + 0\ \vec{b}$	$2.9\ \vec{a}\ -\ 6\ \vec{b}$	$7.1\ \vec{a} + 5.6\ \vec{b}$	1:1	$49.6\ \vec{a}\vec{b}$ †	Fig. 5.3.5
0.4 / 0.45		$6.5\ \vec{a} + 0\ \vec{b}$	$0.2\ \vec{a} + 5.8\ \vec{b}$				$39\ \vec{a}\vec{b}$ ‡	Fig. 5.4.1
0.4 / 0.45		$-0.9\ \vec{a} + 5.1\ \vec{b}$	$-6.9\ \vec{a}\ -1.1\ \vec{b}$				$36.2\ \vec{a}\vec{b}$ †	Fig. 5.4.2
0.5 / 0.40		$1.1\ \vec{a} + 6.1\ \vec{b}$	$-10.6\ \vec{a} + 1.1\ \vec{b}$	+X	+X		$63.5\ \vec{a}\vec{b}$ †	Fig. 5.4.3
0.5 / 0.40		$-4.8\ \vec{a} + 0.6\ \vec{b}$	$-1\ \vec{a}\ -\ 11.5\ \vec{b}$	$10.8\vec{a}+ 3.3\ \vec{b}$	$-2.9\vec{a}+ 4.6\vec{b}$	1:1	$58\ \vec{a}\vec{b}$ ‡	Fig. 5.4.4

Table B.1: All found modulations in dependence of the Pb substitution level. Please compare with Fig. 5.2. Here $\vec{a}$ and $\vec{b}$ are the lattice vectors. From left to right there are: The Pb substitution y, the wavelength of a one-dimensional superstructure, both lattice vectors for the strongest visible 2d modulation, the lattice vectors in the case of a second modulation, the intensity ration of both 2d modulations, the average area spanned by the lattice vectors of the modulation.

†: It could not be figured out which direction is $\vec{a}$ and which $\vec{b}$. The $\vec{a}$ and $\vec{b}$ directions are interchangeable.
‡: The atomic lattice could not be resolved. The orientation was done by the direction of the α phase visible at larger scale. For computing the relative distances, the lengths of the atomic lattice vectors $\vec{a}$,$\vec{b}$ were set to 5.4Å.
+X: Other diffuse modulations appear to be present but could not be resolved.

B.4 Pseudogap by ARPES: Samples and conditions

Sample name	**EDX results** [formula units]					**ACS results** [K]		**ARPES conditions**				
	Bi	Pb	Sr	La	Cu	T$_C$	ΔT$_C$	source	detector	geometry	cleave	Δ E
x0.32	1.44	0.50	1.60	0.32	1.15	35	4	UVS300 HeI	SES100	(c)	T	22 meV
x0.42	1.56	0.40	1.49	0.42	1.14	23	3	UVS300 HeI	SES2002	(b) UP	T	10 meV
x0.58-1	1.46	0.41	1.42	0.58	1.14	30	5	NIM-U1 22eV	SES2002	(a)	M	16 meV
x0.58-2	1.48	0.41	1.40	0.58	1.15	32	3	PGM-U3 22eV	SES2002	(b)	M	16 meV
x0.61	1.45	0.42	1.38	0.61	1.13	< 2	< 2	NIM-U 22eV	SES2002	(a)	M	16 meV
x0.62	1.45	0.43	1.38	0.62	1.14	21	5	NIM-U1 22eV	SES2002	(a)	M	16 meV
x0.66	1.50	0.37	1.35	0.66	1.13	27	5	NIM-U1 22eV	SES2002	(a)	M	16 meV

Table B.2: The characterization results and the measurement conditions for ARPES: The left side shows the results from EDX and AC-susceptibility. The in the ARPES experiment used geometries are marked with (a),(b), (b)UP, and (c). They are depicted in Fig. 6.3 and explained in the text. For the sample cleaved on the manipulator, 'M' is written; for the cleavage by tape in the loadlock 'T' is written.

B.5 Pseudogap by ARPES: Analysis results and comparisons

sample	p [holes/Cu]	T_C[K]	T^*[K]	Δ^*_{mid} [meV]	$\bar{\Delta}^*_{mid}$	Δ^*_{sym} [meV]	$\bar{\Delta}^*_{sym}$
x0.32	0.187	35	100±10	6 ± 4	1.4	20± 10	4.6
x0.42	0.172	23	100±20	5 ± 4	1.2	19±10	4.4
x0.58-1	0.148	30	80±20	5 ± 3	1.5	18± 6	5.2
x0.58-2	0.149	32	100±40	5 ± 4	1.2	12 ± 5	2.8
x0.61	0.144	< 2	170±20	12 ± 3	1.6	-	-
x0.62	0.142	21	180±30	8 ± 3	1.0	31 ± 6	4
x0.66	0.136	27	180±20	12 ± 3	1.6	26 ± 6	3.4

Table B.3: The results of the leading edge analysis from the spectra near the antinodal point. Please compare also with tab. B.2. T^* and Δ^*_{mid} were refined as indicated in Fig. 6.4. Additionally, Δ^*_{sym} - the gap by the symmetrization method is shown. Also given is the reduced pseudogap $\bar{\Delta}^*_{...}$ for both gap estimates which is calculated as $2\Delta^*_{...}/k_B\ T^*$. The hole concentration was calculated by Eq. (4.4) of Chapter 4.3.2. The error is about ± 0.015 holes per Cu.

sample	ref.	T_C[K]	Δ^*_{mid} [meV]	Δ^*_{est} [meV]
$Bi_2Sr_{2-x}La_xCuO_{6+\delta}$ x=0.35	[231]	29	10 ± 2	-
$Bi_{2-y}Pb_ySr_{2-x}La_xCuO_{6+\delta}$	[234]	35	9.5 ± 1.5	$35^{(b)}$
$Bi_{2+z}Sr_{2-z}CuO_{6+\delta}$ z=0.3	[231]	< 4	7 ± 3	-
$Bi_{2+z}Sr_{2-z}CuO_{6+\delta}$ z=0.1	[231]	8	0 ± 2	-
UD $Bi_{1.8}Pb_{0.38}Sr_{2.01}CuO_{6-\delta}$	[251]	18	4 ± 2 $^{(d)}$	14 $^{(c)}$
UD $Bi_{1.8}Pb_{0.38}Sr_{2.01}CuO_{6-\delta}$	[250]	19	4 ± 2 $^{(d)}$	14 $^{(c)}$
OD $Bi_{1.8}Pb_{0.38}Sr_{2.01}CuO_{6-\delta}$	[251]	13	1 ± 2 $^{(d)}$	-
OD $Bi_{1.8}Pb_{0.38}Sr_{2.01}CuO_{6-\delta}$	[250]	10	0	0

Table B.4: Some ARPES results on the antinodal gap in Bi2201 from the literature.
$^{(b)}$ estimated by the symmetrization method. $^{(c)}$ estimated by a BCS-like fit. $^{(d)}$ as taken from the figures included in the publication.

Acknowledgements

This work could only succeed by the continuous support of many people, whom I would like to thank:

First place is reserved to Prof. Dr. Recardo Manzke. He gave me the opportunity and the freedom to conduct the experiments. I thank him for the discussions and his continuous interest in the results. I will never forget the measurement sessions at the SRC. For the outstanding samples and the introduction to the crystal growth, I thank Dr. Alica Krapf - also for her helpful advice. I thank Dr. Christoph Janowitz for the many hints and tricks, among other things with the construction process of the 'little Scienta'. Most corrections to this manuscript were done by Dipl. Phys. Beate Müller. I also thank her for her excellent co-operation during many measurement sessions. I thank Dr. Helmut Dwelk for the numerous characterizations by AC-susceptibility, as well as the constant assistance and organization in all situations. For the conduction of many STM measurements here, as well as for excellent co-operation, I thank Mr. Dipl. Phys. Olaf Lübben. Mr. Dipl. Phys. Hendrik Glowatzki provided his STM measurements of Bi2212 for processing. Many useful tips and tricks concerning the STM were provided by Dr. Ralph-Peter Blum. I would like to thank PD Dr. W. Kraak and Professor Dr. N. Minina for introducing me to the conductivity measurements. I would also like to thank Dr. S. Rogaschwewksi and his successor Dr. P. Schäfer for the characterization by EDX.

I thank the staff of the synchrotron radiation center (SRC) for the excellent support and the pleasant atmosphere. I would especially like to thank Dr. Hartmut Höchst for many explanations about ARPES. I would like to thank the staff of the 'Berliner Elektronenspeicherring - Gesellschaft für Synchrotronstrahlung' (BESSY), in particular Dr. G. Reichardt.

I thank Mrs. Dagmar Kaiser for her help in the chemical laboratory and for typing the characterization list. I thank Mr. Stefan Schmidt for the assistance with electronic questions. I thank the Helium department and the mechanical workshop, Mr. J. Sölle, as well as the electronic workshop for the numerous assistance. I thank Dipl. Phys. Thorsten Zandt for excellent co-operation. I thank Dr. Ralph Müller for the numerous discussions and Dipl. Ing. Lap Van Vu.

I also thank all other present and former members of the EES group.

I thank Prof. Dr. Y.G. Ponomarov for the kind hospitality in Moscow and many explanations. I thank Dr. Victor P. Martovitsky for the hospitality, the discussions and the introduction to x-ray diffraction. For other interesting discussions or hints in the context of this work, I thank PD Dr. J. Röhler, Prof. Dr. W. Neumann, Prof. Dr. W. Nolting, Prof. Dr. A. Damascelli, and Prof. Dr. G. Sawatzky. I thank Paul McCormick for the correction of my English.

I thank Anna, my family, and my friends.

Bibliography

[1] B. Brecht. *Leben des Galilei.* Aufbau-Verlag, Berlin, 1960.

[2] J. G. Bednorz and K. A. Müller. Possible high Tc superconductivity in the Ba-La-Cu-O system. *Zeitschrift für Physik B Condensed Matter*, 64:189, 1986.

[3] L. Gao, Y. Y. Xue, F. Chen, Q. Xiong, R. L. Meng, D. Ramirez, C. W. Chu, J. H. Eggert, and H. K. Mao. Superconductivity up to 164 K in $HgBa_2Ca_{m-1}Cu_mO_{2m+2+\delta}$ (m= 1, 2, and 3) under quasihydrostatic pressures. *Phys. Rev. B*, 50:4260, 1994.

[4] J. Bardeen, L. N. Cooper, and J. R. Schrieffer. Theory of Superconductivity. *Phys. Rev.*, 108:1175, 1957.

[5] T. Timusk and B. Statt. The pseudogap in high-temperature superconductors: An experimental survey. *Rep. Prog. Phys*, 62:61, 1999.

[6] A. R. Moodenbaugh, Y. Xu, M. Suenaga, T. J. Folkerts, and R. N. Shelton. Superconducting properties of $la_{2-x}ba_xcuo_4$. *Phys. Rev. B*, 38:4596, 1988.

[7] M. R. Presland, J. L. Tallon, R. G. Buckley, R. S. Liu, and N. E. Flower. General trends in oxygen stoichiometry effects on T_C in Bi and Tl superconductors. *Physica C*, 176:95, 1991.

[8] S. Komiya, H. D. Chen, S. C. Zhang, and Y. Ando. Magic doping fractions for high-temperature superconductors. *Phys. Rev. Lett.*, 94:207004, 2005.

[9] J. Orenstein and A. J. Millis. Advances in the physics of high-temperature superconductivity. *Science*, 288(5465):468, 2000.

[10] J. M. Tranquada, B. J. Sternlieb, J. D. Axe, Y. Nakamura, and S. Uchida. Evidence for stripe correlations of spins and holes in copper oxide superconductors. *Nature*, 375:561, 1995.

[11] N. Ichikawa, S. Uchida, J. M. Tranquada, T. Niemöller, P. M. Gehring, S.-H. Lee, and J. R. Schneider. Local magnetic order vs. superconductivity in a layered cuprate. *Phys. Rev. Lett.*, 85:1738, 2000.

[12] P. Abbamonte, A. Rusydi, S. Smadici, G. D. Gu, G. A. Sawatzky, and D. L. Feng. Spatially modulated 'Mottness' in $La_{2-x}Ba_xCuO_4$. *Nature Physics*, 1:155, 2005.

[13] A. Rusydi. *Resonant soft x-ray scattering and charge density waves in correlated systems.* Dissertation, RU Groningen, 2006.

[14] C. Michel, M. Hervieu, M. M. Borel, A. Grandin, F. Deslandes, J. Provost, and B. Raveau. Superconductivity in the Bi-Sr-Cu-O system. *Zeitschrift für Physik B Condensed Matter*, 68:421, 1987.

[15] Ø. Fischer, M. Kugler, I. Maggio-Aprile, C. Berthod, and C. Renner. Scanning tunneling spectroscopy of high-temperature superconductors. *Rev. Mod. Phys.*, 79:353, 2007.

[16] T. Hanaguri, C. Lupien, Y. Kohsaka, D. H. Lee, M. Azuma, M. Takano, H. Takagi, and J. C. Davis. A 'checkerboard' electronic crystal state in lightly hole-doped $Ca_{2-x}Na_xCuO_2Cl_2$. *Nature*, 430:1001, 2004.

[17] M. Vershinin, S. Misra, S. Ono, Y. Abe, Y. Ando, and A. Yazdani. Local ordering in the pseudogap state of the high-T_C superconductor $Bi_2Sr_2CaCu_2O_{8+\delta}$. *Science*, 303:1995, 2004.

[18] K. Kudo, T. Nishizaki, N. Okumura, and N. Kobayashi. STM studies on the hole doping dependence of the hidden order in Pb-doped Bi2201. *Physica C*, 463:40, 2007.

[19] M. R. Norman, D. Pines, and C. Kallin. The pseudogap: friend or foe of high T_C? *Adv. Phys.*, 54:715, 2005.

[20] S. Hüfner, M. A. Hossain, A. Damascelli, and G. A. Sawatzky. Two gaps make a high-temperature superconductor? *Rep. Prog. Phys.*, 71:062501, 2008.

[21] J. P. Joule and W. Thomson. On the thermal effects experienced by air in rushing through small apertures. *The London, Edinburgh and Dublin Phil. Mag.*, 4(4):481, 1852.

[22] C. Linde. Process and apparatus for attaining lowest temperatures for liquefying gases. *Engineer (Lond.)*, 82:509, 1896.

[23] H.K. Onnes. The liquefaction of helium. *Comm. Phys. Lab. Leiden*, 108:3, 1908.

[24] H.K. Onnes. The resistance of pure mercury at helium temperatures. *Leiden Comm.*, 120b, 1911.

[25] P. Drude. Zur Elektronentheorie I/II. *Annalen der Physik*, 3(369):4, 1900.

[26] W. Meissner and R. Ochsenfeld. Ein neuer Effekt bei Eintritt der Supraleitfähigkeit. *Naturwissenschaften*, 21(44):787, 1933.

[27] F. London and H. London. The electromagnetic equations of the supraconductor. *Proc. Roy. Soc. London. Ser. A*, 149(866):71, 1935.

[28] V. L. Ginzburg and L. D. Landau. Theory of superconductivity. *Zh. Éksp. Teor. Fiz.*, 20: 1064, 1950.

[29] A. A. Abrikosov. On the magnetic properties of superconductors of the second group. *Sov. Phys. JETP*, 5:1174, 1957.

[30] T. G. Berlincourt. Type ii superconductivity. *Rev. Mod. Phys.*, 36(1):19, 1964.

[31] E. Maxwell. Isotope effect in the superconductivity of mercury. *Phys. Rev.*, 78:477, 1950.

[32] C. A. Reynolds, B. Serin, W. H. Wright, and L. B. Nesbitt. Superconductivity of isotopes of mercury. *Phys. Rev.*, 78:487, 1950.

[33] H. Fröhlich. Theory of the superconducting state. i. the ground state at the absolute zero of temperature. *Phys. Rev.*, 79:845, 1950.

[34] I. Giaever. Energy gap in superconductors measured by electron tunneling. *Phys. Rev. Lett.*, 5:147, 1960.

[35] J. Nicol, S. Shapiro, and P. H. Smith. Direct measurement of the superconducting energy gap. *Phys. Rev. Lett.*, 5:461, 1960.

[36] B. D. Josephson. Possible new effects in superconductive tunnelling. *Phys. Lett.*, 1:251, 1962.

[37] A. B. Migdal. Interaction between electrons and the lattice vibrations in a normal metal. *Zh. Éksp. Teor. Fiz.*, 34, 1958.

[38] G. M. Eliashberg. Interactions between electrons and lattice vibrations in a superconductor. *Sov. Phys. JETP*, 11:696, 1960.

[39] W. L. McMillan. Transition temperature of strong-coupled superconductors. *Phys. Rev.*, 167:331, 1968.

[40] J. R. Gavaler. Superconductivity in $\mathrm{nb_3ge}$ films above 22 k. *Appl. Phys. Lett.*, 23:480, 1973.

[41] L. R. Testardi, J. H. Wernick, and W. A. Royer. Superconductivity with onset above 23 k in nb—ge sputtered films. *Solid State Comm.*, 15:1, 1974.

[42] J. Bardeen. Electron-phonon interactions and superconductivity. *Science*, 181:1209, 1973.

[43] R. J. Cava, R. B. van Dover, B. Batlogg, and E. A. Rietman. Bulk superconductivity at 36 k in $\mathrm{la_{1.8}sr_{0.2}cuo_4}$. *Phys. Rev. Lett.*, 58:408, 1987.

[44] M. K. Wu, J. R. Ashburn, C. J. Torng, P. H. Hor, R. L. Meng, L. Gao, Z. J. Huang, Y. Q. Wang, and C. W. Chu. Superconductivity at 93 k in a new mixed-phase yb-ba-cu-o compound system at ambient pressure. *Phys. Rev. Lett.*, 58:908, 1987.

[45] H. Maeda, Y. Tanaka, M. Fukutomi, and T. Asano. A New High-Tc Oxide Superconductor without a Rare Earth Element. *Jpn. J. Appl. Phys.*, 27:209, 1988.

[46] C. W. Chu, J. Bechtold, L. Gao, P. H. Hor, Z. J. Huang, R. L. Meng, Y. Y. Sun, Y. Q. Wang, and Y. Y. Xue. Superconductivity up to 114 k in the bi-al-ca-sr-cu-o compound system without rare-earth elements. *Phys. Rev. Lett.*, 60:941, 1988.

[47] R. M. Hazen, C. T. Prewitt, R. J. Angel, N. L. Ross, L. W. Finger, C. G. Hadidiacos, D. R. Veblen, P. J. Heaney, P. H. Hor, R. L. Meng, Y. Y. Sun, Y. Q. Wang, Y. Y. Xue, Z. J. Huang, L. Gao, J. Bechtold, and C. W. Chu. Superconductivity in the high-tc bi-ca-sr-cu-o system: Phase identification. *Phys. Rev. Lett.*, 60:1174, 1988.

[48] A. Schilling, M. Cantoni, J. D. Guo, and H. R. Ott. Superconductivity above 130 K in the Hg-Ba-Ca-Cu-O system. *Nature*, 363:56, 1993.

[49] C. Buzea and T. Yamashita. Review of the superconducting properties of MgB_2. *Supercond. Sci. Technol.*, 14:R115, 2001.

[50] M. Lang and J. Mueller. *The Physics of Superconductors Vol.* **2** *ed. by K.-H. Bennemann and J. B.Ketterson.* Springer, Berlin Heidelberg, 2003. and cond-mat/0302157.

[51] A. S. Sefat, M. A. McGuire, B. C. Sales, R. Jin, J. Y. Howe, and D. Mandrus. Electronic correlations in the superconductor $LaFeAsO_{0.89}F_{0.11}$ with low carrier density. *Phys. Rev. B*, 77:174503, 2008.

[52] H. Takagi, S. Uchida, and Y. Tokura. Superconductivity produced by electron doping in cuo$_2$-layered compounds. *Phys. Rev. Lett.*, 62:1197, 1989.

[53] Y. Tokura, H. Takagi, and S. Uchida. A superconducting copper oxide compound with electrons as the charge carriers. *Nature*, 337:345, 1989.

[54] M. G. Smith, A. Manthiram, J. Zhou, J. B. Goodenough, and J. T. Markert. Electron-doped superconductivity at 40 k in the infinite-layer compound sr$_{1˘y}$nd$_y$cuo$_2$. *Nature*, 351: 549, 1991.

[55] J. Singleton and C. Mielke. Quasi-two-dimensional organic superconductors: a review. *Contemporary Physics*, 43:63, 2002. and cond-mat/0202442.

[56] Jérome, D. and Mazaud, A. and Ribault, M. and Bechgaard, K. Superconductivity in a synthetic organic conductor (tmtsf)$_2$pf$_6$. *Journ. Phys. Lett.*, 41(4):95, 1980.

[57] A. M. Kini, U. Geiser, H. H. Wang, K. D. Carlson, J. M. Williams, W. K. Kwok, K. G. Vandervoort, J. E. Thompson, D. L. Stupka, D. Jung, and M. Whangbo. A new ambient-pressure organic superconductor, κ-$(ET)_2Cu[N(CN)_2]Br$, with the highest transition temperature yet observed (inductive onset T_C= 11.6 K, resistive onset = 12.5 K). *Inorg. Chem.*, 29:2555, 1990.

[58] A. F. Hebard, M. J. Rosseinsky, R. C. Haddon, D. W. Murphy, and S. H. Glarum. Superconductivity at 18 K in potassium-doped C_{60}. *Nature*, 350(6319):600, 1991.

[59] A.Y. Ganin, Y. Takabayashi, Y.Z. Khimyak, S. Margadonna, A. Tamai, M.J. Rosseinsky, and K. Prassides. Bulk superconductivity at 38 K in a molecular system. *Nature Materials*, 7:367, 2008.

[60] O. Gunnarsson. Superconductivity in fullerides. *Rev. Mod. Phys.*, 69:575, 1997.

[61] J. Nagamatsu, N. Nakagawa, T. Muranaka, Y. Zenitani, and J. Akimitsu. Superconductivity at 39 K in magnesium diboride. *Nature*, 410:63, 2001.

[62] Amy Y. Liu, I. I. Mazin, and Jens Kortus. Beyond eliashberg superconductivity in mgb$_2$: Anharmonicity, two-phonon scattering, and multiple gaps. *Phys. Rev. Lett.*, 87:087005, 2001.

[63] M. Iavarone, G. Karapetrov, A. E. Koshelev, W. K. Kwok, G. W. Crabtree, D. G. Hinks, W. N. Kang, Eun-Mi Choi, Hyun Jung Kim, Hyeong-Jin Kim, and S. I. Lee. Two-band superconductivity in mgb$_2$. *Phys. Rev. Lett.*, 89:187002, 2002.

[64] H.J. Choi, D. Roundy, H. Sun, M.L. Cohen, and S.G. Louie. The origin of the anomalous superconducting properties of MgB_2. *Nature*, 418:758, 2002.

[65] Y. Kamihara, H. Hiramatsu, M. Hirano, R. Kawamura, H. Yanagi, T. Kamiya, and H. Hosono. Iron-based layered superconductor: Laofep. *Journ. American Chem. Soc.*, 128:10012, 2006.

[66] Y. Kamihara, T. Watanabe, M. Hirano, and H. Hosono. Iron-Based Layered Superconductor $La[O_{1-x}F_x]FeAs$ (x= 0.05-0.12) with T_C=26 K. *J. Am. Chem. Soc*, 130(11):3296, 2008.

[67] H. Takahashi, K. Igawa, K. Arii, Y. Kamihara, M. Hirano, and H. Hosono. Superconductivity at 43 K in an iron-based layered compound $LaO_{1-x}F_xFeAs$. *Nature*, 453:376, 2008.

[68] C. Wang, L. Li, S. Chi, Z. Zhu, Z. Ren, Y. Li, Y. Wang, X. Lin, Y. Luo, S. Jiang, X. Xu, G. Cao, and Z. Xu. Thorium-doping induced superconductivity up to 56 k in $gd_{1-x}th_x feaso$. cond.mat:0804.4290v2, 2008.

[69] F. Jean, D. Colson, G. Collin, N. Blanchard, Z. Konstantinović, G. Le Bras, A. Forget, and M. Andrieux. Structure and charge transfer driven by the controlled amount of additional oxygen in cation-stoichiometric $bi_2sr_2cuo_{6+\delta}$. *Phys. Rev. B*, 68:174511, 2003.

[70] A. Müller. *Interlayer coupling and non Fermi liquid behavior in p-type high Tc superconductors.* Dissertation, HU Berlin, 2000.

[71] G. Burns. *High temperature superconductivity: An introduction.* Academic Press, San Diego, 1992.

[72] E. Pellegrin, J. Fink, C. T. Chen, Q. Xiong, Q. M. Lin, and C. W. Chu. Experimental hole densities in $hgba_2ca_{n-1}cu_no_{2n+2+\delta}$ compounds from near-edge x-ray-absorption spectroscopy. *Phys. Rev. B*, 53:2767, 1996.

[73] C. E. Gough, M. S. Colclough, E. M. Forgan, R. G. Jordan, and M. Keene. Flux quantization in a high-T_C superconductor. *Nature*, 326:855, 1987.

[74] C. C. Tsuei and J. R. Kirtley. Pairing symmetry in cuprate superconductors. *Rev. Mod. Phys.*, 72:969, 2000.

[75] M. Gurvitch and A. T. Fiory. Resistivity of $la_{1.825}sr_{0.175}cuo_4$ and $yba_2cu_3o_7$ to 1100 k: Absence of saturation and its implications. *Phys. Rev. Lett.*, 59:1337, 1987.

[76] S. Martin, A. T. Fiory, R. M. Fleming, L. F. Schneemeyer, and J. V. Waszczak. Normal-state transport properties of $bi_{2+x}sr_{2-y}cuo_{6+\delta}$ crystals. *Phys. Rev. B*, 41:846, 1990.

[77] H. Takagi, B. Batlogg, H. L. Kao, J. Kwo, R. J. Cava, J. J. Krajewski, and W. F. Peck. Systematic evolution of temperature-dependent resistivity in $la_{2-x}sr_xcuo_4$. *Phys. Rev. Lett.*, 69:2975, 1992.

[78] C. M. Varma, P. B. Littlewood, S. Schmitt-Rink, E. Abrahams, and A. E. Ruckenstein. Phenomenology of the normal state of cu-o high-temperature superconductors. *Phys. Rev. Lett.*, 63:1996, 1989.

[79] L. D. Landau. The theory of a Fermi liquid. *Sov. Phys. JETP*, 3:37, 1957.

[80] F. Ronning, C. Kim, D. L. Feng, D. S. Marshall, A. G. Loeser, L. L. Miller, J. N. Eckstein, I. Bozovic, and Z.-X. Shen. Photoemission evidence for a remnant Fermi surface and a d-wave-like dispersion in insulating $Ca_2CuO_2Cl_2$. *Science*, 282:2067, 1998.

[81] J. M. Tranquada. Neutron scattering studies of antiferromagnetic correlations in cuprates. cond-mat/0512115 To appear in: *Treatise of high-temperature superconductivity*, edited by J. R. Schrieffer, 2006.

[82] D. Vaknin, S. K. Sinha, D. E. Moncton, D. C. Johnston, J. M. Newsam, C. R. Safinya, and H. E. King Jr. Antiferromagnetism in La_2CuO_{4-y}. *Phys. Rev. Lett.*, 58:2802, 1987.

[83] C. Niedermayer, C. Bernhard, T. Blasius, A. Golnik, A. Moodenbaugh, and J. I. Budnick. Common phase diagram for antiferromagnetism in $La_{2-x}Sr_xCuO_4$ and Y_{1-x} Ca_x Ba_2 Cu_3 O_6 as seen by muon spin rotation. *Phys. Rev. Lett.*, 80:3843, 1998.

[84] A. E. Schlögl, J. J. Neumeier, J. Diederichs, C. Allgeier, and J. S. Schilling. Transport, structuralm and magnetic properties of the single-copper-oxygen layer $Bi_2Sr_{2-x}La_xCuO_y$ system. *Physica C*, 216:417, 1993.

[85] H. A. Jahn and E. Teller. Stability of Polyatomic Molecules in Degenerate Electronic States. I. Orbital Degeneracy. *Proc. Roy. Soc. London, Ser. A*, 61:220, 1937.

[86] J. Fink, N. Nücker, H. A. Romberg, and J. C. Fuggle. Electronic structure studies of high-T_C superconductors by high-energy spectroscopies. *IBM J. Res. Dev.*, 33:372, 1989.

[87] A. Maeda, M. Hase, I. Tsukada, K. Noda, S. Takebayashi, and K. Uchinokura. Physical properties of $bi_2sr_2ca_{n-1}cu_no_y$ (n=1,2,3). *Phys. Rev. B*, 41:6418, 1990.

[88] Y. He, T. S. Nunner, P.J. Hirschfeld, and H. P. Cheng. Local electronic structure of $Bi_2Sr_2CaCu_2O_8$ near Oxygen dopants: A window on the high-$T-C$ pairing mechanism. *Phys. Rev. Lett.*, 96:197002, 2006.

[89] S. Massidda, J. Yu, and A. J. Freeman. Electronic structure and properties of $Bi_2Sr_2CaCu_2$ O_8, the third high-T_C superconductor. *Physica C*, 152:251, 1988.

[90] D. J. Singh and W. E. Pickett. Structural modifications in bismuth cuprates: Effects on the electronic structure and fermi surface. *Phys. Rev. B*, 51:3128, 1995.

[91] N. F. Mott. Transition to the metallic state. *Phil. Mag.*, 6:287, 1961.

[92] J. Hubbard. Electron correlations in narrow energy bands. iii. an improved solution. *Proc. Roy. Soc. London Proc. Ser. A*, 281:401, 1964.

[93] J. Zaanen, G. A. Sawatzky, and J. W. Allen. Band gaps and electronic structure of transition-metal compounds. *Phys. Rev. Lett.*, 55:418, 1985.

[94] J. Wagner, W. Hanke, and D. J. Scalapino. Optical, magnetic, and single-particle excitations in the multiband hubbard model for cuprate superconductors. *Phys. Rev. B*, 43: 10517, 1991.

[95] A. Fujimori, E. Takayama-Muromachi, Y. Uchida, and B. Okai. Spectroscopic evidence for strongly correlated electronic states in La-Sr-Cu and Y-Ba-Cu oxides. *Phys. Rev. B*, 35:8814–, 1987.

[96] J. M. Tranquada, S. M. Heald, A. Moodenbaugh, and M. Suenaga. X-ray absorption studies of la$_{2-x}$(ba,sr)$_x$ cuo$_4$ superconductors. *Phys. Rev. B*, 35:7187, 1987.

[97] N. Nücker, J. Fink, B. Renker, D. Ewert, C. Politis, P. J. W. Weijs, and J. C. Fuggle. Experimental electronic structure studies of La$_{2-x}$Sr$_x$CuO$_4$. *Zeitschrift für Physik B Condensed Matter*, 67:9, 1987.

[98] J. Spalek. tJ Model then and now: A personal perspective from the pioneering times. *Acta Phys. Pol. A*, 111:409, 2007. and cond-mat/0706.4236.

[99] F. C. Zhang and T. M. Rice. Effective hamiltonian for the superconducting cu oxides. *Phys. Rev. B*, 37:3759, 1988.

[100] N. B. Brookes, G. Ghiringhelli, O. Tjernberg, L. H. Tjeng, T. Mizokawa, T. W. Li, and A. A. Menovsky. Detection of Zhang-Rice singlets using spin-polarized photoemission. *Phys. Rev. Lett.*, 87:237003, 2001.

[101] E. H. Lieb and F. Y. Wu. Absence of mott transition in an exact solution of the short-range, one-band model in one dimension. *Phys. Rev. Lett.*, 20:1445, 1968.

[102] P. W. Anderson. Is there glue in cuprate superconductors? *Science*, 316:1705, 2007.

[103] A. A. Abrikosov. Theory of high-Tc superconducting cuprates based on experimental evidence. *Physica C*, 341:97, 2000.

[104] A. S. Alexandrov. Polaron dynamics and bipolaron condensation in cuprates. *Phys. Rev. B*, 61:12315, 2000.

[105] D. Monthoux, P. andPines and G. G. Lonzarich. Superconductivity without phonons. *Nature*, 450:1177, 2007.

[106] D. J. Scalapino, E. Loh Jr., and J. E. Hirsch. d-wave pairing near a spin-density-wave instability. *Phys. Rev. B*, 34:8190, 1986.

[107] P. W. Anderson, P. A. Lee, M. Randeria, T. M. Rice, N. Trivedi, and F. C. Zhang. The physics behind high-temperature superconducting cuprates: The "plain vanilla" version of RVB. *J. Phys. Condens. Mat.*, 16:R755, 2004. and cond-mat/0311467.

[108] P. W. Anderson. The resonating valence bond state in La$_2$CuO$_4$ and superconductivity. *Science*, 235:1196, 1987.

[109] J. Zaanen and O. Gunnarsson. Charged magnetic domain lines and the magnetism of high-T$_C$ oxides. *Phys. Rev. B*, 40:7391, 1989.

[110] V. J. Emery, S. A. Kivelson, and O. Zachar. Spin-gap proximity effect mechanism of high-temperature superconductivity. *Phys. Rev. B*, 56:6120, 1997.

[111] S. A. Kivelson, E. Fradkin, and V. J. Emery. Electronic liquid crystal phases of a doped Mott insulator. *Nature*, 393:550, 1998.

[112] V. J. Emery. Theory of the quasi-one-dimensional electron gas with strong "on-site" interactions. *Phys. Rev. B*, 14:2989, 1976.

[113] S. C. Zhang. A unified theory based on SO(5) symmetry of superconductivity and antiferromagnetism. *Science*, 275:1089, 1997.

[114] S. C. Zhang. The SO(5) theory of high T_C superconductivity. *Physica C*, 282:265, 1997.

[115] H. D. Chen, S. Capponi, F. Alet, and S. C. Zhang. Global phase diagram of the high-T_C cuprates. *Phys. Rev. B*, 70:024516, 2004.

[116] M. Troyer and U.-J. Wiese. Computational complexity and fundamental limitations to Fermionic quantum Monte Carlo simulations. *Phys. Rev. Lett.*, 94:170201, 2005.

[117] S. Sachdev. Quantum criticality: Competing ground states in low dimensions. *Science*, 288:475, 2000.

[118] C. M. Varma. Pseudogap phase and the quantum-critical point in copper-oxide metals. *Phys. Rev. Lett.*, 83:3538, 1999.

[119] J.D. Dow and D.R. Harshmanh. High-temperature superconductivity: The hole-pairing is s-wave, and the holes are on the SrO, BaO, or interstitial Oxygen. *Journ. Low Temp. Phys.*, 131(3):483, 2003.

[120] P. W. Anderson. A suggested 4 x 4 structure in underdoped cuprate superconductors: A wigner supersolid. cond-mat/0406038, 2004.

[121] H. C. Fu, J. C. Davis, and D.-H. Lee. On the charge ordering observed by recent stm experiments. cond-mat/0403001, 2004.

[122] H. D. Chen, O. Vafek, A. Yazdani, and S. C. Zhang. Pair density wave in the pseudogap state of high temperature superconductors. *Phys. Rev. Lett.*, 93:187002, 2004.

[123] N. N. Kovaleva, A. V. Boris, T. Holden, C. Ulrich, B. Liang, C. T. Lin, B. Keimer, C. Bernhard, J. L. Tallon, D. Munzar, and A. M. Stoneham. *c*-axis lattice dynamics in bi-based cuprate superconductors. *Phys. Rev. B*, 69:054511, 2004.

[124] R. S. Roth, C. J. Rawn, and L. A. Bendersky. Crystal chemistry of the compound $sr_2bi_2cuo_6$. *J. Mater. Res.*, 5(1):46, 1990.

[125] F. Weill, B. Darriet, M. Ducau, J. Darriet, and J. Etourneau. Preparation and electron diffraction study of $Bi_2Sr_2CuO_6$. *Solid State Comm.*, 77:679, 1991.

[126] M. Nevřiva, E. Pollert, and P. Honskus. Solid-liquid equilibria and crystallization in the Bi-Sr-Cu-(O) system. *Physica C*, 199:328, 1992.

[127] J. Darriet, F. Weill, B. Darriet, X. F. Zhang, and J. Etourneau. Crystal structure of Bi_2 Sr_2 CuO_6: a structure based on periodic crystallographic shear planes in the "2201" structure. *Solid State Comm.*, 86:227, 1993.

[128] S. Legner. *Die Fermifläche des Kupratsupraleiters $Bi_2Sr_2CaCu_2O_{8+\delta}$: Ergebnisse der winkelaufgelösten Photoemissionsspektroskopie.* Dissertation, IFW Dresden/TU Dresden, 2003.

[129] A. Bansil and M. Lindroos. Importance of matrix elements in the arpes spectra of bisco. *Phys. Rev. Lett.*, 83:5154, 1999.

[130] E. V. Antipov and N. R. Khasanova. Bi-2201 phases: Synthesis, structures and superconducting properties. *Physica C*, 246:241, 1995.

[131] H. Komatsu, Y. Kato, S. Miyashita, T. Inoue, and S. Hayashi. In situ observations of crystal growth of Bi-based oxide superconductors. *Physica C*, 190:14, 1991.

[132] I. Chong, T. Terashima, Y. Bando, M. Takano, Y. Matsuda, T. Nagaoka, and K. Kumagai. Growth of heavily Pb-substituted Bi-2201 single crystals by a floating zone method. *Physica C*, 290:57, 1997.

[133] H. Luo, L. Fang, G. Mu, and H.-H. Wen. Growth and characterization of $bi_{2+x}sr_{2-x}cuo_{6+\delta}$ single crystals. *Journal of Crystal Growth*, 305:222, 2007.

[134] I. Matsubara, H. Tanigawa, T. Ogura, H. Yamashita, M. Kinoshita, and T. Kawai. Superconducting whiskers and crystals of the high t_c $bi_2sr_2ca_2cu_3o_10$ phase. *Appl. Phys. Lett.*, 58:409, 1991.

[135] W. L. Yang, H. H. Wen, Y. M. Ni, J. W. Xiong, H. Chen, C. Dong, F. Wu, Y. L. Qin, and Z. X. Zhao. Crystal growth and superconductivity of heavily La-doped Bi-2201 single crystals. *Physica C*, 308:294, 1998.

[136] J. I. Gorina, G. A. Kaljushnaia, V. I. Ktitorov, V. P. Martovitsky, V. V. Rodin, V. A. Stepanov, and S. I. Vedeneev. Growth from solution-melt in KCl and properties of high-quality low-T_C phase(2201) single crystals. *Solid State Comm.*, 91:615, 1994.

[137] V. P. Martovitsky, J. I. Gorina, and G. A. Kaljushnaia. Improved Bi-(2201) single crystals grown in cavities formed in KCl solution-melt. *Solid State Comm.*, 96:893, 1995.

[138] Y. I. Gorina, G. A. Kalyuzhnaya, V. V. Rodin, N. N. Sentyurina, V. A. Stepanov, and S. G. Chernook. Mechanism of growth of $Bi_{2+x}Sr_{2-y}CuO_{6+\delta}$ single crystals in gas cavities in a KCl melt. *Crystallography Reports*, 52:735, 2007.

[139] S. Kishida, H. Tokutaka, M. Katayama, M. Chihaya, H. Imao, K. Nishimori, and N. Ishihara. Growth of 80-K-phase Bi-Sr-Ca-Cu-O bulk single crystals using the flux containing Li or Sb. *Physica C*, 190:110, 1991.

[140] A. Krapf. private communications, 2008.

[141] Z. Jianwu, Z. Changjin, T. Shun, X. Gaojie, and Z. Yuheng. 47 K superconductivity in $Bi_{1.6}Pb_{0.4}Sr_{1.65}La_{0.35}CuO_z$. *Supercond. Sci. Techn.*, 14:599, 2001.

[142] M. Schneider, R. S. Unger, R. Mitdank, R. Müller, A. Krapf, S. Rogaschewski, H. Dwelk, C. Janowitz, and R. Manzke. Evolution of the density of states at the Fermi level of $Bi_{2-y}Pb_ySr_{2-x}La_xCuO_{6+\delta}$ and $Bi_2Sr_{2-x}La_xCuO_{6+\delta}$ cuprates with hole doping. *Phys. Rev. B*, 72:014504, 2005.

[143] R. D. Shannon. Revised effective ionic radii and systematic studies of interatomic distances in halides and chalcogenides. *Acta Crystallographica A*, 32:751, 1976.

[144] S. Kambe and O. Ishii. Correlation between tc, in-plane cu-o-cu bond length, and buckling of the cuo_2 plane in cuprate superconductors. *Physica C*, 341:555, 2000.

[145] J. Röhler. private communications, 2008.

[146] J. Röhler. The bulge in the basal plane area of cuprate superconductors. *Int. J. Mod. Phys. B*, 19:255, 2005.

[147] O. Eibl. Crystal structure of $(Bi,Pb)_2Sr_2Ca_{n-1}Cu_nO_{4+2n+\delta}$ high-T_C superconductors. *Physica C*, 168:215, 1990.

[148] V. P. Martovitsky, A. Krapf, and L. Dudy. Existence of two types of perfect $Bi_2Sr_{2-x}La_xCuO_{6+\delta}$ single crystals. *JETP Letters*, 85:292, 2007.

[149] P. W. Barnes, M. W. Lufaso, and P. M. Woodward. Structure determination of $A_2M^{3+}TaO_6$ and $A_2M^{3+}NbO_6$ ordered perovskites: octahedral tilting and pseudosymmetry. *Acta Crystallographica B*, 62:384, 2006.

[150] N. W. Thomas. The compositional dependence of octahedral tilting in orthorhombic and tetragonal perovskites. *Structural Science*, 52:16, 1996.

[151] M. Zhiqiang, F. Chenggao, S. Lei, Y. Zhen, Y. Li, W. Yu, and Z. Yuheng. Multiple $bi_2sr_{2-x}ba_xcuo_y$ microstructures and the effect of element doping (ba,la,pb) on the 2:2:0:1 phase. *Phys. Rev. B*, 47:14467, 1993.

[152] Y. Hongjie, M. Zhiqiang, and Z. Yuheng. Superconductivity and the valence state of the sr site in defective $bi_{1.8}pb_{0.2}sr_2cuo_y$. *Phys. Rev. B*, 61:15436, 2000.

[153] J. Zhang, W. Wang, C. Zhang, E. Jang, J. H. Choy, and Y. Zhang. Study of anomalous microstructure changes in Mn-doped Bi2201 system. *Physica C*, 419:85, 2005.

[154] M. Zhiqiang, X. Gaojie, Z. Shuyuan, T. Shun, L. Bin, T. Mingliang, F. Chenggao, X. Cunyi, and Z. Yuheng. Relation of the superstructure modulation and extra-oxygen local-structural distortion in $bi_{2.1-y}pb_ysr_{1.9-x}la_xcuo_z$. *Phys. Rev. B*, 55:9130, 1997.

[155] H. W. Zandbergen, W. A. Groen, F. C. Mijlhoff, G. van Tendeloo, and S. Amelinckx. Models for the modulation in $A_2B_2Ca_nCu_{1+n}O_{6+2n}$, A, B= Bi, Sr OR Tl, Ba and n= 0, 1, 2. *Physica C*, 156:325, 1988.

[156] H. W. Zandbergen, W. A. Groen, A. Smit, and G. van Tendeloo. Structure and properties of $(Bi,Pb)_2Sr_2(Ca,Y)Cu_2O_{8+\delta}$. *Physica C*, 168:426, 1990.

[157] X. B. Kan and S. C. Moss. Four-dimensional crystallographic analysis of the incommensurate modulation in a $Bi_2Sr_2CaCu_2O_8$ single crystal. *Acta Crystallographica B*, 48:122, 1992.

[158] G. Ertl and J. Küppers. *Low energy electrons and surface chemistry.* VCH, Weinheim, 1985.

[159] I. Chong, Z. Hiroi, M. Izumi, J. Shimoyama, Y. Nakayama, K. Kishio, T. Terashima, Y. Bando, and M. Takano. High critical-current density in the heavily Pb-doped $Bi_2Sr_2CaCu_2O_{8+\delta}$ superconductor: Generation of efficient pinning centers. *Science*, 276: 770, 1997.

[160] Z. Hiroi, I. Chong, and M. Takano. Two-phase microstructures generating efficient pinning centers in the heavily Pb-substituted $Bi_2Sr_2CaCu_2O_{8+\delta}$ single crystals. *Journ. Solid State Chem.*, 138:98, 1998.

[161] T. Nishizaki, K. Kudo, N. Okumura, and N. Kobayashi. STM studies on structural modulation and two-phase microstructures in Pb-doped Bi2201 single crystals. *Physica C*, 460: 156, 2007.

[162] O Lübben. *Rastertunnelmikroskopische Untersuchungen von (Bi,Pb)-2201 in Abhängigkeit des Bleigehalts.* Diploma thesis, HU Berlin, 2008.

[163] L. Shan, A. Ejov, A. Volodin, V. V. Moshchalkov, H. H. Wen, and C. T. Lin. STM studies of the surface structure in cleaved $Bi_2Sr_2CuO_{6+\delta}$ single crystals. *Europhys. Lett.*, 61:681, 2003.

[164] M. D. Kirk, J. Nogami, A. A. Baski, D. B. Mitzi, A. Kapitulnik, T. H. Geballe, and C. F. Quate. The Origin of the superstructure in $Bi_2Sr_2CaCu_2O_{8+\delta}$ as revealed by scanning tunneling microscopy. *Science*, 242:1673, 1988.

[165] A. Inoue, H. Mukaida, M. Nakao, and R. Yoshizaki. Study on the cleaved surface structure of $Bi_2Sr_2CaCu_2O_{8+\delta}$ by scanning tunneling microscopy. *Physica C*, 233:49, 1994.

[166] A. Inoue, M. Nakao, and R. Yoshizaki. Cleaved surface structure of $Bi_2Sr_2CuO_{6+\delta}$ by scanning tunneling microscopy. *Physica C*, 249:151, 1995.

[167] C. K. Shih, R. M. Feenstra, and G. V. Chandrashekhar. Scanning tunneling microscopy and spectroscopy of bi-sr-ca-cu-o 2:2:1:2 high-temperature superconductors. *Phys. Rev. B*, 43:7913, 1991.

[168] H. Mashima, N. Fukuo, Y. Matsumoto, G. Kinoda, T. Kondo, H. Ikuta, T. Hitosugi, and T. Hasegawa. Electronic inhomogeneity of heavily overdoped $Bi_{2-x}Pb_xSr_2CuO_y$ studied by low-temperature scanning tunneling microscopy/spectroscopy. *Phys. Rev. B*, 73:060502, 2006.

[169] G. Kinoda, T. Hasegawa, S. Nakao, T. Hanaguri, K. Kitazawa, K. Shimizu, J. Shimoyama, and K. Kishio. Observations of electronic inhomogeneity in heavily pb-doped $bi_2sr_2cacu_2o_y$ single crystals by scanning tunneling microscopy. *Phys. Rev. B*, 67:224509, 2003.

[170] H. Glowatzki. *Strukturelles Verhalten von* $Bi_{2-x}Pb_xSr_2CaCu_2O_{8+\delta}$ *bei Variation des Bleigehaltes.* Diploma thesis, HU Berlin, 2004.

[171] H. Ding, A. F. Bellman, J. C. Campuzano, M. Randeria, M. R. Norman, T. Yokoya, T. Takahashi, H. Katayama-Yoshida, T. Mochiku, K. Kadowaki, G. Jennings, and G. P. Brivio. Electronic excitations in $bi_2sr_2cacu_2o_8$: Fermi surface, dispersion, and absence of bilayer splitting. *Phys. Rev. Lett.*, 76:1533, 1996.

[172] L. Dudy, B. Müller, B. Ziegler, A. Krapf, H. Dwelk, O. Lübben, R. P. Blum, V. P. Martovitsky, C. Janowitz, and R. Manzke. Charge modulation driven Fermi surface of Pb-Bi2201. *Solid State Comm.*, 143:442, 2007.

[173] R. J. Cava, B. Batlogg, C.H. Chen, E. A. Rietman, S. M. Zahurak, and D. Werder. Oxygen stoichiometry, superconductivity and normal-state properties of $YBa_2Cu_3O_{7\text{\char`~}\delta}$. *Nature*, 329:423, 1987.

[174] J. L. Tallon, G. V. M. Williams, N. E. Flower, and C. Bernhard. Phase separation, pseudogap and impurity scattering in the HTS cuprates. *Physica C*, 282:236, 1997.

[175] W. L. Yang, H. H. Wen, and Z. X. Zhao. Discrete superconducting transition temperatures and pronounced t_c depression related to the 18 problem in $bi_2sr_{2-x}la_xcuo_{6+\delta}$ single crystals. *Phys. Rev. B*, 62:1361, 2000.

[176] A. K. Ariffin, B. Müller, R. Mitdank, L. Dudy, H. Dwelk, A. Krapf, C. Janowitz, and R. Manzke. The hole density of cuo_2-layer of single crystals determined by xas. to be published, 2009.

[177] J. Heckel and P. Jugelt. Quantitative analysis of bulk samples without standards by using peak-to-background ratios. *X-Ray Spectrometry*, 13:159, 1984.

[178] Y. Ando, Y. Hanaki, S. Ono, T. Murayama, K. Segawa, N. Miyamoto, and S. Komiya. Carrier concentrations in $bi_2sr_{2-z}la_zcuo_{6+\delta}$ single crystals and their relation to the hall coefficient and thermopower. *Phys. Rev. B*, 61:R14956, 2000.

[179] Z. Z. Li, H. Raffy, S. Bals, G. van Tendeloo, and S. Megtert. Interplay of doping and structural modulation in superconducting $Bi_2Sr_{2-x}La_xCuO_{6+\delta}$ thin films. *Phys. Rev. B*, 71:174503, 2005.

[180] V. P. Martovitsky. private communications, 2007.

[181] H. Kanai, J. Mizusaki, H. Tagawa, S. Hoshiyama, K. Hirano, K. Fujita, M. Tezuka, and T. Hashimoto. Defect Chemistry of $La_{2-x}Sr_xCuO_{4-\delta}$: Oxygen Nonstoichiometry and Thermodynamic Stability. *Journ. Solid State Chem.*, 131:150, 1997.

[182] S. Scheurell, E. Kemnitz, G. N. Maso, S. Y. Kasin, S. W. Naumov, and Y. N. Badun. Determination of the complete stoichiometry of Bi-Pb-Sr-Ca-Cu-O-superconductors. *Analytical and Bioanalytical Chemistry*, 340:353, 1991.

[183] M. Karppinen, M. Kotiranta, T. Nakane, H. Yamauchi, S. C. Chang, R. S. Liu, and J. M. Chen. Layer-specific hole concentrations in $bi_2sr_2(y_{1-x}ca_x)cu_2o_{8+\delta}$ as probed by xanes spectroscopy and coulometric redox analysis. *Phys. Rev. B*, 67:134522, 2003.

[184] Y. Yasukawa, H. Yamauchi, and M. Karppinen. Accurate oxygen-content determination method for decreased sample amounts of superconductive and other functional oxides. *Appl. Phys. Lett.*, 81:502, 2002.

[185] D. C. Parashar, J. Rai, P. K. Gupta, R. C. Sharma, and K. Lal. Evaluation of oxygen nonstoichiometry in high-T_C superconductors. *Jpn. J. Appl. Phys.*, 27:L2304, 1988.

[186] A. Q. Pham, F. Studer, N. Merrien, A. Maignan, C. Michel, and B. Raveau. Complex influence of the bi-o reservoir and oxygen nonstoichiometry on the hole density in $bi_2sr_2cacu_2o_8$. *Phys. Rev. B*, 48:1249, 1993.

[187] Y. Idemoto and K. Fueki. Oxygen nonstoichiometry and high temperature conductivity of the 2201 phase of the Bi-Sr-Cu-O superconducting oxide. *Physica C*, 190:502, 1992.

[188] S. D. Obertelli, J. R. Cooper, and J. L. Tallon. Systematics in the thermoelectric power of high-t_c oxides. *Phys. Rev. B*, 46:14928, 1992.

[189] J. R. Cooper and J. W. Loram. Some correlations between the thermodynamic and transport properties of high T_C Oxides in the normal state. *J. Phys. I France*, 6:2237, 1996.

[190] Z. Konstantinović, G. Le Bras, A. Forget, D. Colson, F. Jean, G. Collin, Z. Z. Li, H. Raffy, and C. Ayache. Failure of the empirical OCT law in the $Bi_2Sr_2CuO_6$ compound. *Europhys. Lett.*, 62:257, 2003.

[191] Y. Dumont, C. Ayache, and G. Collin. Dragging excitation characteristics from thermoelectric power in $bi_2(sr_{2-y}la_y)cuo_{6+\delta}$ single crystals. *Phys. Rev. B*, 62:622, 2000.

[192] T. Honma and P. H. Hor. Universal optimal hole-doping concentration in single-layer high-temperature cuprate superconductors. *Supercond. Sci. Tech.*, 19:907, 2006.

[193] M. Ronay, A. Santoni, A. G. Schrott, and L. J. Terminello. A new correlation for T_C from Cu 2p absorption. *Solid State Comm.*, 77:699, 1991.

[194] N. Merrien, C. Studer, F. Michel, P. Srivastava, B. R. Sekhar, N. L. Saini, K. B. Garg, and G. Tourillon. XAS and XPS study of electronic structure of the trivalent cuprate $La_2Li_{0.5}Cu_{0.5}O_{4-\delta}$. *J. Phys. Chem. Solids*, 54:499, 1993.

[195] P. Ghigna, G. Spinolo, G. Flor, and N. Morgante. Correlation between hole density and oxygen excess in the $bi_2sr_2cacu_2o_{8+\delta}$ superconductor. *Phys. Rev. B*, 57:13426, 1998.

[196] M. Karppinen, S. Lee, J. M. Lee, J. Poulsen, T. Nomura, S. Tajima, J. M. Chen, R. S. Liu, and H. Yamauchi. Hole doping in pb-free and pb-substituted $(bi,pb)_2sr_2ca_2cu_3o_{10+\delta}$ superconductors. *Phys. Rev. B*, 68:054502, 2003.

[197] A. A. Kordyuk, S. V. Borisenko, M. S. Golden, S. Legner, K. A. Nenkov, M. Knupfer, J. Fink, H. Berger, L. Forró, and R. Follath. Doping dependence of the fermi surface in $(bi,pb)_2sr_2cacu_2o_{8+\delta}$. *Phys. Rev. B*, 66:014502, 2002.

[198] A. Ino, C. Kim, M. Nakamura, T. Yoshida, T. Mizokawa, A. Fujimori, Z.-X. Shen, T. Kakeshita, H. Eisaki, and S. Uchida. Doping-dependent evolution of the electronic structure of $la_{2-x}sr_xcuo_4$ in the superconducting and metallic phases. *Phys. Rev. B*, 65: 094504, 2002.

[199] J. M. Luttinger. Fermi surface and some simple equilibrium properties of a system of interacting fermions. *Phys. Rev.*, 119:1153, 1960.

[200] T. Kondo, T. Takeuchi, U. Mizutani, T. Yokoya, S. Tsuda, and S. Shin. Contribution of electronic structure to thermoelectric power in $(Bi, Pb)_2(Sr, La)_2CuO_{6+\delta}$. *Phys. Rev. B*, 72:024533, 2005.

[201] M. Hashimoto, T. Yoshida, H. Yagi, M. Takizawa, A. Fujimori, M. Kubota, K. Ono, K. Tanaka, D. H. Lu, Z. X. Shen, et al. Doping evolution of the electronic structure in the single-layer cuprate $Bi_2Sr_{2-x}La_xCuO_{6+\delta}$: Comparison with other single-layer cuprates. *Phys. Rev. B*, 77:94516, 2008.

[202] M. Suzuki and M. Hikita. Resistive transition, magnetoresistance, and anisotropy in $la_{2-x}sr_xcuo_4$ single-crystal thin films. *Phys. Rev. B*, 44:249, 1991.

[203] T. Kimura, K. Kishio, T. Kobayashi, Y. Nakayama, N. Motohira, K. Kitazawa, and K. Yamafuji. Compositional dependence of transport anisotropy in large $(La,Sr)_2CuO_4$ single crystals and second peak in magnetization curves. *Physica C*, 192:247, 1992.

[204] Y. Nakamura and S. Uchida. Anisotropic transport properties of single-crystal $la_{2-x}sr_xcuo_4$: Evidence for the dimensional crossover. *Phys. Rev. B*, 47:8369, 1993.

[205] P. G. Radaelli, D. G. Hinks, A. W. Mitchell, B. A. Hunter, J. L. Wagner, B. Dabrowski, K. G. Vandervoort, H. K. Viswanathan, and J. D. Jorgensen. Structural and superconducting properties of $la_{2-x}sr_xcuo_4$ as a function of sr content. *Phys. Rev. B*, 49:4163, Feb 1994.

[206] T. Shibauchi, H. Kitano, K. Uchinokura, A. Maeda, T. Kimura, and K. Kishio. Anisotropic penetration depth in $la_{2-x}sr_xcuo_4$. *Phys. Rev. Lett.*, 72:2263, 1994.

[207] Y. Fukuzumi, K. Mizuhashi, K. Takenaka, and S. Uchida. Universal superconductor-insulator transition and t_c depression in zn-substituted high- t_c cuprates in the underdoped regime. *Phys. Rev. Lett.*, 76:684, 1996.

[208] M. Willemin, C. Rossel, J. Hofer, H. Keller, and A. Revcolevschi. Anisotropy scaling close to the ab plane in $la_{1.9}sr_{0.1}cuo_4$ by torque magnetometry. *Phys. Rev. B*, 59:R717, 1999.

[209] T. Sasagawa, Y. Togawa, J. Shimoyama, A. Kapitulnik, K. Kitazawa, and K. Kishio. Magnetization and resistivity measurements of the first-order vortex phase transition in $(la_{1-x}sr-x)_2cuo_4$. *Phys. Rev. B*, 61:1610, 2000.

[210] J. Hofer, T. Schneider, J. M. Singer, M. Willemin, H. Keller, T. Sasagawa, K. Kishio, K. Conder, and J. Karpinski. Torque magnetometry on single-crystal high-temperature superconductors near the critical temperature: A scaling approach. *Phys. Rev. B*, 62:631, 2000.

[211] T. Matsuzakia, M. Ido, N. Momonoa, R. M. Dipasupila, T. Nagataa, A. Sakaib, and M. Oda. Superconducting gap and pseudogap behavior in high-tc cuprates. *Journ. of Phys. and Chem. of Solids*, 62:29, 2001.

[212] O. Yuli, I. Asulin, O. Millo, and G. Koren. Scanning tunneling spectroscopy characterization of the pseudogap and the x= 1/8 anomaly in $La_{2-x}Sr_xCuO_4$ thin films. *Phys. Rev. B*, 75:184521, 2007.

[213] S. H. Pan, J. P. O'Neal, R.L. Badzey, C. Chamon, H. Ding, J. R. Engelbrecht, Z. Wang, H. Eisaki, S. Uchida, A. K. Gupta, K.-W. Ng, E. W. Hudson, K. M. Lang, and J. C. Davis. Microscopic electronic inhomogeneity in the high-T_C superconductor $Bi_2Sr_2CaCu_2O_{8+x}$. *Nature*, 413:282, 2001.

[214] S. Sugita, T. Watanabe, and A. Matsuda. Atomic image of a cuo_2 plane in the stm image of a $bi_2sr_2cacu_2o_{8+\delta}$ cleaved surface. *Phys. Rev. B*, 62:8715, 2000.

[215] W. Bauhofer, H. Mattausch, R. K. Kremer, P. Murugaraj, and A. Simon. Superconductivity in the system $bi_2sr_{2-x}la_xcuo_{6+\delta}$: Hole formation by $(lao)^+$. *Phys. Rev. B*, 39:7244, 1989.

[216] K. Zhang, G. Seidler, B. H. Ma, and C. U. Segre. Structure and superconductivity in the single Cu-O layered $(Bi_{2-x}Pb_x)(Sr_{2-y}La_y)CuO_{6+\delta}$ system. *Physica C*, 179:405, 1991.

[217] K. Kudo, T. Nishizaki, N. Okumura, and N. Kobayashi. STM studies on the electronic state of the overdoped Bi2201. *Physica C*, 460:948, 2007.

[218] M. Izquierdo, S. Megtert, J. P. Albouy, J. Avila, M. A. Valbuena, G. Gu, J. S. Abell, G. Yang, M. C. Asensio, and R. Comes. X-ray diffuse scattering experiments from bismuth-based high-T_C superconductors. *Phys. Rev. B*, 74:54512, 2006.

[219] A. Mans, I. Santoso, Y. Huang, W. K. Siu, S. Tavaddod, V. Arpiainen, M. Lindroos, H. Berger, V. N. Strocov, M. Shi, L. Patthey, and M. S. Golden. Experimental proof of a structural origin for the shadow Fermi surface of $Bi_2Sr_2CaCu_2O_{8+\delta}$. *Phys. Rev. Lett.*, 96:107007, 2006.

[220] R. L. Withers, J. G. Thompson, L. R. Wallenberg, J. D. Fitz Gerald, J. S. Anderson, and B. G. Hyde. A transmission electron microscope and group theoretical study of the new Bi-based high-T_C superconductors and some closely related Aurivillius phases. *Journ. Phys. C*, 21:6067, 1988.

[221] S. Hüfner. *Photoelectron Spectroscopy: Principles and Applications.* Springer, Berlin Heidelberg, 2003.

[222] K. McElroy, D. H. Lee, J. E. Hoffman, K. M. Lang, J. Lee, E. W. Hudson, H. Eisaki, S. Uchida, and J. C. Davis. Coincidence of checkerboard charge order and antinodal state decoherence in strongly underdoped superconducting $Bi_2Sr_2CaCu_2O_{8+\delta}$. *Phys. Rev. Lett.*, 94:197005, 2005.

[223] K. Widder, A. Zibold, M. Merz, H. P. Geserich, A. Erb, and G. Müller-Vogt. Ordering of chain oxygen in $YBa_2Cu_3O_x$. Optical investigations on single-domain crystals. *Physica C*, 232:82, 1994.

[224] A. Ourmazd and J. C. H. Spence. Detection of oxygen ordering in superconducting cuprates. *Nature*, 329:425, 1987.

[225] C. Chaillout, M. A. Alario-Franco, J. J. Capponi, J. Chenavas, J. L. Hodeau, and M. Marezio. Oxygen-vacancy ordering in the $ba_2ycu_3o_{7-x}$ ($0 \leq x \leq 1$) superconducting system. *Phys. Rev. B*, 36:7118, 1987.

[226] H. F. Poulsen, N. H. Andersen, J. V. Andersen, H. Bohr, and O. G. Mouritsen. Relation between superconducting transition temperature and oxygen ordering in $YBa_2Cu_3O_{6+x}$. *Nature*, 349:594, 1991.

[227] K. Segawa and Y. Ando. Transport properties of untwinned $YBa_2Cu_3O_y$ single crystals and the origin of the 60-K plateau. *Journ. Low Temp. Phys.*, 131:821, 2003.

[228] J. L. Tallon and J. W. Loram. The doping dependence of T*-what is the real high-T_C phase diagram? *Physica C*, 349:53, 2001.

[229] M.V. Sadovskii. Models of the pseudogap state in high-temperature superconductors. cond-mat/0408489v1, 2007.

[230] H. Ding, M. R. Norman, J. C. Campuzano, M. Randeria, A. F. Bellman, T. Yokoya, T. Takahashi, T. Mochiku, and K. Kadowaki. Angle-resolved photoemission spectroscopy study of the superconducting gap anisotropy in $bi_2sr_2cacu_2o_{8+x}$. *Phys. Rev. B*, 54:R9678, 1996.

[231] J. M. Harris, P. J. White, Z.-X. Shen, H. Ikeda, R. Yoshizaki, H. Eisaki, S. Uchida, W. D. Si, J. W. Xiong, Z.-X. Zhao, and D. S. Dessau. Measurement of an anisotropic energy gap in single plane $bi_2sr_{2-x}la_xcuo_{6+\delta}$. *Phys. Rev. Lett.*, 79:143, 1997.

[232] A. Damascelli, Z. Hussain, and Z.-X. Shen. Angle-resolved photoemission studies of the cuprate superconductors. *Rev. Mod. Phys.*, 75:473, 2003.

[233] J. Mesot, M. R. Norman, H. Ding, M. Randeria, J. C. Campuzano, A. Paramekanti, H. M. Fretwell, A. Kaminski, T. Takeuchi, T. Yokoya, T. Sato, T. Takahashi, T. Mochiku, and K. Kadowaki. Superconducting gap anisotropy and quasiparticle interactions: A doping dependent photoemission study. *Phys. Rev. Lett.*, 83:840, 1999.

[234] T. Kondo, T. Takeuchi, A. Kaminski, S. Tsuda, and S. Shin. Evidence for two energy scales in the superconducting state of optimally doped $(Bi,Pb)_2(Sr,La)_2CuO_{6+\delta}$. *Phys. Rev. Lett.*, 98:267004, 2007.

[235] W. S. Lee, I. M. Vishik, K. Tanaka, D. H. Lu, T. Sasagawa, N. Nagaosa, T. P. Devereaux, Z. Hussain, and Z.-X. Shen. Abrupt onset of a second energy gap at the superconducting transition of underdoped Bi2212. *Nature*, 450:81, 2007.

[236] V. J. Emery and S. A. Kivelson. Importance of phase fluctuations in superconductors with small superfluid density. *Nature*, 374:434, 1995.

[237] J. L. Tallon, J. W. Loram, G. V. M. Williams, J. R. Cooper, I. R. Fisher, J. D. Johnson, M. P. Staines, and C. Bernhard. Critical doping in overdoped high-t_c superconductors: A quantum critical point? *Phys. Stat. Sol. (b)*, 215:531, 1999.

[238] Y. Ando, S. Komiya, K. Segawa, S. Ono, and Y. Kurita. Electronic phase diagram of high-t_c cuprate superconductors from a mapping of the in-plane resistivity curvature. *Phys. Rev. Lett.*, 93:267001, 2004.

[239] M. R. Norman and C. Pepin. The electronic nature of high temperature cuprate superconductors. *Rep. Prog. Phys.*, 66:1547, 2003.

[240] D. S. Inosov. *Angle-resolved photoelectron spectroscopy studies of the many-body effects in the electronic structure of high-T_C cuprates.* Dissertation, IFW Dresden/TU Dresden, 2008.

[241] A. Santoni, L. J. Terminello, F. J. Himpsel, and T. Takahashi. Mapping the fermi surface of graphite with a display-type photoelectron spectrometer. *Appl. Phys. A*, 52:299, 1991.

[242] M. Randeria, H. Ding, J. C. Campuzano, A. Bellman, G. Jennings, T. Yokoya, T. Takahashi, H. Katayama-Yoshida, T. Mochiku, and K. Kadowaki. Momentum distribution sum rule for angle-resolved photoemission. *Phys. Rev. Lett.*, 74:4951, 1995.

[243] J. Mesot, M. Randeria, M. R. Norman, A. Kaminski, H. M. Fretwell, J. C. Campuzano, H. Ding, T. Takeuchi, T. Sato, T. Yokoya, T. Takahashi, I. Chong, T. Terashima, M. Takano, T. Mochiku, and K. Kadowaki. Determination of the fermi surface in high-t_c superconductors by angle-resolved photoemission spectroscopy. *Phys. Rev. B*, 63:224516, 2001.

[244] L. Kipp, K. Roßnagel, C. Solterbeck, T. Strasser, W. Schattke, and M. Skibowski. How to determine fermi vectors by angle-resolved photoemission. *Phys. Rev. Lett.*, 83:5551, 1999.

[245] X. J. Zhou, T. Yoshida, S. A. Kellar, P. V. Bogdanov, E. D. Lu, A. Lanzara, M. Nakamura, T. Noda, T. Kakeshita, H. Eisaki, S. Uchida, A. Fujimori, Z. Hussain, and Z.-X. Shen. Dual nature of the electronic structure of $(\mathrm{la}_{2-x-y}\mathrm{nd}_y\mathrm{sr}_x)\mathrm{cuo}_4$ and $\mathrm{la}_{1.85}\mathrm{sr}_{0.15}\mathrm{cuo}_4$. *Phys. Rev. Lett.*, 86:55781, 2001.

[246] M.R. Norman, H. Ding, M. Randeria, J.C. Campuzano, T. Yokoya, T. Takeuchi, T. Takahashi, T. Mochiku, K Kadowaki, P. Guptasarma, and D.G. Hinks. Destruction of the Fermi surface in underdoped high-Tc superconductors. *Nature*, 392:157, 1998.

[247] A. A. Kordyuk, S. V. Borisenko, M. Knupfer, and J. Fink. Measuring the gap in angle-resolved photoemission experiments on cuprates. *Phys. Rev. B*, 67:064504, 2003.

[248] A. A. Kordyuk, S. V. Borisenko, V. B. Zabolotnyy, R. Schuster, D. S. Inosov, R. Follath, A. Varykhalov, L. Patthey, and H. Berger. Non-monotonic pseudo-gap in high-tc cuprates. cond-mat/0801.2546v2, 2008.

[249] T. Valla, A. V. Fedorov, J. Lee, J. C. Davis, and G. D. Gu. The ground state of the pseudogap in cuprate superconductors. *Science*, 314:1914, 2006.

[250] T. Sato, Y. Naitoh, T. Kamiyama, T. Takahashi, T. Yokoya, J. Mesot, A. Kaminski, H. Fretwell, J.C. Campuzano, H. Ding, I. Chong, T. Terashima, M. Takano, and K. Kadowaki. Superconducting gap, pseudogap, and Fermi surface of Bi2201: High energy-and momentum-resolution photoemission study. *Physica C*, 341:2091, 2000.

[251] T. Sato, Y. Naitoh, T. Kamiyama, T. Takahashi, T. Yokoya, J. Mesot, A. Kaminski, H. Fretwell, J. C. Campuzano, H. Ding, I. Chong, T. Terashima, M. Takano, and K. Kadowaki. High-resolution angle-resolved photoemission study of Pb-substituted Bi2201. *Journ. Phys. Chem. Sol.*, 62:157, 2001.

[252] X. J. Zhou, T. Yoshida, D.-H. Lee, W. L. Yang, V. Brouet, F. Zhou, W. X. Ti, J. W. Xiong, Z. X. Zhao, T. Sasagawa, T. Kakeshita, H. Eisaki, S. Uchida, A. Fujimori, Z. Hussain, and Z.-X. Shen. Dichotomy between nodal and antinodal quasiparticles in underdoped ($\mathrm{la}_{2-x}\mathrm{sr}_x$)$\mathrm{cuo}_4$ superconductors. *Phys. Rev. Lett.*, 92:187001, 2004.

[253] B. Bucher, P. Steiner, J. Karpinski, E. Kaldis, and P. Wachter. Influence of the spin gap on the normal state transport in $\mathrm{yba}_2\mathrm{cu}_4\mathrm{o}_8$. *Phys. Rev. Lett.*, 70:2012, 1993.

[254] F. Vidal, J. A. Viera, J. Maza, J. J. Ponte, F. García-Alvarado, E. Morán, J. Amador, C. Cascales, A. Castro, M. T. Casais, and I. Rasines. Excess electrical conductivity in polycrystalline Bi-Ca-Sr-Cu-O compounds and thermodynamic fluctuations of the amplitude of the superconducting order parameter. *Physica C*, 156:807, 1988.

[255] Y. Ando and K. Segawa. Magnetoresistance of untwinned $\mathrm{yba}_2\mathrm{cu}_3\mathrm{o}_y$ single crystals in a wide range of doping: Anomalous hole-doping dependence of the coherence length. *Phys. Rev. Lett.*, 88:167005, 2002.

[256] T. Ito, K. Takenaka, and S. Uchida. Systematic deviation from t-linear behavior in the in-plane resistivity of $\mathrm{yba}_2\mathrm{cu}_3\mathrm{o}_{7-y}$: Evidence for dominant spin scattering. *Phys. Rev. Lett.*, 70:3995, 1993.

[257] L. Cândido, P. Phillips, and D. M. Ceperley. Single and paired point defects in a 2d wigner crystal. *Phys. Rev. Lett.*, 86:492, 2001.

[258] R. Young, J. Ward, and F. Scire. Observation of metal-vacuum-metal tunneling, ffield emission, and the transition region. *Phys. Rev. Lett.*, 27:922, 1971.

[259] G. Binnig and H. Rohrer. Scanning tunneling microscopy - from birth to adolescence. *Rev. Mod. Phys.*, 59:615, 1987.

[260] J. Bardeen. Tunnelling from a many-particle point of view. *Phys. Rev. Lett.*, 6:57, 1961.

[261] J. Bardeen. Tunneling into superconductors. *Phys. Rev. Lett.*, 9:147, 1962.

[262] J. Tersoff and D. R. Hamann. Theory and application for the scanning tunneling microscope. *Phys. Rev. Lett.*, 50:1998, 1983.

[263] J. Tersoff and D. R. Hamann. Theory of the scanning tunneling microscope. *Phys. Rev. B*, 31:805, 1985.

[264] L. Hedin and S. Lundquist. *Solid State Physics Vol. 23 ed. by H. Ehrenreich, F. Seitz and D. Turnbull.* Academic, New York, 1969.

[265] G. Borstel. Theoretical aspects of photoemission. *Appl. Phys. A*, 38:193, 1985.

[266] X. J. Zhou et al. *Handbook of High-Temperature Superconductivity: Theory and Experiment ed. by J. S. Brooks and J. R. Schrieffer.* Springer, Berlin Heidelberg, 2007.

[267] M. P. Seah and W. A. Dench. Quantitative electron spectroscopy of surfaces: A standard data base for electron inelastic mean free paths in solids. *Surf. Interf. Anal.*, 1:2, 1979.

[268] C. N. Berglund and W. E. Spicer. Photoemission studies of copper and silver: Theory. *Phys. Rev.*, 136:A1030, 1964.

[269] D. A. Shirley. High-resolution x-ray photoemission spectrum of the valence bands of gold. *Phys. Rev. B*, 5:4709, 1972.

[270] W. A. Gardner. *Introduction to random processes.* McGraw-Hill, New York, 1985.

[271] H. G. Natke. *Einführung in Theorie und Praxis der Zeitreihen- und Modalanalyse.* Vieweg, Braunschweig Wiesbaden, 1988.

[272] A. Schuster. citation not confirmed by author/ provided by wikipedia.de. *Terrestrial Magnetism and Atmospheric Electricity*, 3:13, 1898.

[273] G. M. Jenkins and M. B. Priestley. The spectral analysis of time series. *Journ. Royal Stat. Soc. B*, 19:1, 1966.

[274] J. W. Cooley and J. W. Tukey. An algorithm for the machine calculation of complex Fourier series. *Math. Comput.*, 19:297, 1965.

[275] R. B. Blackman and J. W. Tukey. *The measurement of power spectra.* Dover Publications, New York, 1959.

[276] F. J. Harris. On the use of windows for harmonic analysis with the DFT. *Proc. IEEE*, 66: 51, 1978.

Selbständigkeitserklärung

Hiermit versichere ich, die vorliegende Arbeit selbständig und ohne unerlaubte fremde Hilfe angefertigt zu haben. Ich versichere, mich nicht anderweitig um einen Doktorgrad beworben zu haben. Die dem Verfahren zu Grunde liegende Promotionsordnung der Mathematisch-Naturwissenschaftlichen Fakultät I der Humboldt-Universität zu Berlin habe ich zur Kenntnis genommen.

Lenart E. Dudy